TeraWatt

# TeraWatt Position Papers

## A "toolbox" of methods to better understand and asses the effects of tidal and wave energy arrays on the marine environment.

Published by MASTS

University of the Highlands and Islands
Oilthigh na Gàidhealtachd agus nan Eilean

THE UNIVERSITY of EDINBURGH

HERIOT WATT UNIVERSITY

University of Strathclyde Glasgow

University of St Andrews

Swansea University Prifysgol Abertawe

EPSRC
Engineering and Physical Sciences Research Council

SUPERGEN UKCMER

marinescotland science

The Scottish Government
Riaghaltas na h-Alba


## TeraWatt Consortium

The project consortium formed under the Marine Alliance for Science and Technology for Scotland (MASTS) consists of scientists from Heriot Watt University, University of Edinburgh, University of Strathclyde, University of the Highlands and Islands, University of Swansea and the University of St Andrews together with Marine Scotland Science.

National co-ordination with other Marine Challenge Fund projects will be achieved through SUPERGEN UKCMER.

**The TeraWatt Consortium gratefully acknowledges financial support for this work from the EPSRC Grand Challenge award (EPSRC Grant Ref: EP/J010170/1), and contributions from Marine Scotland Science and the Marine Alliance for Science and Technology in Scotland (MASTS). We acknowledge the support of the various representatives who have served on the Steering Group for this research and would like to thank the numerous industry personnel who have contributed to these meetings and our workshops and discussions, from the software, marine renewables device and project developer community. A special thanks should go to those organisations who provided data for the research.**

# CONTENTS

# DATA ACQUISITION AND PROCESSING FOR TERAWATT

# 01

R.B. O'Hara Murray

MARINE SCOTLAND SCIENCE,
SCOTTISH GOVERNMENT, MARINE LABORATORY, 375 VICTORIA ROAD, ABERDEEN, AB11 9DB

AUGUST 2015: REVISION 1.1

back to contents

## 01/1 INTRODUCTION

This report is the first of a series of position papers produced by the Engineering and Physical Science Research Council funded TeraWatt project. One aim of the TeraWatt project was the development of numerical regional scale wave and tidal hydrodynamic models for the assessment of the consequences of wave and tidal energy extraction on the physical and ecological environment. The project focused on the Pentland Firth and Orkney Waters (PFOW), although the Scottish east coast was also modelled as part of a sediment transport study. The main purpose of the models was to simulate the hydrodynamics for both baseline cases and cases with tidal and/or wave energy extraction, enabling an assessment of the changes to be made. Regional scale hydrodynamic models require a number of different datum types for pre-processing, e.g. preparing the model bathymetry, and post-processing, e.g. validating the model output with observational data.

A large number of datasets were amassed during the TeraWatt project. The aspiration of the project was to use only data that were freely available, in order for others to use the same data easily. However, on a number of occasions it became apparent that the most suitable data would require special permissions and/or licences.

The Crown Estate (TCE) has performed a similar exercise to aid their modelling studies (The Crown Estate, 2012b), and have shared some of the data gathered with the TeraWatt project. One of the gaps identified during the project was a lack of measurements of current speeds and directions in the area. This is undoubtedly partly because the extreme current speeds make measurements particularly challenging. Therefore, Marine Scotland Science (MSS) conducted a number of instrument deployments and vessel surveys during the TeraWatt project to obtain additional data for model validation.

This collection of data now forms a unique dataset. The aim of this report is to list the data, provide metadata, provide some rationale behind why they were used within the project, and, in the case of the freely available data, to direct others to where these data can be obtained. This report divides the measured data into broad types: bathymetry (Section 01/2), coastline (Section 01/3), seabed sediments (Section 01/5), water elevations (Section 01/6), currents (Section 01/7) and waves (Section 01/8). Section 01/9 reports on the modelled data used within TeraWatt, primarily for model forcing and boundary conditions. Finally, Section 01/10 examines which data were the most useful for TeraWatt and presents a table listing where the data can be obtained.

## 01/2 BATHYMETRY DATA

Bathymetry data were required early on in the model development process and a number of datasets were amassed, including multi beam echo sounder (MBES) data, digitalized admiralty chart data, data amalgamated from ships' echo sounders and satellite altimetry data. In addition to these data, TCE also examined data from three more sources. Figure 1.1 shows the extent of the bathymetry data obtained by TCE, which includes much of the high resolution data that were independently obtained by the TeraWatt project.

### 01/2.1 BATHYMETRY DATA PROVIDED BY THE CROWN ESTATE

The Crown Estate (TCE) made both a MIKE21-FM-SW wave and a MIKE21-FM-HD tidal model available to the TeraWatt project, together with most of the underlying bathymetry data. These models were originally commissioned by TCE to better understand the marine energy resource of the PFOW and to develop a baseline understanding of the area to help assess the future exploitation of the resource (The Crown Estate, 2012a). As part of the TCE modelling projects, a comprehensive review of the available bathymetry data was conducted by ABP Marine Environmental Research Ltd (The Crown Estate, 2012b), and a combined dataset was created. A number of key sources of data were identified and these are shown in Figure 1.1. Figure 1.1 shows that a large area of the PFOW has been surveyed at high resolution using MBES by the UK Hydrographic Office (UKHO), the Maritime and Coastguard Agency (MCA), and MSS. TCE also identified a small section covering the Sandy Riddle feature (east of the Pentland Firth) collected as part

of the UK Governments Strategic Environmental Assessment 5 (SEA 5). One dataset identified covering a large spatial area (Smith & Sandwell, 1997) had a relatively coarse resolution of 900 m. These data covered a large area of the PFOW but there were significant gaps in the high resolution data. These gaps were filled using data from the Digital Elevation Model (DEM) developed on behalf of Department of Environment, Food & Rural Affairs (DEFRA) (Astrium OceanWise, 2011). The combined bathymetry dataset was created by adjusting all the data to common datums and interpolating to a 20 m regular grid (The Crown Estate, 2012b). The newer high resolution, and openly available, bathymetry was prioritized, with the lower resolution data only filling gaps where necessary.

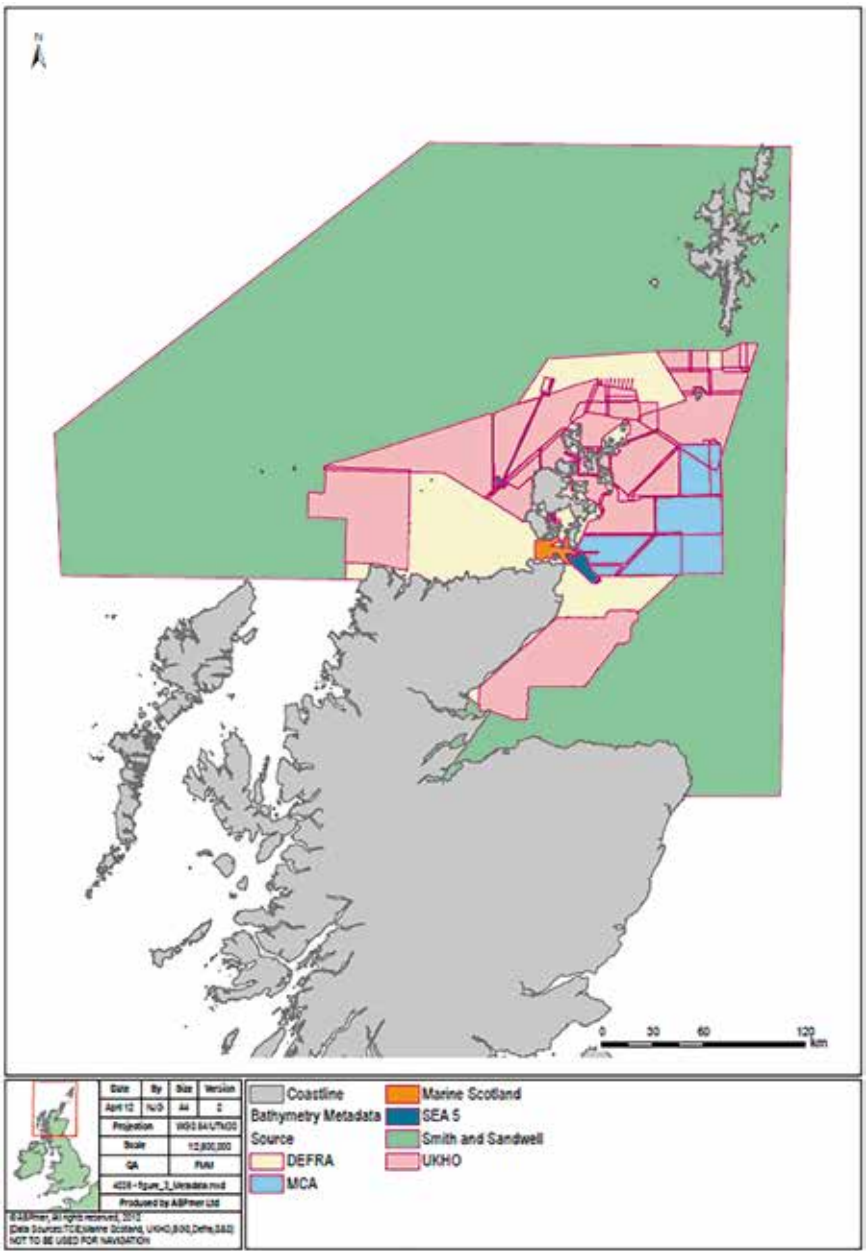


**Fig 1.1** The spatial extent of bathymetry data obtained by (after The Crown Estate, 2012b).

The derived dataset, on a 20 m grid, proved to be most valuable during the TeraWatt project, as it was deemed to be of a suitable spatial resolution for interpolation onto the hydrodynamic and waves model grids. This was because it was a good balance between file size and being of high enough resolution to resolve all the bathymetric features that would be resolved by the model grid (with length scales typically of the order 100 m).

TCE also commissioned a number of surveys west of Orkney mainland (The Crown Estate, 2012c), see Section 01/4 for further information. These surveys included MBES surveys of the nearshore zone to the 2 m depth contour in some places. Figure 1.2 shows an extract of the data obtained from the Bay of Skaill, which was an area of interest to the TeraWatt project.

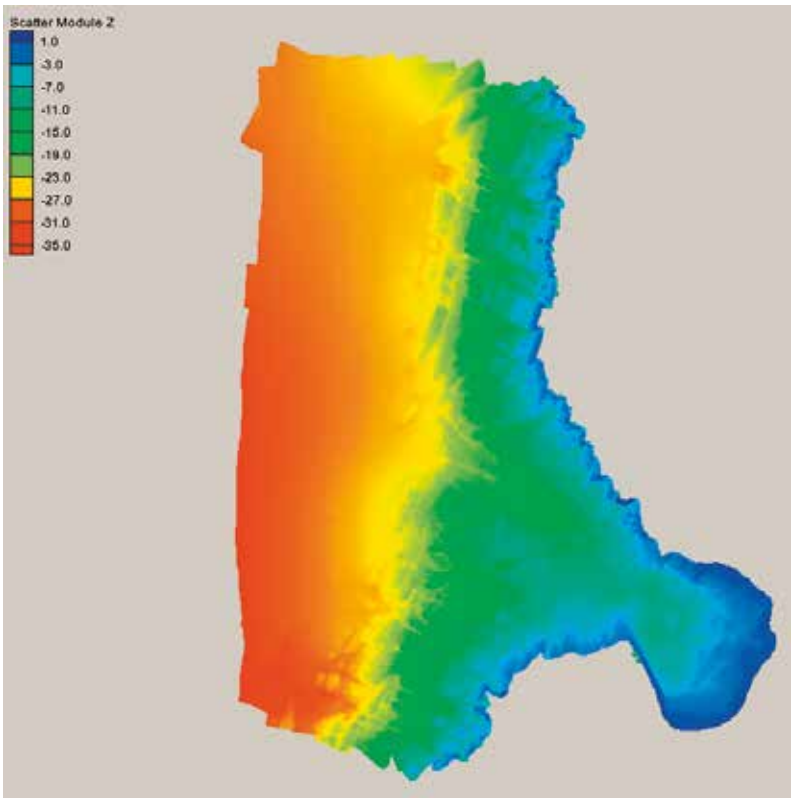


**Fig 1.2** Multi beam echo sounder bathymetry data for the Bay of Skaill and surrounding areas, provided by TCE (The Crown Estate, 2012c).

## 01/2.2 UKHO BATHYMETRY DATA

During the course of the TeraWatt project, MSS carried out a desk exercise to gather bathymetry data for an independent project on the modelling of Scottish Shelf waters. The MBES data from around the PFOW obtained from the UKHO generally had a very fine spatial resolution which proved to be unmanageable, due to limitations in computational power, when incorporating these data into the Scottish Shelf waters models. The typical resolution was considerably higher than the smallest model grid elements being considered, which was of the order 100 m. The resolution was therefore reduced and combined into a single dataset. Figure 1.3 shows the extent of these data, along with the data obtained by MSS and ICIT (see Sections 01/2.3 and 01/2.4).

Since the initial data gathering phase of the TeraWatt project, the UKHO have introduced a new data portal in compliance with the Infrastructure for Spatial Information in Europe (INSPIRE) initiative. The UKHO are accredited by the Marine Environmental Data and Information network (MEDIN) as the national Data Archive Centre for bathymetric surveys, and have a geospatial viewer for convenient data visualization and download, https://www.gov.uk/inspire-portal-and-medin-bathymetry-data-archive-centre.

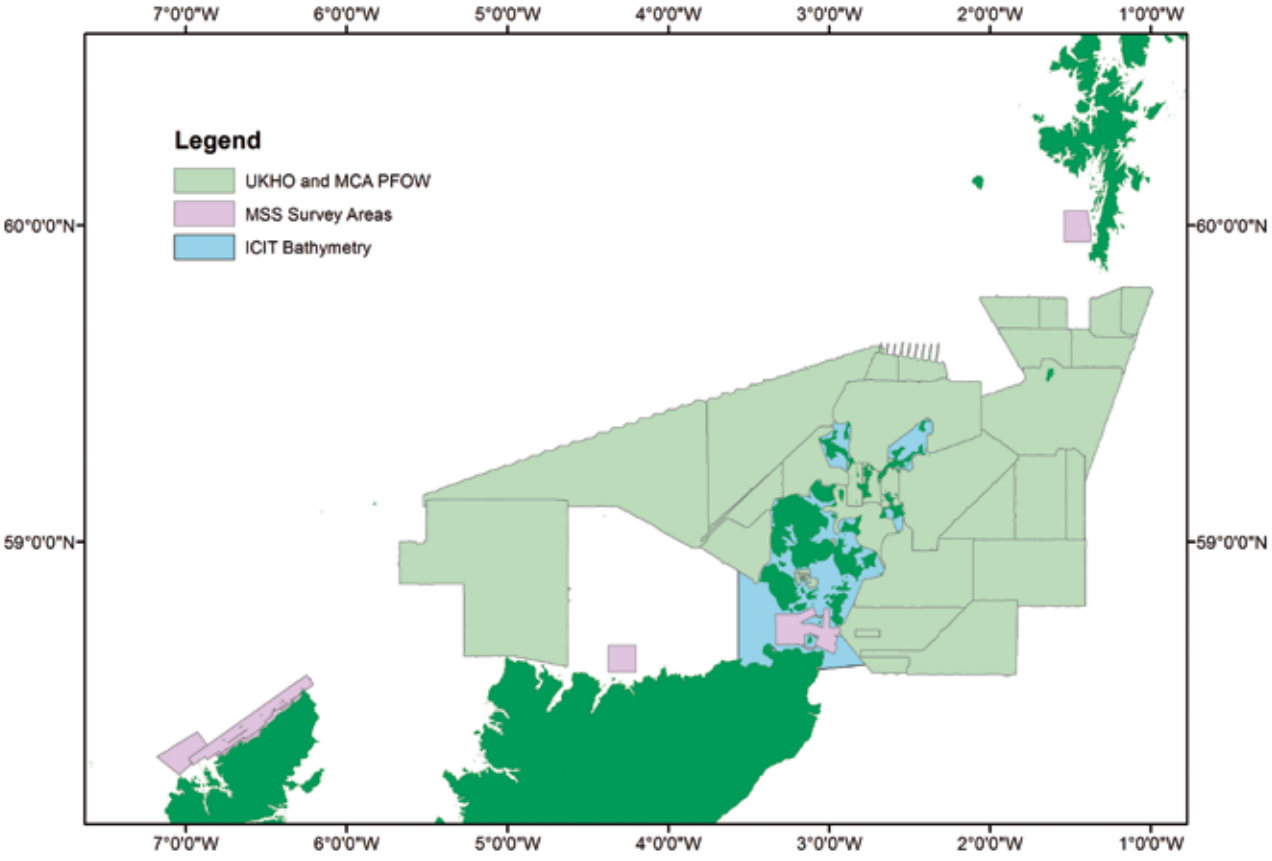


**Fig 1.3** The spatial extent of bathymetry data from the UKHO, MSS and ICIT.

## 01/2.3 MARINE SCOTLAND SCIENCE BATHYMETRY DATA

MSS has conducted a number of MBES bathymetry surveys in areas of potential renewable energy developments. These areas include the Pentland Firth and the west coast of Lewis. These data are publicly available on Marine Scotland Interactive, http://www.scotland.gov.uk/Topics/marine/science/MSInteractive, in a variety of file formats. Figure 1.3 shows the extent of the data.

## 01/2.4 ADMIRALTY CHART BATHYMETRY DATA FROM ICIT

The International Centre for Island Technology (ICIT), Heriot-Watt University, have previously digitalized admiralty chart data for model development. These data were made available for TeraWatt as potential data for filling the gaps between higher resolution datasets. Figure 1.3 shows the extent of these data around Orkney.

## 01/2.5 STONEHAVEN BATHYMETRY DATA

In 2006, MSS carried out a MBES bathymetry survey off Stonehaven between latitudes of 56°54' – 57°03' N and 2-12 km from the shore (Serpetti, Heath, Armstrong, & Witte, 2011). These data were used within the TeraWatt consortium in the development of a hydrodynamic model of the Stonehaven area.

## 01/3 COASTLINE DATA

Coastline data are a useful way of defining the coastal boundary of hydrodynamic models. One source of coastline data used within TeraWatt was the Global Self-consistent, Hierarchical, High-resolution Geography Database (GSHHG) available from the NOAA National Centers for Environmental Information (https://www.ngdc.noaa.gov/mgg/shorelines/gshhs.html). These data are based on the World Vector Shorelines (WVS) and CIA World Data Bank II (WDBII) datasets.

## 01/4 TCE WEST OF ORKNEY DATA

The Crown Estate commissioned a detailed nearshore survey west of Orkney Mainland which was conducted between August 2011 and July 2012 (The Crown Estate, 2012c). The survey primarily focused on the collection of multibeam and singlebeam echo sounder data, sidescan sonar data and magnetometer data. Figure 1.4 shows the spatial extent of this survey.

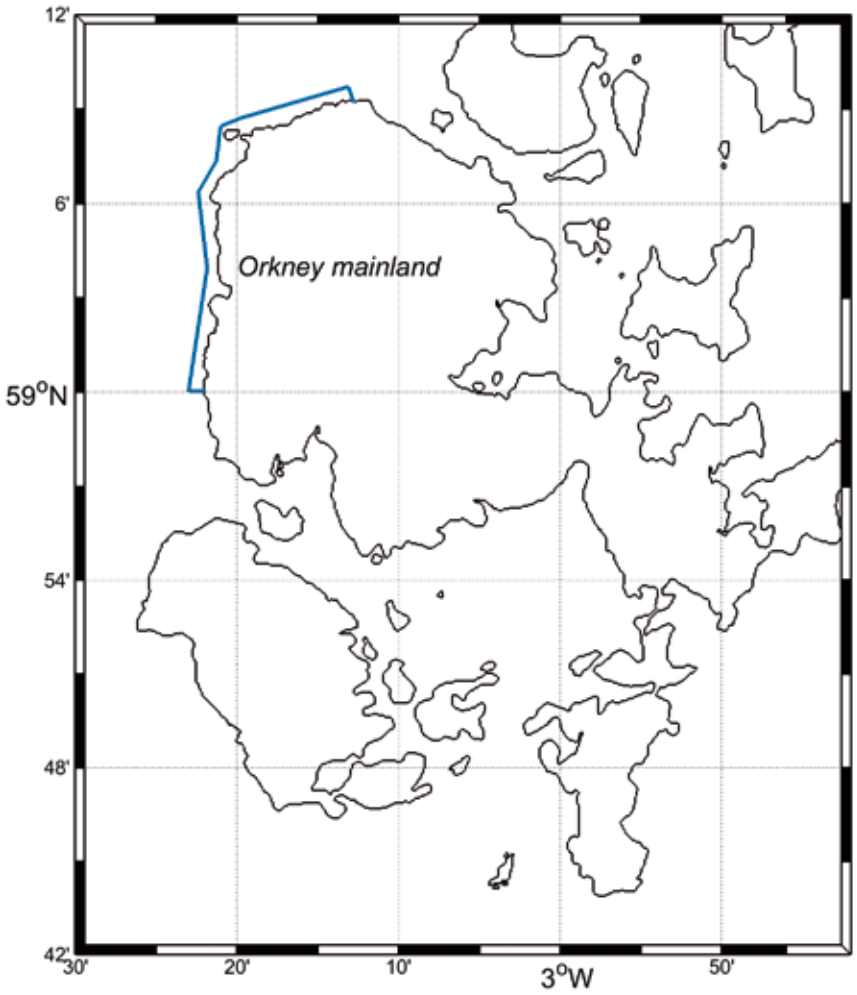


**Fig 1.4** The nearshore zone around the west of Orkney mainland (blue line) surveyed between August 2011 - July 2012.

back to contents

# 01/5 SEABED SEDIMENTS DATA

## 01/5.1 BRITISH GEOLOGICAL SOCIETY SEDIMENTS DATA

The British Geological Society (BGS) provided a database of sediment samples (British Geological Survey, 2013), mainly consisting of seabed samples. These data have been used previously by the BGS to construct a map of sediment type using the Folk classification scheme. This database of sediment samples includes these Folk classifications, but also the percentage mud/sand/gravel, results from a carbonate test, and results from sieving the sediments at either $0.5\phi$ or $1.0\phi$ intervals, where $\phi = -log_2(D/D_0)$ and $D$ and $D_0$ are the sediment grain diameter and a reference diameter, usually 1 mm, respectively. Figure 1.5 shows the extent of the sediment samples, the distribution of samples dominated by gravel/sand/mud and what type of particle size analysis was performed. Note that particle size analysis data were not always available. The database made available to TeraWatt was approximately 90% complete as the BGS is continuing to compile data from samples taken in the recent past.

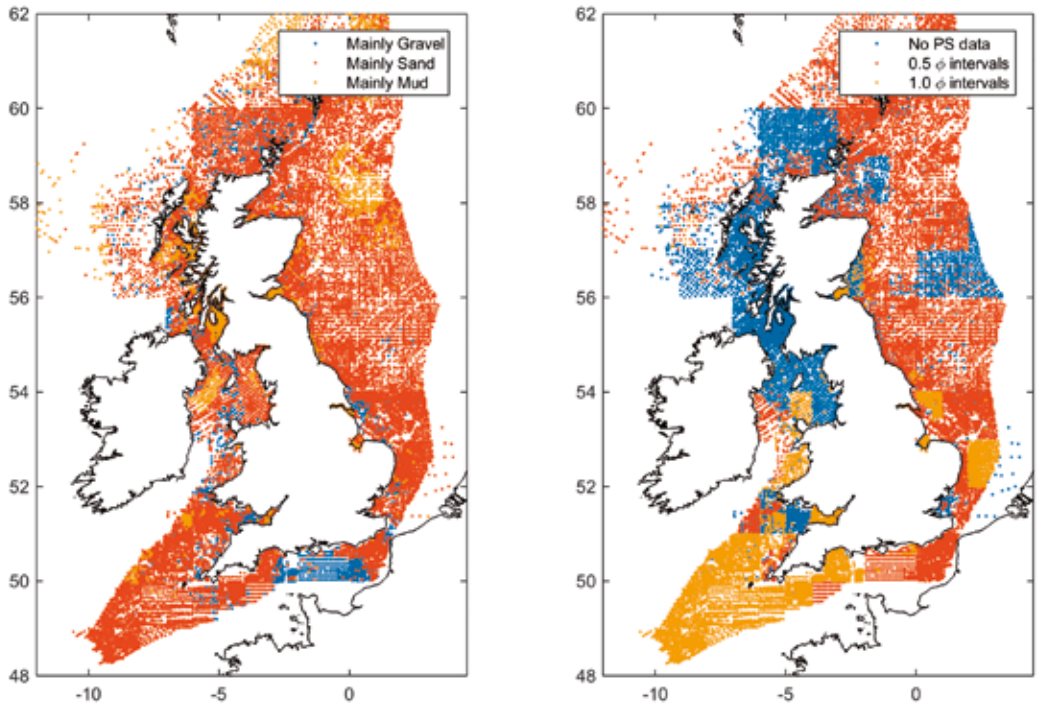


**Fig 1.5** British Geological Survey bed sediment sample locations. (LHS) The spatial distribution of samples dominated by gravel, sand and mud. (RHS) The location of samples where there was no particle size (PS) analysis and sieving at $0.5\phi$ and $1.0\phi$ intervals.

The results from the sieved data were saved in the database as a mass distribution in the form of the weight of sediment that has not passed through each sieve. This kind of distribution can be thought of as a "coarser-than" distribution. The mass distributions were converted to cumulative distributions and the median grain size of each distribution was calculated by fitting a line between class intervals either side of 50%. Figure 1.6 shows a map of the calculated median grain diameters.

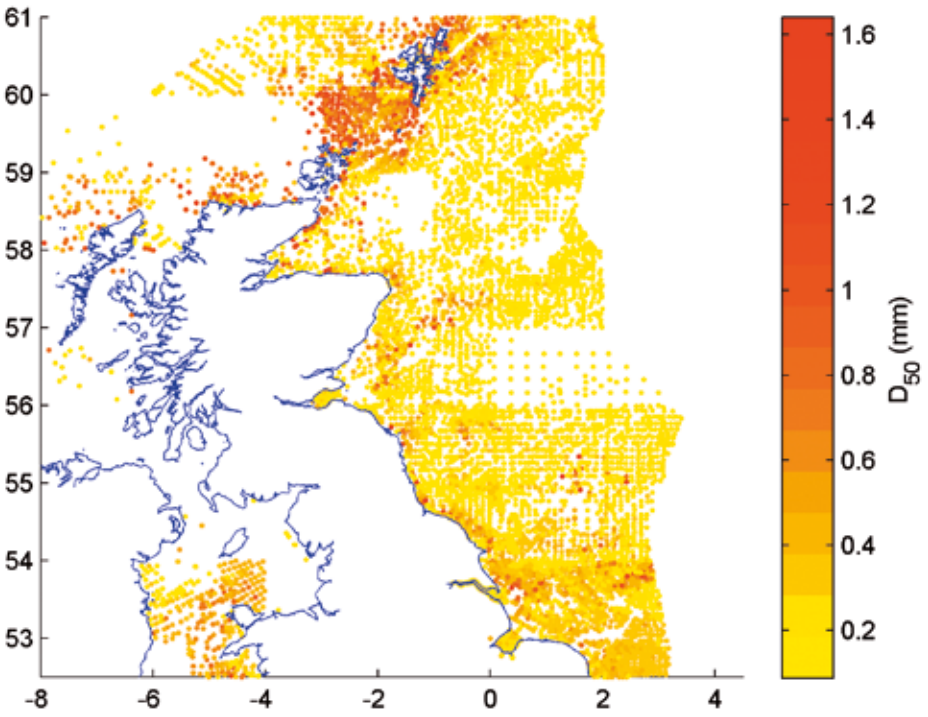


**Fig 1.6** Calculated median grain diameters ($D_{50}$) based on the sieved BGS sediment samples.

These data are now freely available under Open Government Licence on the Internet (http://www.bgs.ac.uk/GeoIndex/offshore.htm).

## 01/5.2 STONEHAVEN SEDIMENTS DATA

Single beam RoxAnn acoustic surveys (SIMRAD EK60 38 kHz echo sounder) were carried out by MSS off Stonehaven in 2006 and 2008 between latitudes 56° 54' – 57° 03' N and 2-12 km from the shore (Serpetti, Heath, Rose, & Witte, 2012). These acoustic data were used to map the seabed sediment at high resolution (Serpetti et al., 2012) which was used by TeraWatt to conduct sediment transport modelling in the Stonehaven hydrodynamic MIKE model.

## 01/6 WATER ELEVATION MEASUREMENTS

The UK National Tide Gauge Network consists of 44 coastal locations recording tidal elevations. Data from a number of locations were used during the TeraWatt project. These data are available from the British Oceanographic Data Centre, http://www.bodc.ac.uk/projects/uk/ntslf.

## 01/7 CURRENTS MEASUREMENTS

## 01/7.1 GARDLINE PENTLAND FIRTH ADCP DATASET

The Maritime and Coastguard Agency contracted Gardline to make a number of tidal stream observations in and around the Pentland Firth in September 2001 (Gardline Surveys, 2001). These data were made available to the TeraWatt consortium by David Woolf, Environmental Research Institute, The North Highland Collage, University of the Highlands and Islands. These measurements consisted of three 30-day fixed upward looking ADCP deployments, starting on 14 September 2001, and four vessel mounted ADCP transects along the boundaries of the Pentland Firth. Figure 1.7 shows the position of the four VMADCP surveys conducted. The vessel mounted ADCP measurements were made between 17-23 September 2001.

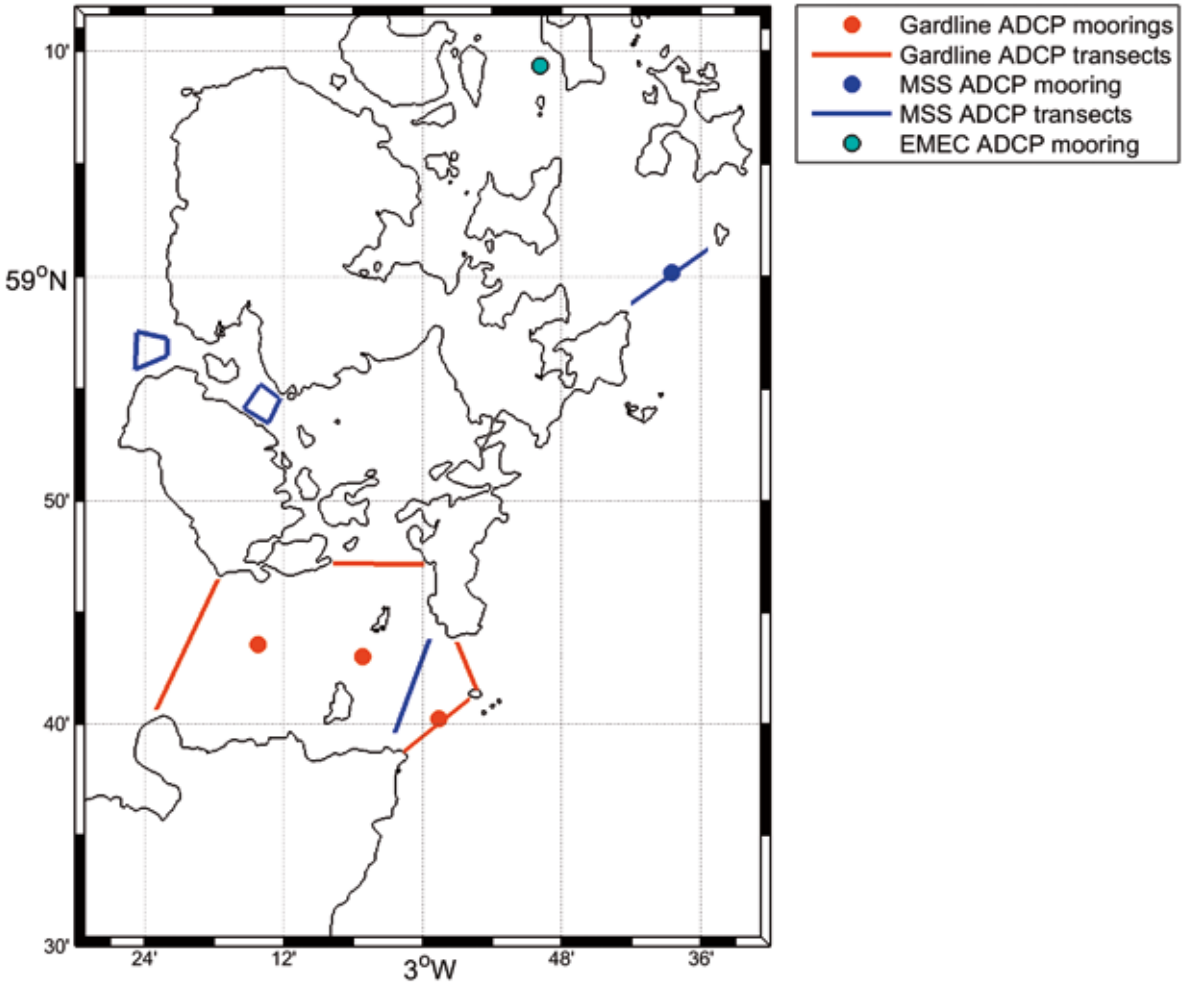


**Fig 1.7** The location of the Gardline, Marine Scotland Science (MSS) and European Marine Energy Centre (EMEC) ADCP measurements used in the TeraWatt project.

back to contents

## 01/7.2 EMEC ADCP DATA

The European Marine Energy Centre (EMEC) have deployed a number of ADCPs within the Fall of Warness test area. A 12 week ADCP dataset, starting on 14 July 2010, were purchased by the TeraWatt project. The ADCP was deployed at 59° 9.360' N, 02° 49.860' W (Figure 1.7). These data were primarily used for hydrodynamic model calibration and validation.

## 01/7.3 MARINE SCOTLAND SCIENCE DATA

### 01/7.3.1 CURRENT METER DATA

MSS have a number of current meter datasets around Scotland which have been obtained through various projects over the last 50 years. Figure 1.8 shows the location of these data near Orkney by decade. The data gathered in 2008 in the Fair Isle channel were of interest to TeraWatt and were made available to TeraWatt.

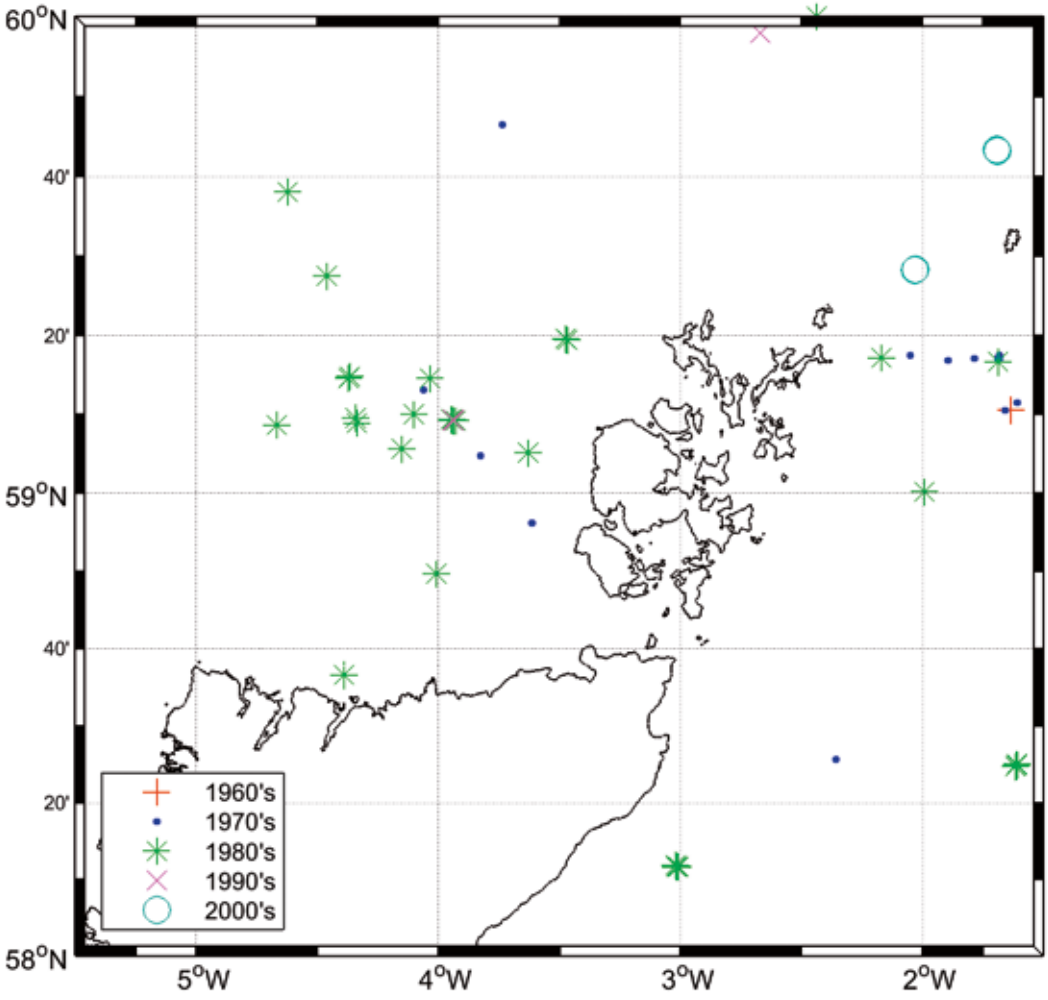


**Fig 1.8** Marine Scotland Science current meter data around Orkney.

Figure 1.9 shows the location of data off the east coast of Scotland. All these data, and metadata, were made available to TeraWatt.

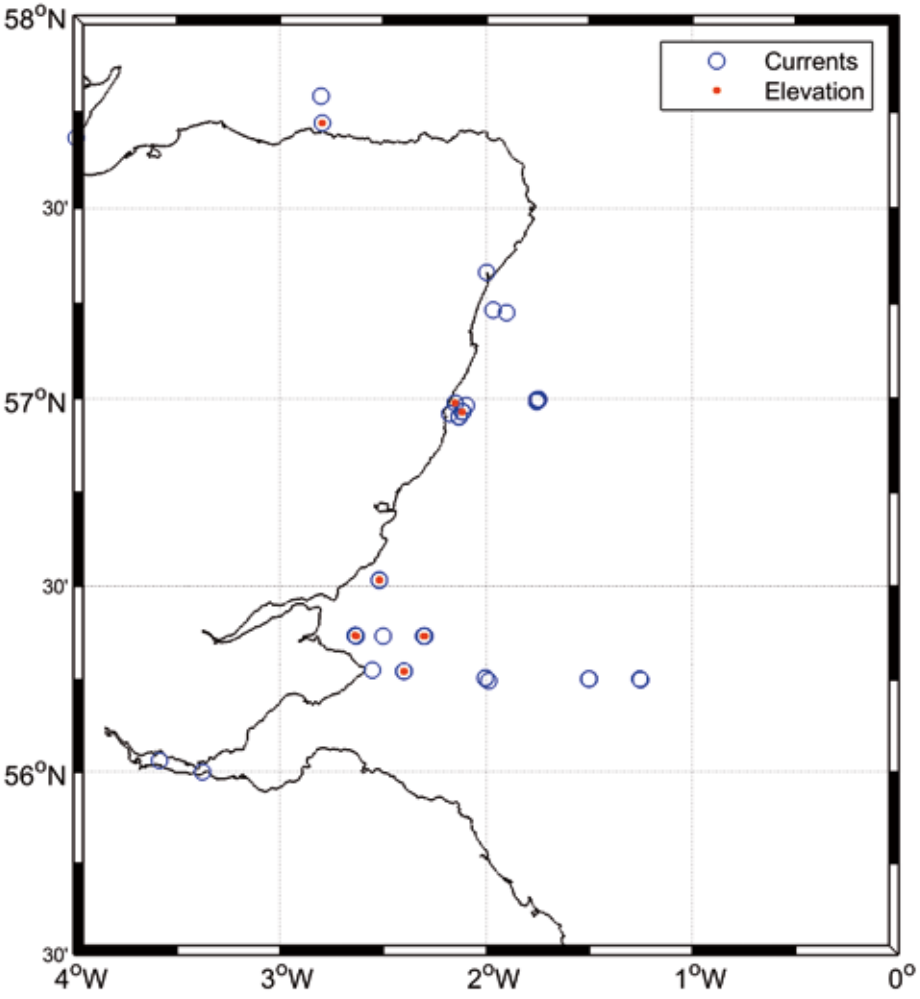


**Fig 1.9** Marine Scotland Science current meter data off the east coast of Scotland.

## 01/7.3.2 ADCP DATA FROM STRONSAY FIRTH

MSS deployed a Workhorse Sentinel 600 kHz ADCP in Stronsay Firth on 21/05/2014. The processed data were exported to ASCII format for the TeraWatt project. The ADCP was deployed in an instrument frame on the bed, upward looking, for 12 hours at 59° 00.17' N, 02° 38.52' W, where the water depth was 42 m (Figure 1.7). The bin size was 2.0 m and the ensemble interval was 5 minutes.

## 01/7.3.3 VESSEL MOUNTED ADCP DATA

During the TeraWatt project, MSS conducted a number of vessel mounted ADCP (VMADCP) surveys around Orkney. Figure 1.7 shows the position of the four VMADCP surveys conducted. Each transect was repeated for approximately an M2 tidal cycle, whilst the ship (Scotia) sailed at approximately 5 knots. The vertical bin size was typically set to 4 m. The Hoy Sound and Hoy Mouth surveys were conducted in December 2012 and the transects formed squares. The Hoy Mouth square transects were repeated for 15 hours and the Hoy Sound Survey was conducted for 12 hours. On 21-22 May 2013, MSS conducted a vessel mounted ADCP survey at the eastern end of the Pentland Firth. The transect line ran NE-SW between Duncansby Head and South Ronaldsay. Nine repeat transects were completed in approximately 15 hours, between 14:27 on 21/5/2014 and 05:09 on 22/5/2014. On 20-21 May 2013, MSS conducted a VMADCP survey at the southern end of Stronsay Firth. The transect line ran NE to SW between Orkney mainland Auskerry. Eight repeat transects were completed in approximately 14 hours, between 20:40 on 20/5/2014 and 10:14 on 21/5/2014.The VMADCP data underwent a quality control process prior to ensemble averaging over the measured profiles. Three ensemble averaging methods were used. Ensemble averages were taken over (i) 20 pings (approximately 30 seconds), (ii) 100 m sections of the transects, and (iii) a time period (30 seconds for Pentland and Stronsay Firth transects, 60 seconds for the Hoy transects).

Figure 1.10 presents the results from the Pentland Firth SW-NE transect (Duncansby Head towards South Ronaldsay) and shows that current speeds reached approximately 3 m $s^{-1}$. The first transect was around slack water with slow speeds, transects 2-4 show the flood tide, transects 5 again shows slack water, and transects 6-9 show the ebb tide.

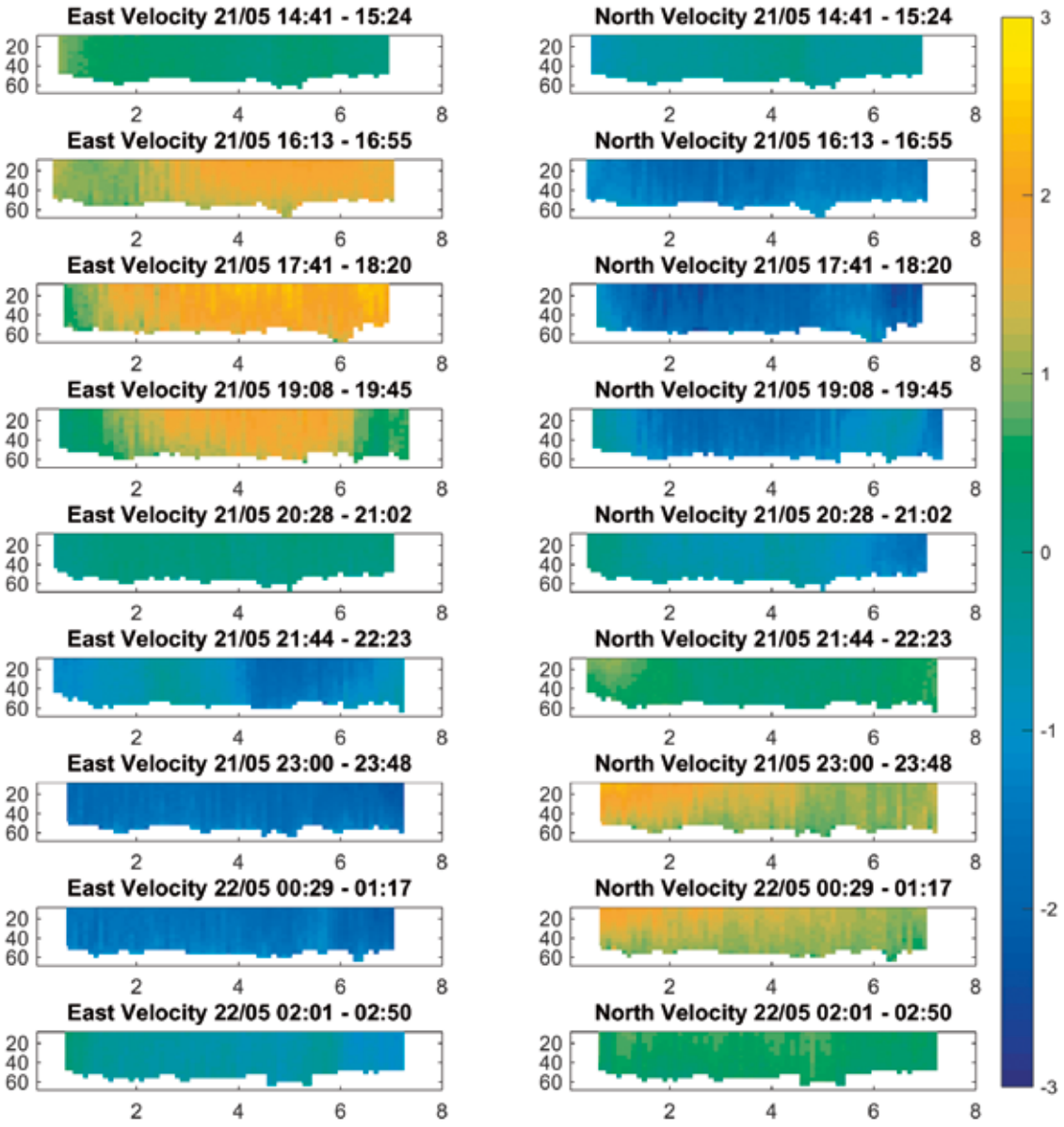


**Fig 1.10** Example VMADCP velocities from the 9 transects along a transect at the eastern end of the Pentland Firth from Duncansby Head towards Ronaldsay (SW-NE). The colour scale is velocity (m $s^{-1}$). The horizontal axis is distance along the transect (km).

Figure 1.11 presents the results from the 8 repeat transects from Auskerry to Orkney mainland (NE-SW) in Stronsay Firth. Figure 1.11 shows that current speeds reached a maximum of 1 m $s^{-1}$. The tidal cycle is visible in the data, with the north velocity initially being positive, towards the north, during the ebb tide, becoming approximately slack during transect 4, and being negative, towards the south, during the flood tide.

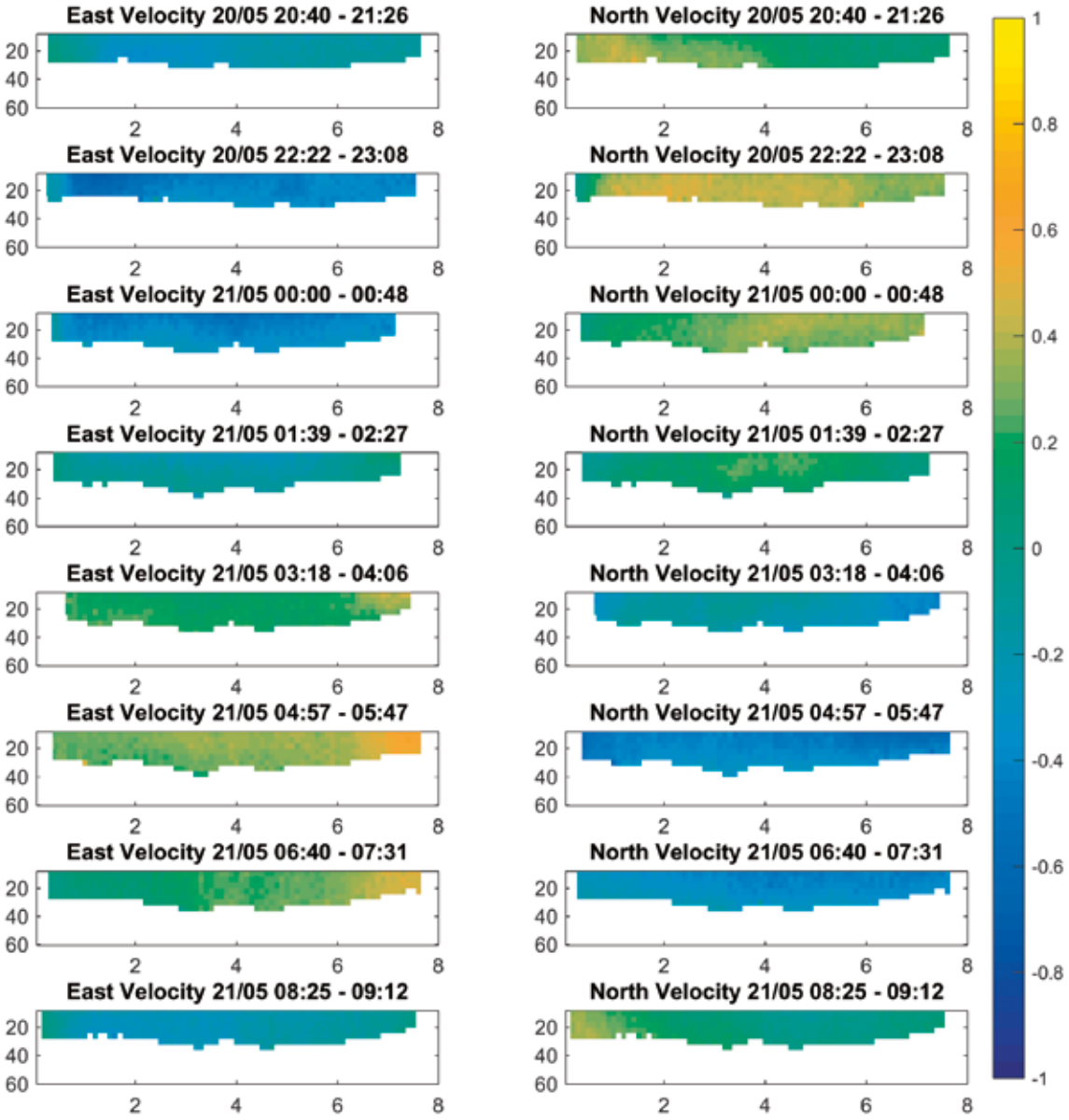


**Fig 1.11** Example VMADCP velocities from the 8 transects along the Auskerry to Orkney mainland (NE-SW) transect in Stronsay Firth. The colour scale is velocity (m $s^{-1}$). The horizontal axis is distance along the transect (km).

## 01/8 WAVES MEASUREMENTS

### 01/8.1 EMEC WAVES DATA

The European Marine Energy Centre has a wave energy test centre, Billia Croo, off the west coast of Orkney mainland. Data from wave rider buoy deployed at Billia Croo at position 58° 58.214' N, 03° 23.454' W were purchased for the TeraWatt project. These data consisted of wave statistics for two complete years, 2010 and 2012, and the 30 minute binned wave statistics and directions were used for model calibration and validation within the TeraWatt project.

### 01/8.2 CEFAS WaveNet

The Centre for Environment, Fisheries and Aquaculture Science (Cefas) have a strategic wave monitoring network, WaveNet, for the United Kingdom. This is a network of wave rider buoys primary sited close to coastal areas at risk of flooding (https://www.cefas.co.uk/publications-data/wavenet/). Most of the data are freely available under an Open Government Licence, although some are restricted to non-commercial government and academic use (http://cefasmapping.defra.gov.uk/). Some of the data can be downloaded for commercial use subject to an extraction fee.

### 01/8.3 HEBRIDEAN MARINE ENERGY FUTURES PROJECT

As part of the Hebridean Marine Energy Futures project (Vögler & Venugopal, 2012) a wave rider buoy was deployed off Bragar, west coast of the Isle of Lewis, Scotland. These data were available for the TeraWatt project for the calibration and validation of spectral wave models.

### 01/8.4 ABERDEEN BAY WAVE RIDER BUOY

The University of Aberdeen deployed a Datawall directional wave rider buoy about 1.5 km off Aberdeen Bay in November 2009. The buoy was positioned at 57° 09.65' N, 02° 03.00' W in a water depth of 10 m CD. The dataset is for approximately 14 months between 1 November 2007-31 May 2009, with gaps between 10 August-1 October 2008 and 9 December 2008-6 March 2009 due to the buoy parting its moorings. These data were made available to the TeraWatt project, for the east coast wave modelling, by Prof. Tom O'Donoghue, University of Aberdeen.

## 01/9 MODELLED DATA

A number of different sources of modelled data were used in the TeraWatt project. These data were typically used to provide model forcing and boundary conditions.

### 01/9.1 TIDAL MODEL DATA

The Oregon State University Tidal Prediction Software (OTPS) is a well-known open source barotropic tidal model based on the Oregon State University tidal inversion of TOPEX/POSEIDON altimeter data and tide gauge data (Egbert, Erofeeva, & Ray, 2010). This model was used in the TeraWatt project to provide boundary conditions for DELFT 3D tidal models. The model can be obtained from http://volkov.oce.orst.edu/tides/otps.html and there is also a Matlab implementation available from http://polaris.esr.org/ptm_index.html. There are both global and regional tidal solutions obtained using the Oregon State University Tidal Inversion Software (OTIS). The global solution is on a 1/4 degree grid and the European Shelf solution, used within TeraWatt, is on a 1/30 degree grid. The MIKE models used the Danish Hydraulic Institute's global tide model, which is also based on the TOPEX/POSEIDON altimeter data, as boundary conditions.

### 01/9.2 ATMOSPHERIC MODEL DATA

A number of the TeraWatt models required atmospheric and wind forcing data across the domain. The wave models, for example, required wind forcing to simulate the local wind generated waves across the domain. Data were obtained from the European Centre for Medium Range Weather Forecast (ECMWF) ERA-40 atmospheric model (Dee et al., 2011). These data can be downloaded from the ECMWF website, http://www.ecmwf.int/en/research/climate-reanalysis/browse-reanalysis-datasets.

## 01/9.3 UKHO VERTICAL OFFSHORE REFERENCE FRAME

The UK Hydrographic Office (OKHO) have developed the Vertical Offshore Reference Frame (VORF) model to convert between vertical datums, such as chart datum, mean sea level and lowest astronomic tide. This tool enabled TeraWatt consortium to convert the bathymetry data from one datum to another. For example, bathymetry data often use chart datum whereas it makes more sense to specify bathymetry relative to mean sea level within hydrodynamic models. The model output consists of surfaces specifying the difference in height between different datums, and is gridded at 0.008 degree intervals. Output form the VORF model was made available to TeraWatt by the UKHO under an Open Government Licence.

## 01/10 CONCLUSIONS

The TeraWatt project developed 3D hydrodynamic ocean models in order to assess the impact of tidal and wave energy development on the physical and ecological environment. The project focused on the PFOW due to this area being of considerable interest to the marine renewable energy industry. Regional scale models require the use of a number of spatial data types in order to realistically simulate the chosen region. This report outlines a number of data obtained during the TeraWatt project, which now forms a unique dataset ideally suited for the development of hydrodynamic models of this region. This dataset therefore contributes to the methods toolbox developed by the TeraWatt consortium. Table 1.1 lists the data reported on here, together with a brief description and, for some data, where they can be found on the TeraWatt FTP site and/or on the Internet.

The bathymetry data examined included a large proportion of MBES covering almost the whole PFOW region. These freely available data are useful for future hydrodynamic model development, especially the reduced resolution data held by MSS. However, the TeraWatt project opted to use the 20 m regular gridded bathymetry developed by ABPmer on behalf of TCE (The Crown Estate, 2012b), which included data from the DEM product (Astrium OceanWise, 2011), because it did not require any gaps to be filled and was of a suitable resolution. It is worth noting though that this dataset was based on much of the high resolution MBES data that are freely available.

The BGS sediments data, that are now available on the UKHO INSPIRE portal, proved to be of primary importance for the sediment transport aspects of the project. Whilst the particle size analysis of these samples did not have a great number of size classes, they were sufficient to get estimates of the median grain size for use within sediment transport models.

It was extremely important for the TeraWatt models to be well validated and the scarcity of measurements of tidal currents and waves presented a number of challenges. The dataset that proved to be of most value for the tidal model development was the Gardline dataset consisting of three simultaneous ADCP measurements in the Pentland Firth. The lack of data was an issue which is why the EMEC ADCP data from the Falls of Warness were purchased for the project. MSS also made additional ADCP measurements in Stronsay Firth. The vessel mounted ADCP data presented a number of difficulties for the TeraWatt consortium due to the complex data analysis required to interpret the data varying in both space and time and to compare these with model output.

## 01/11 ACKNOWLEDGEMENTS

The TeraWatt project was funded by the Engineering and Physical Science Research Council SUPERGEN Marine Challenge. The TeraWatt consortium would like to thank The Crown Estate for providing their MIKE models including model output and much of the underlying bathymetry data; the Maritime and Coastguard Agency, and the Environmental Research Institute, Thurso, for supplying the Gardline ADCP data; the United Kingdom Hydrographic Office for bathymetry data; Marine Scotland Science for a number of data (including additional ADCP surveys by the Oceanography group) and providing the TeraWatt FTP site; and Prof. Tom O'Donoghue, University of Aberdeen, for the waves data.

## 01/12 REFERENCES

Astrium OceanWise. (2011). *Creation of a high resolution digital elevation model (DEM) of the British Isles continental shelf.* DEFRA Report ref: Contract 13820.

British Geological Survey. (2013). *BGS Legacy Particle Size Analysis uncontrolled data export, British Geological Survey.* Retrieved from www.bgs.ac.uk.

Dee, D. P., Uppala, S. M., Simmons, A. J., Berrisford, P., Poli, P., Kobayashi, S., ... Vitart, F. (2011). *The ERA-Interim reanalysis: configuration and performance of the data assimilation system.* Quarterly Journal of the Royal Meteorological Society, 137(656), 553–597. http://doi.org/10.1002/qj.828.

Egbert, G. D., Erofeeva, S. Y., & Ray, R. D. (2010). *Assimilation of altimetry data for nonlinear shallow-water tides: Quarter-diurnal tides of the Northwest European Shelf.* Continental Shelf Research, 30(6), 668–679. http://doi.org/http://dx.doi.org/10.1016/j.csr.2009.10.011.

Gardline Surveys. (2001). *Pentland Firth Tidal Stream Observations.* Report produced for the Navigation Safety Branch of the Maritime and Coastguard Agency, Contract NBSA5B/2959.

Serpetti, N., Heath, M., Armstrong, E., & Witte, U. (2011). *Blending single beam RoxAnn and multi-beam swathe QTC hydro-acoustic discrimination techniques for the Stonehaven area, Scotland, UK.* Journal of Sea Research, 65(4), 442–455. http://doi.org/http://dx.doi.org/10.1016/j.seares.2011.04.001.

Serpetti, N., Heath, M., Rose, M., & Witte, U. (2012). *High resolution mapping of sediment organic matter from acoustic reflectance data.* Hydrobiologia, 680(1), 265–284. http://doi.org/10.1007/s10750-011-0937-4.

Smith, W. H. F., & Sandwell, D. T. (1997). *Global Sea Floor Topography from Satellite Altimetry and Ship Depth Soundings.* Science , 277 (5334 ), 1956–1962. http://doi.org/10.1126/science.277.5334.1956.

The Crown Estate. (2012a). *Pentland Firth and Orkney Waters Hydrodynamic Modelling: Model Calibration.* Report R.1935.

The Crown Estate. (2012b). *Pentland Firth and Orkney Waters Strategic Area: Preparation of Bathymetry to Support Modelling Studies.* Report R.1963.

The Crown Estate. (2012c). *West of Orkney Mainland Nearshore Survey Reports.* Report A4806.

Vögler, A., & Venugopal, V. (2012). *Hebridean Marine Energy Resources: Wave-Power Characterisation Using a Buoy Network.* Proceedings of the ASME 31st International Conference on Ocean, Offshore and Arctic Engineering (Vol. 7, pp. 477–488). http://doi.org/10.1115/OMAE2012-83658.

back to contents

| NAME | TYPE | DESCRIPTION |
|---|---|---|
| Smith and Sandwell | B | Gridded bathymetry (900 m) derived from Satellite Altimetry and Ship Depth Soundings |
| TCE 20 m bathymetry | B | 20 m gridded bathymetry for the PFOW region derived from a number of data |
| UKHO | B | High resolution MBES bathymetry data obtained directly from the UKHO, including data from MCA |
| MSS BMES | B | High resolution MBES bathymetry data from MSS |
| Admiralty Chart | B | ICIT digitalised Admiralty chart data. Raw data and an interpolated version |
| Orkney west coast survey data | B | High resolution BMES data provided by TCE as part of a wider west coast of Orkney mainland survey. |
| Stonehaven Bathymetry data | B | MBES survey 56° 54′ - 57° 03′ N and 2 - 12 km from the shore |
| BGS sediments | S | Seabed sediment samples including the fraction of mud, sand, gravel and results from a particle size analysis |
| UK National Tidal Gauge Network | E | Water elevation measurements at 44 locations around the UK coastline |
| GSHHG | CL | NOAA Global Self-consistent, Hierarchical, High-resolution Geography Database (GSHHG) |
| Gardline ADCP | C | ADCP data made available by MCA from 2001 |
| EMEC ADCP | C | ADCP data from the Falls and Warness, 12 weeks starting 12 July 2010 purchased from EMEC for TeraWatt |
| MSS current meter | C | Fair Isle channel (2008) and Scottish east coast current meter data |
| MSS ADCP | C | 12 hour stationary ADCP data measurements in Stronsay Firth, 21/05/2014. |
| MSS VM ADCP | C | 12 hour stationary ADCP data measurements in Stronsay Firth, 21/05/2014. |
| EMEC Waves | W | Wave rider buoy data, Billia Croo 58° 58.214′ N, 03° 23.454′ W, for complete years 2010 and 2012, purchased from EMEC for TeraWatt |
| Cefas WaveNet | W | A network or wave rider buoys around the UK |
| Aberdeen Uni Wave rider | W | Wave rider buoy data from Aberdeen Bay ° 09.65′ N, 02° 03.00′ W, Nov 572007 - May 2009 |
| VORF | M | Vertical Offshore Reference Frame model for converting between vertical datums |
| ERA-40 | M | ECMWF atmospheric model |
| OTPS and TMD | M | Tidal model based on an inversion of TOPEX/POSEIDON altimeter data and tide gauge data |

**Table 1.1** List of data, grouped by type, and their location on the TeraWatt FTP site and the Internet.
Type codes: B=Bathymetry, S=Sediments, E=Water Elevations, CL=CoastLine, C=Currents, W=Waves, M=Model

| FTP LOCATION (AND SIZE) | EXTERNAL LOCATION | REFERENCE |
|---|---|---|
| TCE_Data/Bathy/ Smith & Sandwell (70 MB) | http://gcmd.nasa.gov/records/GCMD_SIO_NOAA_SEAFLOORTOPO.html | Smith & Sandwell (1997) |
| TCE_Data/Bathy/20m_gridded (3.15 GB) | | The Crown Estate (2012b) |
| Data/Bathymetry/UKHO (8 GB) | https://www.gov.uk/inspire-portal-and-medin-bathymetry-data-archive-centre | |
| Data/Bathymetry/MS (2.68 GB) | http://www.scotland.gov.uk/Topics/marine/science/MSInteractive | |
| Data/Bathymetry/ICIT bathy (1 MB) | | |
| Data/Crown Estate West of Orkney data (75.6 GB) | | The Crown Estate (2012c) |
| | | Serpetti et al. (2011) |
| Data/BGS_PSA (13 MB) | http://www.bgs.ac.uk/GeoIndex/offshore.htm | British Geological Survey (2013) |
| | http://www.bodc.ac.uk/projects/uk/ntslf | |
| | https://www.ngdc.noaa.gov/mgg/shorelines/gshhs.html | |
| Data/Currents/Pentland Firth Gardline Data (32 MB) | | Gardline Surveys (2001) |
| | | |
| Data/Currents/MSS_Current_Meter_Data (11 MB) | | |
| Data/Currents/MSS_ADCP (1 MB) | | |
| Data/Currents/MSS_VMADCP (120 MB) | | |
| | | |
| | http://cefasmapping.defra.gov.uk | |
| | | |
| Model_Data/VORF (30 MB) | | |
| | http://www.ecmwf.int/en/research/climate-reanalysis/browse-reanalysis-datasets | Dee et al. (2011) |
| | http://volkov.oce.orst.edu/tides/otps.html http://polaris.esr.org/ptm_index.html | Egbert et al. (2010) |

# TIDAL STREAM AND WAVE ENERGY ARRAY SCENARIOS FOR THE PENTLAND FIRTH AND ORKNEY WATERS STRATEGIC AREA

02

R.B. O'Hara Murray

MARINE SCOTLAND SCIENCE,
SCOTTISH GOVERNMENT, MARINE LABORATORY, 375 VICTORIA ROAD, ABERDEEN, AB11 9DB

JULY 2015: REVISION 2.2

back to contents

## 02/1 INTRODUCTION

The Orkney Islands and surrounding waters contain a significant portion of Scotland's tidal and wave energy resource. For this reason, a number of tidal and wave energy sites have been granted agreement for lease by The Crown Estate (TCE) as areas for commercial renewable energy development within the region known as the Pentland Firth and Orkney Waters Strategic Area (PFOW). The development sites granted agreements for lease by TCE in 2010 formed the PFOW Round One Development Sites (BVG Associates, 2011; The Crown Estate, 2013) and it is these sites that are being considered in this study. Figure 2.1 shows the PFOW Round One Development Sites, made up by five tidal and six wave energy development sites.

At the time of writing the number of development sites within the PFOW has just been revised; with one more 30 MW site being leased to Scotrenewables Tidal Power Ltd and the number of wave sites being reduce to two, totalling 250 MW, (Marine Scotland, 2015). This revision reflects the rate at which tidal and wave technology has developed in recent years and the current economic climate. The TeraWatt project decided to use the original PFOW Round One Development Sites on the grounds that this was originally considered to be viable by the Scottish Government and TCE (Baxter et al., 2011; BVG Associates, 2011; The Crown Estate, 2013).

The wider TeraWatt study aims to model tidal and wave processes in the PFOW using three dimensional hydrodynamic and spectral wave numerical models, and to include the extraction of tidal and wave energy in the models. Such models will greatly enhance our understanding of the impact that removing tidal and wave energy may have on physical and ecological processes within the region.

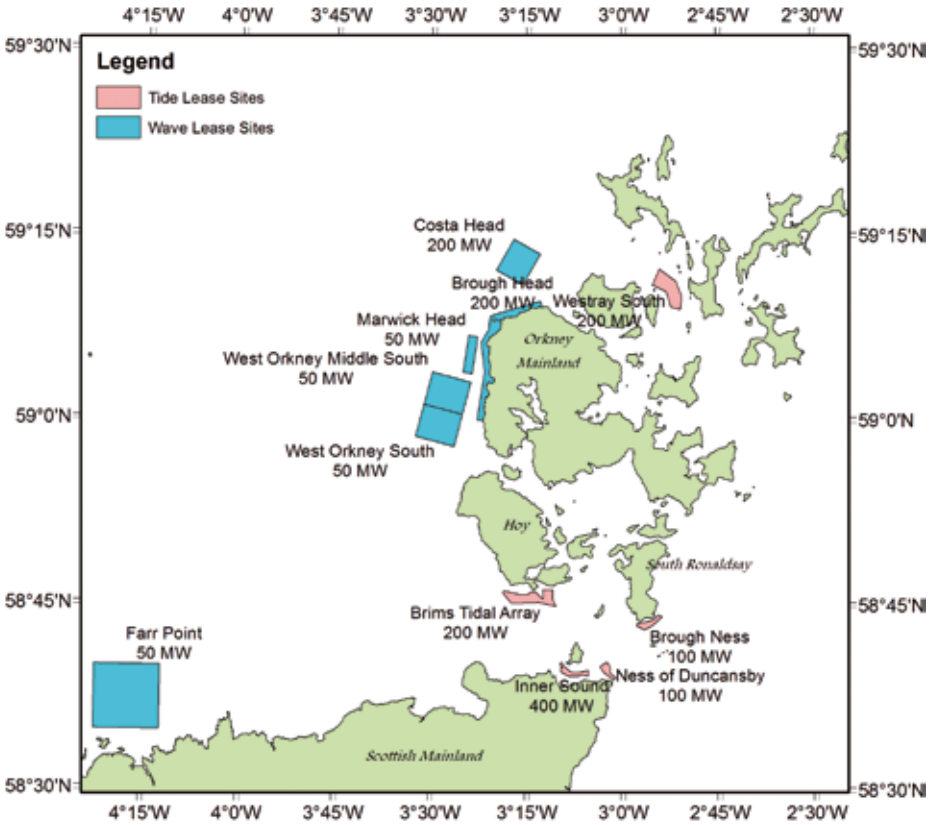


**Fig 2.1** The tidal and wave energy development sites in the Pentland Firth and Orkney Waters Strategic Area being considered by the TeraWatt project.

back to contents

The total planned energy generating capacity of the PFOW Round One Development Sites being considered by TeraWatt is 1.6 GW, with 1 GW and 600 MW being allocated to tidal and wave energy, respectively. In order to include such tidal and wave energy developments in the hydrodynamic models of the wider study, realistic tidal and wave device array scenarios are required. However, there is still considerable uncertainty regarding the type of devices that will be deployed and what form the arrays of devices will take. This paper reports on the process that was undertaken to develop a small number of generic device types and array scenarios for the PFOW, for use in the TeraWatt wave and tidal models of the region.

## 02/2 TIDAL RESOURCE ASSESSMENT

One of the primary sources of information used to constrain the location of the tidal devices was a simple assessment of the spatial distribution of tidal energy across each of the leased sites. The kinetic energy of the tidal stream is proportional to the cube of the tidal current speed. Therefore, the depth average current speed was taken as an indication of the resource available for tidal stream energy production. As part of the wider TeraWatt study a MIKE 3 tidal model was developed for the PFOW, and one month of model output was used for this study. The temporal mean of the depth mean current speed, over one month, was calculated for each grid point within the model domain. These mean speeds were used to help determine the placement of individual tidal turbines within the leased areas (Section 02/4). It is recognized that the undisturbed speed of the tidal stream is not necessarily the most suitable measure of the available energy, but it was deemed to be a good indicator of the spatial distribution of resource. A quantitative resource assessment is beyond the scope of this work.

## 02/3 GENERIC TIDAL STREAM AND WAVE DEVICE TYPES

The wider TeraWatt study aims to include in models of the PFOW the total proposed energy extraction capacity within the PFOW Round One Development Sites. These sites are likely to see a wide range of device types being deployed. There is little information available on the specification of many of these devices and it was decided to focus effort in the specification of a small number of generic device types. The aim for the generic devices was for them to be both realistic, to be accepted by stakeholders as plausible, and to not be too similar to any single device being developed.

Baston et al. (Chapter 04) outlined the key tidal turbine parameters that are required to be specified for the TeraWatt modelling work. A single 1 MW tidal turbine specification was developed and is specified by Baston et al. (Chapter 04) as being a single 20 m rotor, with 1 m/s cut-in speed, 4 m/s cut-out speed, 2.5 m/s rated speed, a rated capacity of 1-1.5 MW, and the current speed dependent thrust coefficient shown in Figure 2.2. For this work, a rated capacity of 1 MW for each turbine was used to estimate the total number of turbines for each development area.

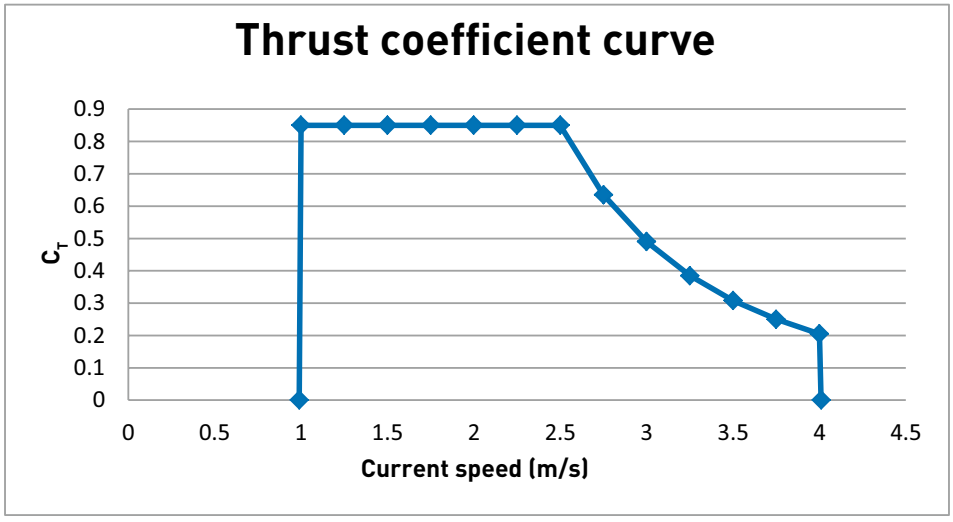


**Fig 2.2** The generic tidal turbine thrust coefficient, $C_T$, curve used in the wider TeraWatt study (Baston et al., 2014, Chapter 04).

MacIver et al. (Chapter 03) reviewed how wave energy extraction can be included in the TeraWatt spectral wave models, and presented a set of generalized characteristics based on numerical modelling. Because of the variety of fundamentally different types of wave energy devices likely to be deployed in PFOW, it was impossible to develop a single generic device. This report therefore considers the three broad device types currently being considered by developers; (i) a 750 kW wave attenuator, (ii) a 2.5 MW wave absorber, and (iii) a 1 MW oscillating wave surge converter.

In order to determine the number of devices to place in each development site, it was assumed that the energy generating capacity of each site will eventually be reached, and that each device will operate at the rated power output. Thus, the number of devices can simply be determined by dividing the energy generating capacity by the power rating of a single device.

## 02/4 GENERIC TIDAL ARRAY LAYOUTS

The licensing documentation, scoping documents and Environmental Statements (ES), currently held by Marine Scotland (MS) for the planned developments in the PFOW (www.gov.scot/Topics/marine/Licensing/marine/scoping) were reviewed. Limited information was available regarding the final array layouts. This is due to uncertainties in what the final technologies will be, and that the projects are still being planned. The approach taken by developers for their environmental statements required for licensing, is to consider an envelope (often termed a Rochdale envelope) of potential design characteristics.

Out of all the available licensing documentation, the MeyGen phase 1 ES (MeyGen, 2014) and supporting literature (www.gov.scot/Topics/marine/Licensing/marine/scoping/MeyGen) provided the most comprehensive array layout information and, for this reason, was used primarily for this work. The ES uses an example array layout for the proposed 86 devices forming the phase 1 development. The spacing used in the ES was 45 m cross stream and 160 m down stream, with the rows of turbines being staggered. It was unclear as to whether the cross stream spacing in the ES was hub to hub spacing or blade tip to blade tip spacing. However, assuming that the whole 400 MW designated to this site is eventually utilized, it became apparent that it would be challenging to fit 400 turbines in the designated area with a hub to hub spacing of much more than 45 m.

The generic tidal array layout for 1 MW horizontal axis devices was therefore chosen to have a spacing 45 m cross stream and 160 m down stream, with the rows staggered. All but one of the planned PFOW tidal developments propose using 1 MW single axis tidal devices. The exception is the Brough Ness development which is most likely to use the Marine Current Turbines 2 MW device, which has two horizontal axis turbines with hub to hub spacing of approximately 30 m. The generic device spacing was simply doubled for this development with 90 m cross stream hub to hub spacing between each 2 MW device and 320 m down stream, staggered, spacing. The cross stream spacing of 90 m equated to 120 m spacing between the centre of each 2 MW device.

The factors considered here to determine the position of the arrays were the number of devices, the water depth, the principal current direction, and the spatial distribution of mean current speed. The bathymetry data used was the 20 x 20 m gridded bathymetry used by the wider study (O'Hara Murray, 2015 (Chapter 01); The Crown Estate, 2012). Output from a MIKE 3 model developed as part of the TeraWatt project was used to calculate the principal current direction and the spatial distribution of temporal mean speeds across each site. A principal component analysis was performed on each modelled time series, from each model grid point, within each development site. The spatial mean and standard deviation of the principal direction for each development site are presented in Table 2.1. The Inner Sound development site had the highest variance of current directions, due to it occupying a large proportion of the length of the Inner Sound of Stroma tidal channel. For this reason, the site was sub-divided into three areas and the mean direction was calculated for each of these sub-sites using a principal component analysis on the modelled currents from each sub-site. The results are shown in Table 2.2.

| SITE NAME | MEAN DIRECTION (degrees) | STANDARD DEVIATION (degrees) |
|---|---|---|
| Inner Sound | 105.7 | 24.1 |
| Ness of Duncansby | 119.0 | 7.2 |
| Brough Ness | 74.1 | 19.0 |
| Brims Tidal Array | 92.4 | 6.9 |
| Westray South | 144.8 | 12.1 |

**Table 2.1** The mean direction and standard deviation of the principal component of tidal currents from the MIKE 3 tidal model for each of the tidal development sites in the PFOW strategic area.

| SITE NAME | MEAN DIRECTION (degrees) | STANDARD DEVIATION (degrees) |
|---|---|---|
| Inner Sound 1 | 126.9 | 9.8 |
| Inner Sound 2 | 96.1 | 5.3 |
| Inner Sound 3 | 79.0 | 4.3 |

**Table 2.2** The mean direction and standard deviation of the principal component of tidal currents from the MIKE 3 tidal model for three sub-sites of the Inner Sound.

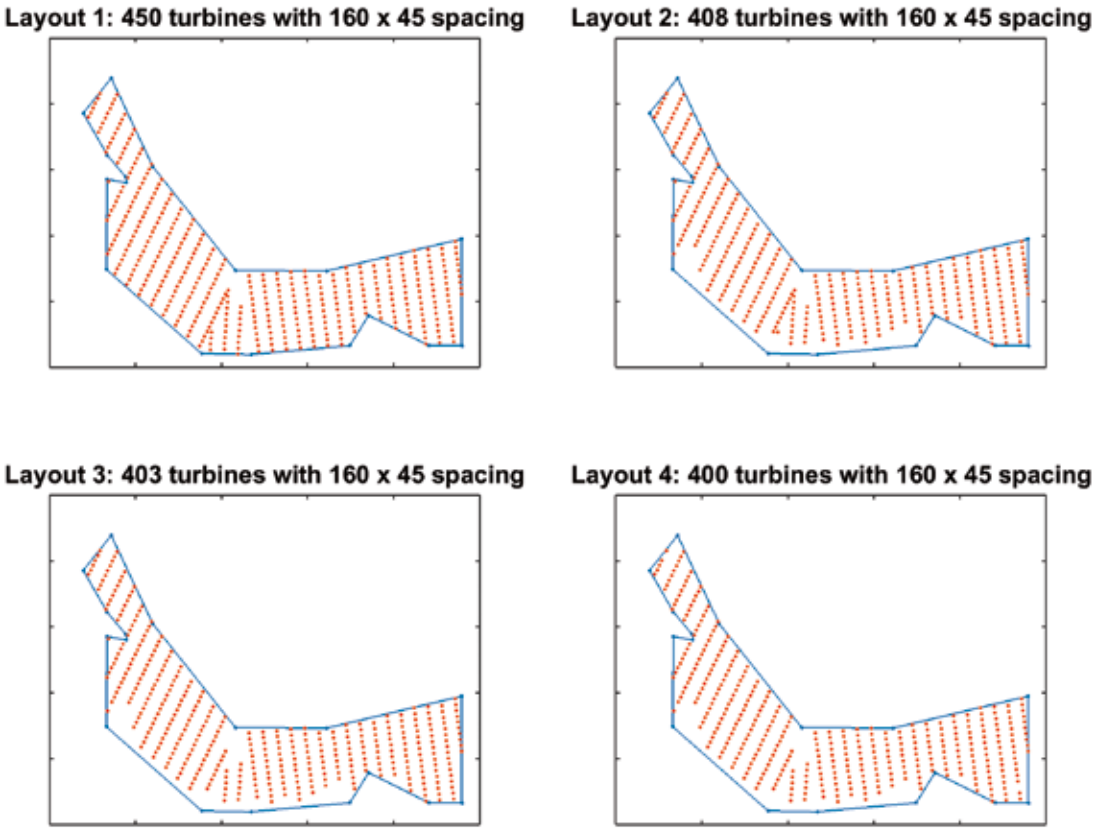


**Fig 2.3** The evolution of the Inner Sound layout using the generic array layout algorithm.

A generic array layout algorithm was developed to position devices in a standard way in each of the PFOW tidal sites. Figure 2.3 shows the evolution of the Inner Sound array layout as the generic array layout algorithm progressed. For each development site, or sub-site in the case of the Inner Sound, a grid of devices was created with the designated generic device layout, centred over the site, or sub-site. The grids were then rotated so that they were correctly aligned with the mean current direction for the site, or sub-site. This formed layout 1, shown in Figure 2.3 for the Inner Sound.

The bathymetry data used for the TeraWatt hydrodynamic model development, on a 20 x 20 m grid, was interpolated to the device locations, and the devices in depths, relative to mean sea level, of less than 27.5 m were removed. This was to ensure that the 20 m diameter blades of the devices were always below the water surface. This formed layout 2 (Figure 2.3).

Because the Inner Sound development site was sub divided into three sub-sites, there were a few devices, along the boundaries of the sub-sites, positioned too close together. Layout 3 (Figure 2.3) was formed by removing these devices that were too close together. Layout 4 (Figure 2.3) was formed by removing the devices within each site that were in the poorest tidal energy resource, until only the desired number of turbines remained. The resource was simply assessed by interpolating the temporal mean speed from the MIKE 3 hydrodynamic model to the device locations. This last process was performed iteratively, ensuring that there were no isolated turbines. It was considered unlikely for isolated turbines, many 100s of meters away from the main array, to be constructed on account of a very small patch of, potentially marginally, higher current speeds.

Figure 2.4 shows the evolution of the Ness of Duncansby array using the generic array layout algorithm. Unlike the Inner Sound, this and the remaining three development sites were not sub-divided. This was due to the mean direction not varying significantly within the site. This made layouts 2 and 3 identical. Due to this development site having a lower energy generation target than the Inner Sound site, despite having a similar area, there is a much larger difference between layouts 3 and 4 where the best resource is targeted by a smaller number of turbines.

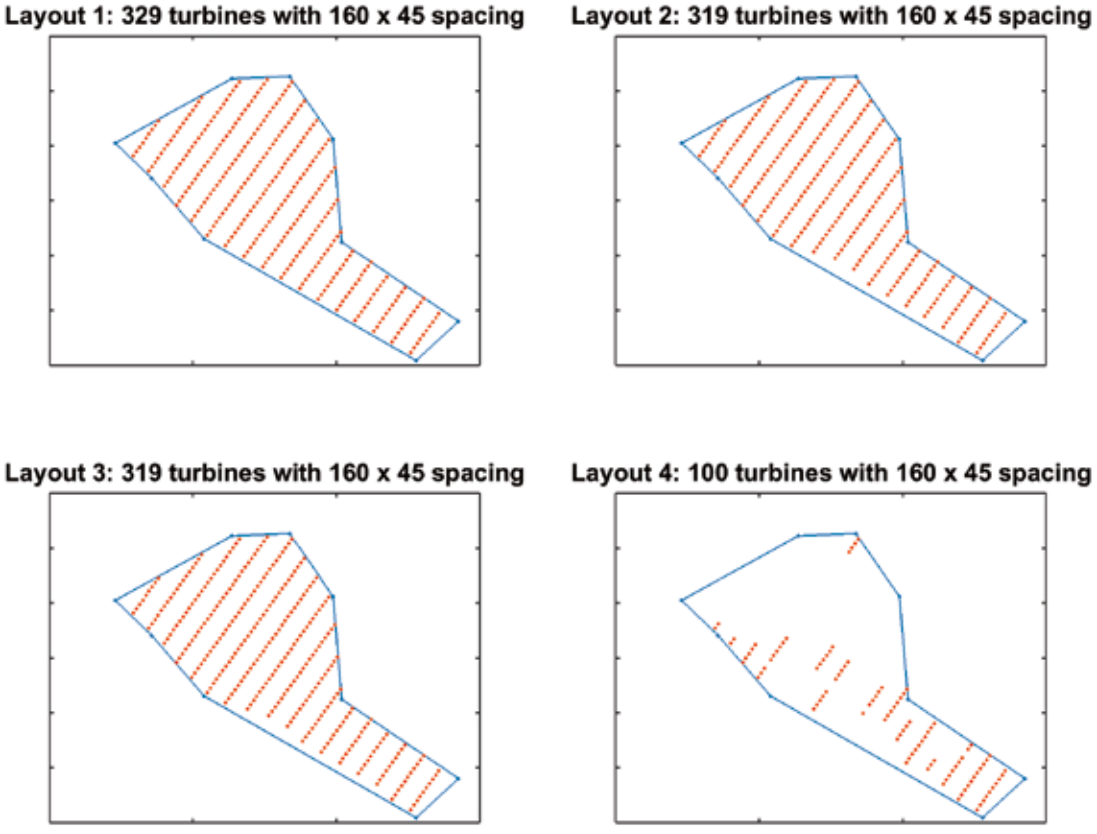


**Fig 2.4** The evolution of the Ness of Duncansby layout using the generic array layout algorithm.

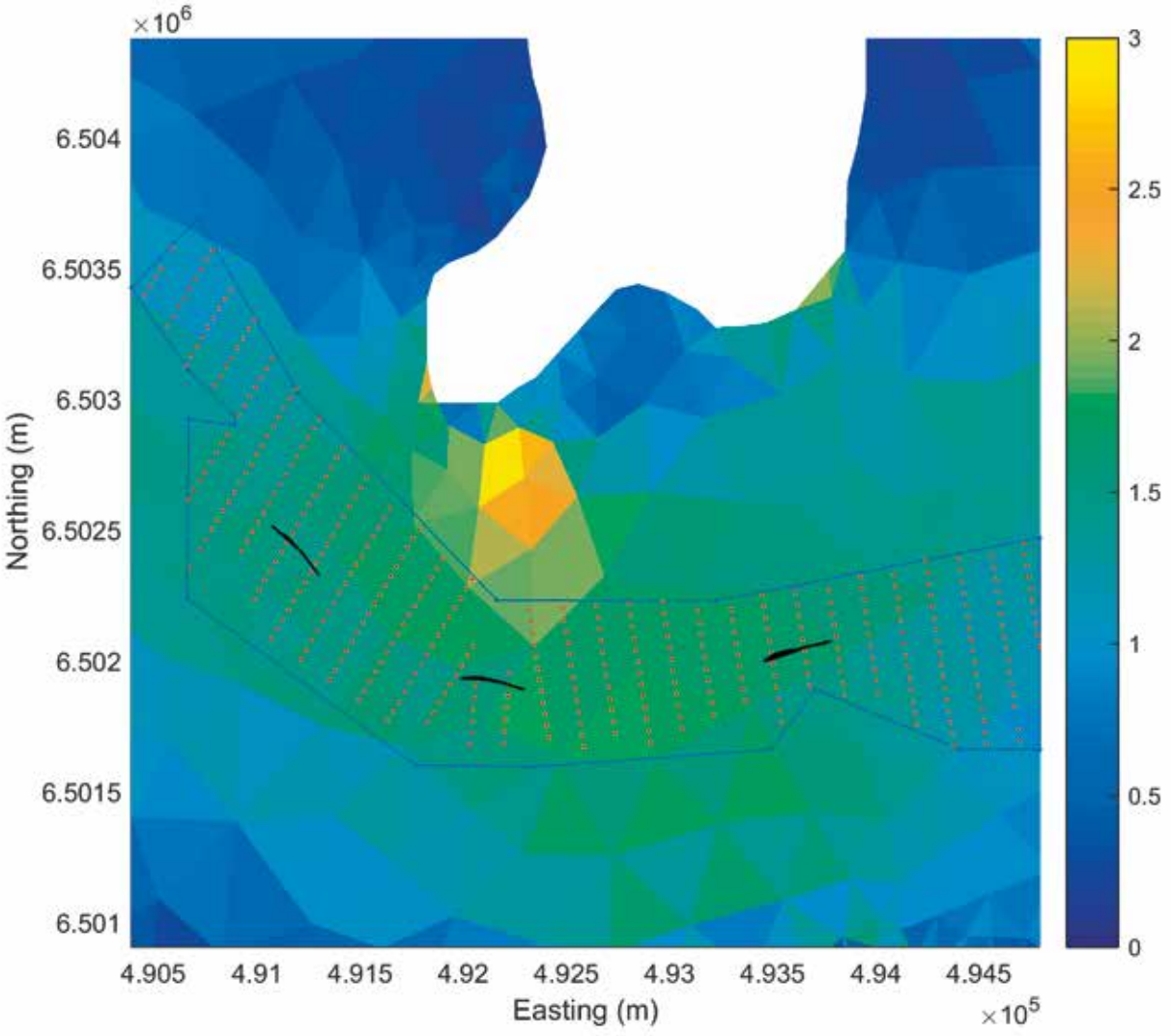


**Fig 2.5** The final array layout for the 400 MW Inner Sound development overlaying the mean depth average current speed (m/s) from the MIKE 3 output. The tidal ellipses for the three sub-sites are indicated by the black lines.

Figures 2.5 to 2.8 show the final array layouts for the Inner Sound, Ness of Duncasby, Brims Tidal Array and Westray South, respectively, overlaying the mean depth average current speed (m/s) from the MIKE 3 output for the region around each development site. The array layouts for these developments all have 45 x 160 m (across stream x down stream) down stream staggered spacing of 1 MW devices. Figure 2.9 shows the final Brough Ness development which has 50 x 2 MW devices, each made up of two 20 m diameter turbines, with a down stream staggered array spacing of 90 x 320 m (across stream x down stream). The position of each 20 m diameter turbine is shown in Figure 2.9.

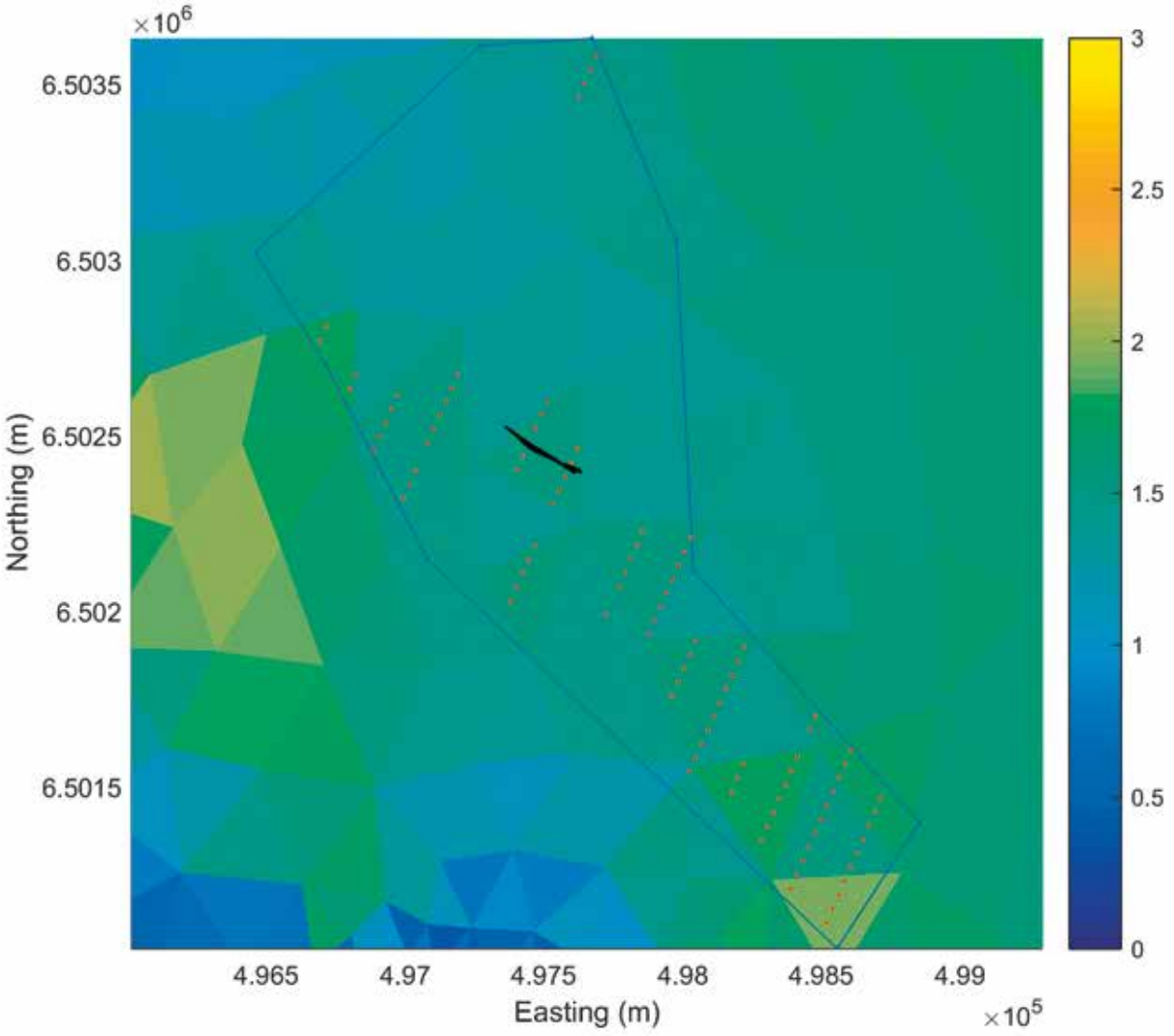


**Fig 2.6** The final array layout for the 100 MW Ness of Duncansby development overlaying the mean depth average current speed (m/s) from the MIKE 3 output. The tidal ellipse for the site is indicated by the black line.

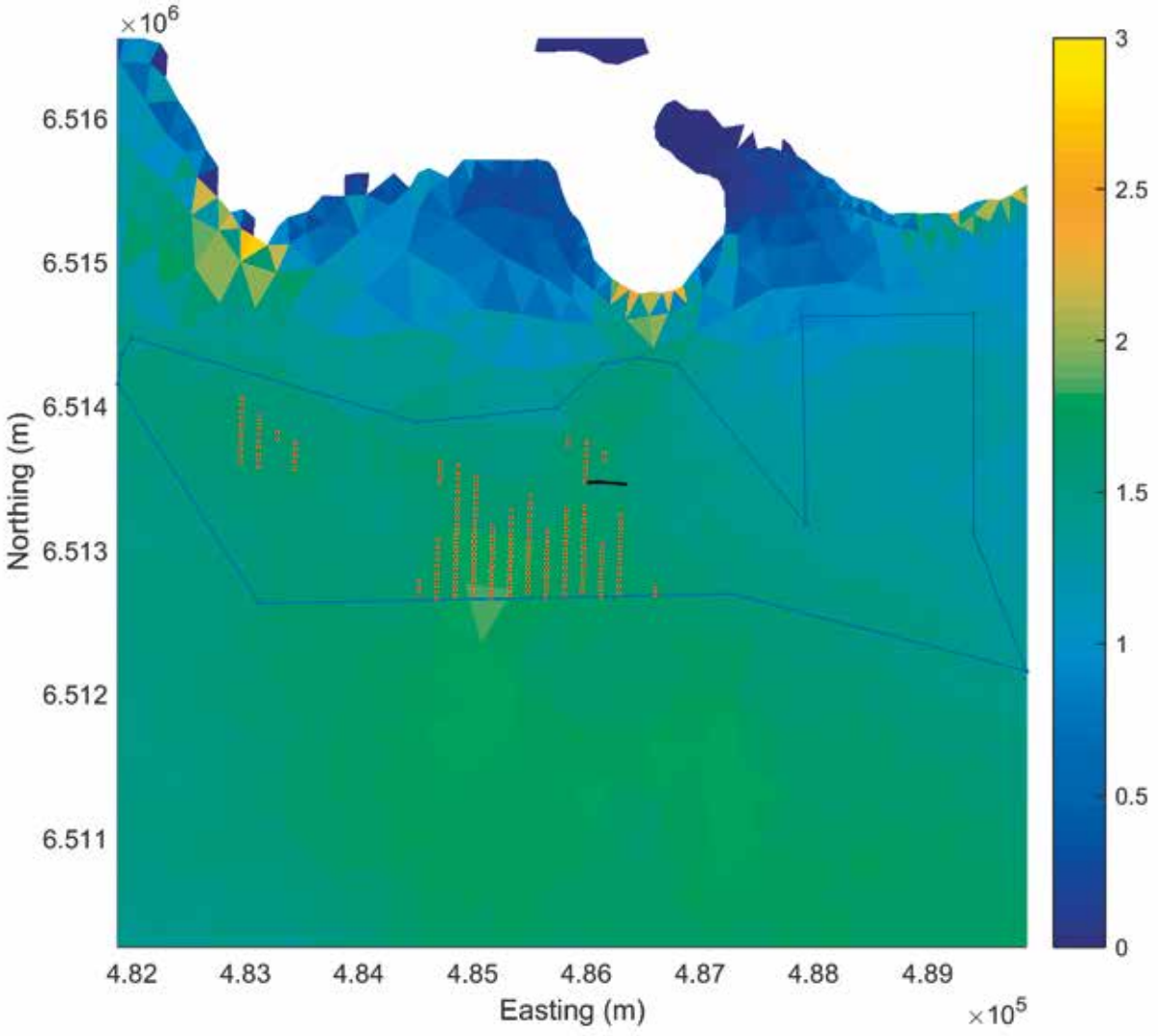


**Fig 2.7** The final array layout for the 200 MW Brims Tidal Array development overlaying the mean depth average current speed (m/s) from the MIKE 3 output. The tidal ellipse for the site is indicated by the black line.

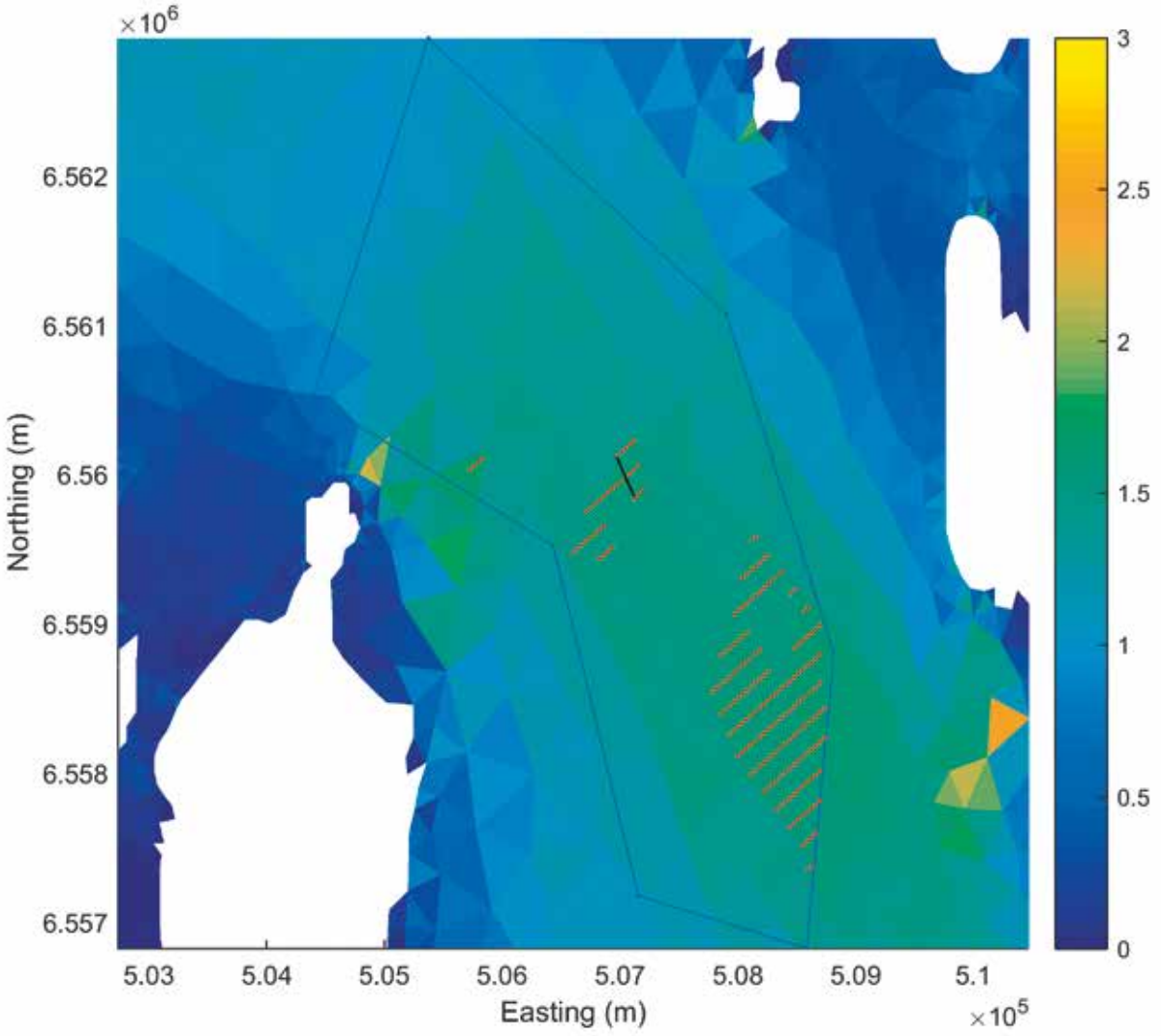


**Fig 2.8** The final array layout for the 200 MW Westray South development overlaying the mean depth average current speed (m/s) from the MIKE 3 output. The tidal ellipse for the site is indicated by the black line.

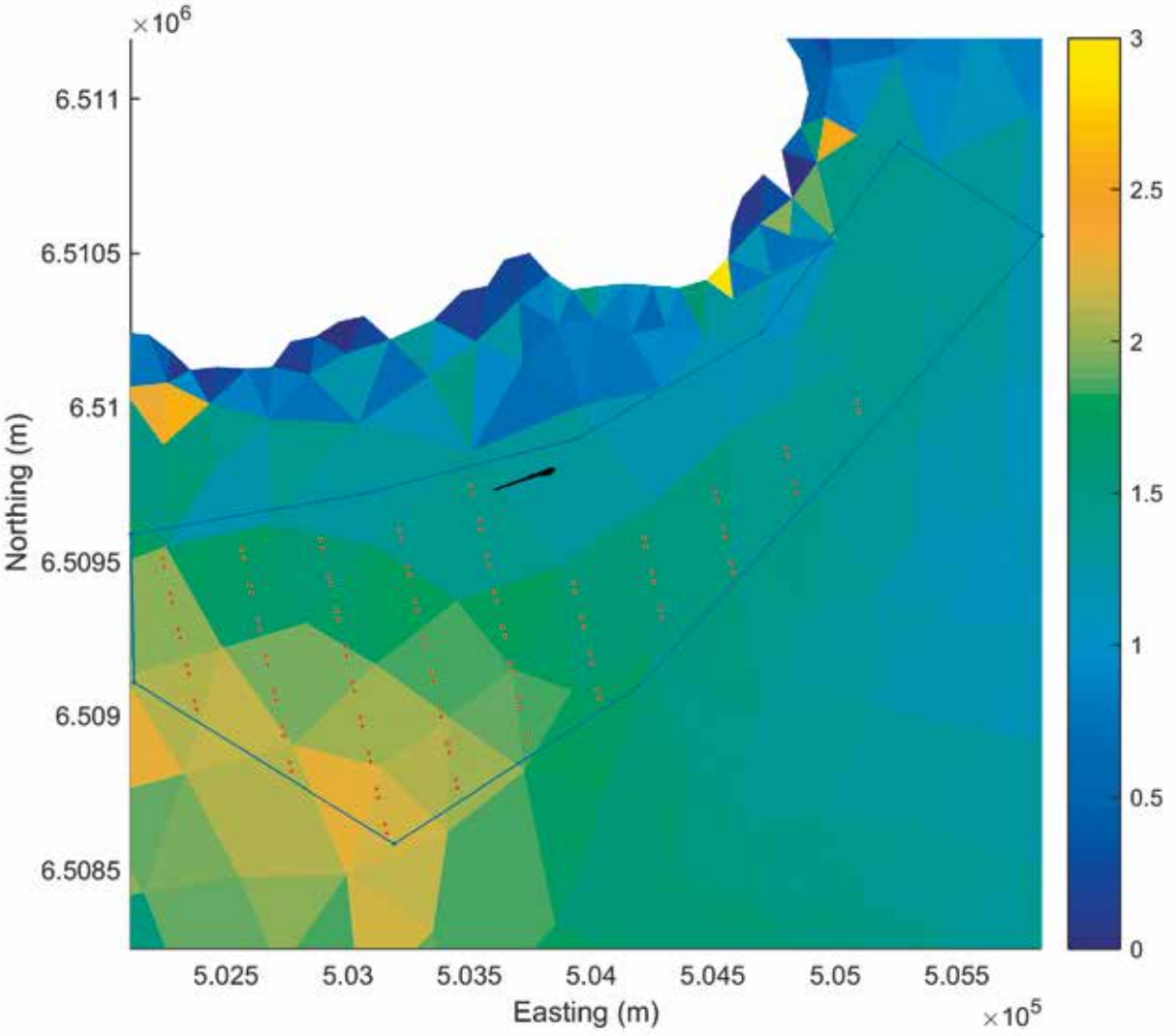


**Fig 2.9** The final array layout for the 100 MW Brough Ness development overlaying the mean depth average current speed (m/s) from the MIKE 3 output. The tidal ellipse for the site is indicated by the black line.

## 02/5 GENERIC WAVE ARRAY LAYOUTS

Four out of the six wave development sites within the PFOW planned to use the 750 kW Pelamis II wave attenuator device. The scoping report for the West Orkney South development site (www.gov.scot/Topics/marine/Licensing/marine/scoping/WestOrkneySouthWaveEnergySite) indicated that the Pelamis devices would most likely be deployed in arrays of 22 devices, in two staggered rows, with a space of 10 times the device length between arrays (1800 m). The most efficient way to fill the proposed West Orkney South development area with arrays of this size was to use a 400 x 400 m (centre to centre) spacing of devices (Figure 2.10). This array layout was not possible within the Marwick Head development site, so an array of 66 devices with a 350 x 400 m (cross stream x down stream) staggered spacing across 4 rows was developed (Figure 2.11).

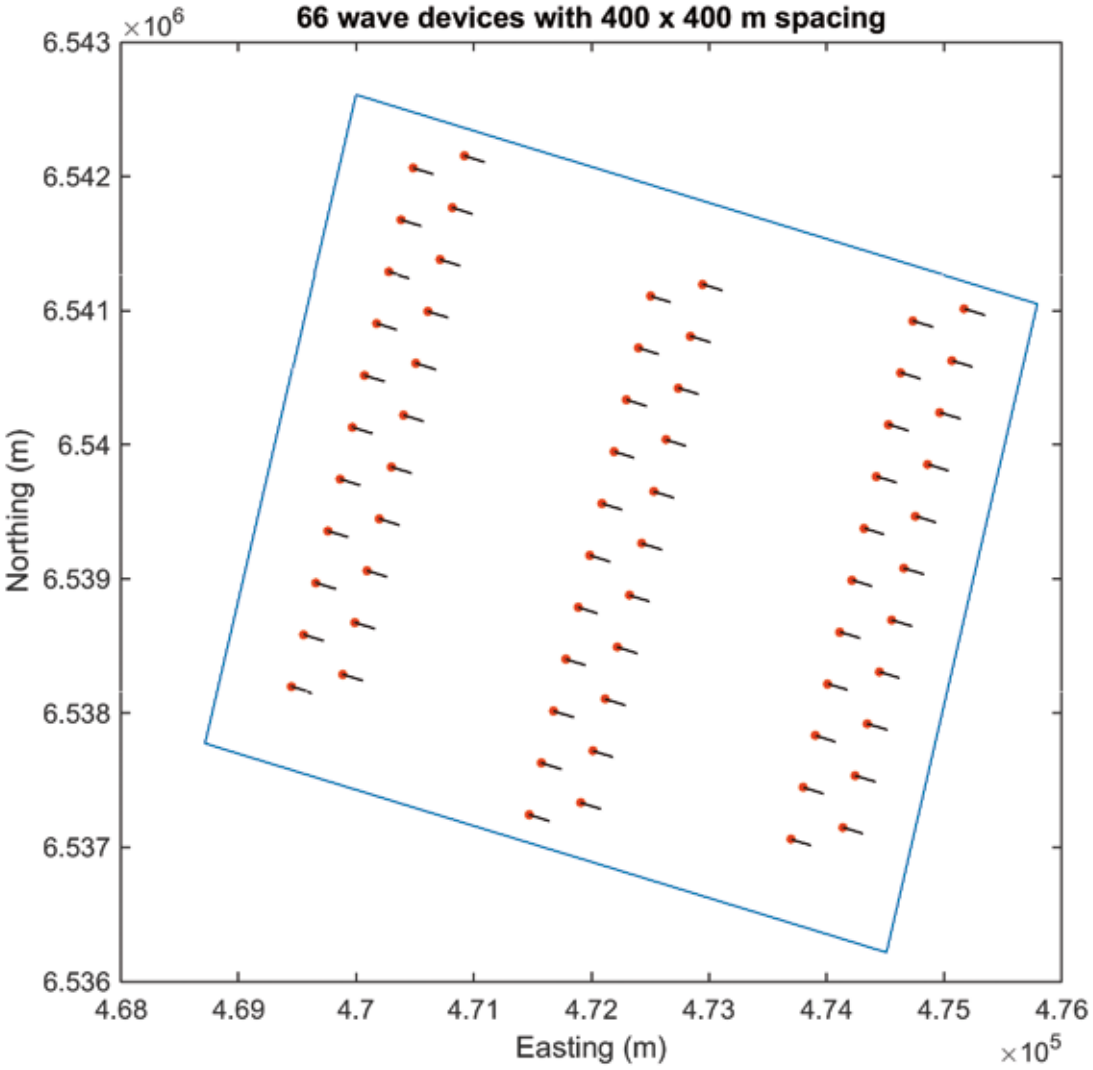


**Fig 2.10** The proposed West Orkney South Pelamis P2 wave farm array layout.

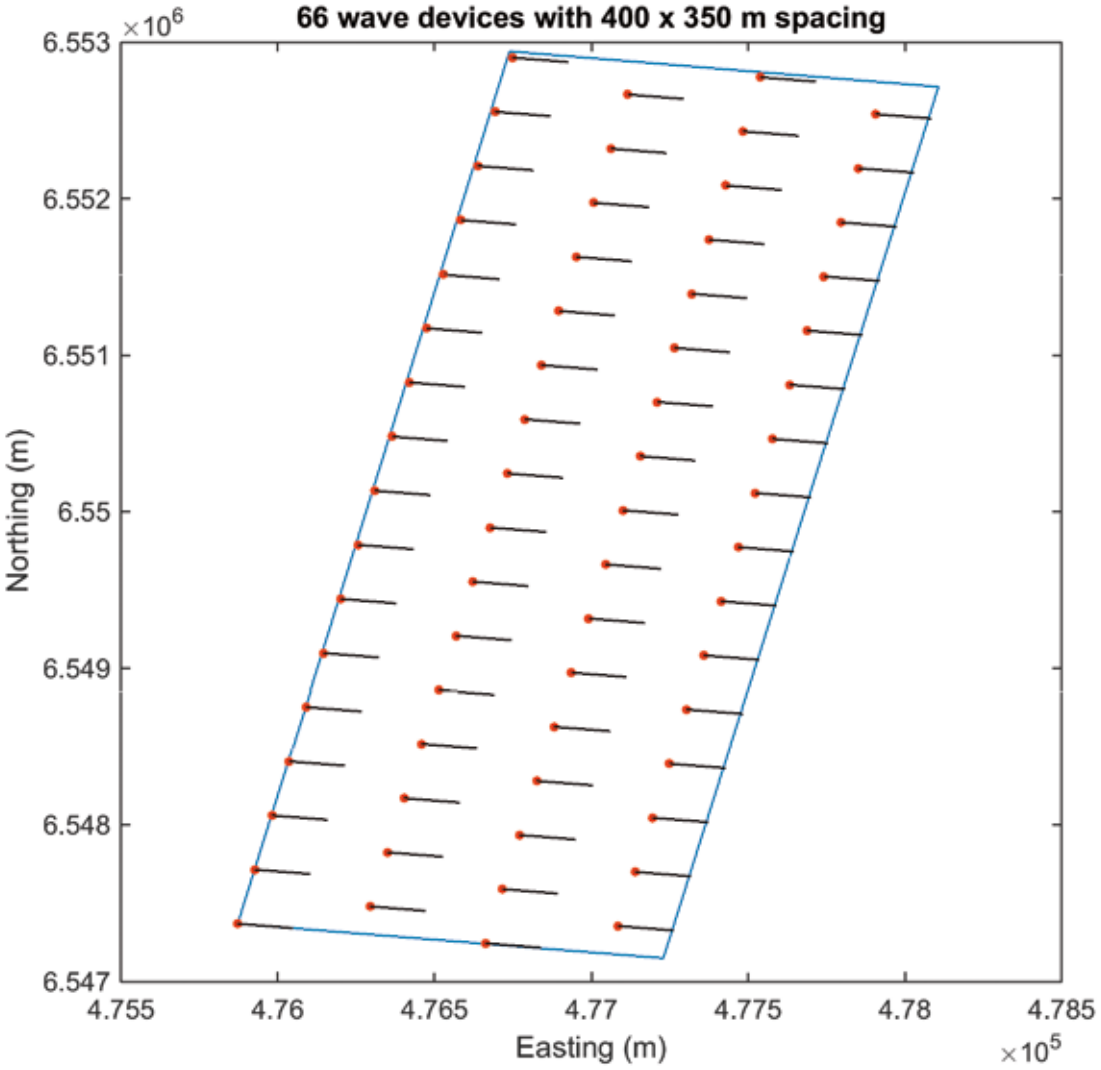


**Fig 2.11** The proposed Marwick Head Pelamis P2 wave farm array layout.

The Costa Head development plans to use the 2.5 MW AWS III flexible membrane wave absorber (www.gov.scot/Topics/marine/Licensing/marine/scoping/costa).

In order to fit 80 of these devices (200 MW) within the development area, a 550 x 600 m (cross stream x down stream) staggered array was used (Figure 2.12).

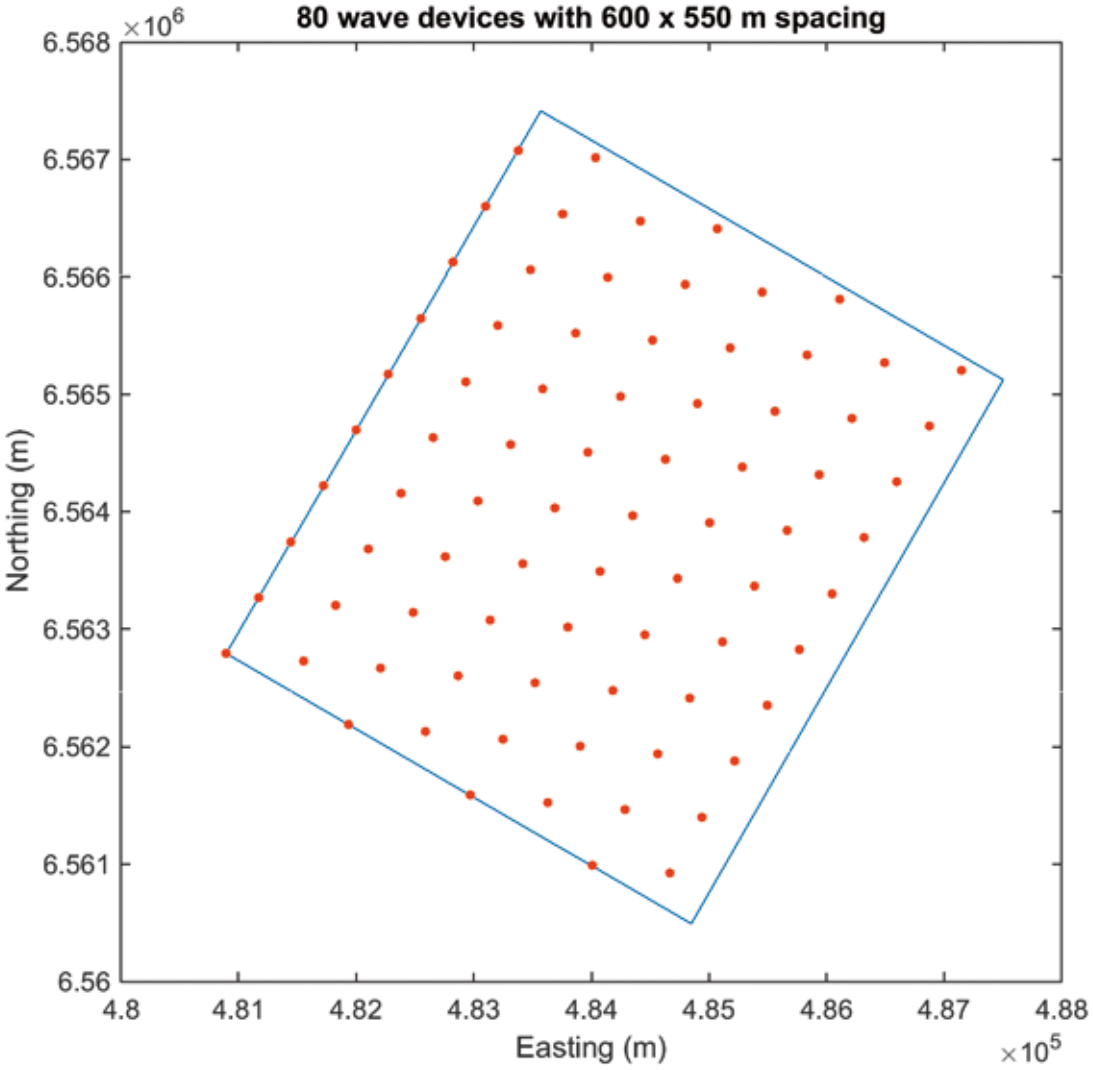


**Fig 2.12** The proposed Costa Head AWS III wave farm array layout.

The Brough Head development site plans to use the 1 MW Oyster III oscillating wave surge converter (www.gov.scot/Topics/marine/Licensing/marine/scoping/broughhead). The example array provided in the Brough Head coastal processes impact assessment report suggested that the devices should have a spacing of between 25-65 m. A spacing of 45 m was chosen for this study. The devices are 26 m wide, which gave a centre to centre spacing of 71 m. The licensing documentation revealed that the devices should be in 10-15 m water depth. Therefore, for this study the devices were distributed in approximately 5 arrays of 40 devices (200 MW total) along the 12.5 m depth contour (Figure 2.13). Bathymetry data provided by The Crown Estate on a 20 m grid was used (O'Hara Murray, 2015 (Chapter 01); The Crown Estate, 2012).

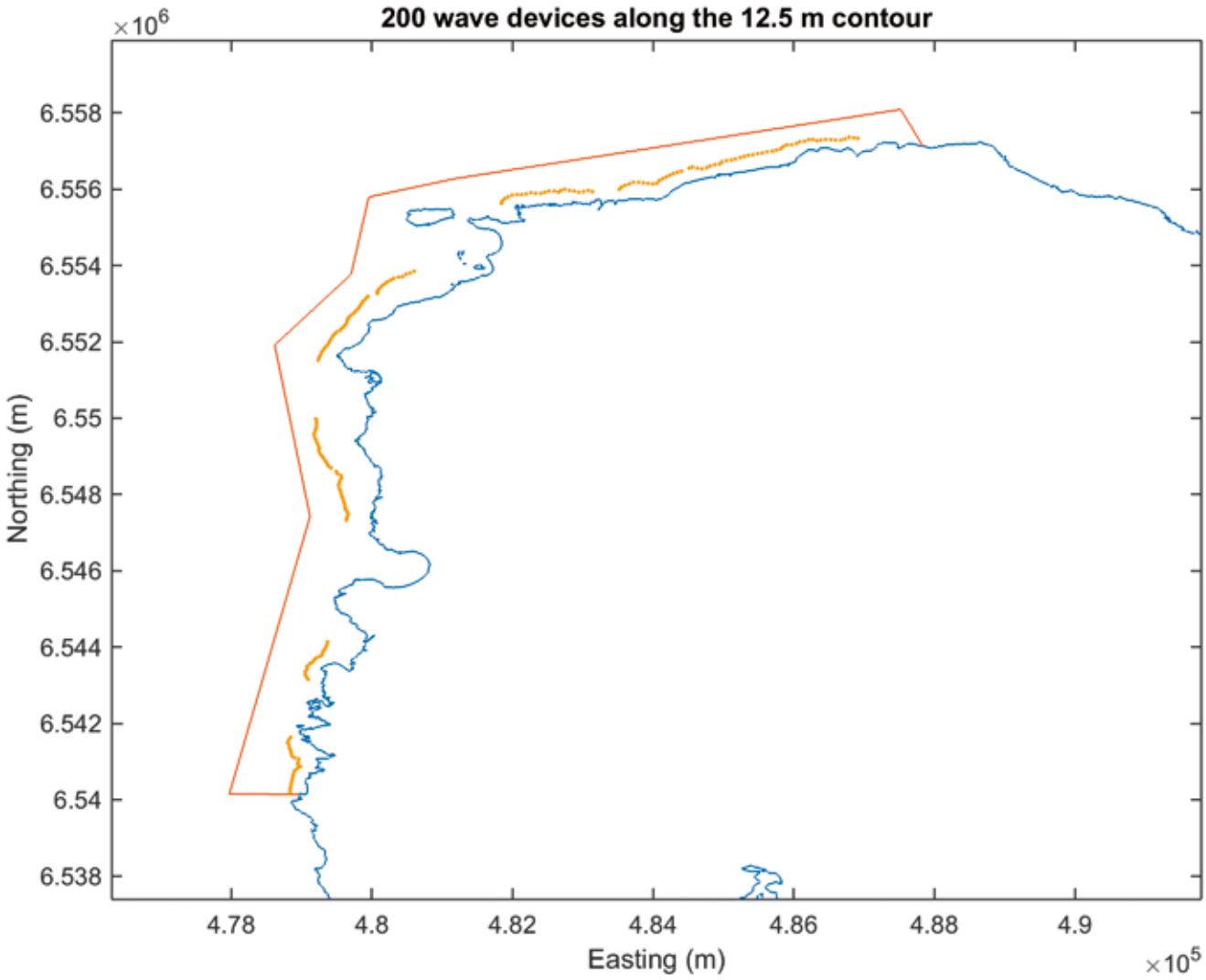


**Fig 2.13** The proposed Brough Head Oyster III wave farm array layout.

## 02/6 DISCUSSION AND CONCLUSIONS

This paper reports on the development of realistic tidal and wave energy array scenarios for the PFOW Round One Development Sites. This work assumed that the energy generating capacity allocated to each of the leased sites can be achieved by simply including the required number of devices, each with a particular power rating, to reach the target capacity. For example, in the case of the 400 MW Inner Sound development, 400 x 1 MW devices were placed in the array. In reality this is unrealistic as the performance of individual devices will vary through the tidal cycle and spatially across the array, due to spatial variations in the resource and to interactions between devices (Vennell et al., 2015). Still, this was deemed to be an appropriate simplification due to detailed array design being beyond the scope of this work, and that the target generating capacity is both a nominal and rough target.

The array designs were primarily based on the licensing documentation held by MS for the planned developments. For the case of the tidal energy arrays, a number of constraints were also considered, including the spatial distribution of tidal resource and the water depth. For the case of the wave energy arrays, the array layouts suggested in the licensing documentation were almost solely used, with only the Brough Head oscillating wave surge converter array requiring additional depth data.

In reality there will be further constraints on where wave and tidal devices will be placed, such as limits on the navigational restriction allowed in some areas. There are other detailed engineering considerations such as the seabed conditions and economic considerations limiting the spacing between devices. This last point regarding economics was partly captured by using the array layouts from the licensing documentation. As far as was practical, generic devices and generic array layouts were used for all the development sites. This enabled a standardized method to be developed and to simplify the inclusion of a large number of devices in the hydrodynamic models.

The array layouts resulting from the work presented here have been used in the wider TeraWatt project to model the wave and tidal processes of the PFOW with and without the inclusion of wave and tidal energy extraction. One aim of TeraWatt is to improve our understanding of how wave and tidal stream energy extraction could change the physical and ecological processes in the PFOW. Another aim is to develop a methods toolbox for the numerical modelling of the PFOW, which this paper contributes to.

## 02/7 ACKNOWLEDGEMENTS

The TeraWatt project was funded by the Engineering and Physical Science Research Council SUPERGEN Marine Challenge. The author would like to thank Simon Waldman, Heriot-Watt University, and Alejandro Gallego and Ian Davies, Marine Scotland Science, for their helpful comments regarding this work; the TeraWatt consortium and steering group for their support; and the renewable energy developers who participated in the project.

## 02/8 REFERENCES

Baxter, J. M., Boyd, I. L., Cox, M., Donald, A. E., Malcolm, S. J., Miles, H., ... Moffat, C. F. (2011). *Scotland's Marine Atlas: Information for the national marine plan.* Marine Scotland, Edinburgh.

BVG Associates. (2011). *Wave and tidal energy in the Pentland Firth and Orkney waters: How the projects could be built.* A report prepared for The Crown Estate, retrieved from http://www.thecrownestate.co.uk/media/5406/pentland-firth-how-the-projects-could-be-built.pdf.

Marine Scotland. (2015). *Pilot Pentland Firth and Orkney Waters Marine Spatial Plan: Consultation Draft.* The Scottish Government.

MeyGen. (2014). *Meygen tidal energy project phase 1 environmental statement.* Retrieved from www.gov.scot/Topics/marine/Licensing/marine/scoping/MeyGen.

The Crown Estate. (2012). *Pentland Firth and Orkney Waters Strategic Area: Preparation of Bathymetry to Support Modelling Studies.* Report R.1963.

The Crown Estate. (2013, July). *Pentland Firth and Orkney Waters Strategic Area review project.* Retrieved from http://www.thecrownestate.co.uk/media/5446/pfow-strategic-area-review-project-2012.pdf.

Vennell, R., Funke, S. W., Draper, S., Stevens, C., & Divett, T. (2015). *Designing large arrays of tidal turbines: A synthesis and review.* Renewable and Sustainable Energy Reviews, 41, 454–472. http://doi.org/10.1016/j.rser.2014.08.022.

# REPRESENTING WAVE ENERGY EXTRACTION IN REGIONAL SCALE NUMERICAL MODELS

## 03

R. MacIver[1], N.T. Reddy[2], V. Venugopal[2]

1 LEWS CASTLE COLLEGE, UHI, CASTLE GROUNDS, STORNOWAY, NA H-EILEANAN AN IAR, HS2 0XR

2 SCHOOL OF ENGINEERING, THE UNIVERSITY OF EDINBURGH, 2 CHARLES STREET, EDINBURGH, EH8 9AD

DRAFT 3.1

## 03/ SUMMARY

Commercial wave energy projects are certain to require the development of ‚farms' or ‚arrays' consisting of multiple wave energy converters. It will be necessary to demonstrate the effects of an individual array, and the cumulative effects of multiple arrays, on the physical and ecological processes of the region hosting the arrays as part of the environmental impact assessment (EIA).

The aim of this document is to present the state of the art in numerical modelling techniques capable of achieving this and to suggest approaches for modelling wave energy extraction for the purpose of stimulating a discussion with device and project developers concerning the most appropriate method.

Spectral wave models and Boussinesq/Mild-slope models are considered the most appropriate for regional scale effects. The advantage of spectral wave models is their computational efficiency which permits the study of large domains and the potential to couple with hydrodynamic and coastal process models.

Accurate representation of wave energy devices will require a parametric description of the wave/structure interaction in terms of a frequency and directionally dependent function for the transmission and reflection coefficient. These coefficients will depend on the device's absorption characteristic and geometry. At present transmission coefficients are inferred from functional relations such as a relative capture width (non-dimensional ratio of absorbed hydrodynamic power typically expressed as a function of frequency) or a power matrix (absorbed hydrodynamic power as a function of frequency and incident wave height).

It is recognised that this is commercially sensitive information. However, through discussion with developers it is intended to establish representative functions for the principle classes of wave energy device that may be used to study the effect of generic wave energy devices.

## 03/1 INTRODUCTION

Commercial wave energy projects are certain to require the development of ‚farms' or ‚arrays' consisting of multiple wave energy converters (WECs). The general location of these farms will be determined from the assessment of the long-term wave resource established using regional wave models. Determining an optimal device configuration at a particular location, and hence the extent of an array, will require knowledge of the hydrodynamic interaction of devices both in the immediate vicinity of the devices (i.e. intra-array) and in the far-field. The former is principally relevant to optimising the productivity of an array, while the latter is relevant to understanding the impact of an individual array, and the cumulative impact of multiple arrays, on the physical and ecological processes of the region hosting the arrays. This regional perspective of the hydrodynamics, and the dependent morphodynamic and ecological processes, is vital when preparing environmental impact assessments (EIAs) that are a necessary part of the consenting process. The accurate representation of regional hydrodynamics in the presence of arrays is the focus of this paper.

The motions of individual devices within an array are interdependent as a result of diffraction at, and waves radiated by, each device as well as energy extraction. The performance of an individual device, and the whole array, is determined by such wave interactions which depend on the device geometry, device spacing within the array, the incident wave conditions and device control strategy. These interactions can be constructive or destructive and can be significant even at large device separations, e.g. up to 2000m (Babarit 2010).

Sufficiently far from individual devices, or indeed an array of devices, the resultant wave field can be considered simply as the sum of incident wave field and the scattered wave fields arising from the devices (consisting of diffracted and radiated waves). While the near-field, phase-dependent, effects are not significant in the far-field, the

consequences of phase-dependent effects arising in the near-field should be accounted for when assessing the environmental impact of arrays.

The hydrodynamic performance of wave energy devices in the real sea is not yet proven and knowledge that has been acquired is rarely placed in the public domain. Consequently a higher level of precision is not justified at this stage.

The TeraWatt project is considering the methodologies for representing the effects of marine energy extraction in the hydrodynamic and wave models regularly used in the commercial marine energy sector, such as the proprietary MIKE21 and MIKE3 suite and the open source Delft3D suite. This position paper presents the current opinion of the TeraWatt project regarding modelling wave energy extraction.

## 03/2 CLASSIFICATION OF WAVE ENERGY CONVERTERS

Wave energy converters can be classified by their operating principle and deployment location (shoreline, nearshore or offshore). Despite the large variation in design concepts (more than 1000 patented designs were being reported as far back as 2002), three operating principles predominate (Drew, Plummer & Sahinkaya 2009). These operating modes are summarised briefly here:

**Attenuator:** An attenuator is a floating device oriented parallel to wave propagation direction (Figure 3.1). These devices capture energy from the relative motion between two sections or arms of the device as the wave passes them. Progressive attenuation of waves occurs along the length of the device as energy is extracted.

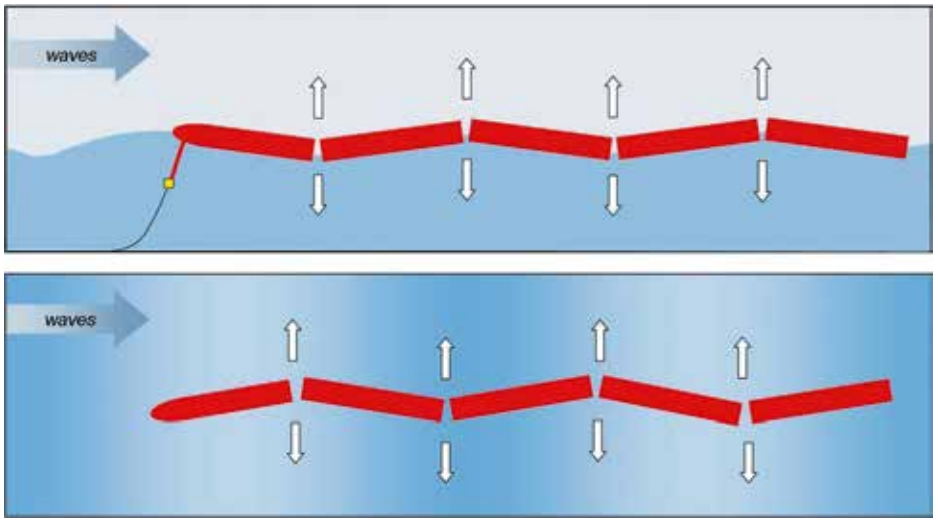


**Fig 3.1** An example of attenuator device – The Pelamis device in elevation (upper) and plan (lower) (http://www.pelamiswave.com/pelamis-technology/).


**Fig 3.2** An example of point absorber device – Ocean Power Technologies' PowerBuoy (http://www.oceanpowertechnologies.com/).

**Point absorber:** Point absorbers are floating wave energy devices which have small horizontal dimensions at the waterline compared with wave length (Figure 3.2). These devices capture energy from the 'heave' motion of the waves. They may be fully or partially submerged.

**Oscillating Wave Surge Converter or Terminator:** Oscillating wave surge converters extract energy from wave surge movement of water particles, for example, Oyster wave power device. Oyster (see Figure 3.3 for an array of Oysters) is a buoyant, hinged flap which is attached to the seabed, pitches backwards and forwards. The movement of the flap is used to drive hydraulic pistons which push high pressure water onshore via a subsea pipeline to drive a conventional hydro-electric turbine.

According to The Crown Estate lease documents, attenuator and oscillating wave surge converters are expected to be deployed in arrays at locations in the Pentland Firth and Orkney Waters and other Scottish waters. It may be possible to model the above three types of devices in Delft3D and MIKE Spectral and Boussinesq models.

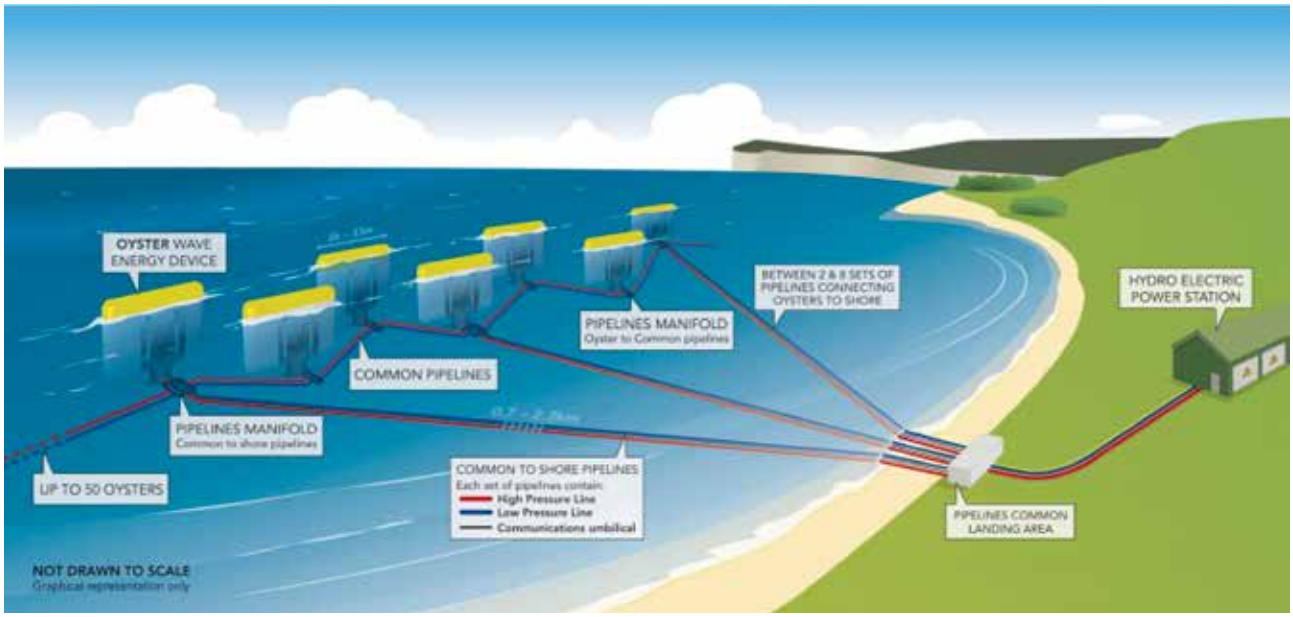


**Fig 3.3** An example of terminator device – Aquamarine Power's Oyster (http://www.aquamarinepower.com/).

## 03/3 MODELLING OF ARRAYS

The presence of any fixed or moving structure in an incident wave field modifies that wave field through the processes of diffraction and radiation (see Figure 3.4) that effectively scatter a proportion of the incident wave field in all directions. When the structure is a wave energy converter, a proportion of the incident energy is also removed from the system through the device's power take-off system. Therefore, accurate representation of wave energy converters in numerical models, both singly and in arrays, must incorporate the wave scattering and energy extraction processes.

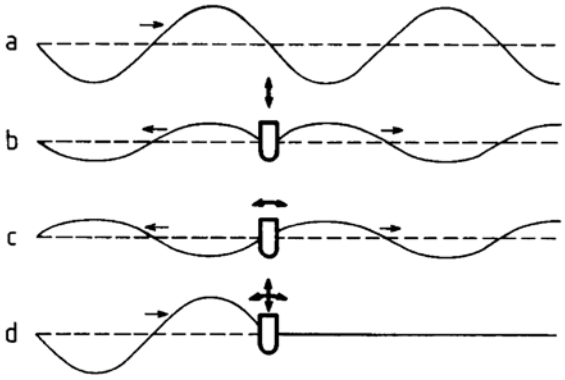


**Fig 3.4** Wave absorption by a wave energy converter operating in heave and surge.
a) undisturbed wave;
b) wave radiated by heave motion;
c) wave radiated by surge motion and
d) resultant wave field after the superposition of wave motions a), b) and c) (Falnes 2002).

Figure 3.5 considers a generic wave array development and proposes a zoning based on the physical processes predominating in each zone:

- Zone A (individual device): wave-structure interactions, viscous effects;
- Zone B (multiple devices): wave-structure interactions, wave reflection, wave scattering and other phase-dependent effects;
- Zone C (array scale): multiple wave-structure interactions within and between arrays;
- Zone D (regional scale): composite array effects (wave scattering), refraction (bathymetry), wave-wave interactions (e.g. triad & quadruplet), dissipation (e.g. wave breaking, bed friction), growth (e.g. wind).

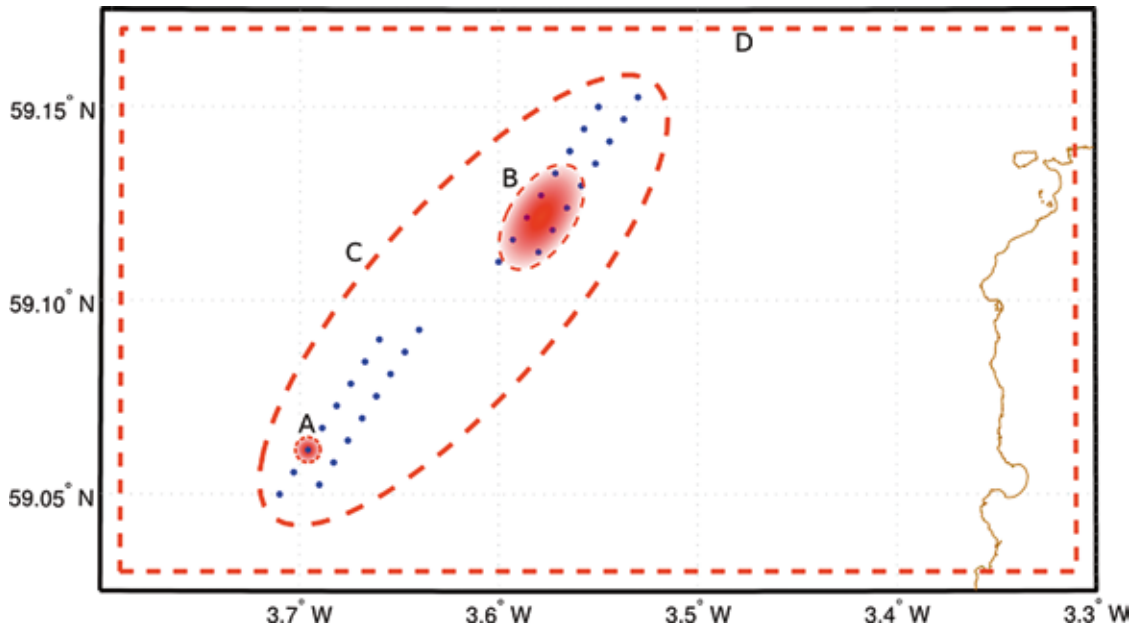


**Fig 3.5** Zoning for numerical model techniques based on significant physical processes.

Folley et al. (2012) categorised the contemporary numerical modelling techniques of arrays and undertook a comparative analysis to suggest the appropriate circumstances for each category on the basis of the model formulation and computational resources (Table 3.1, Appendix A). The study adopted four classes of models: computational fluid dynamic (CFD) models, potential flow models, Boussinesq/mild-slope models, and spectral wave models.

Boussinesq/mild-slope models and spectral wave models were considered best suited for regional scale hydrodynamic models (zone D) where the domains can extend up to several tens, possible hundreds, of kilometres, for example when assessing the regional impact of an array of wave energy converters. Potential flow or CFD models were considered more appropriate for the immediate vicinity of devices (zones A & B).

The challenge for Boussinesq/mild-slope models or spectral wave models is representing the important physical processes associated with wave-device interaction, individually and collectively. In the case of spectral wave models this reduces ultimately to understanding how the wave energy spectrum is modified in both frequency and directional space, which equates to understanding how a device responds to a forcing that varies in frequency, direction and magnitude.

## 03/3.1 GENERIC WEC CHARACTERISTICS

The performance of a particular wave energy converter is commercially sensitive information. However, characteristics can be determined theoretically from numerical solutions of the equations of motion of a generic device. The power absorbed by a device depends on the incident power (determined by the incident wave spectrum, a function of frequency and direction) and the device response to this forcing (determined by the device geometry, relative orientation and tuning parameters).

The incident power is the wave energy flux which in deep water is

$$E = \frac{\rho g^2}{4\pi} m_0 T_e = \frac{\rho g^2}{64\pi} H_{m0}^2 T_E \qquad [1]$$

where $m_0$ is the zeroth spectral moment and $T_E$ is the energy period.

Absorbed power is typically presented as a capture width function (typically a univariate function[1] of wave period) or a power matrix surface[2] (typically a bivariate function of wave period and height).

### 03/3.1.1 POWER MATRIX

A power matrix presents the mean power generated by the device as a bivariate function of the incident wave spectrum, usually the wave energy period and significant wave height – in effect a 'wave-to-wire' power matrix. However, it is the mean wave power absorbed by the device (i.e. the 'wave-to-device' power matrix) that is relevant for wave modelling. This could be recovered from the 'wave-to-wire' power matrix if the conversion efficiency matrix for the power take-off system is known. As this is usually confidential information not publically available, a constant conversion efficiency of 70% is presumed (Vidal et al. 2007, Le Crom, Brito-Melo & Sarmento 2008).

The power matrix of eight generic wave energy converters, each based on different working principles including a point absorber and an oscillating surge device, have been computed using a time domain numerical model integrating a formal equation of motion for the device (Babarit et al. 2012 – Figure 3.6 presents a subset of these). Unidirectional wave forcing was considered (i.e. no directional dependency).

a)

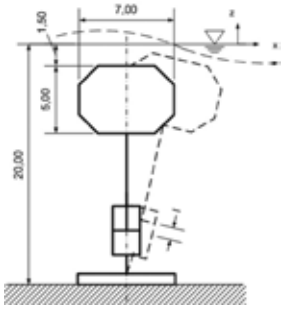


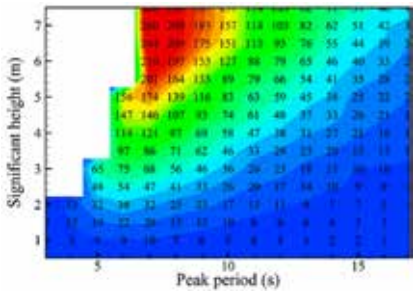


b)

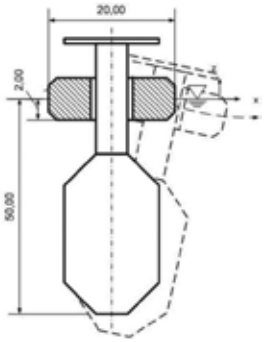


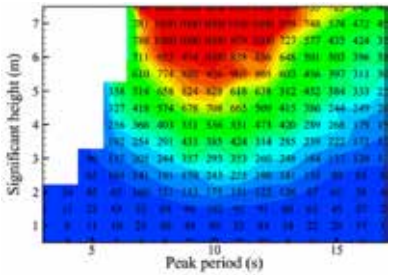


1| Capture width is defined as the ratio of the mean wave power absorbed by the device to the mean wave power per unit crest-length of the incident wave field and as such has the dimensions of length. Mean refers to the average value per wave period (regular waves) or energy period (irregular waves). Capture width is a function of frequency and relative direction although it is generally presented as a univariate function of frequency (i.e. no directional dependency). Relative capture width is the ratio of capture width to the representative dimension (width) of the device and as such is non-dimensional.

2| A power matrix presents the mean power generated by the device as a discrete bivariate function of wave period (usually the energy period) and significant wave height (a two parameter representation of the incident spectrum).

back to contents

c)

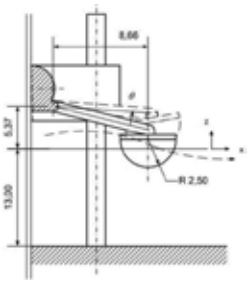

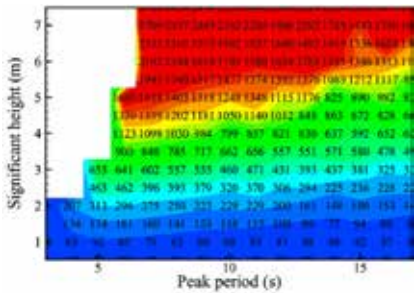


d)

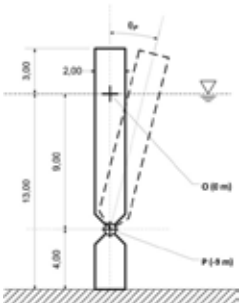

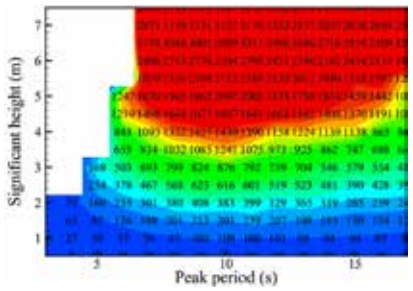


**Fig 3.6** Calculated output power matrices for generic wave energy converters: a) Bottom referenced submerged heaving buoy; b) Floating two-body heaving buoy; c) Heave buoy array; d) Bottom fixed oscillating flap. (Babarit et al. 2012).

The power matrix of the Pelamis750 attenuator device was derived in a similar fashion using an experimentally verified numerical model assuming a two parameter Pierson-Moskowitz spectra as input and taking into account the design constraints and the machine efficiency (Le Crom, Brito-Melo & Sarmento 2008 – see Figure 3.7).

For the present purpose it is the shape of the power matrix that is significant rather than the absolute values. Point absorber devices (Figure 3.6 a) and b)) which rely on a resonant response to wave forcing, are 'tuned' to a relatively narrow frequency range. In contrast a terminator device (Figure 3.6 d)) which responds to large wave excitation forces is relatively insensitive to forcing frequency. The attenuator device response appears to lie somewhere between that response of the point absorber and terminator.

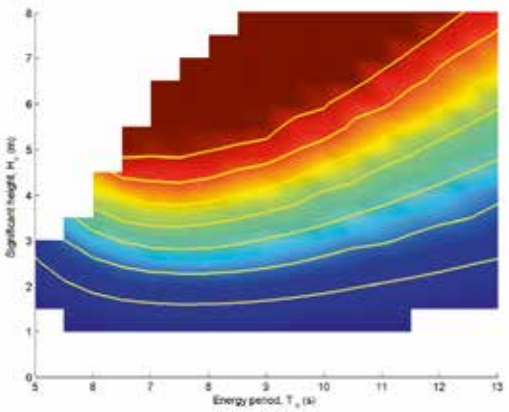


**Fig 3.7** Pelamis750 power matrix (after Le Crom, Brito-Melo & Sarmento 2008, Figure 5).

## 03/3.1.2 CAPTURE WIDTH

Capture width is defined as the ratio of the mean wave power absorbed by the device to the mean wave power per unit crest-length of the incident wave field and as such has the dimensions of length. Mean refers to the average value per wave period (regular waves) or energy period (irregular waves). Relative capture width is the ratio of capture width to the representative horizontal length scale of the device (i.e. diameter, width) and as such is non-dimensional.

Capture width is generally presented as a univariate function of frequency (Figure 3.8) which assumes all directions are absorbed equally – strictly capture width is a function of frequency and relative wave direction.

In practical situations, capture width is also a function of the incident wave energy principally as a consequence of a device's mechanical limits and survival strategy as significant wave height increases. At smaller significant wave heights the proportion of the available energy absorbed (i.e. the capture width function) is insensitive to wave height. As significant wave height increases the capture width decreases progressively. Applying a single capture width function for all sea-states, e.g. one derived at small significant wave heights, will overestimate the absorbed energy.

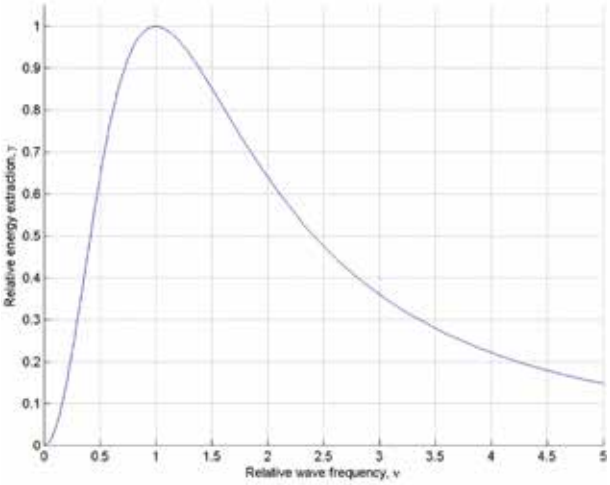


**Fig 3.8** Normalised energy extraction as a function of normalised forcing frequency for a linear single degree of freedom oscillating wave energy converter. Energy extraction normalised by maximum energy extraction, frequency normalised by resonant frequency (after Silverthorne, Folley 2011).

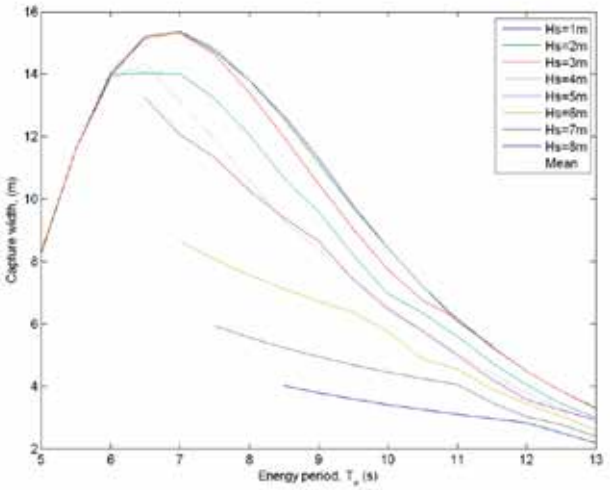


**Fig 3.9** Pelamis750 capture width. Established from Figure 3.7 assuming a constant mechanical to electrical conversion efficiency of 70%. The effects of mechanical limitations are apparent at large significant wave heights.

## 03/3.2 GENERIC WAVE ENERGY CONVERTERS

The characteristics observed in Section 03/3.1.1 are used to develop a generic power matrix for a point absorber, attenuator and terminator device (with a notional rated output).

a)

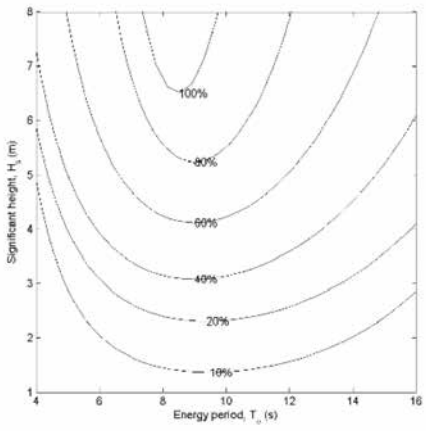


b)

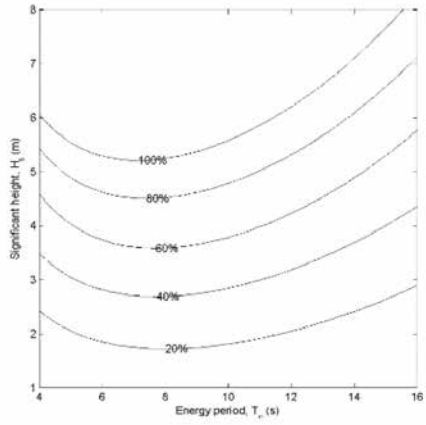


c)

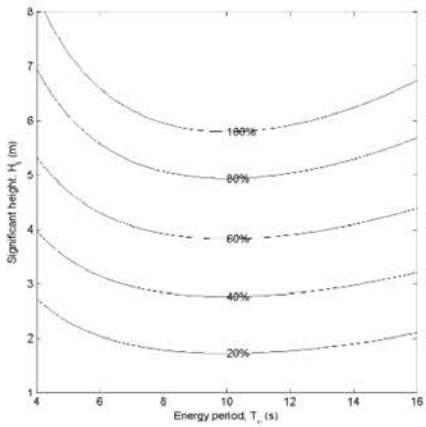


**Fig 3.10** Generic power matrices:
a) Point absorber
b) Attenuator
c) Terminator
Forms are based on those depicting in 03/3.1.1.

### 03/3.2.1 IMPLEMENTING A POWER MATRIX REPRESENTATION

Each point on the power matrix surface describes the global power absorption in response to a particular spectral shape defined by two spectral parameters (usually the energy period $T_e$ and significant wave height $H_{m0}$). A power matrix does not provide explicit information regarding the frequency range over which energy is absorbed, nor the proportions absorbed at each frequency. Additional information is required to determine these characteristics. In the absence of explicit information, the capture width function, derived separately or approximated from the power matrix surface, acts as a proxy.

Given $T_e$ „and" $H_{m0}$, the incident power $P_i$ is given by equation [1] and the absorbed power $P_a$ can be established from the power matrix. Hence the net (i.e. non-absorbed) power can be established and expressed as a proportion of the incident power (i.e. $1 - P_a/P_i$).

Neither the power matrix nor capture width provides explicit information on the directional distribution of the net (i.e. non-absorbed) power. Even the crude partitioning into a transmitted and reflected wave field is not possible as the relative proportions cannot be determined[3]. Any partitioning of the net power must be prescribed.

In the case of the crude partitioning into a transmitted and reflected wave field, prescribing one automatically defines the other wave field as a result of the conservation of energy.

It is presumed the net power is wholly transmitted[4] with a distribution in frequency space being that of the incident wave field modified according to the capture width function of the device. The directional distribution is considered to be unaffected (i.e. it remains that of the incident spectrum).

### 03/3.2.2 IMPLEMENTING CAPTURE WIDTH REPRESENTATION

The capture width function determines the global absorbed power for a particular spectrum represented by the spectral period. In the absence of additional information identifying the frequencies at which energy is extracted, it is assumed the capture width function itself provides a reasonable representation of this behaviour. That is the absorbed power at a particular frequency is the product of capture width value and the incident power at that frequency.

Directional sensitivity must be assumed – the simplest being that the capture width acts uniformly in all directions.

Furthermore it is assumed the device has fixed tuning and the capture width function has no dependency on the energy of the sea state, i.e. no dependency on significant wave height.

## 03/3.3 WEC ENERGY EXTRACTION MODULES

Wave energy project developers desire industry standard codes from recognised software houses, backed by defined quality assurance processes (e.g. ISO9001), to provide credibility of model outputs to third parties. While various research groups had implemented representations of wave energy devices (Smith, Pearce & Millar 2012, Silverthorne, Folley 2011) a wave energy device module had not been implemented in commercially available spectral wave or Boussinesq codes, either proprietary or open source as of 2012 (Table 3.2, Appendix A).

The launch in February 2014 of the WaveFarmer code[5] , developed by Garrad Hassan as part of the PerAWaT project, is arguably the first commercial code to satisfy the desire of wave energy project developers. While WaveFarmer is based on the open source spectral wave model TOMAWAC (Child, Weywada 2013), WaveFarmer is proprietary and as such the modifications to the TOMAWAC source code are not publically available and information on validation of the code is limited.

Elsewhere, Sandia National Laboratory (SNL) has developed a wave energy device module for the open-source SWAN model (Porter, Ruehl & Chartrand 2014, Ruehl, Porter & Roberts 2013). A device is characterised as an obstacle with a

3| This oversimplified representation ignores the directionality of waves radiated by the device.

4| Assuming reflection to be negligible (zero) may be reasonable in the case of a point absorber or attenuator but is questionable in the case of a terminator.

5| http://www.dnvgl.com/news-events/news/wavefarmer-tidalfarmer-software.aspx, Press release accessed 5 March 2014. http://www.gl-garradhassan.com/en/software/WaveFarmer.php, WaveFarmer code overview, accessed 24 April 2014.

transmission coefficient determined from user supplied power matrix surface or relative capture width function. SNL are in discussion with the SWAN code developers (Technical University Delft) regarding incorporating the module as a supported feature of the standard SWAN code

## 03/4 ARRAY MODELLING CONCEPTS IN NUMERICAL MODELS

There follows a brief description of the numerical techniques identified in the preceding section as appropriate for modelling regional scale effects of wave energy converter arrays and a review of studies based on these techniques.

### 03/4.1 SPECTRAL WAVE MODELS

Spectral wave models employ a phase-averaged representation of the wave field and consider the evolution of the two dimensional (frequency and directional) wave spectrum as the short-crested random wave field is transformed by spatial and temporal variations in wind, currents, water depth and various physical processes. In essence spectral wave models solve the wave action conservation equation

$$\frac{\partial}{\partial t}N + \frac{\partial}{\partial x}c_x N + \frac{\partial}{\partial y}c_y N + \frac{\partial}{\partial \sigma}c_\sigma N + \frac{\partial}{\partial \theta}c_\theta N = \frac{S_{tot}}{\sigma}. \quad [2]$$

Here the first term represents the local rate of change of wave action density $N(\sigma, \theta)$ in time, the second and third terms represent the propagation in geographic space (with velocities $c_x$ and $c_y$ in $x$- and $y$-space respectively), the fourth term represents shifts in relative frequency $\sigma$ (with velocity $c_\sigma$ in $\sigma$-space), the fifth term represents depth-induced and current-induced refraction (with velocity $c_\theta$ in $\theta$-space), and the source term $S_{tot}(\sigma, \theta)$ represents the effects of generation, dissipation and non-linear wave-wave interactions. The fully spectral formulation implies that short-crested random wave fields propagating simultaneously from widely different directions can be accommodated (e.g. a wind sea with super-imposed swell).

The representation of wave energy converters in such models, either individually or as an array, can be achieved only through accounting for their influence on the wave energy density spectrum. Specifically phase-dependent effects cannot be accounted for directly, although certain effects, e.g. diffraction, can be modelled approximately. Spectral wave models are widely used in coastal engineering. Examples include the open source codes SWAN (Simulating WAves Nearshore) developed by Technical University of Delft [and incorporated into the Deltares Delft3D suite] and TOMAWAC developed by Electricitié de France, and the proprietary code developed by DHI and provided as part of its MIKE suite.

Early approaches to represent wave energy converters adapted the existing functionality provided for representing coastal structures, e.g. breakwaters, where the dissipation of energy at the structures is accounted for through the specification of a transmission coefficient. The first studies considered an array as a single partially transmitting barrier with constant (i.e. frequency independent) transmission coefficient (Le Crom, Brito-Melo & Sarmento 2008, Millar, Smith & Reeve 2007). Several recognised shortcomings of this approach has been addressed subsequently through implementing frequency dependent transmission coefficients (Smith, Pearce & Millar 2012, Alexandre, Stallard & Stansby 2009, Ruehl, Porter & Roberts 2013) and resolving individual devices within the array (Smith, Pearce & Millar 2012, Carballo, Iglesias 2013, Ruehl, Porter & Roberts 2013). The latter was achieved by increasing the resolution of the computational mesh in the vicinity of the array such that individual devices, and importantly the gaps between individual devices, span several computational cells. This has been termed a ‚supra-grid' approach (Folley et al. 2012). Resolving individual devices explicitly models the regions of full and partial transmission and the subsequent diffraction in the lee of individual devices.

An alternative approach, termed as ‚sub-grid' (Folley et al. 2012), has been to represent the energy absorption characteristics of individual devices as a point source [or sink] of energy at a computational node by including an additional frequency and directionally dependent source term $S_{wec}$ in the governing equation (Silverthorne, Folley 2011, Weywada, Child & Cruz 2012, Greenwood, Christie & Venugopal 2013)

$$S_{wec}(f,\theta) = c_g\, C(f,\theta) E(f,\theta). \qquad [3]$$

Here the coefficient $C(f,\theta)$ represents the energy absorption characteristics of the device. This coefficient has been implemented in various ways: a constant, i.e. frequency and direction independent (Greenwood, Christie & Venugopal 2013); a generalised frequency and directional dependent function (Silverthorne, Folley 2011) (see Figure 3.11); and, a look-up table of a capture-width coefficient derived from frequency or time domain models of the device (Weywada, Child & Cruz 2012).

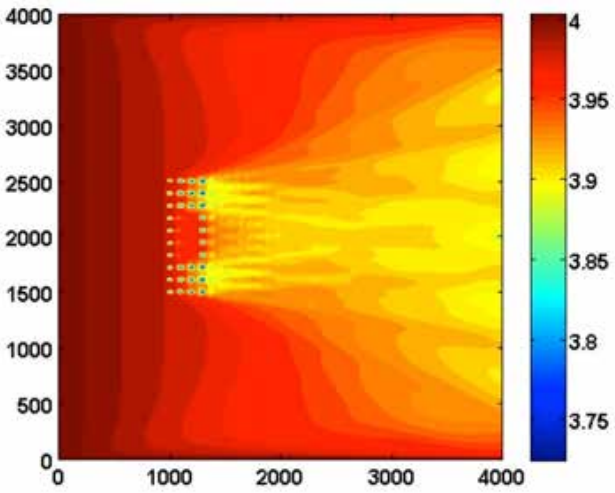


**Fig 3.11** Variation of significant wave height established using a source term representation of individual devices in an array. The wave shadow arising from localised energy extraction is clear but the technique does not account for wave scattering. Implemented in TOMAWAC (Silverthorne, Folley 2011).

Both ‘supra-grid' and ‘sub-grid' spectral wave approaches can represent the extraction of energy from the incident spectrum and model the subsequent re-distribution of energy in wave shadow zone that exists in the lee of the device or array. However, they do not account for the scattering or radiating of energy by the wave energy converters, although diffraction effects can be parametrically modelled with the caveat that the effects are not well reproduced in the immediate vicinity of a structure (i.e. within a few wavelengths).

The advantage of spectral wave models is the capability of incorporating complex bathymetry and their computational efficiency allowing large model domains.

Spectral wave models can be readily coupled to hydrodynamic flow models. Gonzalez-Santamaria et al. (2011) reported a fully coupled wave-hydrodynamic model of the WaveHub site, off the north coast of Cornwall, using a spectral wave model (SWAN) and an ocean circulation model (ROMS) to study wave-current interaction features. The influence of an array of wave energy devices

on the combined wave-current flow field, sediment transport, and the subsequent morphological changes, was also considered. The representation of the array in the spectral wave model follows that of Millar et al. (2007), i.e. as a single partially transmitting barrier with constant (i.e. frequency independent) transmission coefficient.

## 03/4.2 BOUSSINESQ AND MILD-SLOPE MODELS

Boussinesq and Mild-slope equation models are phase-resolving techniques, solving conservation of mass and momentum equations, used widely in nearshore (shallow water) applications, e.g. port and harbour studies. Typical domains extend a few kilometres. The attraction of these formulations is the capability of representing shoaling, refraction, diffraction, dissipation by wave breaking and bed friction, partial reflection and transmission at static structures, non-linear wave-wave interactions, and other physical phenomenon.

The classical Boussinesq approximation eliminates the vertical coordinate from the flow equations. Waves are thereby only described in the horizontal plane. The approximation is performed by the use of Taylor expansion of the velocity potential at a given depth. Mild-slope formulations gain greater computational efficiency as a result of imposing further constraints, e.g. linear waves and mildly varying bathymetry. The classical formulations were derived for shallow water conditions but have been extended to apply to intermediate water conditions [the wave celerity becomes increasingly inaccurate as the relative water depth increases particularly in deep water, $h/\lambda_0 > 0.5$].

Although dynamic structures cannot be modelled explicitly, static structures and the characteristics of the dynamic structures, e.g. the transmission, reflection, absorption, and radiation characteristics, can be represented through the careful use of modelling techniques, e.g. judicious use of ‚sponge' and ‚porosity' layers and wave generation within the model domain. The depth averaged formulation implies that structures are presumed to extend to the sea-bed which is clearly not the case for moored floating structures.

Venugopal & Smith (2007) created a MIKE21-BW model domain 5km by 4.5km, with a 10m spatial resolution, to study the modification to the wave field in the presence of a linear array of 5 devices (Figure 3.12). Each device was represented as a structure with a fixed frontal length of 160m and width of 10m (a single computational cell) and a porosity parameter varying between 0 (a solid structure) and 1 (an open structure). The model output was consistent with the physical processes of reflection, diffraction and absorption. The question is whether a single porosity parameter is sufficient to represent a particular device's reflection, absorption and transmission characteristics.

Beels et al. (2010a) created a mild-slope equation wave model (MildWAVE) in which devices are modelled as individual absorbing structures using a sponge layer technique that provided frequency dependent absorption characteristics (Figure 3.13). Each device spans several computational cells with each cell assigned individual absorption coefficients. By varying the absorption coefficient of individual cells the transmission, and consequently absorption of the structure, can be made effectively independent of the reflection. This avoids the coupling of the reflection and transmission that occurs when applying a constant absorption (or porosity) coefficient, as seen by Venugopal & Smith (2007). Furthermore, the absorption coefficients can be tuned to replicate a particular device's absorption characteristics, e.g. as represented by the power matrix, for a fixed reflection. The model was used to study the modification of the wave field in a domain of constant depth and limited extent, up to 7km by 5km, by an array of devices based on published characteristics of the WaveDragon overtopping device ; (Beels et al. 2010a, Beels et al. 2010b).

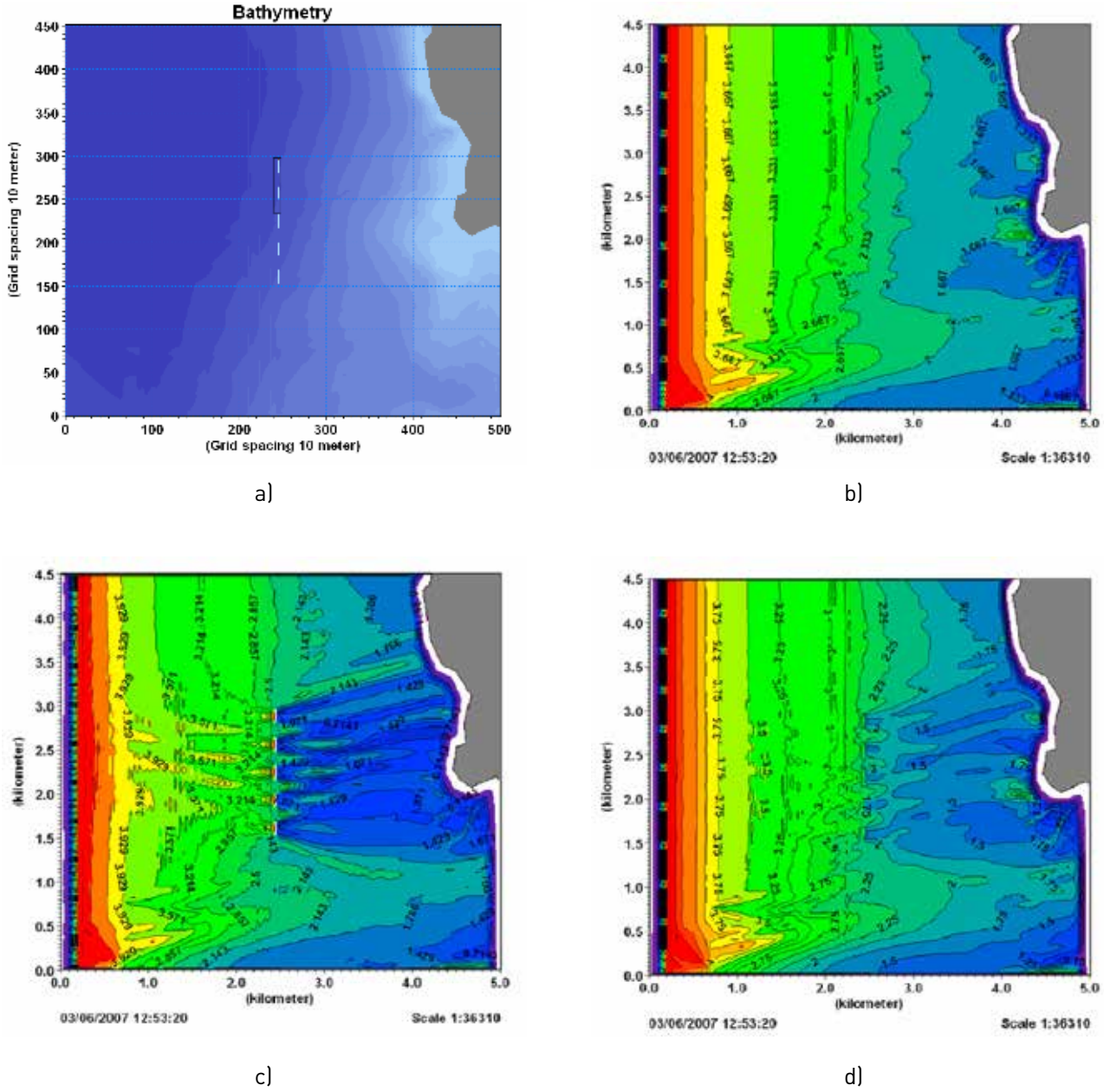


**Fig 3.12** Boussinesq wave modelling of wave energy converters.
a) Domain bathymetry and device locations;
b) undisturbed wave field, long-crested irregular waves $H_s$=4m, $T_p$=10s;
c) solid structures (porosity=0);
d) porous structures (porosity=0.7)
(Venugopal, Smith 2007).

Palha et al. (2010) modified the REFDIF model[6] to study the impact of arrays in the maritime zone off the west coast of Portugal on coastal circulation patterns and surf zone dynamics. The study considered five configurations of arrays of the Pelamis device in a model domain extending approximately 37 km by 35 km. Each array was modelled as a single entity (i.e. individual devices were not resolved). Within an array additional energy dissipation was applied based on a power matrix published by the device developer. However the REFDIF model considers only monochromatic waves, does not account for reflections, and only considers diffraction normal to the wave propagation direction.

Vidal et al. (2007) created a mild slope equation model (OLUCA-SP, based on the parabolic approximation of the mild slope equation) coupled with a coastal current and a morphology model to study the impact on coastal currents and sediment transport by an array of ten point absorber devices (the OPT PB150) deployed in an area 800m by 600m approximately 9 km offshore of the coastline under assessment. The influence of the array is simply presumed to impose a global wave height transmission coefficient of 96% [a value determined from consideration of the hydrodynamic performance of the device and moorings given a reported annual average electrical efficiency and assuming the conversion chain efficiencies].

## 03/4.3 POTENTIAL FLOW MODELS

Boundary element methods (BEMs) can resolve the motions of arbitrarily shaped dynamic structures subject to phase-dependent wave interactions. The formulation is based on linear potential flow theory and considers small amplitude body motions. Application in high sea-states where non-linear effects are significant or where structure motions are large will result in erroneous outputs. Furthermore viscous effects are neglected.

The computational resources required by BEM models increase rapidly as the square of the number of elements. The representation of large

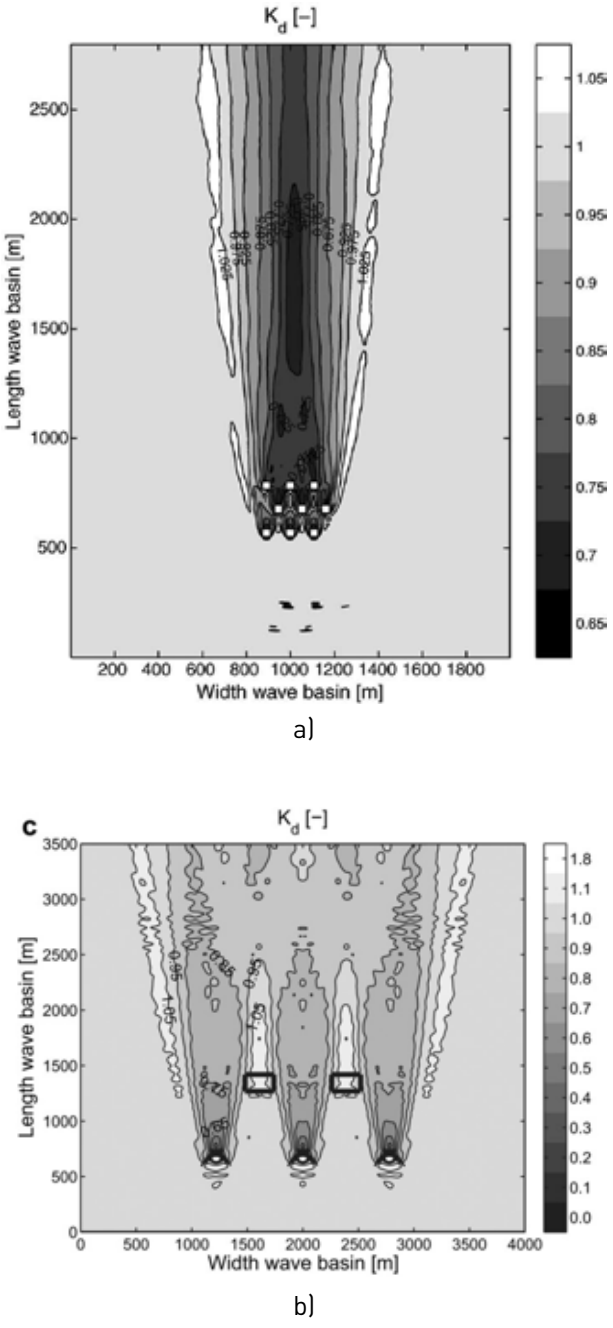


**Fig 3.12** Mild-slope modelling of wave energy converters. Disturbance coefficient for long-crested irregular waves in a wave basin:
(a) 9 hypothetical WEC structures in a staggered grid, $H_s$=1m, $T_p$=5.2s. (Beels et al. 2010a);
(b) 3 WaveDragon devices, $H_s$=4m, $T_p$=9.8s.
Note the resolved shape (Beels et al. 2010b).

6| The REFDIF model (Dalrymple and Kirby, 1991) is based upon the large angle parabolic approximation of the mild slope equation and simulates the propagation of sinusoidal (monochromatic) waves over varying bathymetry.

domains, many devices and arbitrary bathymetry is constrained by the computational requirements. Therefore, it is common for BEM models to presume infinite or constant water depth, to restrict consideration to small domains containing a few devices, less than ten, for reasons of computational efficiency. Acceleration techniques, the Fast Multipole Algorithm, have been implemented which have enabled the consideration of up to 25 devices (Borgarino, Babarit & Ferrant 2012).

An alternative approach to accelerating the calculation of an extended domain is the consideration of far-field analytical solutions for the perturbed velocity potential (Babarit et al. 2013, McNatt, Venugopal & Forehand 2013). An analytical far-field approximation of the perturbation velocity potential, expressed in terms of a Kochin function evaluated on some enclosing cylindrical boundary, represents the effect of the device(s) on the incident velocity potential. It has been proposed that the Kochin function can be used to couple BEM models to larger regional models such as a Boussinesq or spectral wave model. The Kochin function, evaluated separately in a BEM model, would be used to introduce the perturbed wave field propagating away from the device, or array of devices, in a phase resolving model. A mechanism by which this may be achieved has been elaborated although not implemented potential (Babarit et al. 2013).

## 03/5 ENVIRONMENTAL IMPACT ASSESSMENTS SCENARIOS

Environmental impact assessments (EIAs) are prepared as part of the planning application process to provide consenting bodies with evidence of the anticipated consequences of a proposed development. An EIA is typically prepared at an outline design stage in the knowledge that any proposed device layout is likely to be altered in subsequent detailed design stages leading up to construction. Alterations to any approved planning application for a development are subject to the approval of the planning authority which may require aspects of the EIA to be revisited and revised.

### 03/5.1 REPRESENTING AN ARRAY AS A SINGLE ENTITY OR INDIVIDUAL DEVICES

The likelihood that array layouts will change between the outline design stage and the construction stage has led to the view that representing an array as a single entity, or obstacle, might be preferable for the purpose of an EIA. This is attractive from a computational efficiency perspective, as it avoids the fine resolution computational mesh required to resolve individual devices, and is consistent with the draft standard IEC 62600-101 recommendation for a minimum spatial resolution of 500m in numerical models at the feasibility stage (presumed to be equivalent to the stage at which an EIA is developed). For the detailed design stage the draft standard IEC 62600-101 recommends a minimal spatial resolution of 50 m[7]. Even at this resolution, individual devices are unlikely to be resolved.

Spectral wave model obstacles (in this case the array) are presumed to be a linear or piece-wise linear entity with length greater than, but width less than, the computational mesh dimension[8]. Arrays consisting of multiple rows of devices may violate this presumption although it may be possible to represent each row as a separate obstacle.

The single entity approach will not reproduce certain hydrodynamic features observed in the lee of an array, principally the regions of unhindered propagation of energy passing between individual devices. Resolving such features will require a fine resolution computational mesh with dimension smaller than the device width. However, it is not clear how far from the array such features remain significant, and so should be resolved. It can be argued that when considering a regional scale these features are not significant.

A single entity representation may be appropriate at the outline design stage before proceeding to individual device representations as the project design develops.

Intuitively, representing off-shore (deep water) arrays, where the distance to nearshore regions

7| The extent of the model domain is not expected to exceed 25km at the design stage.

8| A SWAN OBSTACLE is considered a sub-grid feature in relation to its width (i.e. is narrow compared to the mesh cell dimension) but is a super-grid feature in relation to its length which should be at least one mesh cell.

is sufficiently large, as a single entity could be appropriate. Near-shore (shallow-water) arrays should resolve individual devices as the lee features referred to above can be expected to be significant.

## 03/5.2 SCENARIOS

It is common for an environmental impact assessment (EIA) to consider a "worst case" scenario for a particular development on the premise that if impacts are deemed acceptable in this scenario then all other scenarios will also be acceptable. A "realistic case" scenario is also presented as a counterpoint. However it is not clear what constitutes a "worst-case" scenario when considering the environmental impact of arrays of wave energy devices.

The complete absorption of the wave energy incident to the array (i.e. zero transmission through the array) is an instinctive choice and while this is arguably appropriate from a hydrodynamic perspective, it is not certain that this situation represents a "worst case" for other processes that are dependent on the hydrodynamics (e.g. nearshore ecology or morphodynamic processes).

It is important for an EIA to assess the sensitivity of environmental parameters to the variations considered in the scenarios. Particular parameters will remain constant between scenarios, for example the incident wave field, with its specific distribution of wave conditions, and the individual wave energy device characteristics. What are likely to change are the extent of the array and the density of devices within the array. Modelling the array as a single entity will require the characteristics of the array to be adjusted to reflect the density of the devices within the array.

The morphodynamic and ecological character of a region are a dependent on the wave climate. This character will respond to variations in the wave climate which can be seasonal variations (e.g. as demonstrated by typical winter and summer beach cross-shore profiles), long term multi-annual variations (e.g. as a result of changing weather patterns), or the step change variations of discrete interventions (e.g. the construction of a wave energy device array). The aspect of a wave climate that determines the character varies. Characteristics may be determined by the severity of peak events (e.g. plant habitats) while other characteristics may be determined relation between peak and mean conditions (e.g. cross shore sediment transport). It is important that EIAs consider the impact over the annual range of the wave climate. Determining whether a response is likely to be significant is a key purpose of an EIA.

## 03/6 MODELLING WECS WITH MIKE21 SPECTRAL WAVE (SW) MODEL

The MIKE21 Flexible Mesh Spectral Wave module (MIKE21FM-SW) uses a cell-centred finite-volume technique on an unstructured mesh to propagate wave action through the model domain using phase averaged equations.

The MIKE21FM-SW model does not have explicit functionality for incorporating the dissipation (by absorption) and redistribution of wave energy by wave energy devices. Consequently, devices must be represented by adapting other functionality. Greenwood et al. (2013) explored two possible methods of removing and redistributing energy from the model domain: (a) a source term approach; and (b) a 'reactive polygon' approach.

## 03/6.1 WEC AS A SOURCE TERM

MIKE21FM-SW can represent the reduction in wave energy behind a structure, in this case a wave energy converter, as a point source term in the wave action equation. MIKE21FM-SW implements the source term equation [3] with a frequency dependent coefficient

$$C(f) = {}^{-c(f)}/_{A} \qquad [4]$$

where $A$ is the area of the cell containing the WEC and $c(f)$ determines the energy absorption

characteristics of the structure. $c(f)$, which is referred to as a 'reflection factor' in the MIKE21 documentation, is specified by a pre-defined or user-defined look-up table describing the factor as a function of water depth and wave period over a specified range of depth and period.

## 03/6.2 WEC AS A 'REACTIVE POLYGON'

An individual WEC can be represented as an artificial island of defined size and shape at the mesh generation stage of MIKE21FM-SW model (Greenwood, Christie & Venugopal 2013). This 'supra-grid' approach has limited applicability as representing the device as land implicitly results in 0% energy transmission through the device, effectively absorbing all incident energy. However, Greenwood et al. (2013) developed the artificial island concept further, incorporating wave boundary conditions imposed at the island's perimeter to represent energy reflected and transmitted by the device.

This two stage process requires the creation of a 'with device' and a 'without device' model. The first stage determines the undisturbed wave field in the absence of devices. At the second stage, the undisturbed wave spectrum at the location of a device is used to determine a reflected and a transmitted spectrum that would be emitted by the device based on the device's frequency and directionally dependent absorption characteristics. The reflected and transmitted spectra are then imposed as additional boundary conditions at the up- and down-stream faces respectively of the artificial islands (i.e. the wave energy devices) in an execution of the 'with device' model.

Greenwood et al. (2013) used frequency and directionally dependent absorption characteristics based on generalised functions that were considered representative of an oscillating surge device (see Figure 3.14).

a)

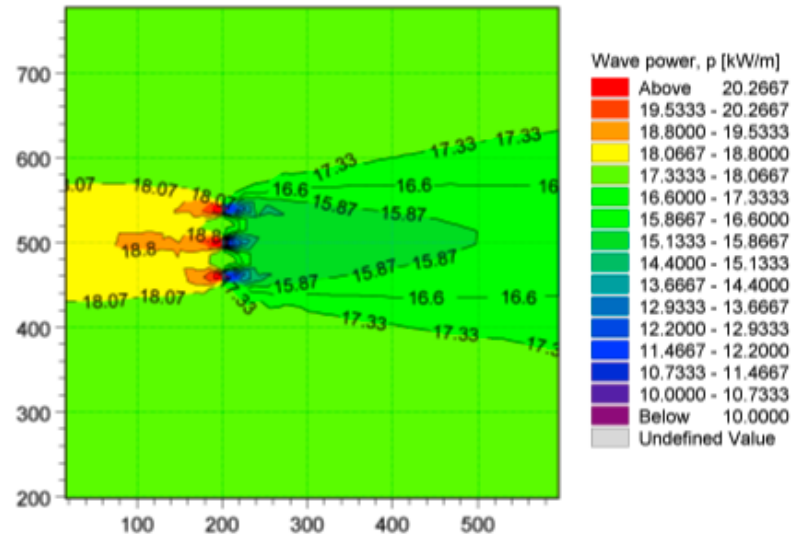


b)

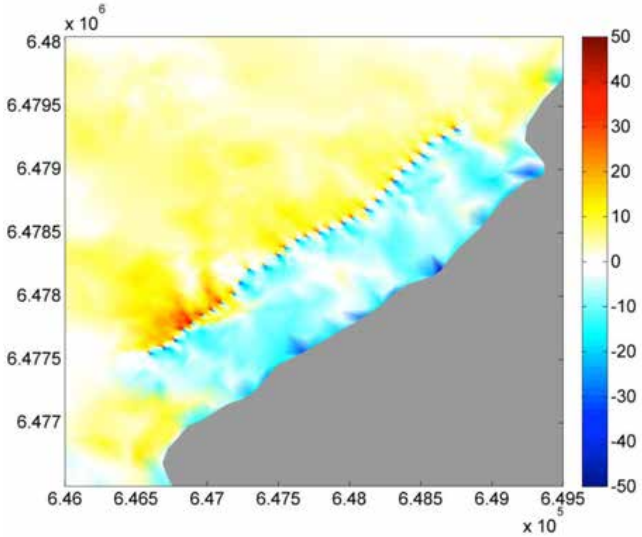


**Fig 3.14**

a) Spatial variation in wave power in the presence of three wave energy devices modelled using the reactive polygon technique;

b) Annual average variation in wave power in the presence of an array of reactive polygon structures off the north-west coast of the Isle of Lewis, Scotland (Greenwood, Christie & Venugopal 2013).

The above method needs further verification and validation. However, in the absence of any other approaches for representing reflection with MIKE21FM-SW, the TeraWatt project will attempt to use this method and validation will be carried out with data available from site measurements or from other numerical models.

## 03/7 MODELLING WECS WITH MIKE21 BOUSSINESQ WAVE (BW) MODEL

The MIKE21-BW model is based on the two dimensional Boussinesq equations with enhanced linear dispersion characteristics in a depth integrated flux-formulation (Madsen, Sorensen 1992).

MIKE21-BW is capable of modelling WEC arrays as porous structures. WECs can be represented by sponge and porosity layers, wherein a specified amount of energy absorption from waves can be imposed. The description of sponge layer and porosity layer generation is given here.

### 03/7.1 SPONGE LAYERS IN MIKE21-BW

Sponge layers are used to introduce artificial damping as waves pass through the layers. These are typically used at domain boundaries to dissipate wave energy incident to the boundary, effectively allowing waves to pass out of the model domain.

In the software this is done by dividing the surface elevation and the flux on a number of grid lines placed next to the boundary at each time step, by a set of numbers which increase towards the open boundary.

Basically, a reduction factor, $\mu$, is specified for each grid-point in the sponge layer. In each time step the surface elevation, $\eta$, is calculated. The surface elevation values in the sponge layers are then multiplied by the corresponding $\mu$-factors. The value in each sponge layer, $\mu$, increases from 1, before the first layer, towards a given value at the last sponge layer following the function $C_{sponge} = a^{r^{i-1}}$ where $a$ and $r$ are parameters which depend on the number of sponge layers, $i = 1 \ldots N_{sponge}$ and $N_{sponge}$ is the number of sponge layers.

DHI (2012) recommends the minimum thickness of a sponge layer equals the wavelength of the most energetic waves (i.e. corresponding to the spectral peak wave period) in order to achieve the best efficiency.

### 03/7.2 POROSITY LAYERS IN MIKE21-BW

A porous structure is considered to partly reflect, partly transmit and partly absorb incident wave energy and can be modelled by the use of porosity layers. These introduce additional laminar and turbulent dissipation terms that represent losses due to flow through the porous structure.
In practice, computational cells within the porosity layers are prescribed a porosity factor n with a value between 0 and 1, where 0 specifies a fully impermeable cell and 1 specifies an open water cell. Porosity layers can introduce partial reflection and absorption if they are backed up by land, and partial reflection and transmission if open water cells are to be found behind the porosity layers.

The transmission and reflection properties of the porosity layers depends on the water depth $h$, wave height $H$, wave period $T$, and width of porous structure $X_{porosity\ layer}$ (DHI 2012).

#### 03/7.2.1 VARIATION OF REFLECTION AND TRANSMISSION COEFFICIENT

A MIKE21 toolbox is provided to estimate the reflection, $K_r$, and transmission, $K_t$, properties of porosity layers. The toolbox is based on an analytical solution for linear shallow water waves and a vertical porous absorber on a horizontal bottom in which the reflection and transmission are dependent on wave period $T$, wave height $H$, water depth $h$, porous layer width $X_{porosity\ layer}$ and porosity factor $S$ (Madsen 1983). It is emphasized that the analytical solution is not particularly accurate when considering reflection of irregular wave trains, due to non-linear effects.

An indication of the dependence of the reflection and transmission coefficients, as by the MIKE21 toolbox is shown in Table 3.1. It is seen that $K_r$ and $K_t$ are coupled.

| INCREASING VALUE OF: | $K_r$ | $K_t$ |
|---|---|---|
| $T$ | Increasing | Increasing |
| $H$ | Increasing | Decreasing |
| $X_{porosity\ layer}$ | Varying | Decreasing |
| $h$ | Decreasing | Increasing |
| $S$ | Decreasing | Increasing |

**Table 3.1** Dependence of increasing parameters, and coupling between $K_r$ and $K_t$.

## 03/7.3 WAVE SCATTERING IN MIKE 21-BW

Incident waves approaching a farm of WECs are redistributed through several different physical processes. Among these is the wave scattering, in the form of diffraction. Diffraction is described by the diffraction/disturbance coefficient $K_d$ which is defined as the diffraction/disturbed wave height divided by the incident wave height, $H/H_i$.

## 03/8 MODELLING WECS WITH DELFT3D

The Delft3D-WAVE module currently implements version 40.72ABCDE of the SWAN wave model (i.e. not the most recent version). The SWAN model is based on the discrete spectral action balance equation and computes the evolution of random, short-crested waves in coastal regions with deep, intermediate and shallow water and ambient currents. Integration of the action balance equation has been implemented with finite difference schemes in all five dimensions (time, geographic space and spectral space) on a curvi-linear structured computational grid.

The only mechanism to incorporate a structure in Delft3D-WAVE is through the code's OBSTACLE function. This specifies the characteristics of a sub-grid obstacle through which waves are transmitted, or against which waves are reflected, or both. Diffraction at the ends of the obstacle is not modelled. However, diffraction effects in irregular short-crested wave fields are only significant within one or two wavelengths of the ends of an obstacle. Therefore, the model is expected to reasonably represent the wave field around an obstacle if the directional spectrum of incoming waves is not too narrow.

The location of the obstacle is defined by a polyline. The obstacle interrupts wave propagation from one grid point to another wherever the polyline intersects the line between two neighbouring grid points of the computational grid. The effective spatial resolution is therefore equal to the computational grid spacing.

Two types of obstacle can be defined:

- **Sheet obstacle:** A constant transmission coefficient is specified and applied along the obstacle.

- **Dam obstacle:** The transmission coefficient is a function of wave height at the obstacle and the obstacle's crest level and two shape parameters, using the expression derived by Goda et al. (1967). Examples of the shape parameters, established by Seelig (1979), for various structures are provided.

The transmission coefficient $K_t$ represents the ratio of transmitted and incident significant wave height. An optional constant reflection coefficient $K_r$ (the ratio of reflected and incident significant wave height) can be specified too, with the choice of specular or diffuse reflection characteristics. The transmission and reflection coefficients must satisfy the criterion ${K_t}^2 + {K_r}^2 \leq 1$.

The standard OBSTACLE function does not affect frequency or directional characteristics, influencing the energy scale of the spectrum only and not the spectral shape. Incorporating a frequency and directional dependency requires recoding of the OBSTACLE function.

Modifications to incorporate a frequency dependent transmission function in the SWAN model have been implemented (Smith, Pearce & Millar 2012, Porter, Ruehl & Chartrand 2014) although an interface to the Delft3D-WAVE module has not been implemented. Device behaviour is represented by a relative capture width function or a power matrix function which characterises the absorption characteristics of the device as function of incident frequency (relative capture width) or incident frequency and energy respectively (power matrix).

## 03/9 CONCLUDING SUMMARY

The paper gives an account of numerical methods available for quantifying hydrodynamic interactions between wave energy converters (WECs) and the impact of arrays of wave energy converters on the surrounding wave climate. The challenge is to use the appropriate model technique in the appropriate situation to resolve the relevant physical processes.

Predicting the environmental impact of an array, or several arrays, of wave energy converters in a region requires the use of spectral wave models. While phase-averaging spectral wave models represent fewer physical processes explicitly than phase resolving models – notably diffraction – their computational efficiency, which permits modelling large domains, makes them extremely useful for resource assessments and for environmental impact. Furthermore, several spectral wave codes are readily available with user friendly interfaces and are relatively simple to use.

However, the standard functionality of most spectral wave codes provides a limited capability for representing wave energy converters. A device's characteristics are incorporated in the spectral wave model through transmission coefficients and reflection coefficients derived from the device's power absorption characteristics. While it is preferable for the coefficients to have a frequency and directional dependency, the ability to incorporate this dependency is limited without modifications to the standard functionality of the current spectral wave codes. The exception appears to be the proprietary ‚WaveFarmer' code developed by Garrad Hassan as part of the PerAWaT project (Rawlinson-Smith et al. 2010) although the form of the modifications are not clear.

A device's absorption characteristics are commonly presented as a capture width function or power matrix function irrespective of the type of wave energy device. These functions are a basic requirement for modelling wave energy devices. It is recognised that the absorption characteristics of a particular device is commercially sensitive information. However, not even generalised device characteristics are readily available in the public domain which limits the value of the numerical modelling studies undertaken to date.

The characteristics of a device, arrays of devices, can be established from scaled physical modelling, such as the large-scale physical modelling of an array of 25 generic heaving devices (Troch et al. 2013), or from numerical modelling techniques such as the potential flow models (Babarit et al. 2013, McNatt, Venugopal & Forehand 2013). With this information it will be possible to represent arrays in spectral wave models. Ultimately, it is hoped that the monitoring of the first full-scale array deployments will provide information to validate the numerical modelling.

It should be noted that spectral wave model formulations do not permit explicit representation of the physical processes associated with wave-structure interactions rather they represent the consequences of the energy absorption characteristics of devices. The wave-structure interaction processes are better evaluated by other model formulations, e.g. potential flow models or CFD.

As stated above, the challenge is to apply appropriate model techniques in appropriate situations to resolve the relevant physical processes. This requires the coupling of phase-averaging spectral wave models to represent extra-array effects with other model techniques, e.g. potential flow models, to establish the intra-array effects.

back to contents

## 03/10 REFERENCES

Alexandre, A., Stallard, T. & Stansby, P.K. 2009. *Transformation of Wave Spectra across a Line of Wave Devices.* Proceedings of the 8th European Wave and Tidal Energy Conference.

Babarit, A., Folley, M., Charraye, F., Peyrard, C. & Benoit, M. 2013. *On the modelling of WECs in wave models using far field coefficients.* Proceedings of the 10th European Wave and Tidal Energy Conference.

Babarit, A., Hals, J., Muliawan, M.J., Kurniawan, A., Moan, T. & Krokstad, J. 2012. *Numerical benchmarking study of a selection of wave energy converters.* Renewable Energy, vol. 41, no. 0, pp. 44-63.

Babarit, A. 2010. *Impact of long separating distances on the energy production of two interacting wave energy converters.* Ocean Engineering, vol. 37, pp. 718.

Beels, C., Troch, P., Backer, G.D., Vantorre, M. & Rouck, J.D. 2010a. *Numerical implementation and sensitivity analysis of a wave energy converter in a time-dependent mild-slope equation model.* Coastal Engineering, vol. 57, no. 5, pp. 471.

Beels, C., Troch, P., Visch, K.D., Kofoed, J.P. & Backer, G.D. 2010b. *Application of the time-dependent mild-slope equations for the simulation of wake effects in the lee of a farm of Wave Dragon wave energy converters.* Renewable Energy, vol. 35, no. 8, pp. 1644.

Borgarino, B., Babarit, A. & Ferrant, P. 2012. *Impact of wave interactions effects on energy absorption in large arrays of wave energy converters.* Ocean Engineering, vol. 41, no. 0, pp. 79.

Carballo, R. & Iglesias, G. 2013. *Wave farm impact based on realistic wave-WEC interaction.* Energy, vol. 51, no. 0, pp. 216.

Child, B.F.M. & Weywada, P.L. 2013. *Verification and validation of a wave farm planning tool.* Proceedings of the 10th European Wave and Tidal Energy Conference.

DHI 2012. *MIKE 21 SW Spectral Waves FM Module User Guide.*

Drew, B., Plummer, A. & Sahinkaya, M.N. 2009. *A review of wave energy converter technology.* Proceedings of the Institution of Mechanical Engineers, Part A: Journal of Power and Energy, vol. 223, no. 8, pp. 887-902. Falnes, J. 2002, Ocean waves and oscillating systems, Cambridge University Press.

Folley, M., Babarit, A., Child, B., Forehand, D., O'Boyle, L., Silverthorne, K., Spinneken, J., Stratigaki, V. & Troch, P. 2012. *A review of numerical modeling of wave energy converter arrays.* International conference on ocean, offshore and arctic engineering, Proceedings ASME, pp. 1.

Goda, Y., Takeda, H. & Moriya, Y. 1967. *Laboratory investigation on wave transmission over breakwaters.* Port and Harbour Technical Research Institute.

Gonzalez-Santamaria, R., Zou, Q. & Pan, S. 2011. *Two-way coupled wave and tide modelling of a wave farm.* Journal of Coastal Research, no. 1, 64, pp. 1038-1042.

Greenwood, C.E., Christie, D. & Venugopal, V. 2013. *The simulation of nearshore wave energy converters and their associated impacts around the Outer Hebrides.* Proceedings of the 10th European Wave and Tidal Energy Conference.

back to contents

Le Crom, I., Brito-Melo, A. & Sarmento, A. 2008. *Maritime \Portugese pilot zone for wave energy conversion: modelling analysis of the impact on surfing conditions.* Proceedings of the 2nd International Conference on Ocean Energy.

Madsen, P.A. & Sorensen, O.R. 1992. *A new form of the Boussinesq equations with improved linear dispersion characteristics. Part 2. A slowly-varying bathymetry.* Coastal Engineering, vol. 18, no. 3-4, pp. 183.

McNatt, J.C., Venugopal, V. & Forehand, D. 2013. *The cylindrical wave field of wave energy converters.* Proceedings of the 10th European Wave and Tidal Energy Conference.

Millar, D.L., Smith, H.C.M. & Reeve, D.E. 2007. *Modelling analysis of the sensitivity of shoreline change to a wave farm.* Ocean Engineering, vol. 34, no. 5-6, pp. 884-901.

Palha, A., Mendes, L., Fortes, C.J., Brito-Melo, A. & Sarmento, A. 2010. *The impact of wave energy farms in the shoreline wave climate: Portuguese pilot zone case study using Pelamis energy wave devices.* Renewable Energy, vol. 35, no. 1, pp. 62.

Porter, A., Ruehl, K. & Chartrand, C. 2014. *Further development of SNL-SWAN, a validated wave energy converter array modelling tool.* Proceedings of the 2nd Marine Energy Technology Symposium (METS).

Rawlinson-Smith, R., Bryden, I., Folley, M., Martin, V.a.S.,T., Stock-Williams, C. & Willden, R. 2010. *The PerAWaT project: Performance Assessment of Wave and Tidal Array Systems.* Proceedings the 3rd International Conference on Ocean Energy.

Ruehl, K., Porter, A. & Roberts, A.P.J. 2013. *Development of SNL-SWAN, a Validated Wave Energy Converter Array Modeling Tool.* Proceedings of the 10th European Wave and Tidal Energy Conference.

Seelig, W.N. 1979. *Effect of Breakwaters on Waves: Laboratory Tests of Wave Transmission by Overtopping.* Coastal Structures ,79ASCE, pp. 941.

Silverthorne, K.E. & Folley, M. 2011. *A New Numerical Representation of Wave Energy Converters in a Spectral Wave Model.* Proceedings of the 9th European Wave and Tidal Energy Conference.

Smith, H.C.M., Pearce, C. & Millar, D.L. 2012. *Further analysis of change in nearshore wave climate due to an offshore wave farm: An enhanced case study for the Wave Hub site.* Renewable Energy, vol. 40, no. 1, pp. 51.

Troch, P., Stratigaki, V., Stallard, T., Forehand, D., Folley, M., Kofoed, J., Benoit, M., Babarit, A., Sanchez, D.G., De Bosscher, L., Rauwoens, P., Elsasser, B., Lamont-Kane, P., McCallum, P., McNatt, C., Angelelli, E., Percher, A., Moreno, E.C., Bellew, S., Dombre, E., Charrayre, F., Vantorre, M., Kirkegaard, J. & Carstensen, S. 2013. *Physical Modelling of an Array of 25 Heaving Wave Energy Converters to Quantify Variation of Response and Wave Conditions.* Proceedings of the 10th European Wave and Tidal Energy Conference.

Venugopal, V. & Smith, G.H. 2007. *Wave climate investigation for an array of wave power devices.* Proceedings of the 7th European Wave and Tidal Energy Conference.

Vidal, C., Méndez, F.J., Díaz, G. & Legaz, R. 2007. *Impact of Santoña WEC installation on the littoral processes.* Proceedings of the 7th European Wave and Tidal Energy Conference.

Weywada, P.L., Child, B. & Cruz, J. 2012. *Implementation of a Spectral Wave Model for Wave Energy Converter Arrays.* Proceedings of the 4th International Conference on Ocean Energy.

back to contents

## 03/11 APPENDIX A

| | Potential flow models | | | |
|---|---|---|---|---|
| | **Linear BEM** | **Semi-analytical techniques** | **Time-domain formulation** | **Nonlinear BEM** |
| **Fundamental** | | | | |
| Definition of hydrodynamics | Implicit body surfaces<br>Explicit coefficients | | | |
| Nonlinear wave dynamics | Not capable | | | Implicitly capable |
| Nonlinear dynamics | Not capable | | Implicit solver | |
| Vortex shedding | Explicit inclusion by linearisation | | Explicit inclusion | |
| WEC radiation | Implicitly capable | | | |
| Diffraction | Implicitly capable | | | |
| Variable bathymetry and marine currents | Not capable | | | |
| **Computational** | | | | |
| Primary dependent | Number of panels | Complexity of function | Number of panels and complexity of equations | Number of panels |
| Secondary dependent | Number of frequencies and directions | | Number of time-steps | |
| Determinate of array "size" | Quadratic increase with number of WECs | | | |
| Solver | Simple and stable | | Simple and poss. unstable | Complex and stable |
| **Usability** | | | | |
| Required skill | Low | High | Medium | High |
| Software availability in 2012 | Commercial code available | Research code only | Commercial code available | Research code only |
| **Suitability ( **** - highly suitable, *** - moderately suitable, ** - poorly suitable, * - not suitable )** | | | | |
| Localised effects | *** | * to *** | *** | *** |
| Dynamic control | * | * | **** | **** |
| AEP (small WEC array) | *** | *** | ** | ** |
| AEP (large WEC array) | ** | *** | ** | ** |
| Environmental impact | * | * | * | * |

[1] Limited to shallow water
[2] Limited to mild-slopes

| | | Spectral wave models | | |
|---|---|---|---|---|
| **Boussinesq** | **Mild-slope** | **Supra-grid** | **Sub-grid** | **CFD** |
| Explicit absorption layers | | Explicit absorption layer | Explicit source strength | Implicit fluid flow |
| Implicitly capable | Not capable | Implicitly capable for phase-averaged dynamics | | Implicitly capable |
| Explicit absorption layers | | Explicit absorption layer | Explicit source strength | Implicit solver |
| Explicit inclusion | | Explicit inclusion | | Implicit inclusion |
| Explicitly capable | | Not capable | Explicitly capable | Implicitly capable |
| Explicitly capable | | Approximated by phase-decoupled refraction-diffraction | | Implicitly capable |
| Implicitly capable[f] | Implicitly capable[f] | Implicitly capable | | Implicitly capable |
| Number of cells | | Number of cells | | Number of cells |
| Number of time-steps | | Number of frequencies and directions | | Number of time-steps |
| Linear increase with spatial area | | Linear increase with spatial area | | Linear inc. with spatial volume |
| Simple and poss. unstable | Simple and stable | Simple and stable | | Complex and poss. unstable |
| Medium | Low | Low | Medium | High |
| Commercial code available, WEC model required | | Open-source code available, WEC model required | | Commercial and open-source code available |
| [illegible] | [illegible] | [illegible] | [illegible] | [illegible] |
| [illegible] | [illegible] | [illegible] | [illegible] | [illegible] |
| [illegible] | [illegible] | [illegible] | [illegible] | [illegible] |
| [illegible] | [illegible] | [illegible] | [illegible] | [illegible] |
| [illegible] | [illegible] | [illegible] | [illegible] | [illegible] |

**Table 3.2** Comparative analysis of numerical modelling techniques for wave energy converter arrays (Table 1 of Folley et al. (2012)).

# MODELLING ENERGY EXTRACTION IN TIDAL FLOWS

# 04

S. Baston, S. Waldman, J. Side

ICIT, HERIOT-WATT UNIVERSITY, THE OLD ACADEMY, BACK ROAD, STROMNESS, ORKNEY, KW16 3AW

JULY 2015: REVISION 3.1

back to contents

# 04/1 EXECUTIVE SUMMARY

## 04/1.1 INTRODUCTION

Using hydrodynamic modelling to predict the environmental effects of energy extraction is of crucial importance for tidal energy development. This document explores the state of the art in how tidal energy extraction is represented in such models, and specifically examines the implementation of tidal turbines in the Delft3D (4.0 version) and MIKE 3 (2012 version) software. For that purpose, an assumption of horizontal axis rotating turbines to represent Tidal Energy Convertors (TECs) is made.

The TeraWatt project uses regional-scale shallow water models, able to simulate wide areas for lengthy periods of time with an achievable computational effort. This allows the consideration of far field effects, which may be important for understanding the environmental impacts of marine renewables.

## 04/1.2 THEORY

Typically, a turbine's rotor is considered as an actuator disc: a thin disc that exerts a retarding force, known as thrust, on the flow. The thrust is dependent on the area of the disc (i.e. the swept area of the rotor), the speed of the flow through the disc, and a thrust coefficient that represents the proportion of the mechanical power that is transferred from the flow to the rotor. For an actively-controlled turbine, the thrust coefficient varies with the speed of the flow.

Where possible, in addition to the rotor, it is important to consider the drag from the supporting structure of the turbine(s). This drag can make a significant contribution to the energy removed from the flow.

## 04/1.3 PRACTICAL IMPLEMENTATIONS

In two-dimensional models, tidal turbines have often been represented by an increase in seabed resistance in the cells that they occupy. This approach is not appropriate in 3-D models, because the resistance would be at the wrong vertical location. Instead, in 2- or 3-D models, an additional drag term can be introduced to the momentum equations that removes the correct amount of momentum from each cell at each time step. This is the approach used by both Delft3D and MIKE 3. Parameterization of this additional drag term is the key to accurately representing energy extraction from the flow by tidal turbines.

Models of the type that we are considering are limited in the extent to which they can represent array effects (i.e. the interactions of turbines within an array). Some attempt can be made using fine scale meshes, where each turbine is alone in its cell, however its accuracy cannot be proved until measurements are available for comparison.

### 04/1.3.1 DELFT3D

Delft3D has no dedicated implementation of tidal turbines, and so they are approximated by porous plates between grid cells. Similarly, the supporting structure is represented as a porous plate. The Orkney model developed within the TeraWatt project uses a regular mesh and requires nested grids for the areas where turbines will be located. For further details of the proposed method with Delft3D, please see Section 04/5.2.

Delft3D has the following specific limitations:

- The current version of Delft3D does not support variable thrust coefficients, so a representative fixed coefficient must be chosen.
- The turbine must have a fixed axis, and cannot yaw over time. Additionally, only the component of the flow parallel to the turbine's axis is considered; no account is taken of the effect of components of flow orthogonal to the axis.
- The model uses a "sigma" coordinate system, which means that the width of the vertical layers changes as the water level rises and falls. The position of a porous plate is specified in terms of these layers, and so modelled turbines will appear to rise and fall slightly in the water column as the tide ebbs and floods.

## 04/1.3.2 MIKE 3

MIKE 3 offers a dedicated "turbine" object, which is implemented as a sub-grid structure. This object can exert a force on the flow both parallel to the axis of the turbine (called drag, and equivalent to thrust mentioned before) and with a specific angle to the main direction of the flow (called lift). The user may specify a lookup table of drag and lift coefficients according to the current speed and direction, so that they can vary with flow conditions. Supporting structures may be approximated using the built in "pier" object, which is a sub-grid obstruction designed to model bridge piers. For details of the proposed method with MIKE 3, please see Section 04/6.3.

MIKE 3 has the following specific limitations:

- The vertical position of turbines must be specified with respect to the seabed, and not the water surface. Therefore, floating turbines cannot be represented correctly.
- It may be difficult to simulate a supporting structure that does not resemble a vertical cylinder, such as a tripod design.
- At small mesh sizes, there is a systematic underestimate of the effects of turbines. This becomes significant when the mesh triangles have sides of less than approx. 150 m (see Section 04/4.3.4).

## 04/1.4 USE IN TERAWATT

For the purposes of the TeraWatt project, an agreement is required between the project members and tidal energy developers on parameters for describing a generic tidal turbine. This theoretical device should be representative of how a real turbine might behave, while remaining sufficiently generic to avoid issues of protected Intellectual Property.

For a summary of the specific parameters that would be required by a modeller using the MIKE 3 or Delft3D packages, please see Section 04/7. For the TEC generic parameters that has been adopted in this project, see Section 04/8.

## 04/1.5 ACKNOWLEDGEMENTS

The authors wish to thank the following for their valuable comments:
- Dr. Iain Fairley
- Dr. Harshinie Karunarathna
- Dr. Ruairi MacIver
- Mr. Alessandro Sabatino
- Rory O'Hara Murray
- Antonia Chatzirodou
- Various tidal developers, under Chatham House rule

## 04/1.6 REVISION HISTORY

| REVISION | DATE | NOTES |
|---|---|---|
| 1 | January 2014 | Initial release to stakeholders for comment. |
| 2.1 | August 2014 | First public release |
| 3 | May 2015 | Corrections & updates from ongoing project. Changes in content as follows: Update of Section 04/4.3.4 on mesh sizes following further work. Formula for calculating $c_{loss}$ updated with new understanding in Section 04/5.2.2. Addition of information on practical implementation of turbines in Delft3D in Section 04/5.2.3. Dimensions of supporting monopole modified in Appendix A. |
| 3.1 | July 2015 | Minor clarifications and disambiguations throughout, in response to comments received. |

## 04/2 INTRODUCTION

Assessment of potential environmental impacts that tidal turbine deployment might have in the marine environment is of crucial importance for the development of the MRE sector and it is a topic of interest for all principal stakeholders (technology developers, government, NGO's, etc.).

Since the MRE is a developing sector there is not a standard methodology to approach the introduction of energy extraction into a numerical model and be able to make predictions on how tidal farm installations might interact with hydrodynamics.

Some approaches to this area of knowledge are listed below:

a) To understand how much energy can be extracted by a specific design, Computational Fluid Dynamic (CFD) models have been used. However, the computational effort required restricts these models to small areas and short periods of time – often instantaneous snapshots.

b) Many studies were focused on the potential effects of a channel full of devices from a theoretical point of view ([1], [2]). In order to achieve analytical solutions, these works make a number of unrealistic assumptions. For example, some studies consider single channels that have turbines installed across their entire widths.

c) In order to analyse the potential far-field effects of tidal turbine deployments, hydrodynamic models using shallow water equation solvers have been used [3]. These codes use different simplifications and assumptions than CFD models, running usually at lower spatial resolutions. The resulting saving in computational effort makes it feasible to model large areas over lengthy time periods.

This document assess the latter approach, using Shallow Water hydrodynamic models. In particular, it will describe how to implement TECs in the MIKE 3 (2012 version) and Delft3D (4.0 version) codes, which were selected for the TeraWatt project, as they are well established models in industry.

The aims of this document are as follows:

- To present the current state of the art in techniques for energy extraction in tidal flow models.
- To describe the methods that the TeraWatt project proposes to employ in the MIKE 3 and Delft3D software.
- To take into account TEC developers experience and advice on these proposed methods, in order to make them useful for industry and regulators.

To model the effects of energy extraction in the framework of this project, modellers and stakeholders have agreed parameters for defining a generic tidal turbine that project members can use to test and demonstrate the methodologies. This device should be representative of how a real turbine might behave, while remaining sufficiently generic to avoid any issues surrounding protected Intellectual Property. See Section 04/7 for detailed information on specific parameters that would be required from developers in a commercial situation, and Appendix B for the generic parameters that have been adopted.

## 04/3 THEORETICAL BASIS

### 04/3.1 STANDARD DESCRIPTION OF A TIDAL TURBINE

There are several designs of Tidal Energy Converters; an overview of those can be found at EMEC website [4] and also a list of tidal turbine developers can be found in the book "The analysis of Tidal Stream Power" [5]. However, the most standardised design to date is the horizontal axis turbine (Figure 4.1) which converts the flow power into rotary motion in order to drive a generator and produce electricity. Figure 4.2 shows an example of a seabed-based tidal turbine on which the main components of a TEC are described: 1) nacelle, where the mechanical power is converted into electrical power, 2) blades, 3) weights and 4) a substructure for support.

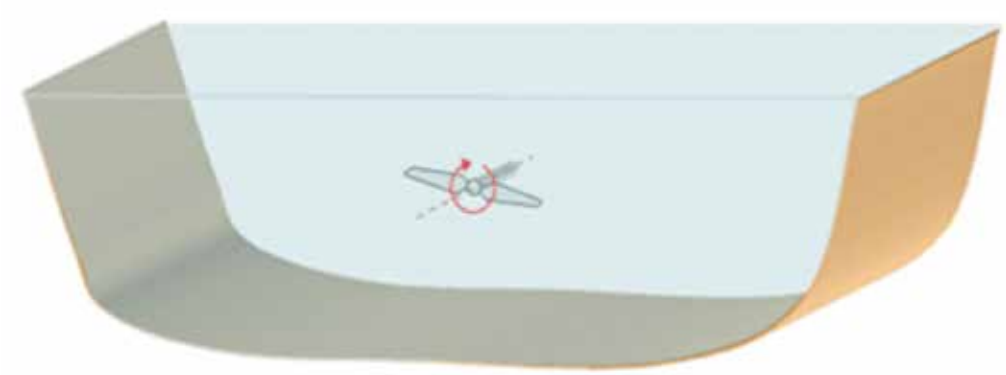

**Fig 4.1** General description of a turbine rotor in a channel. Source: [6]

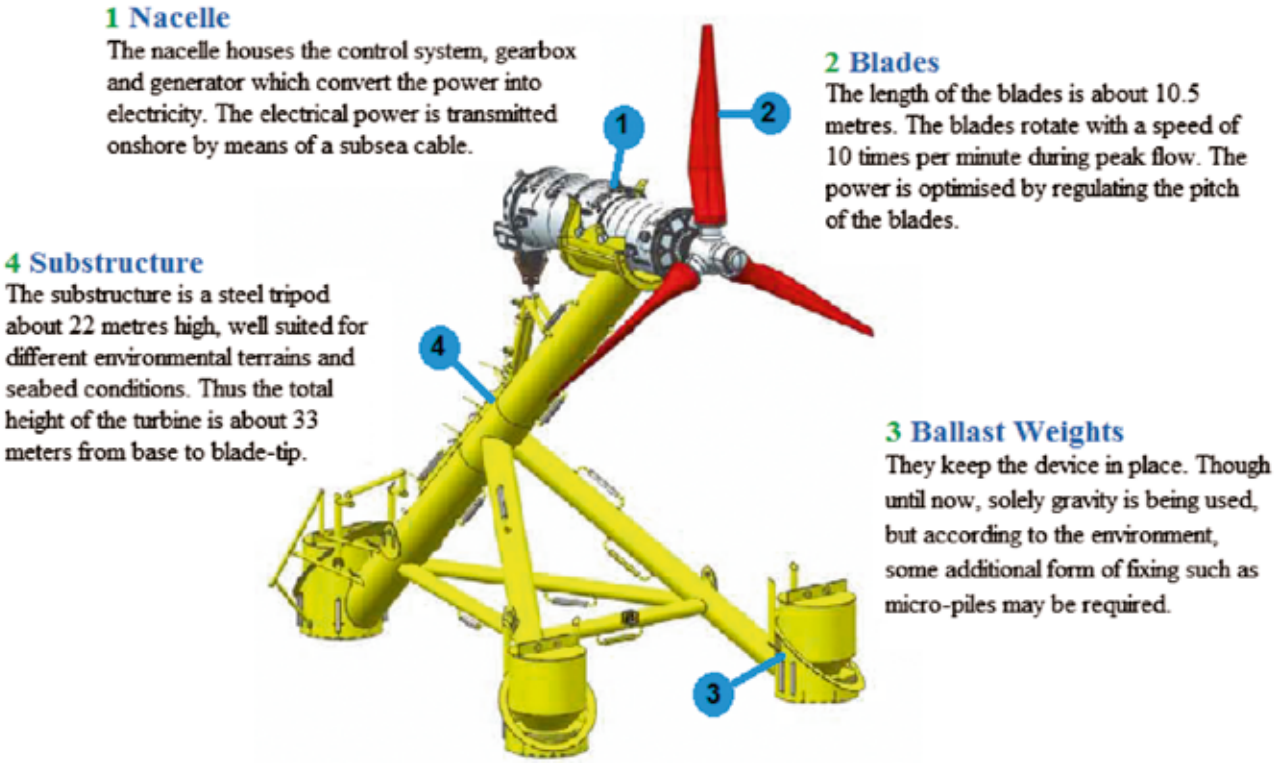


**Fig 4.2** Example of the main parts of a tidal turbine, Andritz Hydro Hammerfest turbine. Source: [7]

The Carbon Trust [6] summarize the main steps for converting the tidal stream's kinetic energy to electrical power by a horizontal-axis turbine as follows:

1) Some of the linear momentum of the moving water is converted to angular momentum of the rotor blades, which delivers mechanical power to the rotor shaft.

2) The shaft power ($P_s$) is the product of torque applied to the rotor ($\tau$) and the speed of rotation ($\omega$). $P_s = \tau\omega$, and is expressed as a fraction of the tidal stream power flux by the coefficient of performance ($C_p$). Note that the torque and speed are strongly influenced by the design of the rotor.

3) In situations where the Betz limit applies, i.e. an infinite stream may be assumed, the maximum value of $C_p$ is 59 %. In practice, the actual performance of a turbine is less than this, first because it is impossible to create a lossless rotor, but also because $C_p$ is a function of rotational speed ($\omega$).

4) Tip Speed Ratio (TSR) is the relationship between the rotational speed and the free-stream velocity, which is defined as the linear speed of the blade tips divided by the free-stream velocity. Power coefficient may be described as a function of the tip speed ratio. For a particular rotor diameter there is a maximum permissible tip speed.

5) Increase the shaft rotational speed/reduce the torque (gearbox).

6) Convert the shaft power into electricity (generator).

7) Convert the generation voltage and frequency to the grid voltage and frequency.

The performance envelope of a TEC is recommended by EMEC [8] to be described by a power curve produced using the measured in-situ data, analysis of the operational status of the device, and the annual energy generated by the facility. The power curve relates the electrical power produced by the TEC to the value of the simultaneous incident resource, which is characterized by the tidal current velocity. This recommended approach is similar to that adopted in the wind industry standard IEC 61400-12-1:2005 [9]. They recognize that the power production in this context is represented by the recorded power at the individual TEC output point and therefore includes losses arising from the drive train. Further losses from transformers, cabling to shore, etc., are not included in this figure.

In this context, the power coefficient of the device has been expressed as:

$$C_{power} = \frac{P}{\frac{1}{2}\rho A U_{perf}^3} \quad (1)$$

where P is the recorded power output, $\rho$ the density of the water, A the power capture area of the device and $U_{perf}$ the averaged performance velocity of the tidal current.

To provide the averaged performance velocity for plotting the power curve, the vertical variations of the tidal current at each time interval must be integrated across the power capture area.

If the TEC is fixed, i.e. it has no yaw capability, then only the component of velocity perpendicular to the power capture surface should be used for the identity of velocity. However, if the TEC device is capable of orientating to the dominant tidal current direction prevailing at a given time, the recorded velocity vector irrespective of direction should be used to define the velocity at the power capture area.

Another term that must be defined at this stage is the thrust, which is the horizontal force applied to the fluid from the turbine and it is related to the speed of the flow following the expression below

$$F_T = \frac{1}{2} C_T \rho u^2 A \quad (2)$$

where $C_T$ is the thrust coefficient, $A$ is the cross-sectional area of the turbine, and $u$ is the current speed.

Note that two different concepts are often referred to using the symbol $C_P$ or the phrase "power coefficient" in the literature: a) the proportion of the tidal power extracted from the water by the rotor as shaft power, referred to in this document as $C_P$; and b) the proportion of the tidal power that becomes available as electricity, referred to in this document as $C_{power}$.

## 04/3.2 LINEAR MOMENTUM ACTUATOR DISC THEORY

Froude's actuator disc theory provides a simple, 1-dimensional approach to the problem of rotor modelling. Its main assumptions, considering an ideal rotor as the one shown in Figure 4.3, are:

1) The disc is essentially a discontinuity moving through the fluid.

2) It is an infinitesimally thin disc of area A, which allows fluid passing through it as frictional forces that are negligible compared with momentum flux and pressure changes (hence can make assumption 5).

3) Thrust loading and velocity are uniform over disc.

4) Far-field is at free-stream pressure both far up and downstream.

5) Inviscid (thus irrotational), incompressible and isotropic flow.

Since the disc acts as a drag device, and by assumption 1, the source of drag must be a pressure difference across the disc, this drag manifests itself as thrust loading along the axis normal to the disc. Noting that assumption 1 states the disc is a discontinuity and that the flow can be considered stationary, Bernoulli's equation is not valid and may not be applied across the disc, but may be applied from the far field to the disc in either direction. Placing a control volume around the disc extending far ahead to the free-stream and considering that the disc serves to slow down the flow, thus allowing mass conservation to define streamlines (as the flow slows, conservation dictates the area increases, i.e. $A_2 > A_1$ in Figure 4.3): Applying Bernoulli in valid areas (see Figure 4.3 for definitions of terms):

$$\Delta p = \frac{1}{2}\rho(U_\infty^2 - u_2^2) \quad (3)$$

Power is equal to the rate of work, which is itself equal to the rate of momentum transfer through the cylindrical control volume.

$$P = \frac{1}{2}\rho A_1 u_1 (U_\infty^2 - u_2^2) \quad (4)$$

where $U_\infty$ is the velocity far upstream, $u_1$ is the velocity at the turbine, and $u_2$ is the velocity downstream of the turbine but before wake mixing has occurred, as per Figure 4.3.

Defining an axial induction factor, called $a$, $u_1 = (1-a)U_\infty$, and therefore $u_2 = (1-2a)U_\infty$. The expressions for Power and Thrust are as follows:

$$P = 2\rho U_\infty^3 a(1-a)^2 A_1 \quad (5)$$

$$T = 2\rho U_\infty^2 a(1-a)A_1 \quad (6)$$

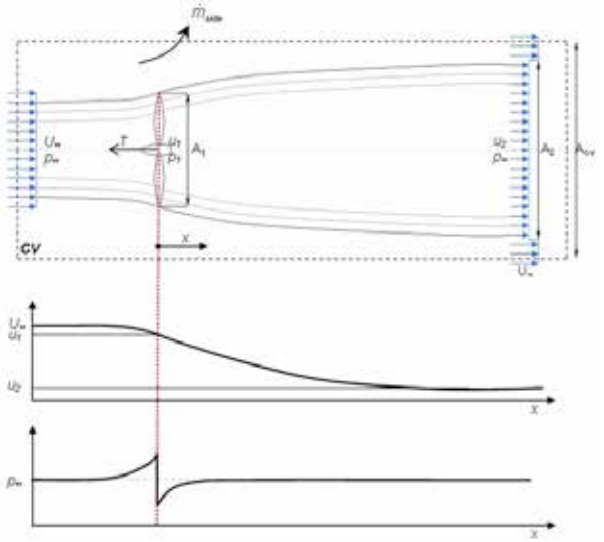


**Fig 4.3** Diagram of effect on the flow from an actuator disc. Source: [10]

Defining $C_P$ as power non dimensionalised by available power through disc area, and similarly defining $C_T$ for thrust,

$$C_P = \frac{P}{\frac{1}{2}\rho U_\infty^3 A_1} = 4a(1-a)^2 \quad (7)$$

$$C_T = \frac{T}{\frac{1}{2}\rho U_\infty^2 A_1} = 4a(1-a) \quad (8)$$

This theory has been the basis for initial approaches of modelling TEC energy extraction. Some works using the theory are summarized below.

LMADT (Linear Momentum Actuator Disc Theory) presented by Garret and Cummins [1] considers an actuator disc in a flow of constant cross-section, bounded by parallel channel walls and a constant free surface profile. Whelan et al. [11] applied LMADT to provide an approximation to the flow field around an actuator disc in an open channel flow with a non-uniform free-surface. Draper et al. [12] used the LMADT in a 2-dimensional vertical (hereafter 2DV) numerical model. In that approach, tidal devices are defined as a function of three parameters: the dimensionless depth change implicitly for a given Froude number; blockage ratio (B), defined as area occupied by the actuator disc over the cross-section (hb) of the channel; and wake induction factor ($\alpha_4$).

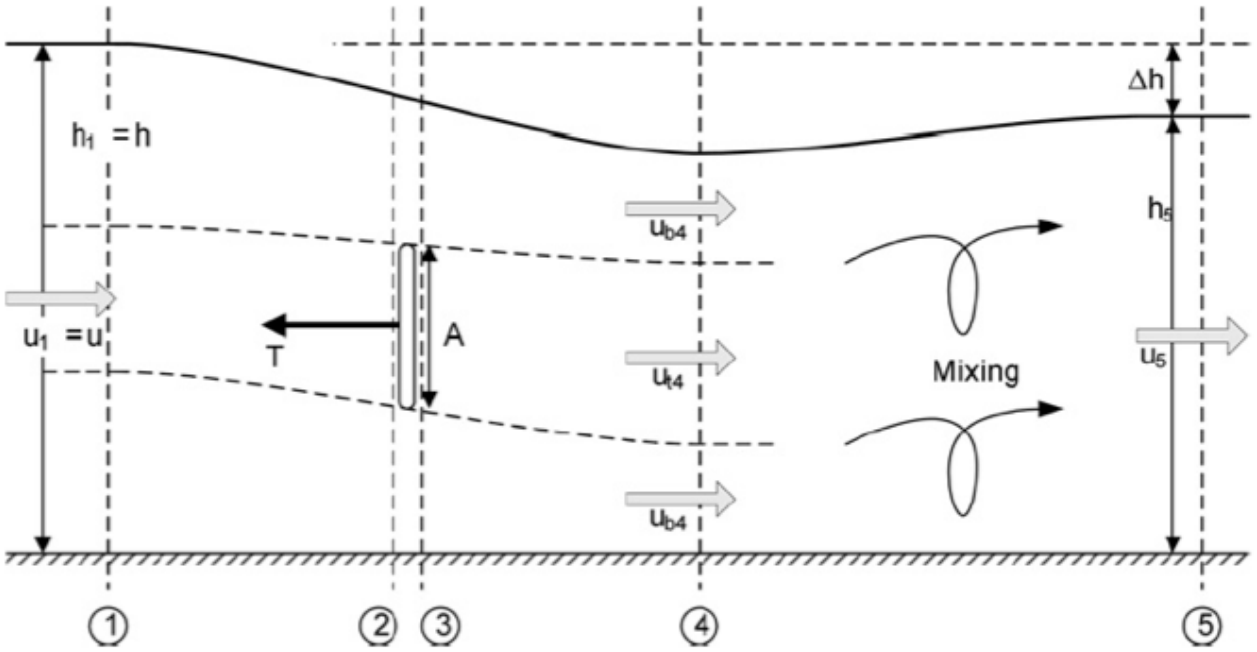


**Fig 4.4** LMADT in an open channel flow. Source: [12]

Figure 4.4 shows a 2DV channel containing an actuator disc with associated downstream mixing. The turbine, idealised as an actuator disc, occupies an area A and so a dimensionless blockage ratio may be defined as B=A/(hb). Velocity at station 4 is defined by $u_{t4} = \alpha_4 u$.

The power and thrust can be determined in terms of a power coefficient $C_P$ and a thrust coefficient $C_T$ as follows

$$P = C_P \frac{1}{2}\rho u^3 Bbh \quad (9)$$

$$T = C_T \frac{1}{2}\rho u^2 Bbh \quad (10)$$

being B blockage ratio, b uniform channel width and h depth of water.

# 04/4 STATE OF THE ART ON TIDAL ENERGY EXTRACTION MODELLING

## 04/4.1 INTRODUCTION

An early method of tidal energy resource estimation was to determine the average kinetic energy (hereafter KE) of a cross-sectional slice across the flow, and then assume that some fraction of that energy could be extracted without significant environmental impacts [13], this fraction being known as the Significant Impact Factor (SIF). However, KE flux can lead to an over- or underestimate of the output power from turbines by an order of magnitude [14] because the KE flux is not related to the power available to a turbine farm as it does not take into account the retardation of the flow by power extraction [15]. The nature of the resource is likely to be site-specific and the interactive and additive effects of multiple extraction sites in the same region on system-wide far-field effects must also be taken into account.

Garrett and Cummins developed a 1-D analytically-solvable numerical model for a channel connecting a bay to the sea [16], and another for a channel connecting two large bodies of water (e.g. two seas) [17]. Many subsequent works have expanded upon their theory, e.g. [2], [18], [19]. It should be noted that many such 1D models make assumptions for an "ideal" channel that are not applicable to any real development, such as assuming that the cross-section of the channel is entirely and evenly filled with turbines.

Numerical models provide excellent tools for in-depth analysis of the tidal energy resource for a particular location given sufficiently "accurate" data to drive the particular model and time to implement. The local and far-field effects of energy extraction upon the tidal flow, also called mesoscale impacts, are usually modelled using Shallow Water Equation (SWE) solvers. Bryden et al. [5], [9], [10] modelled far-field effects using 1D, steady-state flow as a prototype for the more complicated time-dependent problem. This would appear to be the first attempt at demonstrating far-field effects as a consequence of kinetic power extraction from tidal streams. Couch and Bryden [20] also applied 2D models for preliminary investigations of far-field effects.

Depth averaged 2D models are suitable for this purpose. Examples of such models include Sutherland et al. [21], using the TIDE2D model, whose work agreed with the theory proposed by Garrett and Cummins [14]. Blunden and Bahaj [22] employed TELEMAC-2D to model changes in the horizontal velocity field for an array of turbines deployed in the vicinity of Portland Bill (UK). Karsten et al. [23] implemented the 2D FVCOM model to estimate and examine far-field effects of extracting tidal energy in the Bay of Fundy (Canada). Walkington and Burrows [24] researched the energy resource and the impacts of the extraction on hydrodynamics using 2D ADCIRC model. The same model was used by Adcock et al. [25] to investigate the available power from tidal stream turbines in the Pentland Firth (Scotland), and Draper et al. extended this work to examine the effects of energy extraction in one or more sub-channels [26]. Carballo et al. [27] and Ramos et al. [28] evaluated tidal stream energy resources in Galician Rias (NW Spain) using the 2DH mode of the commercial software Delft3D-Flow.

Neither 1D nor 2D models are capable of describing the effects of KE extraction on the vertical flow behaviour. Using 3D hydrodynamic models a distinction between bottom friction and energy extraction might be represented and effects from both processes identified [29]. 3D models are computationally expensive and this cost increases as turbines are included, but this kind of tool is more accurate for representing physical process in the water column. Shapiro [30] used a 3D ocean circulation model (POLCOMS) to estimate the maximum extractable energy at different depths, although some unrealistic assumptions about turbine depth were made. The same model was used by Neill et al. [31] to simulate the impact of TEC arrays on the dynamic formation of headland banks in the Alderney Race. Defne et al. [32] modelled the effects of tidal energy extraction along the Georgia coast using ROMS. Hasegawa et al. [33] evaluated the far-field effects of tidal energy extraction in Minas Passage, Bay of Fundy, using a model based on POM. Yang et al. [34] simulated the effects of tidal energy extraction using a baroclinic FVCOM model. Roc et al. [35] have adapted the ROMS model to assess TEC array layout optimization, and it has been applied in an idealised channel simulation by Thyng and Roc [29].

## 04/4.2 ENERGY EXTRACTION FORMULATION

### 04/4.2.1 BOTTOM FRICTION APPROACH

The tidal energy dissipation associated with the presence of tidal turbines may be approximated by increasing bottom friction at the location of the turbines ([14], [21]). This approach has commonly been used in analytical models and depth-averaged 2D numerical model simulations (e.g. [22], [23]). In these studies the presence of tidal devices is modelled by an additional bed friction source term: $C_d = k_o + k_t$, where $k_o$ is related to natural friction and $k_t$ represents tidal turbines. Note that this approach is not suitable for 3D models, as the increased drag would occur at the wrong vertical position in the water column. Generally, the additional term varies according to the square of the local tidal current velocity. Bryden et al. [36] approached the influence of energy extraction on the flow by adding an artificial stress term to represent the TEC energy extraction, which was defined as:

$$\tau_{ex} = \frac{1}{2}\rho f U^2 \frac{R}{\Delta x} \qquad (11)$$

where $f$ is the fraction of the kinetic energy flux being extracted, $U$ is the longitudinal component of the flow velocity (m/s), $R$ is the hydraulic radius of the channel (m), and $\Delta x$ the length over which the energy is being extracted (m).

The Carbon Trust's methodology [37], which also follows this approach, defines $P_x$ as the power extracted per unit volume (in units of $Wm^{-3}$) and considers a control volume with dimensions $\Delta x$, $\Delta y$, $\Delta z$, making the power extracted from this control volume $\Delta x \Delta y \Delta z P_x$. Assuming a tidal flow of velocity $u$ in the $x$-direction, the equivalent horizontal retarding force acting in the negative $x$-direction on the control volume is:

$$\frac{\Delta x \Delta y \Delta z P_x}{u} \qquad (12)$$

For 2D simulations it is assumed that $P_x$ is constant over the depth. Therefore, rather than prescribe the amount of energy extracted explicitly or propose a notional TEC device performance curve, a percentage of the in-situ kinetic energy in the system is extracted. This does imply a simplification in the analysis. However, the approach is attempting to be technology neutral and its aim is to examine the effect of varying levels of energy extraction without directly apportioning how much of the energy extracted from the system is actually harvested or converted to electricity. So, the model adopts the format of expressing the energy extracted as a percentage of the in-situ kinetic energy flux through the relevant computational cell at that particular time-step.

$$P_x = \frac{P_{\%}\left(\frac{1}{2}\rho h \Delta y U^3\right)}{h \Delta x \Delta y} = \frac{P_{\%}\rho U^3}{2\Delta x} \qquad (13)$$

It must be stressed that the use of the bed resistance parameter is only appropriate for use in 2D models.

### 04/4.2.2 ENERGY EXTRACTION USING A MOMENTUM SINK APPROACH

In this approach, a momentum sink term is added to the momentum equations in 3D models to represent the loss of momentum due to tidal energy extraction by tidal turbines ([22], [27], [30]).

Shapiro [30] defined the flow retarding force per unit volume due to the presence of energy devices as a quadratic law for the loss of kinetic energy of the flow

$$\left[\frac{dKE}{dt} = \frac{1}{2}\beta\rho u^2\right]$$

integrated over the volume of a numerical gridbox, with $\beta$ being equivalent to the Rayleigh friction coefficient often used in meteorology [38]. The hypothetical TEC farm incorporated into the model has a circular shape in the horizontal plane and the TECs were assumed to be able to capture energy throughout the whole water column, from the bottom to the surface. He justified that saying that the exact vertical structure of the TEC is unknown. The box-averaged values of $\alpha$ represent both the number of turbines inside the box and the efficiency of devices; larger values correspond to greater energy losses.

Neill et al. [31] included the parameters $p_x$ and $p_y$ to represent energy extraction as additional friction-type terms to the momentum equations,

being $p_x = -nC_p \frac{P}{\rho UAH} \cos(\theta)$ and

$p_y = -nC_p \frac{P}{\rho UAH} \sin(\theta)$; where $n$ is the number of turbines per model grid cell, $A$ is the area of each grid cell, $\rho$ is the density of seawater, and $\theta$ is the direction of the depth-averaged current.

Defne et al. [32] have also implemented an additional retarding force in the governing momentum equations in ROMS. They defined the extracted power density as

$$P_{ext} = C_{ext} P' \quad (14)$$

where $C_{ext}$ is the coefficient that denotes the amount of extraction and $P'$ is the kinetic power density in the extraction cell at the time of the extraction. It is assumed that $C_{ext}$ is the same in both the $x$ and $y$ directions and its value is adjusted iteratively through successive model runs to meet the desired power removal from the flow.

Hasegawa and Sheng [33] used a 3D ocean circulation model with the turbine drag parameterized by a Rayleigh friction term in the momentum equations, which is a quadratic friction, different from the linear Rayleigh friction scheme used by Shapiro [30]. They justified the use of a 3D model because the tidal current in the area of study exhibit strong vertical variations and the total amount of energy extraction by TECs depends on the vertical position of the turbines. The Rayleigh friction term is defined as

$$\mathrm{F}_t = g(z)\lambda|u|u \quad (15)$$

where $\lambda$ depends on the density of the turbine which is referenced as the turbine drag coefficient and $g(z)$ is a step function which is equal to unity at depths of the flow affected by the turbine and zero otherwise. Therefore energy extraction may take place at any depth of the water column. They evaluated two cases: a) energy extraction taking place in the whole water column and b) energy extraction taking place only in the lower water column within 20 m of the bottom.

The momentum sink approach used by Yang et al. [34] is defined as:

$$\overline{FM} = \frac{1}{2}\rho \frac{C_e A}{V_c} |\vec{u}|\vec{u} = \frac{1}{2V_c}\rho[(C_T + C_b)A]|\vec{u}|\vec{u} \quad (16)$$

where $\overline{FM}$ is the momentum sink rate from a control volume ($V_c$) by tidal turbines, $C_e$ is the total momentum extraction coefficient, $A$ is the flow-facing area of the turbines, $\vec{u}$ is the velocity vector, $C_T$ is the turbine thrust coefficient and $C_b$ the drag coefficient due to the physical structure of turbine blades (together making up $C_e$). Drag coefficients for supporting poles and foundation have been indicated in the formulation but not considered for the purpose of model validation and simplicity. They also indicate that assuming $N$ tidal turbines deployed within one model element (148663 m$^2$) the total tidal energy extracted by all turbines within the element can be calculated as

$$P_{cell} = N\frac{1}{2}\rho C_T A\overline{|\vec{u}|^3} \quad (17)$$

### 04/4.2.3 MODIFICATION TO TURBULENT CLOSURE MODELS (TCM)

Roc et al. [35] presented an adaptation of the ROMS model to represent tidal current turbines, extending the actuator disc concept to 3D simulations. The innovative method treats each individual device as a mid-water column perturbation, accounting for both momentum and turbulent hydrodynamic effects. However, they pointed out that using the actuator disc concept in large-scale numerical models without adapting the models to account for the turbine induced turbulence occurring in the near wake region would lead to a misrepresentation of the wake recovery and impacts in realistic scenarios. Since induced turbulence downstream of the device is not accounted for in closure models as an active contribution in the turbulent dynamics, following techniques adopted for wind turbines, they have added three terms into the turbulent kinetic energy

(TKE) transport equations of 2-equation turbulent closure models (TCM) which are only active at the rotor disc location:

a) $P_P$ to represent turbine induced turbulences, which is defined as being proportional to the cube of flow-velocity in the TKE.

b) $P_d$ to account for energy transferred from large scale turbulence into finer scale turbulence, which is defined as being proportional to the flow-velocity multiplied by the TKE.

c) $P_\psi$ to account for Turbulent Length Scale (TLS) processes, which is defined as proportional to the quadratic production of TKE by shear.

These turbulent correction terms have been implemented in the Generic Length Scale (GLS) closure model in order to permit the user to choose any 2-equation turbulence closure model. For more details on the implementation within the model please refer Roc et al. [35] .

This approach has been adopted by Thyng and Roc [29], treating each individual device as a 3D object and accounting for the momentum capture as well as the sub-grid scale turbulence balance perturbations caused by discrete devices on flow hydrodynamics.

## 04/4.3 COMPLICATIONS AND CORRECTIONS

Incorporating the concepts above into a model at this scale introduces a number of complications, some of which are active research topics.

### 04/4.3.1 FLOW IS NOT ALWAYS RECTILINEAR

Many implementations of energy extraction in models make an assumption that the turbine is always oriented to face into the current.

In areas of strong currents such as the Pentland Firth, complex flows tend to be generated including large eddies, and so the flow is often not simply bidirectional [39]. Some designs of tidal turbine (e.g. [40]) can turn to face in any direction, and for these no additional difficulty is created for modellers. However, some designs are fixed in orientation and are designed to work optimally in flow from directly in front or directly behind (e.g. [41]). In this case consideration should ideally be made in the model of the angle between the flow and the turbine's heading.

### 04/4.3.2 TURBINES DO NOT HAVE CONSTANT THRUST COEFFICIENTS

Much of the modelling work described above has assigned a fixed thrust or drag coefficient to a turbine. This treats the turbine as akin to any other fixed object in the flow, represented by a constant drag coefficient and removing a fixed proportion of the energy in the flow. The reality is that tidal turbines have a cut-in speed below which they produce no electricity, and a rated capacity above which they produce no additional electricity, and they use active control methods (e.g. variable pitch blades) in between these speeds [40]. Therefore, the thrust coefficient will not be constant, but will vary with the speed of the flow through the rotor [30], [42]. It should also be remembered that any turbine has a supporting structure with a fixed drag coefficient, in addition to the rotor with its variable thrust coefficient [43].

In some software, including the 2012 edition of MIKE, the thrust coefficient can be specified as a function of current speed. Easton & Woolf [42] show a method of allowing for this in software that does not support it (in their case, an older version of MIKE 21). They use an iterative approach, using the flow speed at the turbine in iteration $n$ to calculate a time-varying correction for the thrust coefficient in iteration $n+1$. At each iteration, the retarding force of the turbine on the flow is calculated both directly by the model, and by a manual calculation based on the flow speed, and when the difference between these is acceptably small (the RMS difference in the maximum force being <2%) the resulting model is accepted.

Plew and Stevens [43] explore a similar concept in building their model. Instead of including individual turbines in their model they express the retarding stress from the turbines according to a density of turbines per $m^2$. This approach removes the need, faced by Easton & Woolf, to have a maximum of one turbine per cell. However, it means that all turbines in the array must experience the same flow speed and exert the

same force, and that they cannot individually affect one another. This will reduce the model's ability to simulate array effects.

Both of the above works find that allowing the drag coefficient to vary as a function of flow speed makes significant changes to the modelled effect of the turbines on the flow. This is especially noticeable at times of peak current speed, where the turbines are operating at their rated capacity and are thus "shedding" excess energy (see Figure 4.5).

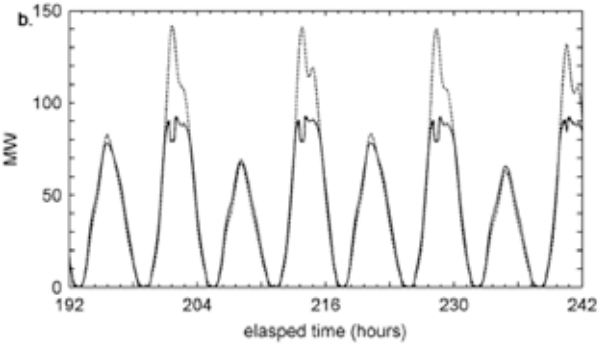


**Fig 4.5** Time series at springs of energy dissipation by an array with (solid) and without (dashed) variable $C_T$. A variable thrust coefficient allows the model to reflect the capacity of the turbine, reducing the peaks in the output. Source: [42]

Shapiro [30] suggests an alternative approximation: he reports, based on experimental work with wind turbines [44], that within the range of a turbine's working velocities, its thrust coefficient is approximately inversely proportional to the flow speed:

$$C_T \cong \frac{\text{const}}{u}$$

Using a quadratic drag law,

$$F_T = \tfrac{1}{2} C_T \rho u^2 A$$

Substituting for $C_T$ in (19), the force becomes proportional to $u$, i.e. the system exhibits linear drag. Assuming that tidal turbines behave in the same way, this suggests a means of representing a TEC in software that permits linear drag but does not allow a variable thrust coefficient. Note that this approach will not take account of turbine cut-in speed and rated capacity.

## 04/4.3.3 ARRAY EFFECTS

An array of turbines cannot simply be considered as a group of turbines that operate independently. Each turbine will affect each other turbine in a number of ways. For example, downstream turbines will experience reduced flow speeds as a result of upstream turbines [45] and increased turbulence if they interact with the upstream turbines' wakes. Mixing between turbine wakes and the surrounding flow removes energy from the system ([12], [46]) in the form of turbulence, which may not be accurately calculated in regional-scale models. These effects, between turbines within an array, are difficult to represent in a mesoscale hydrodynamic model such as MIKE 3 or Delft3D. One approach to mitigate this problem may be to apply a correction factor to account for array effects in general. Shives et al. ([47]) propose a solution where a regional-scale hydrodynamic model and a high-resolution CFD model of a small group of turbines are coupled together, to allow each model to perform at the scale for which it is designed. They show an iterative approach where the regional model provides the flow velocity to the CFD model, and the CFD model returns turbine performance parameters to the regional model, which is computationally expensive.

## 04/4.3.4 CONSIDERATIONS OF GRID / MESH CELL SIZES

The question of grid size is closely linked to the array effects discussed above. If no correction for array effects is to be applied to the model, then it is desirable to make the mesh elements (or grid cells) small enough to have one element per turbine, and ideally an additional element in-between each turbine to allow for flow to pass between. While this can certainly not fully represent interactions between turbines, it does allow each device to experience a different flow velocity, influenced by other turbines in the array. For this reason, some recent works have used high resolution grids around turbines, as for example a regular grid with a resolution of 50m e.g. [28] or an unstructured grid with one third of the rotor diameter resolution [35].

It would be computationally prohibitive to mesh the entire model domain at this scale, and so

a local increase in resolution is required. For models using a flexible mesh (such as MIKE 3 FM) this is straightforward, although it can lead to very short time steps being required. For models using a regular grid (such as the current version of Delft3D), it is necessary to use nested grids. Draper et al. ([12]) comment that the actuator disc approach used to incorporating turbines in their model is valid because the distance downstream over which the wake mixes into the surrounding flow is significantly less than the mesh size of the model (which they describe as "typically" of the order of kilometres). This does not invalidate the use of smaller grids, but it does highlight the need to remember the approximations inherent in the specific formulation used, when considering results.

There is an additional consideration that introduces an error with high resolution grids: when the thrust coefficient for a turbine is calculated, it will normally be derived by measuring or modelling the thrust force at a given flow velocity (i.e. for a given scenario, $C_T \propto \frac{F_T}{u}$). As discussed in [47], the velocity that is conventionally considered – and therefore the velocity that the thrust coefficient is defined in terms of – is the "free stream velocity". This is the velocity far upstream, where the flow has not yet begun to feel the effect of the turbine. When a regional-scale model is performing the reverse calculation (i.e. using $C_T$ and $u$ to find $F_T$), it has only one velocity available to work from: the velocity assigned to that cell of the grid. If a single turbine is modelled and the area of the cell is large compared to the scale of the turbine, then most of the cell will be unobstructed and the velocity of the cell will be close to the free stream velocity. However, as the size of the cell is reduced to approach the scale of the turbine, an increasingly large proportion of the cross-section of the cell will be occupied by the turbine rotor (see Figure 6), which will thus start to have a significant effect on the cell velocity. Where grid cells are small, this may result in an underestimate of the energy extracted at the turbine.

As noted in [47], if an array is being considered rather than a single turbine, it becomes difficult to define exactly what the free stream velocity is for a turbine that is not at the upstream edge of the array, complicating this matter further.

Kramer et al. [48] have recently demonstrated this effect in tests with the MIKE21 and Fluidity models, and have proposed a correction based on actuator disc theory for a single turbine. Within this project, the same effect has been demonstrated in 3D with the MIKE 3 model [49]. It has been observed that the error rises above 5% when the cell width is less than approx. 100m, or triangle face lengths of 150-200m. A correction has been demonstrated for a single turbine in an ideal channel (see Figure 4.7), and a MATLAB package developed to automate this correction for simple MIKE 3 models. Work is ongoing to make this package suitable for, and to test it in, more realistic models.

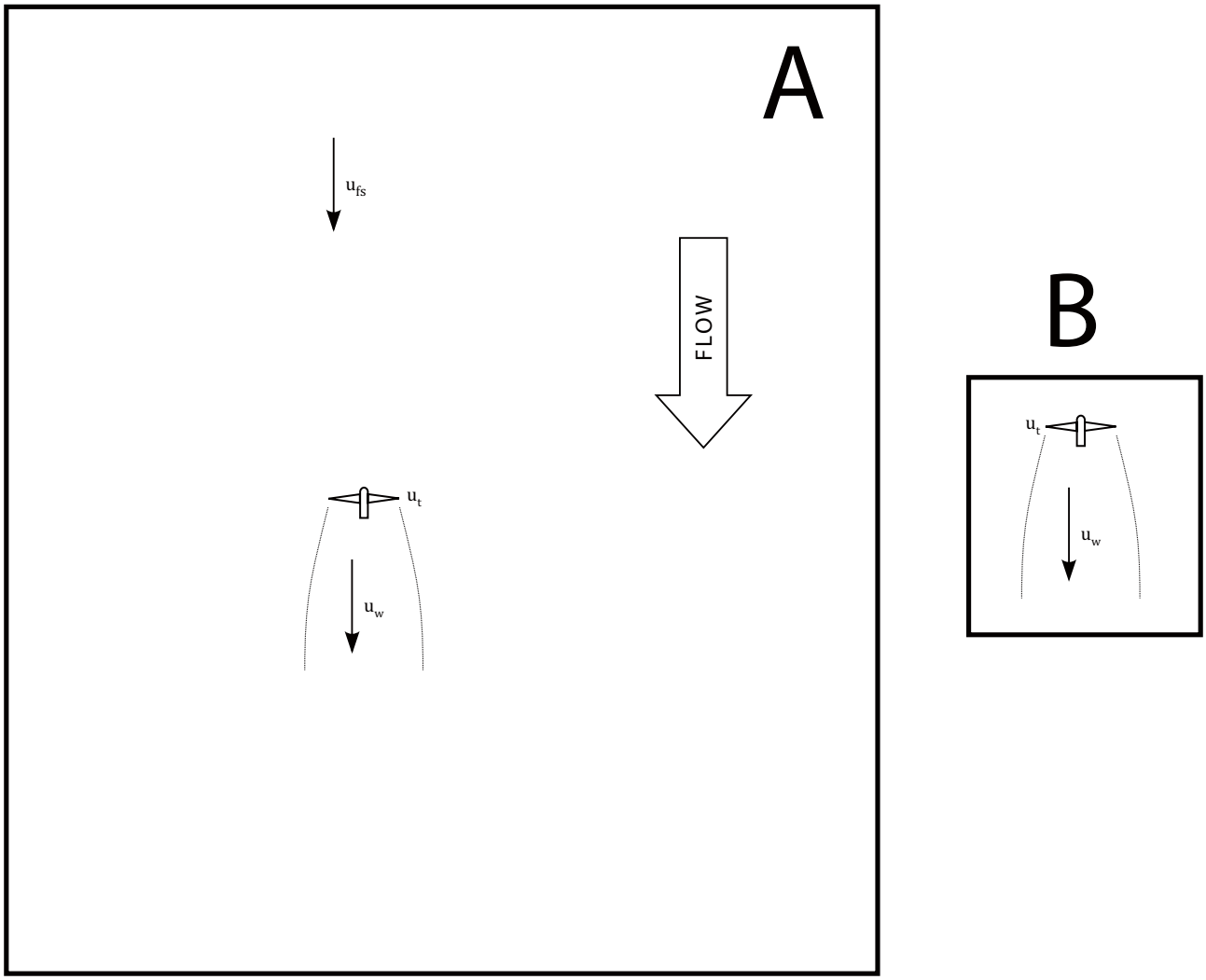


**Fig 4.6** Illustration of the effect of cell size on cell velocity. In the large cell A, the turbine only covers a small proportion of the cell's cross-sectional area, and $u_{cell} \cong u_{fs}$. In the smaller cell B $u_{cell}$ will be closer to $u_t$, the reduced velocity at the turbine, as the rotor occupies a large proportion of the cell's cross-sectional area.

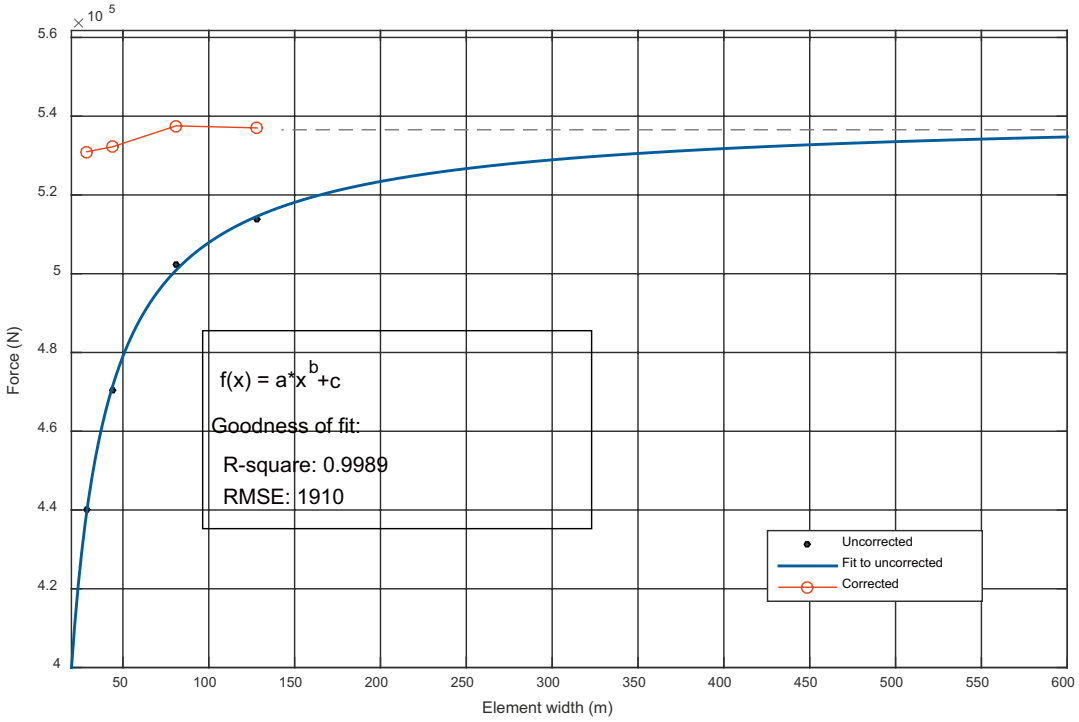


**Fig 4.7** Uncorrected and corrected values for the force exerted on a turbine, modelled at different mesh scales. Note that the a power law fitted to the uncorrected values reaches an assymptote at large mesh scales, and that the corrected values approximate this assymptote.

## 04/4.3.5 BOUNDARY CONDITIONS

Regional-scale hydrodynamic models are driven by their open boundary conditions. These are frequently "clamped" boundaries, in which time-varying water levels or velocities are specified either from observations, or from a wider-scale model that is itself driven by observations. Clamped boundaries are prescribed by the model setup, and cannot be affected by processes within the model.

This difficulty has been well-studied in the context of ocean and coastal modelling, and a number of alternative boundary conditions have been proposed (see below).

When energy extraction is introduced in the model, it changes the hydrodynamics of the region around it. The energy extraction is not present in the observations from which the boundaries are taken, and so clamped boundary conditions cannot reflect the change. As such, the boundary conditions may constrain the response of the model to energy extraction. The use of clamped boundaries may, therefore, be a particular problem for tidal energy extraction, and this was first identified by Garret & Greenberg in 1977 ([50]), and received attention more recently from other authors ([51],[26]). The latter work considers the tide as a wave that enters the domain and is reflected from shorelines, bathymetry, etc. The boundaries are then formed by the sum of the incoming and outgoing wave. On this basis, a tidal array can be considered as a wave maker, producing an artificial wave that cannot propagate through the fixed boundaries. This is equivalent to saying that the boundary produces what the authors describe as an "error" wave exactly opposite to that created by the tidal array that propagates into the domain from the boundary, causing a false change in the flow.

Adcock et al. [51] propose two solutions to this problem, which should ideally be used together:

Firstly, that the domain should be large enough that the wave created by the tidal array is negligible by the time it reaches the boundary. This can be accomplished either by sheer distance, or by extending the domain beyond the continental shelf, where the sudden change in depth will tend to reflect the outgoing wave. Care should be taken to avoid excluding any reflecting features (e.g. sudden changes in channel size or depth) that may cause a resonance effect.

Secondly, that transmissive boundaries should be used that allow the outgoing wave to pass out of the domain, without reflecting an error wave. A number of alternative boundary conditions have been proposed in the past; see [52], Sections 1-3, for a review, and [53] for one that has specifically been developed for finite-volume models. Of these, only that of Flather [54] is available in MIKE. This option requires that both the surface elevation and the velocity is specified at the boundary. Carter and Merrifield [55] note that while elevations are readily available from global models based on satellite altimetry, the velocities given by these models can be unreliable in shallow waters. An alternative approach ([56]) is to initially run the model with clamped elevation boundaries (obtained from a global model) and from this predict the velocities at the boundaries, to be used in a second model run using Flather open boundary conditions. It is not clear, without testing, which approach will result in the smallest (or, perhaps, the most predictable) errors. Delft3D offers an option for a "Weakly reflecting boundary" based on [57], although Deltares note that this method is only strictly correct when the direction of travel of the outgoing wave is normal to the boundary [58]. This method suffers from the same difficulty as MIKE's implementation of the Flather condition: That both the external surface elevation and velocity are required.

Adcock et al. show that the power captured by turbines can be sensitive to the locations of the boundaries. They recommend that sensitivity to boundary changes, with energy extraction in place, should be tested when evaluating a new model.

Draper et al. ([26]) use two methods to check for constraint by the boundary conditions:

Firstly, they specify the open boundaries by setting the water level and they compare the current flowing through the boundaries with and without turbines present. A significant difference would indicate that the effects of the energy extraction reached the boundary, and that unrealistic influences might arise.

Secondly, they test for resonance effects with the open boundary by re-running their simulation using a smaller computational domain and checking for significant differences in the available power.

## 04/4.4 VALIDATION OF ENERGY EXTRACTION METHODS

Validation of flow models in general is a well-studied topic. However, there are few tidal turbines in use around the world, and so energy extraction techniques cannot currently be verified against full-scale measurements.

As noted in Section 04/4.1, one-dimensional analytical models have been developed for certain scenarios. One approach that can be taken is to test the model code (and in particular its implementation of tidal turbines) against an analytic model, by constructing an "ideal" channel that fulfils the assumptions of these scenarios. Admadian et al. [59] show an example of this, comparing against the Bryden & Couch [60] analytical model to gain confidence in their implementation of energy extraction in the DIVAST model code.

Validation against measurements is, of course, the best approach, but this only will become feasible in the future if a greater number of tidal turbines are deployed into the water and a monitoring program is in place.

## 04/4.5 EXAMPLES OF PREVIOUS WORKS INCLUDING ENERGY EXTRACTION

Blunden and Bahaj (2007) [22]: The TELEMAC-2D code was used. Horizontal turbine with rotor disc area Ad=201 $m^2$, 16 m diameter, rated speed Ur=2.5 m/s and thrust coefficient $C_T$=0.8 based on a case study of Batten and Bahaj (2006) [61]. Array density 160 units, 15D by 4D spacing, array area 1680 m by 1216 m = 2.04 $km^2$. Envisaged array rated power based on the number of turbines approximately 90 MW.

Shapiro (2011) [30]: Using POLCOMS modelled three farms a) a small one in which the mean extracted power is 87 MW; b) a medium one, representing a harnessed energy of 473 MW; and c) a large farm with 606 MW of mean extracted power. Being the Rayleigh friction coefficients 10-4, 10-3 and 10-2 respectively.

Yang et al. (2013) [34]: They used the FVCOM model. Turbine thrust coefficient $C_T$ was set to 0.5. Turbine diameter was specified as 10 m, which gives the flow-facing swept area Ab as 78.54 $m^2$. The height of the tidal turbine from the bottom was set to 10 m.

Examples of energy extraction using Delft3D are Carballo et al. [27] and Ramos et al. [28]. Both solved the 2DH momentum equations. Carballo et al. used a $C_p$=0.33, in accordance with [49], to calculate the annual energy output per meter of turbine aperture at the selected locations, with a turbine aperture of 750 $m^2$. Ramos et al. modelled TEC farms formed by eight turbines of 5 m diameter, based on the Evopod Turbine design, with a 15 m separation. They used two values of the thrust coefficient to represent high and low level of extraction, being 0.8 and 0.4 respectively following ([62], [63]).

An example of energy extraction using MIKE21's Flexible Mesh version is [42]. This work is discussed in Section 04/4.3.2 above for its use of a variable thrust coefficient. The authors are not aware of any published work implementing energy extraction in tidal flows in MIKE 3. However, Lalander and Leijon [64] do describe the use of MIKE 3 and its sub-grid turbine structure for modelling run-of-the-river hydroelectric power.

## 04/5 TOOLS WITHIN DELFT3D FOR ENERGY EXTRACTION

The version of the code being used is Delft3D-FLOW 4.0. This version allows the use of curvilinear grids. However, it is noteworthy to mention that the work done within TeraWatt is using rectilinear grids.

### 04/5.1 HOW THE MODEL INCORPORATES HYDRAULIC STRUCTURES

Delft3D allows the user to specify a number of types of sub-grid scale structures that are placed in the flow, such as gates, piers or even floating structures, but not turbines so far.

There is a few assumptions that are worthy to mention in how the model approach the presence of hydraulic structures:

- Obstacles in the flow may generate sudden transitions from flow contraction to flow expansion. The grid resolution is often low compared to the gradients of the water level, the velocity and the bathymetry. The hydrostatic pressure assumption may locally be invalid.

- The obstacles generate energy losses and may change the direction of the flow. The forces due to sub-grid obstacles in the flow, which are not resolved on the horizontal grid, should be parameterised. To model the force of the flow generated by a hydraulic structure, the flow in a computational layer is blocked or a quadratic energy or linear loss term is added to the momentum equation.

- The flow condition at hydraulic structures may be supercritical. For supercritical flow, the downstream water level has no influence on the flow rate. The energy loss formulations presently available in Delft3D-FLOW assume subcritical flow, i.e. the supercritical flow rate is not computed accurately.

- All hydraulic structures within Delft3D are located at velocity points of the staggered grid, i.e. at the edges of the cell, on the interface between two computational cells. Around a hydraulic structure, there will be large horizontal gradients in the water level, the velocity field and in the concentrations. In order to prevent unphysical oscillations in the velocities and concentrations upstream of hydraulic structure points the user can switch the discretisation of the advective terms at such points to an upwind discretization, which preserve energy at the momentum equations.

- A hydraulic structure generates a loss of energy apart from the loss by bottom friction. At those points, an additional force term is added to the momentum equation, to parameterise the extra loss of energy. The term has the form of a friction term with a contraction or discharge coefficient.

- The hydraulic structures are divided into three basic types:
  a) Hydraulic structures with quadratic friction
  b) Hydraulic structures with linear friction
  c) Floating structures

For more information about hydraulic structures please check Delft3D manual [58].

TEC's within Delft3D can be considered as an obstacle to the flow; and obstacles are denoted in Delft3D-FLOW as hydraulic structures. In this project, TEC's has been defined within Delft3D using the porous plate option. Within Delft3D the porous plate represents an actuator disc (see Section 04/3.2 for more information). The manual says that the energy loss coefficient for a porous plate, $c_{loss}$, must be specified by the user as an input [65].

$$M_{\xi} = -c_{loss-U} \frac{U_{m,n}|U_{m,n}|}{\Delta x} \qquad (20)$$

Detailed information on how the porous plate is implemented to represent TECs is shown below.

## 04/5.2 PROPOSED METHOD FOR INCLUDING ENERGY EXTRACTION IN DELFT3D

### 04/5.2.1 IMPLEMENTING POROUS PLATES

The best approach to represent a TEC within Delft3D is by implementing a porous plate. This feature occupies a cell section, hence it would be a quadrilateral section (Figure 4.8) not a circular one as it is typically assumed to define a rotor.

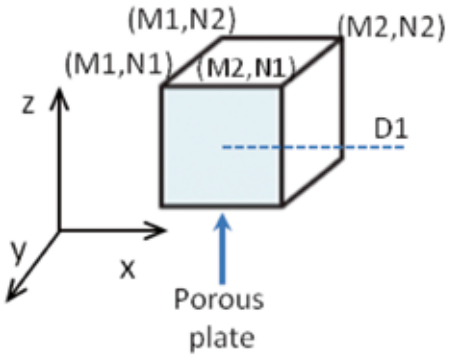


**Fig 4.8** Diagram showing how a porous plate (blue face on the cube) is defined in Delft3D.

The information required to define a porous plate in Delft3D is shown in Table I. Figure 4.9 shows how to define that file using the Graphical User Interface (GUI).In this example two porous plates have been defined. Note that orientation must be defined, i.e. the porous plate is facing the u or v component of the velocity. M1, N1, M2 and N2 are cell coordinates in which the structure is located, D1 and D2 the vertical layers that those structures cover and $c_{loss}$ is the loss coefficient. Indication on how to define $c_{loss}$ is below.

| IDENTIFIER | ORIENTATION | M1 | N1 | M2 | N2 | D1 | D2 | $c_{loss}$ |
|---|---|---|---|---|---|---|---|---|
| 1 | U | 226 | 41 | 226 | 42 | 6 | 9 | 0.02 |
| 2 | U | 256 | 148 | 256 | 149 | 2 | 4 | 0.007 |

**Table 4.1** Example of porous plate definition (turbine.ppl file)

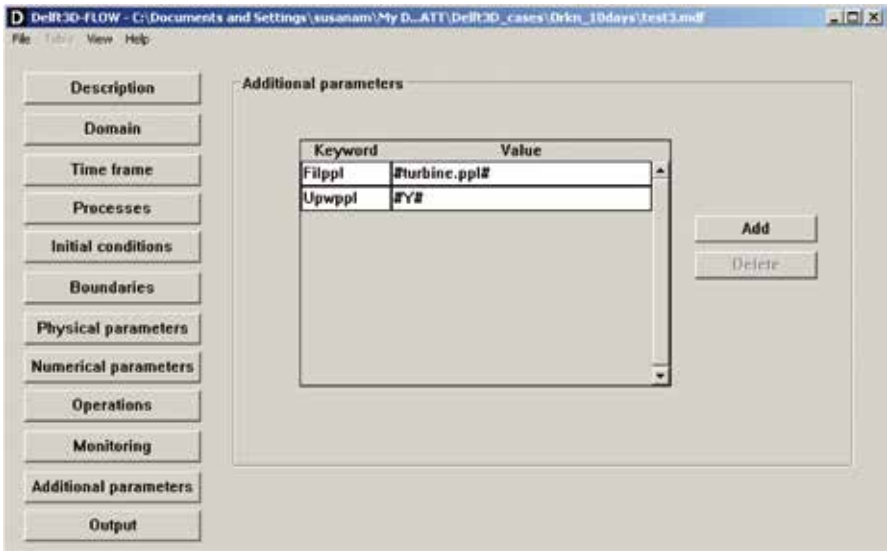


**Fig 4.9** Capture screen of the Delft3D GUI showing how to include the porous plate input file into the model.

## 04/5.2.2 DETERMINING $c_{loss}$ COEFFICIENT : THEORY

In calculating this coefficient, it is important to bear in mind the difference between the free-stream velocity $u_{fs}$, which is the velocity that the thrust coefficient is expressed in terms of, and the velocity at the porous plate, which is the cell velocity $u_{cell}$ (see previous discussion in Section 04/4.3.4).

From the Delft3D manual [58] (equation 10.87, but reducing the vector components to a scalar for simplicity),

$$M = -\frac{c_{loss}}{\Delta x} u_{cell}^2 \qquad (21)$$

where $M$ is the change of momentum per second per unit mass.

Assuming a 2D model, so that the turbine's force is not divided into vertical layers, the drag force of $N$ turbines is the sum of their individual drag forces:

$$F = N\frac{1}{2} C_d \rho A_t u_{fs}^2 \qquad (22)$$

Force is equal to change in momentum per second, while Equation (21) deals with change in momentum per second per unit mass. Therefore, by dividing (22) by the mass of one grid cell we can equate the two:

$$M = -\frac{c_{loss}}{\Delta x} u_{cell}^2 = \frac{N\frac{1}{2} C_d \rho A_t u_{fs}^2}{\rho \Delta x \Delta y H} \qquad (23)$$

and hence (still for a 2D model),

$$c_{loss} = -\frac{C_d N A_t}{2\,\Delta y \mathrm{H}} \cdot \frac{u_{fs}^2}{u_{cell}^2} \tag{24}$$

This leaves us with the difficulty of finding the ratio $\frac{u_{fs}^2}{u_{cell}^2}$, hereafter referred to as $\alpha$. A number of theoretical approaches are possible, as well as the practical ones of reading a velocity some distance upstream from the model (see [66] Appendix E) or of using the velocity at the turbine's location when turbines are not present (see [67] for a discussion of this idea). All are approximations, because the concept of the "free-stream velocity" is unclear for any scenario other than a single turbine in an unbounded flow.

The approach adopted here is based on actuator disc theory and can be expressed as,

$$\alpha = \frac{4}{\left(1+\sqrt{1-\gamma}\right)^2} \tag{25}$$

where $\gamma$ is a parameter representing the proportion of the momentum passing through the cell that is removed (see [49] for derivation). Note that the first part of the right hand side of Equation (24) already describes the proportion of momentum removed from the cell, so (24) can be written as,

$$c_{loss} = -\frac{\gamma}{2}\alpha \tag{26}$$

## 04/5.2.3 PRACTICAL IMPLEMENTATION

This approach has been implemented in a MATLAB script which produces a set of porous plate specifications in Delft3D's "PPL" file format. Two elaborations are required on the theoretical approach above: firstly, accounting for flow directions that are not along a grid axis, and secondly, for turbines that occupy more than one vertical layer in the 3D model.

Delft3D only supports porous plates that align with grid axes or are at exactly 45° to them. For a more general approach, we assume that each cell with turbines will have two porous plates, one in the $u$ direction and one in the $v$ direction, which provide components of the total force. Instead of using an area per turbine and the number of turbines as in Equation (22), we calculate the total effective area of turbine rotor that is visible along these two grid axes (see Figure 10).

In a 3D Delft3D model, a porous plate must occupy a whole number of vertical layers. In our current implementation the mean vertical hub position of turbines in the cell is calculated, and the porous plate is defined to include all layers that would be intersected by the rotor of a turbine at this mean elevation.

Thus for the $u$ direction,

$$\gamma_u = \frac{C_d A_u}{\Delta y\, \Delta z\, n} \tag{27}$$

where n is the number of layers that the porous plate occupies and

$$A_u = \sum A_t |\sin\theta|,$$

where $\theta$ is the angle between the $u$ direction and the turbine's axis and the summation is over all turbines in that cell. From Equations (26) and (25), for the $u$ direction,

$$c_{loss-u} = -\frac{\gamma_u}{2} \cdot \frac{4}{\left(1+\sqrt{1-\gamma_u}\right)^2} = \frac{-2\gamma_u}{\left(1+\sqrt{1-\gamma_u}\right)^2} \tag{28}$$

Similarly, for the $v$ direction:

$$c_{loss-v} = \frac{-2\gamma_v}{\left(1+\sqrt{1-\gamma_v}\right)^2}$$

$$\gamma_v = \frac{C_d A_v}{\Delta x\, \Delta z\, n} \tag{29}$$

$$A_v = \sum A_t |\cos\theta|$$

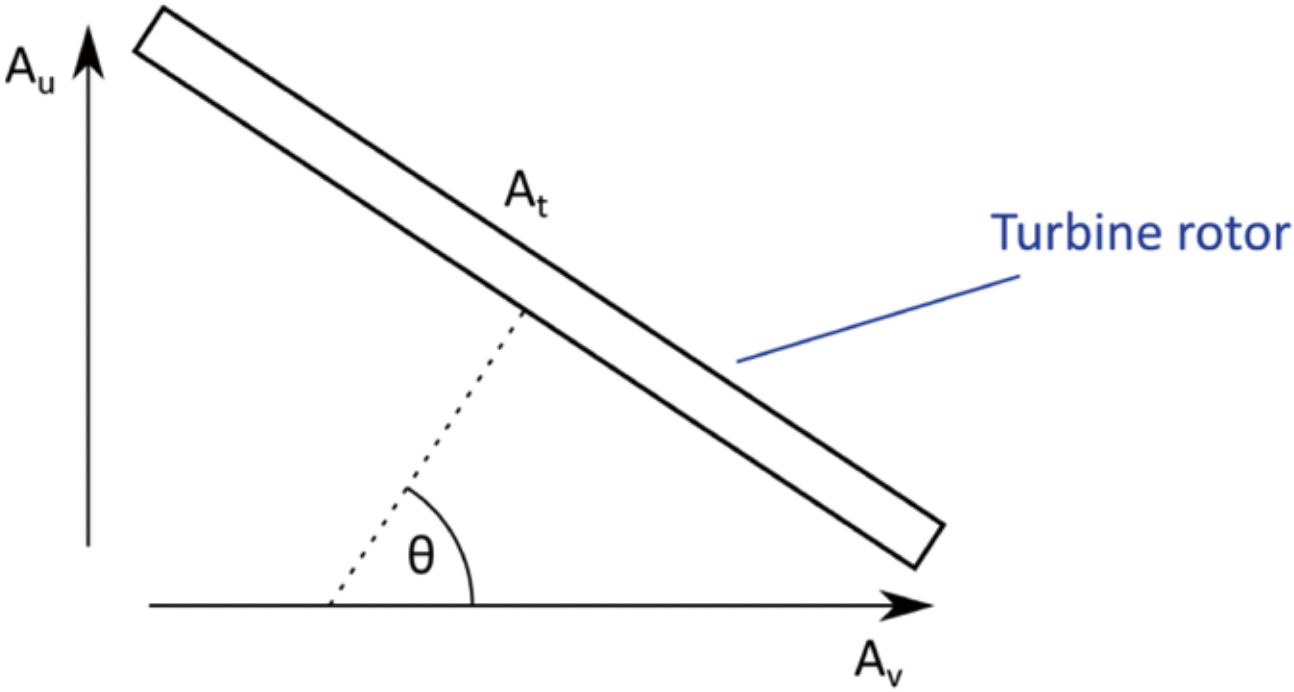


**Fig 4.10** Calculation of areas of two porous plates for each cell. The turbine has area $A_t$, with an arbitrary angle $\theta$ between the $x$-axis and the axis of the turbine. The area $A_u$ represents the total area of rotor that is represented by the porous plate aligned perpendicular to the $x$-axis (i.e. impeding flow in the $u$ direction). The area $A_v$ represents the total area of turbine that is represented by the porous plate aligned perpendicular to the $y$-axis.

Delft3D presumes a constant $c_{loss}$ (it does not vary with time). We therefore set $C_d$ equal to the value at the turbine's rated velocity.

## 04/5.2.4 LIMITATIONS

There are several limitations on including tidal devices into a mesoscale model. Within this project the following limitations have been identified when using Delft3D:

a) In order to represent a single device in a single cell of the grid, the grid size must be sufficiently small. Therefore, this is only possible if another domain with a higher resolution grid is nested inside the bigger domain. Even so, the computational effort will be large.

b) If the grid size is big enough as to represent a farm of devices as a whole, then the turbine wakes are assumed to keep inside of the cell [12]. Hence, wake effect between turbines must be neglected or an extra parameter to include that phenomenon must be developed and included.

c) The scale of the processes shown with these models is of order of kilometres, therefore results are able to evaluate far-field effect, as a consequence of the assumptions implicit to the models, but not near-field effect.

d) Vertical discretization is another issue for the Delft3D model developed within the TeraWatt project. It currently uses sigma-layer and results are associated with those layers, not with absolute depths within the water column. The model requires that the sigma layer in which the turbine will be placed is indicated. Therefore, since sigma layer width depends on the water level, the turbine location must be tracked every time step to calculate what layers it is occupying. This means that with each time step the tidal turbine is moving up and down but also changing its size because of that. A Z-level approach would simplify this, but in Delft3D it is not compatible with domain decomposition (i.e. nested grids). Most of the works discussed in this document have used sigma-layer models, recalculating the layers intersected by the rotor on each time step. This facility is not available in the current version

of Delft3D, so the mean positions of the model's layers were used to calculate, once, which layers experience force from a porous plate.

e) Support structures can be defined below the turbine as a pier in the bottom layer. This will cut all the flow through that layer. Alternatively – and perhaps more realistically – an additional porous plate can be defined with a different coefficient than the one representing the turbine, based on the resistance of the flow caused by the support structure. In this work they have not been included.

## 04/6 TOOLS IN MIKE 3 FOR ENERGY EXTRACTION

For further information on the contents of this Section see the MIKE manual [68, Sec. 6.14] and help file [69].

### 04/6.1 TURBINE STRUCTURES

MIKE allows the user to specify a number of types of sub-grid scale structures that are placed in the flow. One of these is a "turbine". Turbines are assumed to be of the horizontal axis type. The parameters that can be specified for a turbine are:

- Horizontal location;
- Orientation of the turbine relative to projection north;
- Diameter of the turbine;
- Vertical position of the centre of the turbine (in z-coordinates). Note that this can only be set in absolute terms, and not relative to the water level. It is therefore not possible to include floating turbines correctly;
- Either
  A fixed drag coefficient. In this case the turbine behaves as a simple, unchanging object in the flow. Its drag coefficient is the same from any direction.
- Or
  A lookup table of "lift" and "drag" coefficients according to the current speed at the turbine and the angle between the axis of the turbine and the flow direction, as per Figure 4.11. This is likely to be more appropriate for a real, actively-controlled turbine. For conditions in-between those specified in the table, linear interpolation is used. For conditions outside those specified in the table there is no extrapolation – instead, the nearest value in the table will be used. This allows for cut-in speeds and maximum speeds beyond which there is no change in the turbine's hydrodynamics.

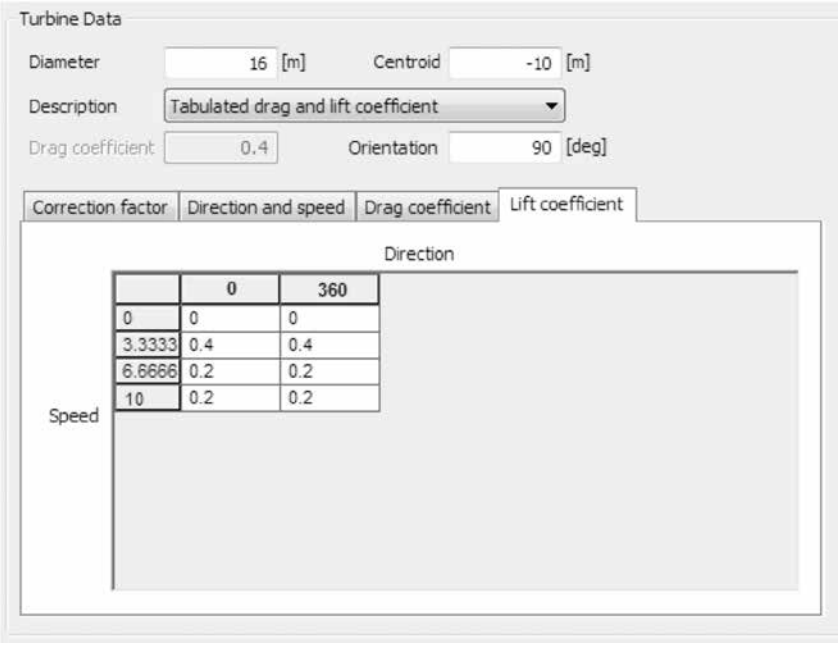


**Fig 4.11** Example of a table of lift coefficients specified in MIKE 3 (actual values are arbitrary).

The "drag" and "lift" forces determined by these coefficients represent the components of the force exerted by the turbine on the flow that are parallel to and orthogonal to the flow respectively (see Figure 4.12). In the case of a turbine with axis oriented parallel to the flow, the drag coefficient will be equal to the thrust coefficient, as described elsewhere in this document, and the lift coefficient will be zero. The drag and lift forces are calculated from the specified drag and lift coefficients as follows:

$$F_D = \frac{1}{2}\rho\alpha C_D A_e V^2 \quad (30)$$

$$F_L = \frac{1}{2}\rho\alpha C_L A_e V^2 \quad (31)$$

where $\rho$ is the density of water, $\alpha$ is a correction factor (which can be specified on a time-varying basis), $C_D$ and $C_L$ are the drag and lift coefficients respectively, $A_e$ is the effective area of the turbine exposed to the current, and $V$ is the current speed.

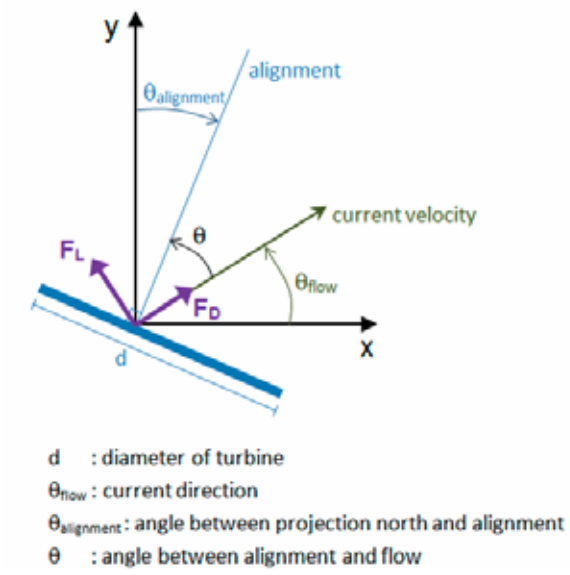


**Fig 4.12** Diagram showing directions of turbine alignment, flow velocity, drag force and lift force as modelled in MIKE. Source: [68, Fig. 6.11]

Each turbine's angle is fixed with respect to North, and so "weathervaning" devices (i.e. those that rotate to face into any current direction) are not explicitly supported. However, since the lift and drag coefficients can be specified as functions of the angle between the flow and the device's heading ($\theta$), this can be worked around. For devices that freely weathervane to point into the flow direction at any given moment (such that $\theta$=0 at all times), identical lift values can be given for every value of ($\theta$).

In MIKE 3, the conversion between z coordinates in which the turbine's vertical position is specified and the $\sigma$ coordinates of the model is made automatically. Two simplifications are made:

1) The current speed used to look up the lift and drag coefficients and to calculate the force applied is the mean speed from all the layers that are intersected by the turbine. In other words, vertical shear over the turbine's disc is neglected.

2) The forces applied by the turbine are equally distributed over all of the layers intersected by the turbine. No account is made of the circular shape of the rotor disc, and hence its varying area intersecting each layer.

If it is desired, an output file can be produced giving time series of the following parameters for each turbine:

- Lift and drag force
- Current speed and direction

## 04/6.2 COMPOSITE STRUCTURES

When a tidal turbine is installed in the water column, in addition to the variable hydrodynamics of the rotor itself there are fixed elements – both of the turbine itself and its supporting structure (see Figure 2). It is possible that an allowance for these may have been made when calculating the drag and

lift coefficients used to specify the turbine above, but these coefficients may simply represent the rotor disc. For some devices it would be inappropriate to include the supporting structure in the turbine parameters, as the drag would be applied to the wrong layer(s) of the model. In this case a "composite structure" can be used, consisting of two parts: A "turbine" structure to represent the rotor, and another structure type for the supporting structure. If the two structures are created with identical location coordinates, MIKE will consider them together as a composite structure.

The most appropriate structure type would seem to be the "pier", which is intended to simulate bridge piers. As such it models a vertical column of circular, rectangular or elliptical cross-section, with a width that may vary with depth. The width may vary to zero, thus allowing a pile that does not reach the surface. The drag force from a fixed pier structure is calculated as

$$F = \frac{1}{2}\rho\delta C_D A_e V^2 \qquad (32)$$

where $\delta$ is the streamline factor, $C_D$ is the drag coefficient for the pier, and $A_e$ is the effective area of the pier exposed to the current. The streamline factor ($\delta$) is described as "a factor that is multiplied on the total drag force to take into account the increased flow velocity due to the blocking of piers"[69].

## 04/6.3 PROPOSED METHOD FOR INCLUDING ENERGY EXTRACTION IN MIKE 3

1) The developer provides a table of lift and drag coefficients as per the example in Figure 4.11. This should include one data point at the cut-in speed of the turbine and one just below, and a similar arrangement at any fixed maximum that is reached for either of these coefficients, as well as sufficient intermediate velocities to adequately resolve the variation in the coefficients. At a minimum, two different directions will need to be specified for most turbines – one facing into the flow and one facing away from it. Providing more directions will give more accurate results in a flow that is not perfectly rectilinear. These coefficients are likely to be provided by developers based on their own testing or modelling work.

2) If the supporting structure occupies the same vertical position in the water column as the turbine, then ideally the coefficients provided in step 1 should include the effects of fixed parts of the turbine and supporting structures. If they do not, then details of the shape of supporting structures will be required so that they can be modelled separately. If they are not of the form of vertical piers, it will be necessary to estimate an equivalent of this form or of one of the other structure types that MIKE supports.

3) The optimum size of the model cells is a topic that requires some attention. The considerations in Section 04/4.3.3 suggest that the density of the mesh should be at least sufficient to permit one element per turbine, and preferably higher. Meanwhile, the potential effect outlined in Section 04/4.3.4 suggests that a mesh that is too fine will give less accurate predictions unless a correction can be established. Further research will be required to establish the optimum grid resolution with respect to turbine spacing.

   It may be necessary to manually move mesh nodes to take account of turbine locations. Any manipulation of the mesh must be done before baseline simulations (without turbines) are run so that the mesh is the same with and without turbines present.

4) The turbines should be entered as sub-grid structures, as shown in Figure 4.13, and their parameters specified in the related screens.

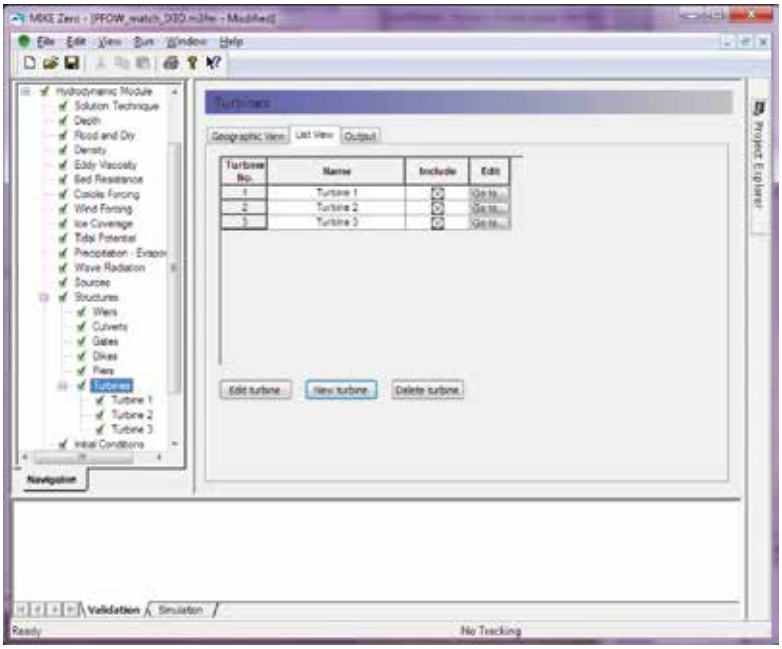


**Fig 4.13** View of the MIKE Zero application showing three turbines listed.

5) Using a regional scale hydrostatic shallow-water model such as MIKE 3FM, it is not practical to fully model intra-array effects. While the reduction of momentum in an upstream cell will certainly affect downstream cells, effects such as mixing in wakes and streaming of current between turbines will not be simulated. If these effects can be parameterized by other means, then the correction factor $\alpha$ (used in equations (30) & (31)) may be used to approximate them.

6) If it is necessary to enter supporting structures separately, these should be entered as Pier structures, ensuring that their coordinates are identical to those given for the turbines.

7) It is difficult to check for sensitivity to boundary locations in MIKE, because moving the boundary necessitates remeshing the whole domain – a lengthy process that is unlikely to be practical in commercial situations. However, some reassurance can be gained by verifying that the modelled far field effects of energy extraction do not extend close to any open boundaries. If the boundaries are specified by water level, the modeller should check that the current through the open boundaries does not change significantly when turbines are added. If the boundaries are specified in terms of currents, then they should check that the water level does not change. It is possible that the use of Flather boundary conditions may offer an improvement over clamped ones, as detailed in Section 04/4.3.5, but this has not been tested within the TeraWatt project.

## 04/7 SUMMARY OF INFORMATION NEEDED FROM DEVELOPERS

A modeller studying a proposed development would require the following information on turbine parameters from the developer. For the purposes of TeraWatt, generic parameters will be assumed, and these are listed in Appendix A.

### 04/7.1 FOR DELFT3D

- Horizontal and vertical locations of turbines
- Diameter of rotor
- Reference thrust coefficient or thrust coefficient curve as a function of flow velocity to parameterize a coefficient to represent the energy extraction.

- Parameters for supporting structures. Those can only to be simulated as single objects approximated to bridge piers, i.e. monopiles cannot be accurate described into the model. Alternatively, estimation of its effect into the flow in the form of energy dissipation must be included in the coefficient that represents energy extraction.

## 04/7.2 FOR MIKE 3

- Horizontal and vertical locations of turbines
- Headings (alignments) of turbines, for types with fixed yaw
- Parameters of turbines
  - Diameter of rotor
  - Tables for lift and drag coefficients by speed and alignment to flow, as per Figure 4.11
- Parameters for supporting structures (if not included in the turbine parameters). Note that MIKE can only directly simulate single objects that can be approximated to bridge piers. For example, a monopile can be considered to be a circular pier that finishes below the surface, and a cuboid concrete weight can be described as a short and wide rectangular pier.
  - Shape of pier (circular, rectangular or elliptical)
  - Horizontal dimensions of pier, including any vertical variation in these dimensions
  - Vertical extent of pile
  - Estimate of streamline factor

## 04/8 AGREED PARAMETERS FOR GENERIC TIDAL TURBINE

In a commercial setting, the modeller would be supplied by their client with parameters for the specific turbines being considered, as outlined in Section 04/7. For the purposes of modelling in the TeraWatt project, however, it is necessary for parameters for a generic tidal turbine to be used that are sufficiently realistic as to be acceptable to stakeholders as plausible and relevant, while not being so similar to any individual company's device as to raise issues of commercial confidentiality.

A workshop with developers was held in Aberdeen on 14th March 2014. Following this workshop a generic thrust coefficient curve was proposed, based loosely on the tank measurements presented in [63]. This curve was substantially modified based on advice received from a number of tidal developers under the Chatham House Rule. As a result of this process, the following parameters has been proposed for its use in TeraWatt tidal modelling:

**General format:** Single rotor connected to the seabed by a monopole.

**Rotor diameter:** 20 m

**Cut-in speed:** 1 m/s

**Cut-out speed:** 4 m/s

**Rated speed:** 2.5 m/s

**Rated capacity:** 1 – 1.5 MW approx. (for information only; the planned modelling work is concerned only with hydrodynamic effects and not electricity generated)

**Thrust coefficient:**

| CURRENT SPEED (m/s) | $C_T$ | THRUST (KN) |
|---|---|---|
| 0.99 | 0.000 | 0 |
| 1 | 0.850 | 547 |
| 1.25 | 0.850 | 855 |
| 1.5 | 0.850 | 1232 |
| 1.75 | 0.850 | 1676 |
| 2 | 0.850 | 2190 |
| 2.25 | 0.850 | 2771 |
| 2.5 | 0.850 | 3421 |
| 2.75 | 0.635 | 3093 |
| 3 | 0.490 | 2840 |
| 3.25 | 0.385 | 2619 |
| 3.5 | 0.308 | 2430 |
| 3.75 | 0.250 | 2264 |
| 4 | 0.205 | 2212 |
| 4.01 | 0.000 | 0 |

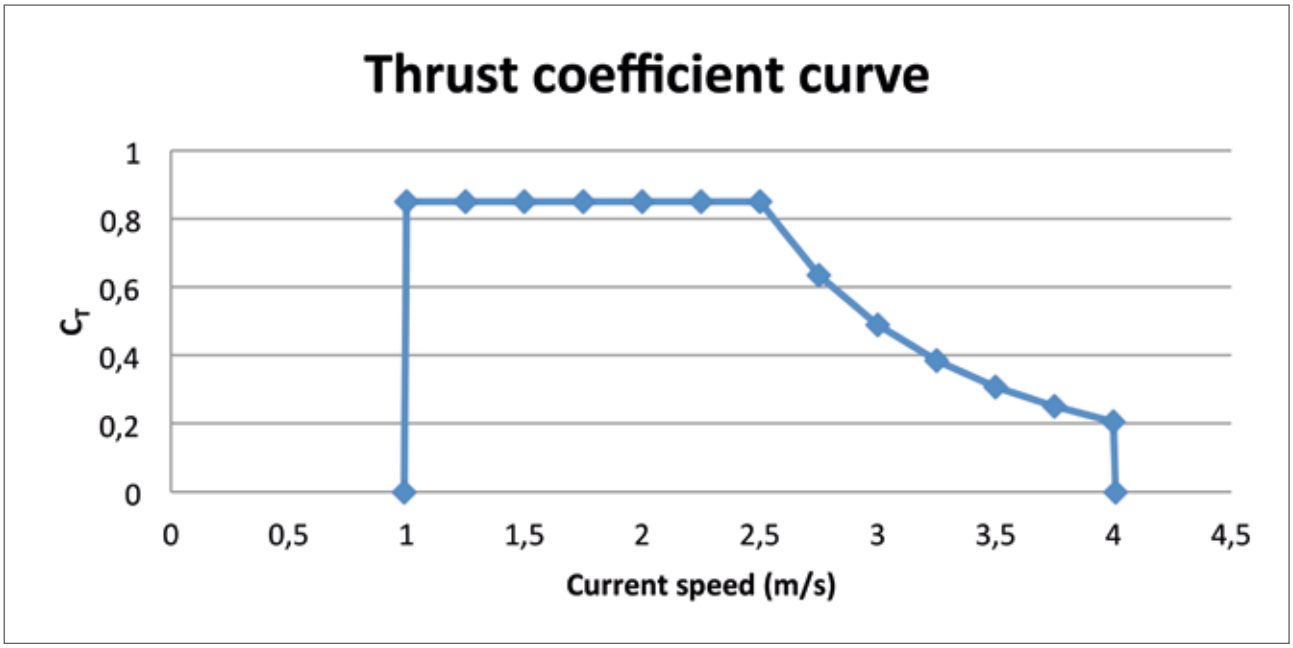


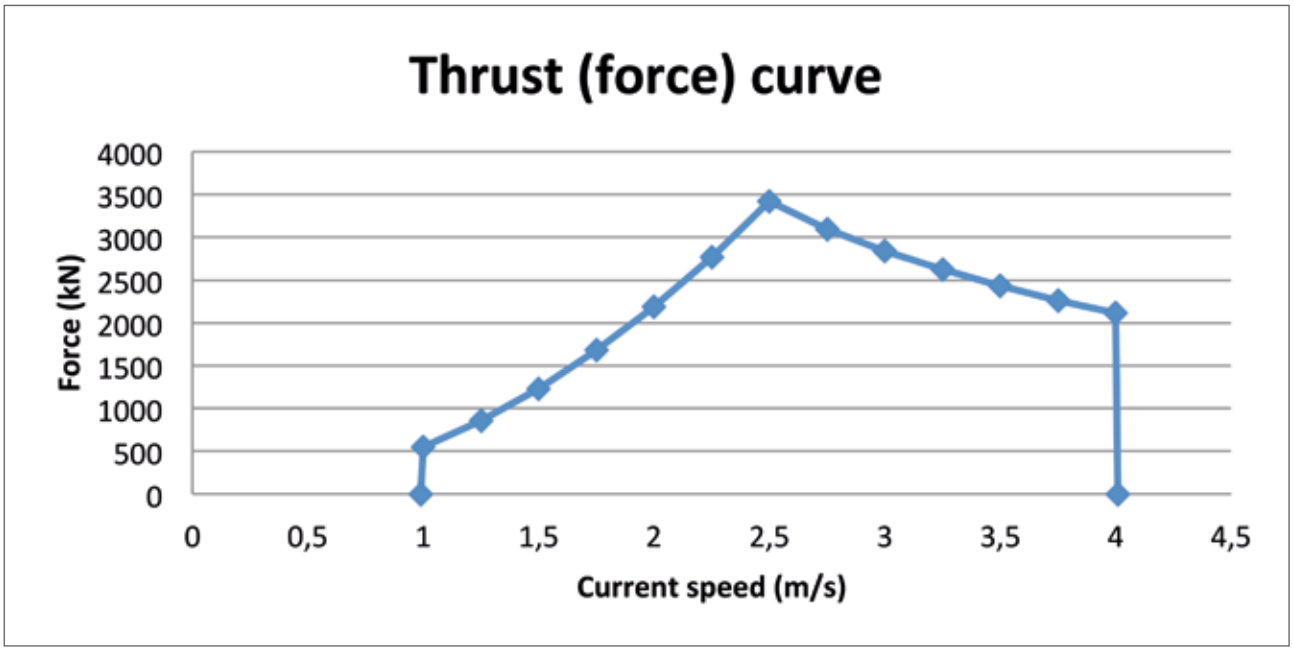


**Supporting structure:** Circular monopile of 2.5 m diameter, extending from seabed to rotor hub height.

## 04/9 REFERENCES

[1] C. Garrett and P. Cummins. *The efficiency of a turbine in a tidal channel.* J. Fluid Mech., vol. 588, no. -1, pp. 243–251, 2007.

[2] R. Vennell. *Tuning tidal turbines in-concert to maximise farm efficiency.* J. Fluid Mech., vol. 671, no. -1, pp. 587–604, 2011.

[3] I. Walkington and R. Burrows. *Modelling tidal stream power potential*. Appl. Ocean Res., vol. 31, no. 4, pp. 239–245, 2009.

[4] *Tidal clients : EMEC: European Marine Energy Centre.* [Online]. Available: http://www.emec.org.uk/about-us/our-tidal-clients/. [Accessed: 25-Nov-2013].

[5] J. Hardisty. *The analysis of tidal stream power.* John Wiley & Sons Inc, 2009.

[6] Carbon Trust. *Tidal streams and tidal stream energy device design.*

[7] *Tidal turbine technology* | Andritz Hydro Hammerfest. [Online]. Available: http://www.hammerfeststrom.com/.

[8] R. Swift. *Assessment of Performance of Tidal Energy Conversion Systems.* EMEC Br. Stand. Inst. ISBN, pp. 978–0, 2009.

[9] W. Turbines. *Part 12-1: Power performance measurements of electricity producing wind turbines; IEC TC/SC 88.* IEC 61400-12-1, 2005.

[10] *Marine Power Project : Froude's Momentum Theory for an Actuator Disk.* [Online]. Available: http://www.esru.strath.ac.uk/EandE/Web_sites/05-06/marine_renewables/technology/Froude.htm. [Accessed: 25-Nov-2013].

[11] J. I. Whelan, J. M. R. Graham, and J. Peiro. *A free-surface and blockage correction for tidal turbines.* J. Fluid Mech., vol. 624, no. 1, pp. 281–291, 2009.

[12] S. Draper, G. T. Houlsby, M. L. G. Oldfield, and A. G. L. Borthwick. *Modelling tidal energy extraction in a depth-averaged coastal domain.* IET Renew. Power Gener., vol. 4, no. 6, p. 545, 2010.

[13] I. G. Bryden and S. J. Couch. *How much energy can be extracted from moving water with a free surface: A question of importance in the field of tidal current energy?* Renew. Energy, vol. 32, no. 11, pp. 1961–1966, Sep. 2007.

[14] C. Garrett and P. Cummins, *The power potential of tidal currents in channels.* Proc. R. Soc. Math. Phys. Eng. Sci., vol. 461, no. 2060, pp. 2563 –2572, 2005.

[15] B. L. Polagye and P. C. Malte. *Far-field dynamics of tidal energy extraction in channel networks.* Renew. Energy, vol. 36, no. 1, pp. 222–234, Jan. 2011.

[16] C. Garrett and P. Cummins. *Generating Power from Tidal Currents.* J. Waterw. Port Coast. Ocean Eng., vol. 130, no. 3, pp. 114–118, 2004.

[17] C. Garrett and P. Cummins. *The power potential of tidal currents in channels.* Proc. R. Soc. Math. Phys. Eng. Sci., vol. 461, no. 2060, pp. 2563 –2572, 2005.

[18] J. Blanchfield, C. Garrett, P. Wild, and A. Rowe. *The extractable power from a channel linking a bay to the open ocean.* Proc. Inst. Mech. Eng. Part J. Power Energy, vol. 222, no. 3, pp. 289–297, May 2008.

[19] R. Vennell. *Tuning turbines in a tidal channel.* J. Fluid Mech., vol. 663, pp. 253–267, 2010.

[20] S. J. Couch and I. G. Bryden. *Large-scale physical response of the tidal system to energy extraction and its significance for informing environmental and ecological impact assessment.* In OCEANS 2007 - Europe, 2007, pp. 1–5.

[21] G. Sutherland, M. Foreman, and C. Garrett. *Tidal current energy assessment for Johnstone Strait, Vancouver Island.* Proc. Inst. Mech. Eng. Part J. Power Energy, vol. 221, no. 2, pp. 147–157, 2007.

[22] L. S. Blunden and A. S. Bahaj. *Effects of tidal energy extraction at Portland Bill, southern UK predicted from a numerical model.* In 7th European Wave and Tidal Energy Conference, Porto, Portugal, 2007.

[23] R. H. Karsten, J. M. McMillan, M. J. Lickley, and R. D. Haynes. *Assessment of tidal current energy in the Minas Passage, Bay of Fundy.* Proc. Inst. Mech. Eng. Part J. Power Energy, vol. 222, no. 5, pp. 493–507, 2008.

[24] I. Walkington and R. Burrows. *Modelling tidal stream power potential.* Appl. Ocean Res., vol. 31, no. 4, pp. 239–245, 2009.

[25] T. A. Adcock, S. Draper, G. T. Houlsby, A. G. Borthwick, and S. Serhadlıoğlu. *The available power from tidal stream turbines in the Pentland Firth.* Proc. R. Soc. Math. Phys. Eng. Sci., vol. 469, no. 2157, 2013.

[26] S. Draper, T. A. A. Adcock, A. G. L. Borthwick, and G. T. Houlsby. *Estimate of the tidal stream power resource of the Pentland Firth.* Renew. Energy, vol. 63, pp. 650–657, Mar. 2014.

[27] R. Carballo, G. Iglesias, and A. Castro. *Numerical model evaluation of tidal stream energy resources in the Ría de Muros (NW Spain).* Renew. Energy, vol. 34, no. 6, pp. 1517–1524, 2009.

[28] V. Ramos, R. Carballo, M. Álvarez, M. Sánchez, and G. Iglesias. *Assessment of the impacts of tidal stream energy through high-resolution numerical modeling.* Energy, 2013.

[29] K. M. Thyng and T. Roc. *Tidal current turbine power capture and impact in an idealised channel simulation.* Presented at the EWTEC 2013, Aalborg, 2013.

[30] G. I. Shapiro. *Effect of tidal stream power generation on the region-wide circulation in a shallow sea.* Ocean Sci., vol. 7, pp. 165–174, 2011.

[31] S. P. Neill, J. R. Jordan, and S. J. Couch. *Impact of tidal energy converter (TEC) arrays on the dynamics of headland sand banks.* Renew. Energy, vol. 37, no. 1, pp. 387–397, 2012.

[32] Z. Defne, K. A. Haas, and H. M. Fritz. *Numerical modeling of tidal currents and the effects of power extraction on estuarine hydrodynamics along the Georgia coast, USA.* Renew. Energy, vol. 36, no. 12, pp. 3461–3471, 2011.

[33] D. Hasegawa, J. Sheng, D. A. Greenberg, and K. R. Thompson. *Far-field effects of tidal energy extraction in the Minas Passage on tidal circulation in the Bay of Fundy and Gulf of Maine using a nested-grid coastal circulation model.* Ocean Dyn., vol. 61, no. 11, pp. 1845–1868, Nov. 2011.

[34] Z. Yang, T. Wang, and A. E. Copping. *Modeling tidal stream energy extraction and its effects on transport processes in a tidal channel and bay system using a three-dimensional coastal ocean model.* Renew. Energy, vol. 50, pp. 605–613, 2013.

[35] T. Roc, D. C. Conley, and D. Greaves. *Methodology for tidal turbine representation in ocean circulation model.* Renew. Energy, vol. 51, pp. 448–464, Mar. 2013.

[36] I. G. Bryden, S. J. Couch, A. Owen, and G. Melville. *Tidal current resource assessment.* In IMechE, 2007, vol. 221 Part A: J. Power and Energy.

[37] Carbon Trust. *UK Tidal Current Resource & Economics.* Jul-2011. [Online]. Available: http://www.carbontrust.com/media/77264/ctc799_uk_tidal_current_resource_and_economics.pdf.

[38] B. Stevens, J. Duan, J. C. McWilliams, M. Münnich, and J. D. Neelin. *Entrainment, Rayleigh friction, and boundary layer winds over the tropical Pacific.* J. Clim., vol. 15, no. 1, pp. 30–44, 2002.

[39] A. Owen and I. G. Bryden. *Energy extraction implications of structurally significant velocity variation in tidal currents.* In OCEANS 2007 - Europe, 2007, pp. 1–5.

[40] Alstom. *Tidal Power Solutions.* 2013. [Online]. Available: http://www.alstom.com/Global/Power/Resources/Documents/Brochures/tidal-power-solutions-ocean-energy.pdf.

[41] Siemens. *Energy Capture | Marine Current Turbines.* Marine Current Turbines website. [Online]. Available: http://www.marineturbines.com/SeaGen-Technology/Energy-Capture.

[42] M. C. Easton and D. K. Woolf. *The influence of non-linear turbine dynamics on the environmental stress of tidal stream arrays.* Presented at the EWTEC 2013, Aalborg, 2013.

[43] D. R. Plew and C. L. Stevens. *Numerical modelling of the effect of turbines on currents in a tidal channel – Tory Channel, New Zealand.* Renew. Energy, vol. 57, pp. 269–282, Sep. 2013.

[44] S. T. Frandsen. *Turbulence and turbulence-generated structural loading in wind turbine clusters.* Doctoral thesis, Risø National Laboratory, Roskilde, 2007.

[45] T. Stallard, R. Collings, T. Feng, and J. Whelan. *Interactions between tidal turbine wakes: experimental study of a group of three-bladed rotors.* Philos. Trans. R. Soc. Math. Phys. Eng. Sci., vol. 371, no. 1985, 2013.

[46] C. R. Vogel, R. H. J. Willden, and G. T. Houlsby. *A Correction for Depth-Averaged Simulations of Tidal Turbine Arrays.* Presented at the EWTEC 2013, Aalborg, 2013.

[47] M. Shives, C. Crawford, C. Hiles, and R. Walters. *Combining Numerical Methods for Basin and Turbine Scales for Improved Modelling of in-situ Turbine Arrays.* Presented at the EWTEC 2013, Aalborg, 2013.

[48] S. Kramer, M. D. Piggott, J. Hill, L. Kregting, D. Pritchard, and B. Elsaesser. *The modelling of tidal turbine farms using multi-scale, unstructured mesh models.* In Proceedings of the 2nd International Conference on Environmental Interations of Marine Renewable Energy Technologies, Stornoway, 2014.

[49] S. Waldman, G. Genet, S. Baston, and J. Side. *Correcting for mesh size dependency in a regional model's representation of tidal turbines.* Submitted for EWTEC-2015.

[50] C. Garrett and D. Greenberg. *Predicting Changes in Tidal Regime: The Open Boundary Problem.* J. Phys. Oceanogr., vol. 7, no. 2, pp. 171–181, Mar. 1977.

[51] T. A. A. Adcock, A. G. L. Borthwick, and G. T. Houlsby. *The Open Boundary Problem in Tidal Basin Modelling with Energy Extraction.* In Proceedings of the 9th European Wave and Tidal Energy Conference. Southampton, UK, 2011.

[52] E. Blayo and L. Debreu. *Revisiting open boundary conditions from the point of view of characteristic variables.* Ocean Model., vol. 9, no. 3, pp. 231–252, 2005.

[53] B. F. Sanders. *Non-reflecting boundary flux function for finite volume shallow-water models.* Adv. Water Resour., vol. 25, no. 2, pp. 195–202, 2002.

[54] R. A. Flather. *A tidal model of the northwest European continental shelf.* Mem Soc R Sci Liege, vol. 10, no. 6, pp. 141–164, 1976.

[55] G. S. Carter and M. A. Merrifield. *Open boundary conditions for regional tidal simulations.* Ocean Model., vol. 18, no. 3–4, pp. 194–209, 2007.

[56] R. A. Flather. *A tidal model of the northeast pacific*. Atmosphere-Ocean, vol. 25, no. 1, pp. 22–45, 1987.

[57] G. K. Verboom and A. Slob. *Weakly-reflective boundary conditions for two-dimensional shallow water flow problems.* Adv. Water Resour., vol. 7, no. 4, pp. 192–197, Dec. 1984.

[58] Deltares. *Delft3D-FLOW User Manual, Hydro-Morphodynamics, Version 3.15.34158.* May 2014.

[59] R. Ahmadian, R. Falconer, and B. Bockelmann-Evans. *Far-field modelling of the hydro-environmental impact of tidal stream turbines.* Renew. Energy, vol. 38, no. 1, pp. 107–116, Feb. 2012.

[60] I. G. Bryden and S. J. Couch. *ME1—marine energy extraction: tidal resource analysis.* Renew. Energy, vol. 31, no. 2, pp. 133–139, Feb. 2006.

[61] W. M. J. Batten, A. S. Bahaj, A. F. Molland, and L. S. Blunden. *Yawed performance of horizontal axis marine current turbines.* In INTERNATIONAL SOLAR ENERGY SOCIETY UK SECTION-CONFERENCE-C, 2006, vol. 85, p. 151.

[62] R. Ahmadian and R. A. Falconer. *Assessment of array shape of tidal stream turbines on hydro-environmental impacts and power output.* Renew. Energy, vol. 44, pp. 318–327, 2012.

[63] A. S. Bahaj, A. F. Molland, J. R. Chaplin, and W. M. J. Batten. *Power and thrust measurements of marine current turbines under various hydrodynamic flow conditions in a cavitation tunnel and a towing tank.* Renew. Energy, vol. 32, no. 3, pp. 407–426, Mar. 2007.

[64] E. Lalander and M. Leijon. *In-stream energy converters in a river – Effects on upstream hydropower station.* Renew. Energy, vol. 36, no. 1, pp. 399–404, Jan. 2011.

[65] Delft Hydraulics. *Delft3D-FLOW user manual, Version 3.15..* 2011.

[66] S. Mungar. *Hydrodynamics of horizontal-axis tidal current turbines; A modelling approach based on Delft3D.* Masters thesis, TU Delft, 2014.

[67] T. Roc, D. Greaves, K. M. Thyng, and D. C. Conley. *Tidal turbine representation in an ocean circulation model: Towards realistic applications.* Ocean Eng., Jan. 2014.

[68] DHI. *MIKE 3 Flow Model FM Hydrodynamic Module User Guide*. 2012.

[69] DHI. *MIKE by DHI 2012 help file.* 2012.

# MODELLING THE IMPACTS OF MARINE ENERGY EXTRACTION ON NON-COHESIVE SEDIMENT TRANSPORT AND MORPHODYNAMICS

05

I. Fairley and H. Karunarathna

COLLEGE OF ENGINEERING, SWANSEA UNIVERSITY, SINGLETON PARK, SWANSEA, SA2 8PP

## 05/ SUMMARY

This report summarises the methodologies and philosophies used within the TeraWatt Project to study the impact of marine energy extraction on non-cohesive sediment dynamics using examples from the Pentland Firth and Orkney Waters. The actual extraction of energy and hydrodynamic modelling methodologies are comprehensively dealt with in the relevant TeraWatt position papers and hence aspects relating solely to sediment transport are focused on here. Certain hydrodynamic aspects are discussed, however, due to their importance to sediment transport. It must be emphasized that without accurate simulation of hydrodynamic and wave parameters morphodynamic predictions will be inaccurate.

Rather than only discuss modelling techniques, much of this report discusses the preparation of input data. Of primary importance is access to spatially varying data on sediment size and spatial distribution, and the methodologies for deriving information in the face of limited data are presented. It is the opinion of the TeraWatt consortium that for areas such as the Pentland Firth, adequate spatial representation should be prioritised over absolute data quality. Calibration data for both the wave and tidal forcing and, ideally, the morphodynamic change is also important. Wave and tidal scenarios are considered together because there are some common themes that run between both technology types.

For many wave deployment areas, pragmatism is required: high energy, wave exposed environments often have limited mobile sediment between hard rock geology and in such situations not only is the likelihood of accurate predictions low, but the severity of impact is likely to be minimal as well. Therefore, one can rely on conceptual models to suggest likely changes rather than numerical coastal models. Pragmatism is also required with regards to the balance between mesh size and resolution and computational expense.

## 05/1 INTRODUCTION

Tidal stream turbines can only be deployed in specific resource areas where tidal current velocities exceed a certain device dependant level, typically these are in areas constrained by channels, islands or headlands [1-4]. Implementation of turbine arrays is likely to lead to areas of reduced tidal current due to energy extraction and also accelerated tidal flows in other areas due to blockage effects [5-7]. Importantly, global tidal connectivity means that far field impacts are possible for large scale developments. If mobile sediment is present, this might lead to changes in sediment transport regime and also to the morphology of sandy areas.

Likewise wave energy extraction will affect the down-wave energy and hence potentially affect coastal morphodynamics.

This report is structured as follows: firstly previous work on the impact of tidal energy extraction on sediment dynamics is discussed and the tidal case site presented; secondly past work on wave energy impacts is discussed; thirdly, the required sediment data and techniques to derive it are described; fourthly, domains and meshes for fully coupled models are discussed; and finally lessons learnt from non-cohesive sediment transport modelling in the TeraWatt project are discussed.

## 05/2 TIDAL ENERGY EXTRACTION

Relatively little academic interest has focussed on the impacts to sediment transport compared to other areas such as hydrodynamics [6, 8] or biological receptors [9, 10]. It is believed that this is due to the relative scarcity of sediment in many first generation deployment sites. Previously Neill et al. [11] used a 1D model to demonstrate that, for a relatively long channel with variations in tidal asymmetry, morphological impacts are increased if energy extraction occurs in regions of asymmetry. Case studies in the Channel Islands [12] and Anglesey [13] have used 2D coastal area models to investigate the impacts of array deployment on sediment transport and morphodynamics. Neill et al. [12] investigated the impact of large (300MW) arrays on headland sandbanks for both idealised and realistic scenarios. They found that energy extraction of this magnitude could have significant impacts on the morphology of local sandbanks, but that careful siting of the array could mitigate

this impact. Robins et al. [13] found that for smaller array deployments of 10-50 MW the impact of energy extraction was less than the natural variability, but that as array sizes increased over 50MW significant impacts on sediment transport were observable. They highlight the fact that results for the impact of tidal stream energy on sediment transport are case specific. This is due to the range of hydrodynamic, bathymetric and sedimentary properties of sites where energy extraction is being planned. In high energy environments, suitable for tidal stream sites, sediment is often spatially varying with regions of swept rock, sand and gravel [14]. Robins et al. [13] also note that use of 3D modelling would give more accurate results. Use of a 3D model allows for energy to be extracted at a specific level in the water column which allows for more realistic representation of the hydrodynamic impacts which will force changes to sediment transport. Robins et al. [15] highlight the option for focussing on the changes to bed shear stress rather than actual sediment transport which could be appropriate for regions where detailed description of sediment is unavailable. However, it is debatable whether regulatory bodies would accept such a proxy. Certainly it would be a useful initial step to identify areas where changes to bed shear stress are likely and if these correspond to areas where sediment is present then more detail investigations could be conducted.

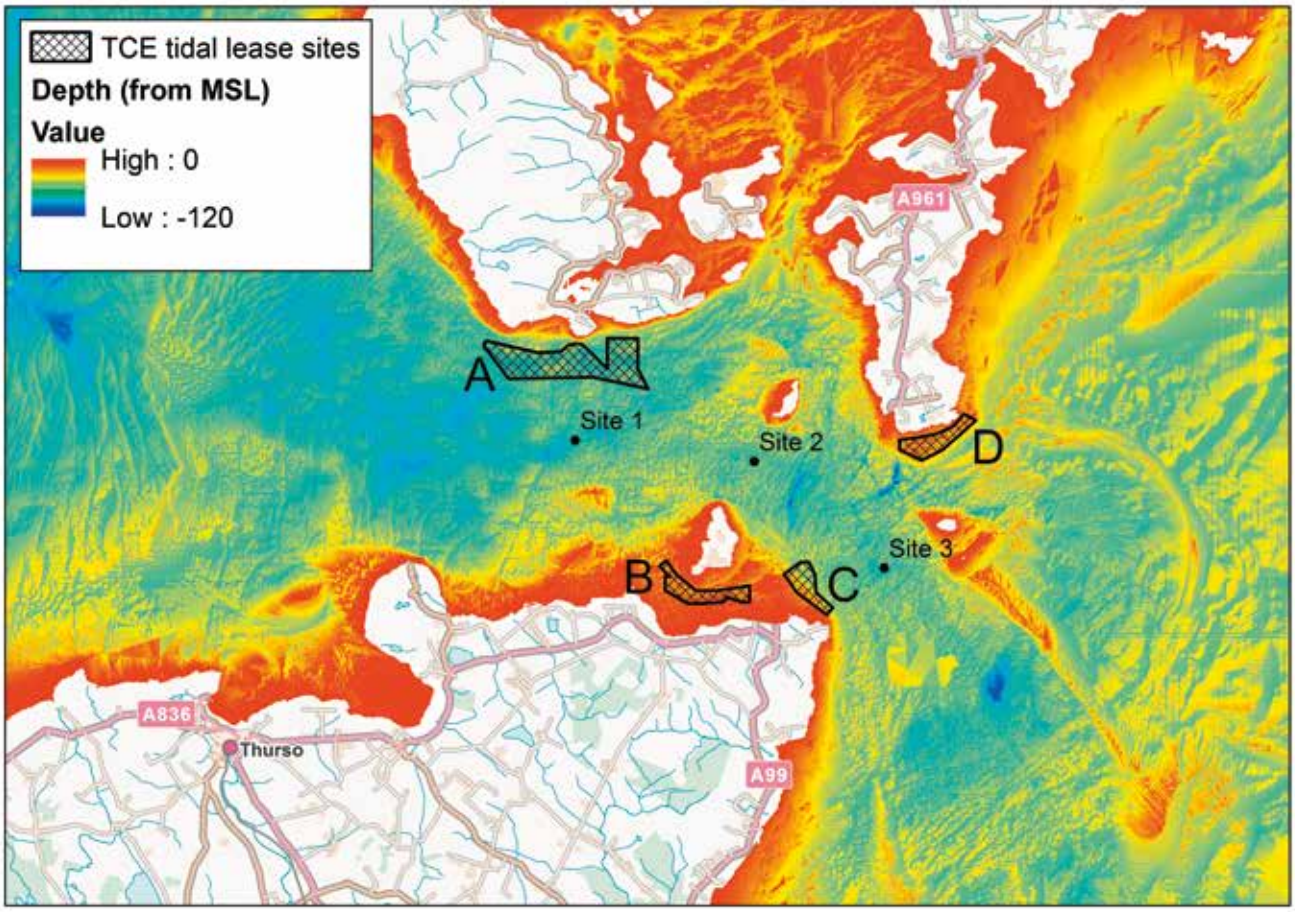


**Fig 5.1** The bathymetry of the Pentland Firth, the turbine deployment sites (hatched areas) and the location of the moored ADCPs used for validation (black dots). Reproduced from [33]

## 05/2.1 THE PENTLAND FIRTH TIDAL EXAMPLE SITE

In this report, reference is made to a modelling study of the Pentland Firth (PF) conducted as part of the TeraWatt project (Figure 5.1). Much of the PF is swept rock, and the PF has been identified as a bedload parting zone with transport directed into the North Sea in the eastern section and into the north Atlantic in the western section[16]. Nonetheless, despite the strong currents, above the threshold of motion for the observed particle sizes, there are areas of mobile sediment associated with headlands, islands or areas of weaker current. It has been recognised that elsewhere in the Orkney Islands sub-tidal sand areas are highly mobile: Farrow et al. [17] considered two surveys from the spring of 1974 and June 1977 and identified areas of bedrock in the first survey that were covered in large areas of mega-rippled sand in the second and vice versa. There are two primary areas of sediment in the PF that are the focus of this study: the Sandy Riddle to the east and an area of sand waves to the west of the island of Stroma (Figure 5.2).

The Sandy Riddle can be classed as a banner bank associated with four rocky islets named the Pentland Skerries. It is around 12km in length and crest depths range from 16m to 60m below mean sea level (MSL). The bank is covered in sand waves and megaripples. Much of the mobile sediment in the region is composed of coarse sand to gravel sized shell fragments and highly calcareous sand [18]. Flather [19] suggests that under storm surge conditions strong easterly driven flows will be superimposed on the strong tidal currents. Additionally, Light and Wilson [18] report that linear wave theory suggests sediments would be mobilised up to a depth of 200m by the 50 year return period wave conditions and therefore larger wave events could also impact on sediment transport over the shallower Sandy Riddle. Therefore it has been surmised [20]that the crest of the Sandy Riddle would be the most active region for bedload transport in the area.

As far as the authors are aware, no attention has been given to the area of sand waves west of Stroma. They cover an oval shaped area 4km long by 2 km wide and consist of medium to coarse sand. The crest of the sandbank containing the sand waves is -25 m MSL with deeper areas around 70 m based on multibeam data collected by Marine Scotland Science in 2009. The area is unsheltered from swell and wind waves coming from the North Atlantic. The most defined sandwaves are present on the northern flank, with wavelengths ranging from 150 m in the west to 400 m in the east. The sandwaves are saw-toothed in shape with the steeper slope to the east, indicating a residual eastward transport along that flank. The sand waves on this flank arise from bifurcations of less regular sandwaves over the crest and southern flank.

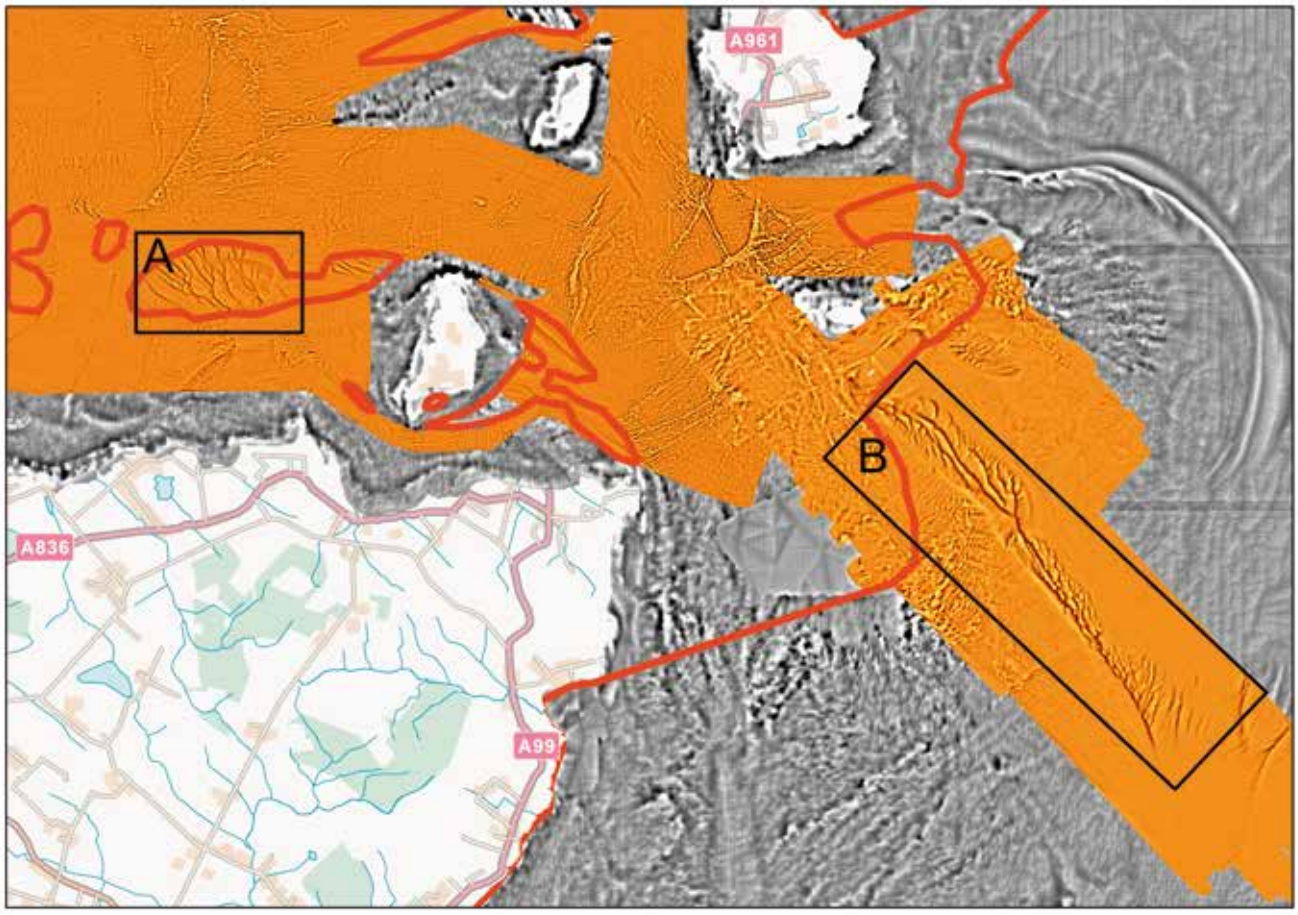


**Fig 5.2** A plot of the Pentland Firth showing the textural surface used to identify mobile sediment areas based on the presence of sandwaves/ripples. The sand coloured area is the area covered by multibeam data and the grey area the area where a 20 m grid was used. Area A is a large area of sand waves and area B is the large banner bank of the Sandy Riddle. Reproduced from [33]

## 05/3 WAVE ENERGY EXTRACTION

Similarly to tidal stream impact studies, work has concentrated on the impact to wave fields and local wave climate, and methods of accurately representing wave energy converters in numerical models. Less work has considered modelling of the changes to sediment transport and morphology. Abanades et al. [21, 22] studied the impact that WECs might have on beach morphodynamics at Perranporth, a large sandy beach in SW England. They used a high resolutions spectral wave model, Swan [23], to force both an X-Beach [24] cross-shore profile model and a 2DH (two dimensional horizontal) coastal area model, again using X-Beach. Keeping the morphological model to the region of interest with a wave model being used to model the impact of WECs on the wave climate over a wider area allowing a reduction in computational expense. This is the methodology advocated within the TeraWatt project. For the situation modelled they found a substantial impact on beach dynamics with a reduction of erosion of 50%. Given the sandy nature of both the intertidal and subtidal areas, a constant D50 was used. It should be noted that in neither study was a morphodynamic validation undertaken, possibly due to the hypothetical nature of the study.

Mendoza et al. [25] have taken a slightly different approach whereby a numerical wave model was used to simulate the impact of WEC's on the local wave climate and then analytical equations used to calculate longshore sediment transport and coastline evolution. This approach was applied to sandy beaches in Santander, Spain and Las Glorias, Mexico.

A key difference between these examples and the areas of interest in the Pentland Firth and Orkney Waters is the uniformity and abundance of sediment.

### 05/3.1 THE CASE STUDY SITE USED: THE BAY OF SKAILL

The Bay of Skaill is the largest west facing sandy beach on Mainland Orkney (Figure 5.3) and is of recreational importance due to its sandy nature and archaeological significance due to the presence of a Neolithic village, Skara Brae. The beach is situated in an embayment 1km wide bounded by hard rock headlands. It is backed by a cobble storm beach and low lying sandy hinterland, the sub tidal bay floor is largely bedrock: therefore mobile sediment forms a narrow strip, primarily in the intertidal region. It is believed that cross-shore transport dominates and that there is a seasonal variation to this change with the sediment being stripped from the beach face by winter storms and migrating back onshore in calmer periods.


**Fig 5.3** A map of Orkney showing the Bay of Skaill.

## 05/4 DEFINITION OF SEDIMENT SIZE AND SPATIAL COVERAGE

A significant problem for modelling studies involving sediment transport in areas such as the Pentland Firth is the highly spatially variable nature of the natural sediment in terms of both abundance and grain size. Within the model domain are a wide range of seabed types including but not limited to: swept bedrock areas, sand veneers on bedrock, large cobbles with interstitial sand and gravel, large sandbanks and sand wave fields. Unfortunately data availability in areas such as this is often poor, with sparse point data of varying quality. Two aspects need to be considered for application into the model: maps of erodible sediment areas and maps of the spatial variation in grain size. These are considered separately below.

### 05/4.1 SPATIAL VARIATION IN MOBILE SEDIMENT

In areas such as the North and West of Scotland, it is insufficient to interpolate between sparse sediment samples and assume uniform sediment coverage: there are substantial areas of swept bedrock, with deeper sediment deposits in the lower flow areas. For a complete description of the sedimentary regime, sub-bottom profiling to determine mobile sediment layer thickness would be required and where possible this should be obtained. However it is recognised that this is expensive to obtain and therefore other techniques are needed. Often high resolution multibeam data is available, whether previously collected or collected in the process of planning a marine energy development. Sophisticated automatic classification techniques have been suggested [26, 27], and commercial packages such as RoxAnn are available for automated ground discrimination based on bathymetry and backscatter (Figure 5.4). However since these require access to the backscatter data as well as the multibeam bathymetry it is unlikely to be achievable if previously collected databases are used. In cases where such data is available, these types of techniques should be utilised as good quality results are likely to be achieved. Where only the multi-beam data is available, seabed type can still be inferred via a manual classification and the methodology is described in the next paragraph.

De-trended high resolution bathymetry can be used to provide a textural surface which can be used to infer seabed type. Such a methodology was utilised for the tidal sediment example and the work flow is as follows:

1) Multibeam echosounder data was interpolated onto a regular grid with 3m spacing.

2) A smoothed bathymetry surface was produced by applying a moving window average to the gridded data and this surface used to de-trend the gridded bathymetry and produce a textural surface (Figure 5.2).

3) Different sediment types are clearly observable in this surface, with sand areas indicated by very smooth surfaces or rippled surfaces whereas bedrock areas are indicated by an irregular, creviced surface.

4) The spatial extent and distribution of sand patches was manually defined in a GIS package (Figure 5.2).

This methodology was ground-truthed using available data from Marine Scotland Science video trawls in the region (Figure 5.5). A similar manual classification can be conducted using side-scan sonar data (Figure 5.6). This approach was used for the wave energy site, and is similar to the methodology used in the multibeam case, except that the data does not need to be de-meaned. The sidescan shows up the seabed texture directly and can be used to classify the seabed into sand and rock regions. While these manual approaches are not fool-proof and are time consuming, it is important to utilise whatever data is available to map the regions of subtidal mobile sediment.

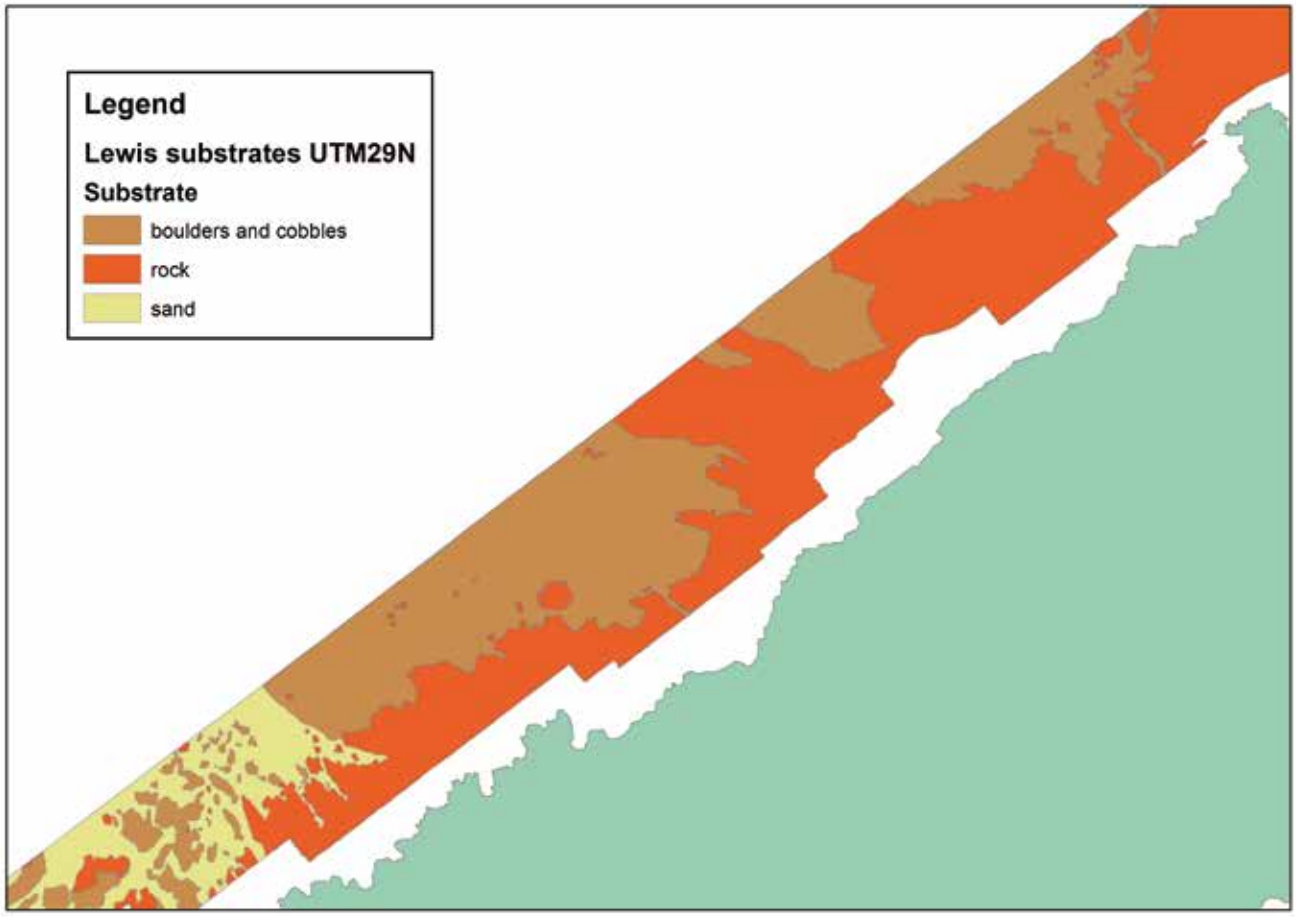


**Fig 5.4** An example of RoxAnn data on seabed sediment type from the Marine Scotland Interactive website (http://www.gov.scot/Topics/marine/science/MSInteractive).

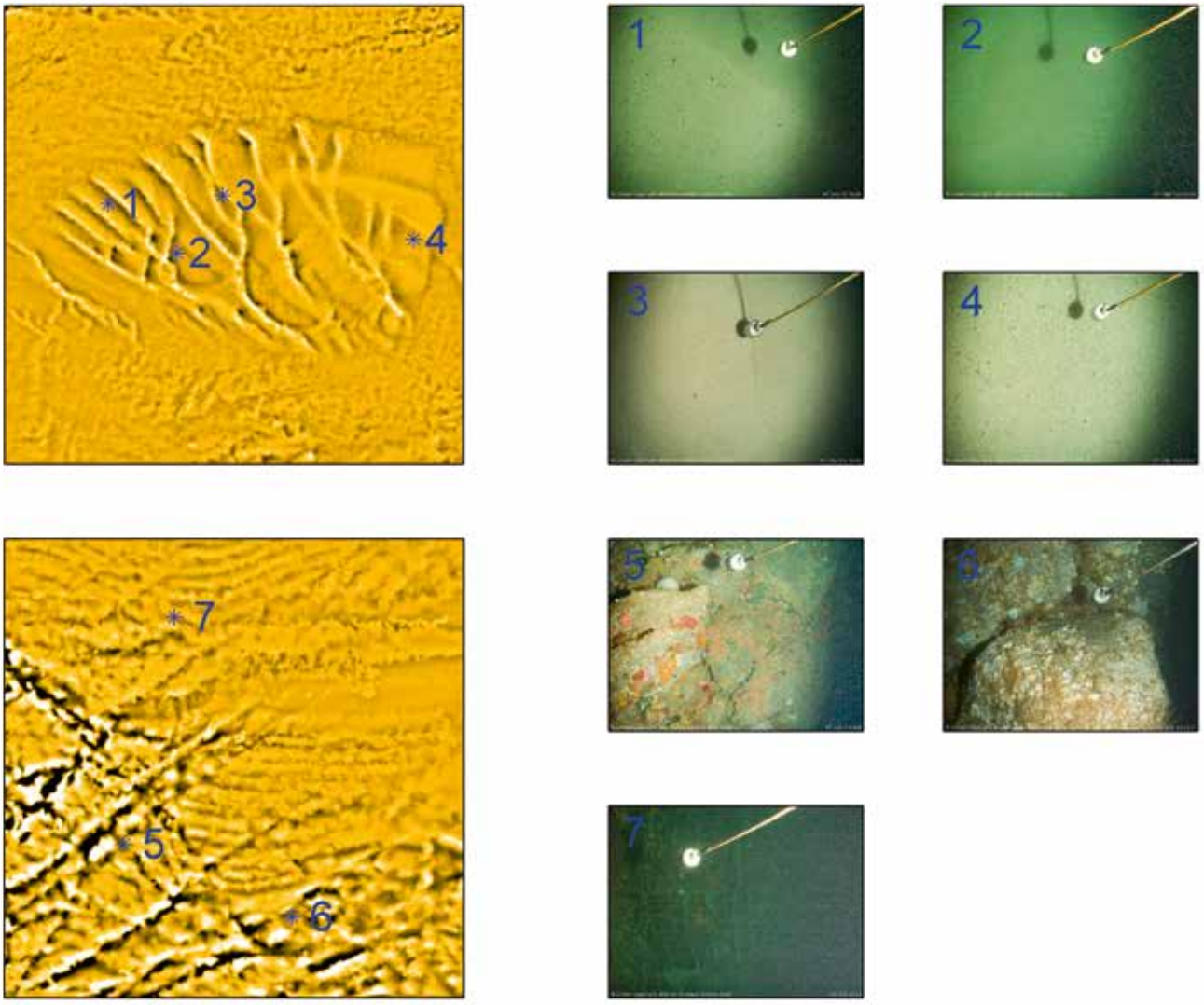


**Fig 5.5** Ground-truthing of the textural classification, with the textural surface for a sand area in the top left, a textural surface for a rock area on the bottom left and images from Marine Scotland Science video trawls showing the bottom type. Reproduced from [33]

**Fig 5.6** Sidescan sonar data with sand areas ringed in yellow.

## 05/4.2 SEDIMENT SIZE DISTRIBUTION

In both wave and tidal energy extraction areas, the high energy environment means that sediment size is likely to be highly variable. Where possible, grab samples should be taken covering all mobile areas of the study area. Where this is not possible, or to supplement data campaigns, previously collected data is available: the British Geological Survey (BGS) has a database of seabed samples around the UK [28]. The BGS data has two levels of accuracy: some have a phi class- weight table from which median grain size D50 could be estimated, others only had a Folk classification [29]. For those with a Folk classification and no weights, it is suggested that D50 can be ascribed based on median values for sand, gravel and mud within the Folk classification. Similarly, for Scottish waters, Marine Scotland Science (MSS) has conducted a series of Benthic video trawls in which a seabed description is given, a value for D50 can be assigned based on the median value of the seabed descriptor on the ISO sediment scale. For example, if the seabed descriptor was 'medium sand' a grain size of 0.415 mm was assigned to that location based on the corresponding value given on the sediment scale. While clearly these two latter methods are less accurate than measured grain size, it is believed that having a better spatial coverage far outweighed the lack of accuracy. Sensitivity tests, conducted via altering assigned grain size did not affect patterns of change although magnitude was altered slightly. Once all different types of sediment size information have been collated, the data can be interpolated onto a regular grid for input into the modelling system used. Figure 5.7 shows a map of the study area with interpolated grain size and the location of the MSS video trawls and BGS point samples for the Pentland Firth. Different interpolation techniques were trialled in Matlab: it was believed that Matlab's nearest neighbour interpolation was most appropriate.

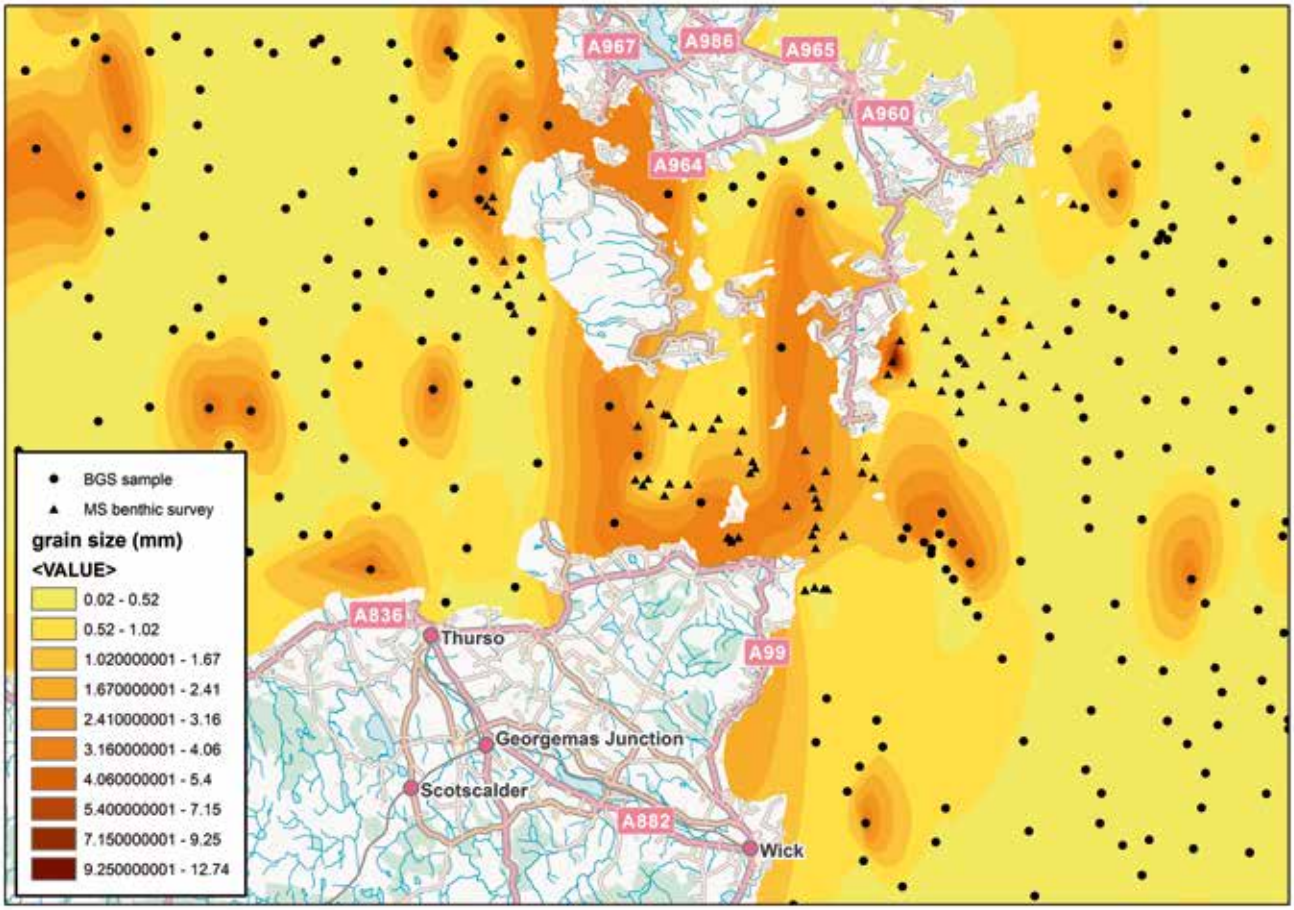


**Fig 5.7** Sediment size distribution based on BGS sediment samples and Marine Scotland Science seabed classifications for the Pentland Firth example. Reproduced from [33]

## 05/4.3 APPLICATION INTO THE NUMERICAL MODEL

Once information has been obtained on sediment size and their spatial distribution it must be input into the numerical model. Sediment size can be applied as a regular grid for DHI's MIKE model (as used in these examples). There are two options within MIKE for defining non-erodible areas: either a variable layer thickness can be assigned as a grid or an unrealistically large grain size of 9999mm (significantly greater than the threshold of motion) can be assigned to non-erodible areas. Given the lack of knowledge of sediment layer thicknesses, this second approach was utilised within the TeraWatt project.

## 05/4.4 A NOTE ON INTERTIDAL AREAS

The previous sections have focussed on sub-tidal areas: for most tidal developments it is likely that subtidal sandbanks will be the most affected, however for wave energy extraction intertidal regions are more or equally likely to be affected.

Intertidal areas can be surveyed and sediment samples taken far easier than for sub-tidal areas. Therefore, samples should be taken in areas where there are sandy foreshore sediments. It is recommended that samples are taken from both the lower- and upper- intertidal areas as well as several longshore locations to ascertain whether there ae gradients in sediment size.

Accurate Digital Terrain maps (DTM) should be surveyed prior to modelling effort. In areas where there are mixed sediment beaches, consideration must be given to defining the sand and gravel regions. It is suggested that repeat surveys are made of intertidal areas to facilitate model calibration (see Section 05/5.2). Significant seasonal variation can be observed and therefore, observations should be made both during summer and winter to develop understanding of the seasonal fluctuations. Where the mobile sediment is clearly geologically constrained estimates should be made of the sediment layer thickness.

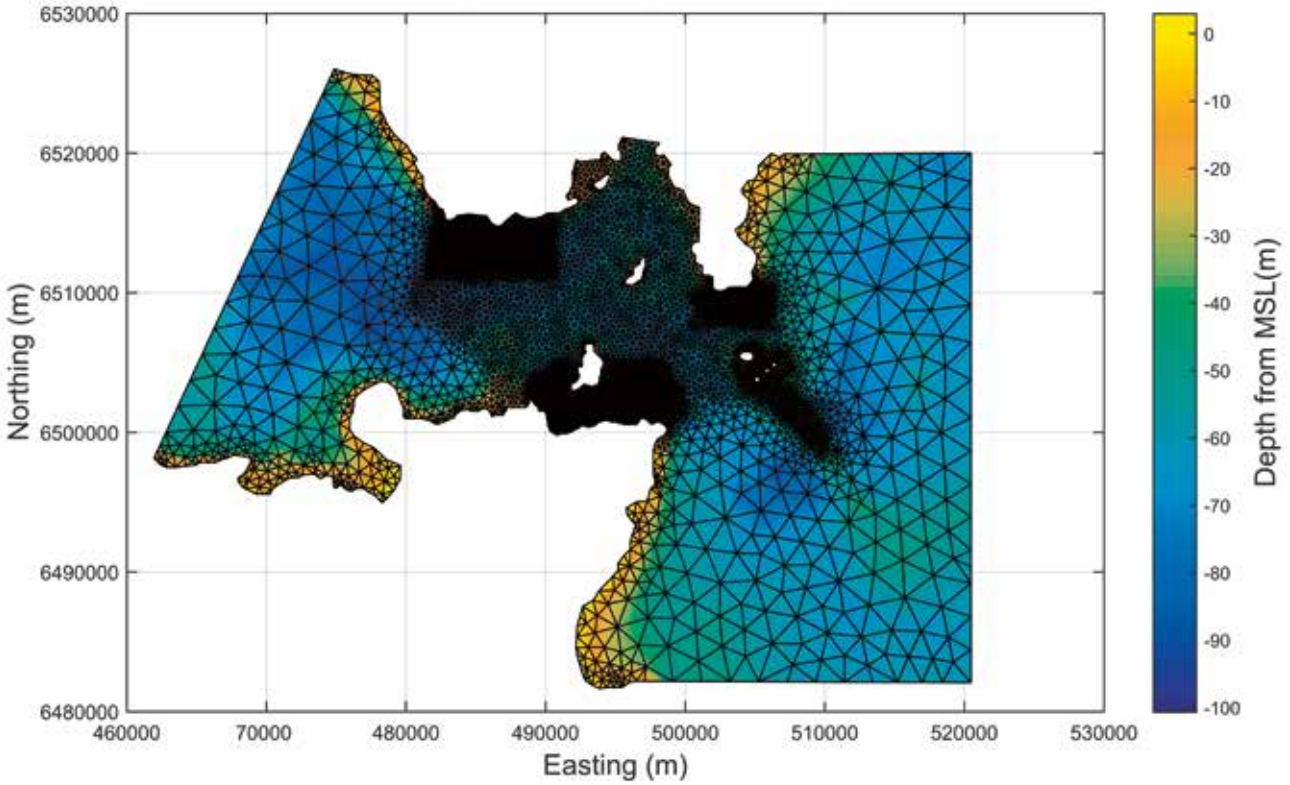


**Fig 5.8** The mesh and interpolated bathymetry used in the example study of the Pentland Firth. Reproduced from [33]

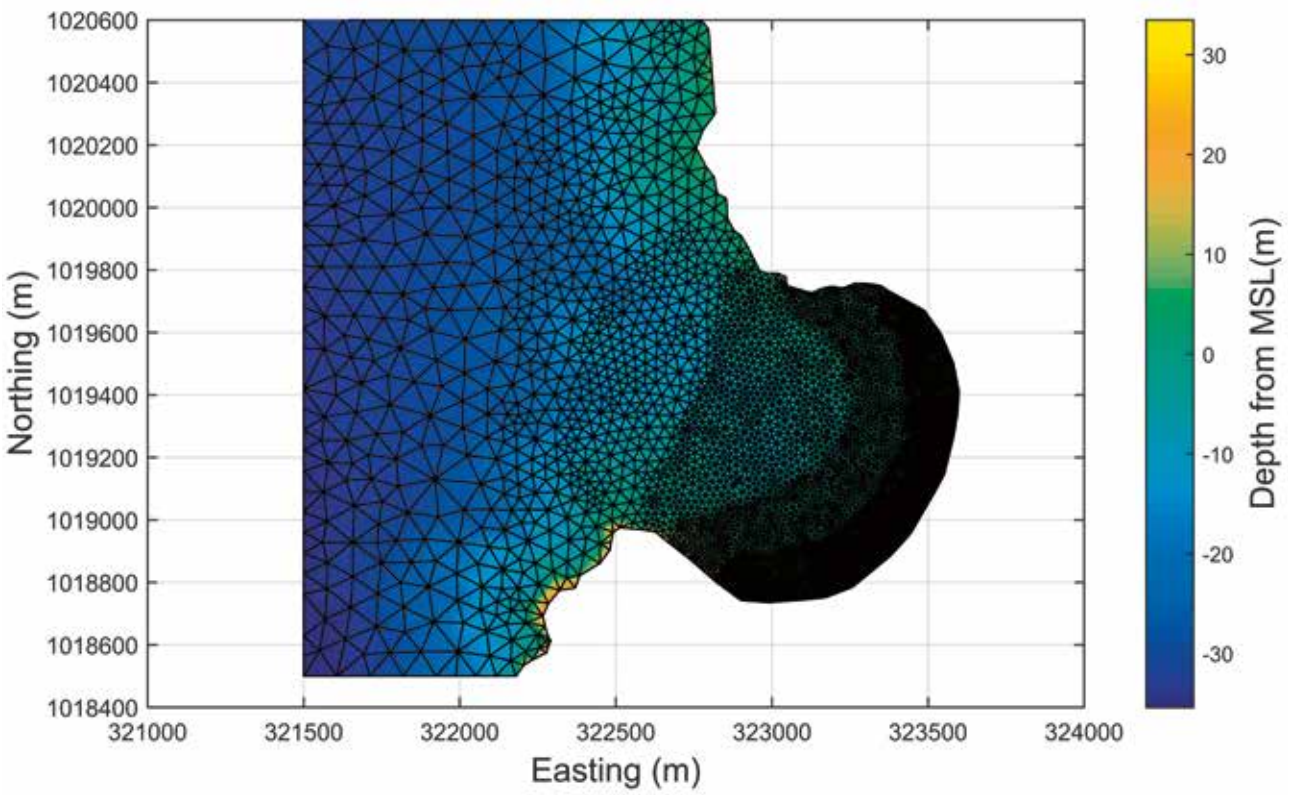


**Fig 5.9** The Mesh and interpolated bathymetry used in the Bay of Skaill study.

## 05/5 MODELLING CONSIDERATIONS

### 05/5.1 MODEL DOMAIN AND MESH

The computation expense of running three dimensional fully coupled wave, hydrodynamics and sediment transport simulations mean that care must be taken to optimise the model mesh. Modelling suites that cater for unstructured meshes are recommended since they focus computation effort on the area of interest by allowing coarser grid resolution in less important areas. Alternatively the nesting of a fine regular grid within a coarser regular grid is an approach that could be taken. For both the wave and tidal example sites, a triangular mesh was developed using DHI's MIKE mesh generator and optimised using a Matlab toolbox provided by DHI. For the tidal study, areas where turbines would be represented or areas with mobile sediment were prescribed higher grid resolution (Figure 5.8). For the Bay of Skaill wave energy extraction study, mesh resolution increased in shallower water and in the intertidal region (Figure 5.9).

Practical concerns over computational expense can also restrict the size of the model domain especially when coupled sediment transport is included. In the case of wave energy studies, unless near array impacts are a concern, it is suggested that two models should be set up: firstly a stand-alone wave model over a larger domain in which energy extraction can be implemented; secondly, a finer resolution, smaller domain size, coupled morphodynamic model for key receptor areas. Boundary conditions for the second model can then be extracted from simulations run using the larger wave model. For tidal energy extraction

studies, arguments have been made that model domains should be made as large as possible to reduce the influence of boundary effects on marine energy installation modelling [30]. If the model is intended to be run on a desktop PC, large domains are often unachievable. Confidence can be gained in the models accuracy in the undisturbed case via verification against measured current and water level data. In order to verify the applicability of a size restricted domain to cases including tidal energy extraction, it is suggested that comparison of hydrodynamic only model energy extraction results be compared against results from a hydrodynamic model with a much larger domain.

For the Pentland Firth example, the TCE model [31, 32] which was used to provide boundary conditions for the smaller domain (Figure 5.10) was run with and without turbines in place to examine differences caused by the smaller domain. A comparison is made in the difference between the baseline (no turbine case) and the model run with four tidal stream turbine arrays at peak flood and ebb currents (Figure 5.11). While there are some differences noticeable in the array near field, there are minimal changes in mean current speed difference over the mobile sediment areas of primary interest for that study and hence the domain was considered sufficiently large.

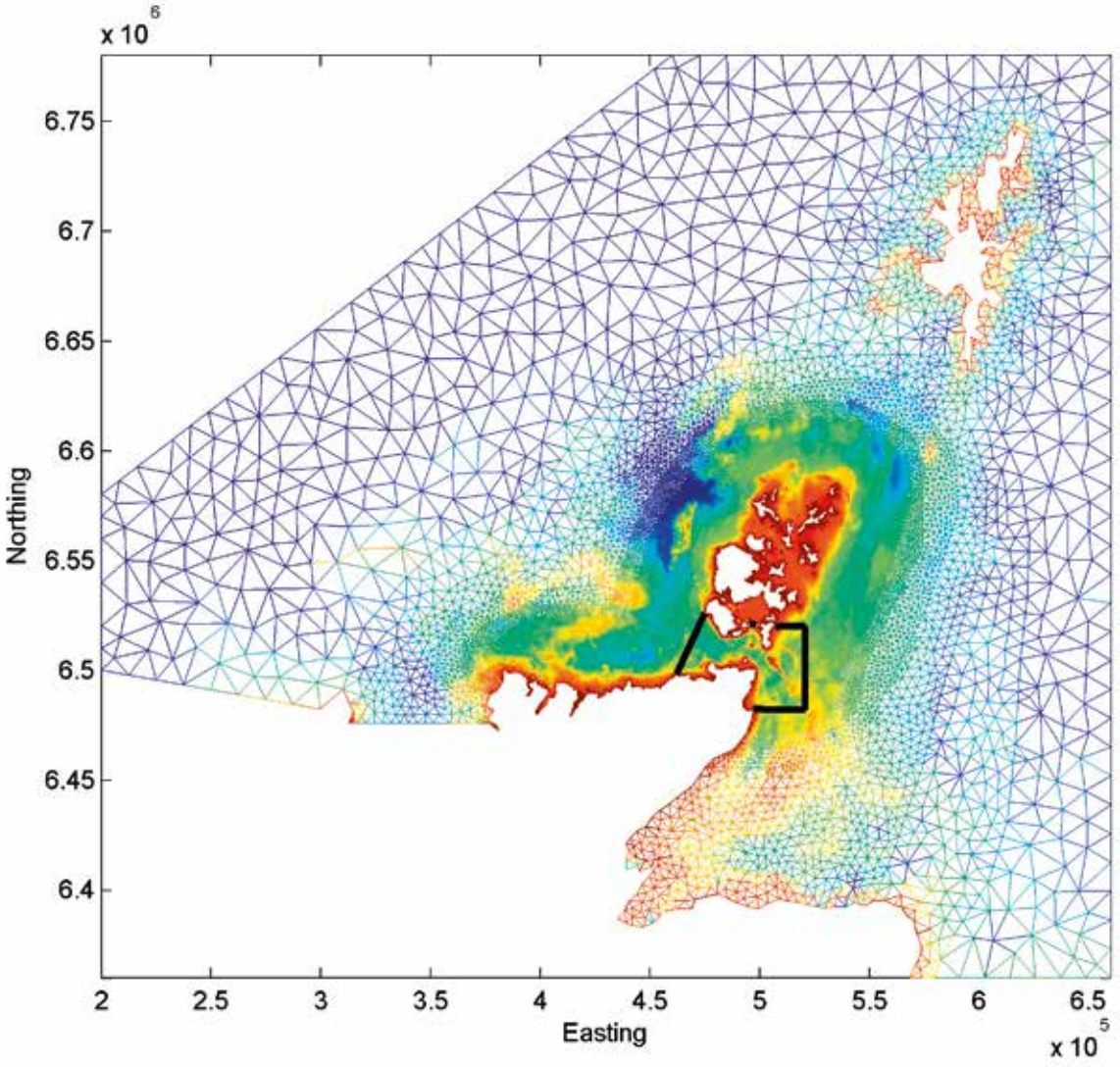


**Fig 5.10** A map showing the mesh used in the ABPmer/TCE study which was used to provide boundary conditions for our local model. The black lines indicate model boundaries for the local mesh. Reproduced from [33]

back to contents

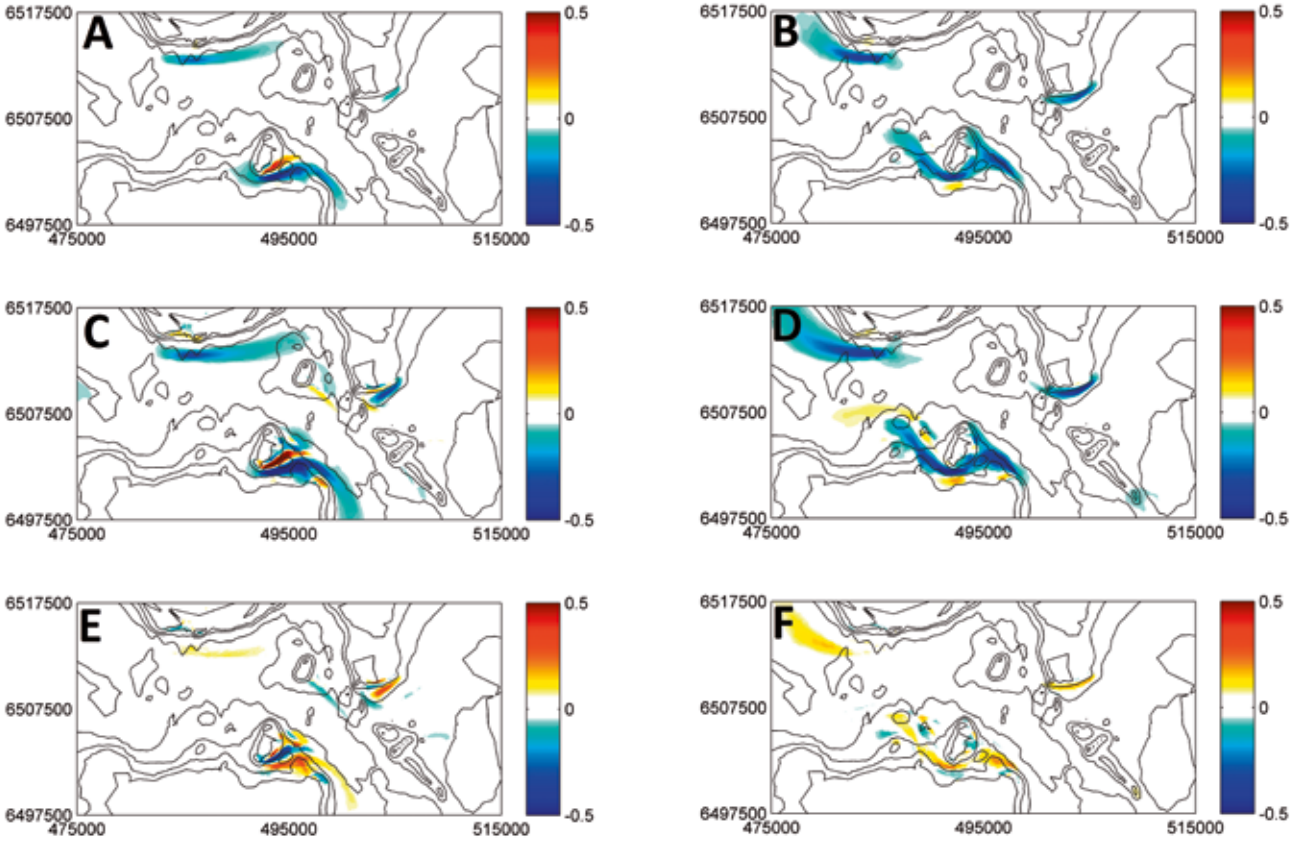


**Fig 5.11** A plot showing the difference in depth averaged current speed between the case with turbines and with no turbines for
a) the mesh used in this study on a peak spring flood current,
b) the mesh used in this study for a peak spring ebb current,
c) the TCE mesh on a peak spring flood current,
d) the TCE mesh for a peak spring ebb current,
e) the difference between the two meshes for the flood case,
f) the difference between the two cases for the ebb case.
Reproduced from [33]

back to contents

## 05/5.2 MODEL CALIBRATION AND VALIDATION

Model validation and calibration is covered within a separate TeraWatt position paper and thus only points relating to validation of the sediment transport are considered here. Before considering sediment transport or morphological change, efforts should be made to accurately replicate wave and tidal measurements. For tidal stream sites it is likely that tidal effects alone will be considered but for wave sites, tidal conditions must also be included: not only may tidal currents transport sediment in the near-shore zone but water level variations will affect the dissipation of wave energy on the beach face.

Given the resolution of numerical models, both horizontally and vertically, it is likely that calibration against point measurements of sediment transport will prove difficult. It is suggested therefore that where possible calibration against morphological change may be more fruitful. For wave energy projects, repeat intertidal surveys can be used, either cross-shore profiles or DTMs. For tidal stream sites the cost and time of multibeam surveys mean repeat measurements may not be achievable.

## 05/6 LESSONS LEARNED WITHIN THE TERAWATT PROJECT

Two key points were made evident whilst the TeraWatt project was underway. Firstly, the environments in the Pentland Firth and Orkney Waters are highly complex and not necessarily similar to the more sand-dominated environments where many sediment transport models have shown predictive success. Two tools were used to predict morphodynamic change within the Bay of Skaill: DHI's sand transport module with a coupled MIKE3 model and DHI's Litprof, a 2D crosshore profile model. Neither approach was successful in replicating measured change at the Bay of Skaill. This may be attributed to the limited amount of mobile sediment (intertidal only) and the dominance of swash zone transport. Therefore, for such complex environments it was deemed that conceptual models based on observations might be more useful.

Secondly, data availability is paramount. There has been limited previous interest in the morphodynamics of many energy extraction areas due to the lack of coastal management and engineering issues on hard geology coastlines. Therefore existing datasets are limited compared to other areas. Equally the high energy nature of these environments means that data collection is non-trivial. During the TeraWatt project an Acoustic Doppler Current Profiler deployed to collect wave and tidal data at Bay of Skaill for model calibration was lost. This meant confidence in wave and hydrodynamic conditions for the Bay of Skaill model was low. Hence sufficient time and funds must be set aside for data collection to support modelling. It is recommended that future projects might aim to provide more detailed maps of sediment in the Pentland Firth and Orkney Waters to remove the burden of such data collection from individual developers. Such maps would be beneficial to both wave and tidal developers. Equally important would be repeat multi-beam surveys to allow for increased confidence in models of sub-tidal morphodynamics related to tidal stream developments.

## 05/7 ACKNOWLEDGEMENTS

This work was supported by the EPSRC funded TeraWatt project EP/J010170/1. The authors would like to thank BGS, the Crown Estate, UKHO and Marine Scotland for the data sharing with the TeraWatt consortium.

## 05/8 REFERENCES

[1] P. F. Cummins. *On the Extractable Power from a Tidal Channel.* Journal of Waterway Port Coastal and Ocean Engineering-Asce, vol. 138, pp. 63-71, Jan-Feb 2012.

[2] Z. Defne, K. A. Haas, H. M. Fritz, L. Jiang, S. P. French, X. Shi, B. T. Smith, V. S. Neary, and K. M. Stewart. *National geodatabase of tidal stream power resource in USA.* Renewable & Sustainable Energy Reviews, vol. 16, pp. 3326-3338, Jun 2012.

[3] I. Fairley, P. Evans, C. Wooldridge, M. Willis, and I. Masters. *Evaluation of tidal stream resource in a potential array area via direct measurements.* Renewable Energy, vol. 57, pp. 70-78, Sep 2013.

[4] N. Yates, I. Walkington, R. Burrows, and J. Wolf. *Appraising the extractable tidal energy resource of the UK's western coastal waters.* Philosophical Transactions of the Royal Society a-Mathematical Physical and Engineering Sciences, vol. 371, Feb 28 2013.

[5] D. R. Plew and C. L. Stevens. *Numerical modelling of the effect of turbines on currents in a tidal channel – Tory Channel, New Zealand.* Renewable Energy, vol. 57, pp. 269-282, 2013.

[6] V. Ramos, R. Carballo, M. Alvarez, M. Sanchez, and G. Iglesias. *Assessment of the impacts of tidal stream energy through high-resolution numerical modeling.* Energy, vol. 61, pp. 541-554, Nov 2013.

[7] Z. Q. Yang, T. P. Wang, and A. E. Copping. *Modeling tidal stream energy extraction and its effects on transport processes in a tidal channel and bay system using a three-dimensional coastal ocean model.* Renewable Energy, vol. 50, pp. 605-613, Feb 2013.

[8] I. Masters, R. Malki, A. J. Williams, and T. N. Croft. *The influence of flow acceleration on tidal stream turbine wake dynamics: A numerical study using a coupled BEM-CFD model.* Applied Mathematical Modelling, vol. 37, pp. 7905-7918, Sep 1 2013.

[9] D. R. Schlezinger, C. D. Taylor, and B. L. Howes. *Assessment of Zooplankton Injury and Mortality Associated With Underwater Turbines for Tidal Energy Production.* Marine Technology Society Journal, vol. 47, pp. 142-150, Jul-Aug 2013.

[10] J. J. Waggitt and B. E. Scott. *Using a spatial overlap approach to estimate the risk of collisions between deep diving seabirds and tidal stream turbines: A review of potential methods and approaches.* Marine Policy, vol. 44, pp. 90-97, Feb 2014.

[11] S. P. Neill, E. J. Litt, S. J. Couch, and A. G. Davies. *The impact of tidal stream turbines on large-scale sediment dynamics.* Renewable Energy, vol. 34, pp. 2803-2812, Dec 2009.

[12] S. P. Neill, J. R. Jordan, and S. J. Couch. *Impact of tidal energy converter (TEC) arrays on the dynamics of headland sand banks.* Renewable Energy, vol. 37, pp. 387-397, Jan 2012.

[13] P. E. Robins, M. J. Lewis, and S. P. Neill. *Impact of tidal-stream arrays in relation to the natural variability of sedimentary processes.* Renewable Energy, vol. accepted to, 2014.

[14] MeyGen. *MeyGen Tidal Enery Project - Phase 1: Environmental Statement.* 2012.

[15] P. E. Robins, S. P. Neill, and M. J. Lewis. *Impacts of tidal-stream energy converter TEC arrays in realtion to the natural variability of sedimentary processes.* Presented at the EIMR2014, Stornoway, Scotland, 2014.

[16] M. A. Johnson, N. Kenyon, R. H. Belderson, and A. H. Stride. *Sand Transport.* In Offshore tidal sands. Processes and deposits, A. H. Stride, Ed., ed: Chapman and Hall, 1982, pp. 58-94.

[17] G. E. Farrow, N. H. Allen, and E. B. Akpan. *Bioclastic carbonate sedimentation on a high latitude, tide-dominated shelf: northeast Orkney Islands, Scotland.* Journal of Sedimentary Petrology, vol. 54, pp. 373-393, 1984.

[18] J. M. Light and J. B. Wilson. *Cool-water carbonate deposition on the West Shetland Shelf: a modern distally steepened ramp.* Geological Society, Special Publications, vol. 149, pp. 73-105, 1998.

[19] R. A. Flather. *Estimates of extreme conditions of tide and surge using a numerical model of the north-west European continental shelf.* Estuarine, Coastal and Shelf Science, vol. 24, pp. 69-93, 1987.

[20] N. H. Kenyon and B. Cooper. *Sand banks, sand transport and offshore windfarms.* 2005.

[21] J. Abanades, D. Greaves, and G. Iglesias. *Coastal defence through wave farms.* Coastal Engineering, vol. 91, pp. 299-307, Sep 2014.

[22] J. Abanades, D. Greaves, and G. Iglesias. *Wave farm impact on the beach profile: A case study.* Coastal Engineering, vol. 86, pp. 36-44, Apr 2014.

[23] N. Booij, R. C. Ris, and L. H. Holthuijsen. *A third-generation wave model for coastal regions 1. Model description and validation.* Journal of Geophysical Research C: Oceans, vol. 104, pp. 7649-7666, 1999.

[24] D. Roelvink, A. Reniers, A. Van Dongeren, J. Van Theil de Vries, R. McCall, and J. Lescinski. *Modelling storm impacts on beaches, dunes and barrier islands.* Coastal Engineering, vol. 56, pp. 1133-1152, 2009.

[25] E. Mendoza, R. Silva, B. Zanuttigh, E. Angelelli, T. Lykke Andersen, L. Martinelli, J. Q. H. Nørgaard, and P. Ruol. *Beach response to wave energy converter farms acting as coastal defence.* Coastal Engineering, vol. 87, pp. 97-111, 2014.

[26] K. I. Ahmed and U. Demsar. *Improving seabed classification from Multi-Beam Echo Sounder (MBES) backscatter data with visual data mining.* Journal of Coastal Conservation, vol. 17, pp. 559-577, Sep 2013.

[27] A. Micallef, T. P. Le Bas, V. A. I. Huvenne, P. Blondel, V. Huehnerbach, and A. Deidun. *A multi-method approach for benthic habitat mapping of shallow coastal areas with high-resolution multibeam data.* Continental Shelf Research, vol. 39-40, pp. 14-26, May 15 2012.

[28] *BGS Legacy Particle Size Analysis uncontrolled data export (2013).* British Geological Survey, www.bgs.ac.uk.

[29] R. L. Folk, P. B. Andrews, and D. W. Lewis. *Detrital sedimentary rock classification and nomenclature for use in New Zealand.* New Zealand Journal of Geology and Geophysics, vol. 13, pp. 937-968, 1970.

[30] T. A. A. Adcock, A. G. L. Borthwick, and G. T. Houlsby. *The open boundary problem in tidal basin modelling with energy extraction.* Presented at the EWTEC, Southampton, 2011.

[31] G. R. Osborn, C. L. Hinton, and W. S. Cooper. *Pentland Firth and Orkney Waters Hydrodynamic Modelling: Model Calibration.* ABPmer / The Crown Estate R.1935, 2012.

[32] G. R. Osborn, C. L. Hinton, and W. S. Cooper. *Pentland Firth and Orkney Waters Strategic Area: Marine Energy Resources.* ABPmer / The Crown Estate R.1936, 2012.

[33] Fairley I, Masters I, Karunarathna H. *The cumulative impact of tidal stream turbine arrays on sediment transport in the Pentland Firth.* Renewable Energy 80:755-769. 2015

# USE OF OCEAN COLOUR REMOTE SENSING TO MONITOR SEA SURFACE SUSPENDED SEDIMENTS

06

A.D. Sabatino[1], R. Clement[2], M.R. Heath[1] and D. McKee[2]

1 DEPARTMENT OF MATHEMATICS AND STATISTICS,
UNIVERSITY OF STRATHCLYDE, 16 RICHMOND STREET, GLASGOW, G1 1XQ

2 DEPARTMENT OF PHYSICS,
UNIVERSITY OF STRATHCLYDE, 16 RICHMOND STREET, GLASGOW, G1 1XQ

JULY 2015: REVISION 1

back to contents

## 06/1 INTRODUCTION

Ocean colour remote sensing (OCRS) from satellite platforms has revolutionised our ability to monitor the interplay of physical and biogeochemical processes in surface waters of the ocean. Since the launch of SeaWiFS in 1996, a continuous time series of OCRS data has been accumulated from a series of satellite sensors giving near daily global coverage. These sensors measure top of atmosphere (TOA) spectral radiance which is corrected for atmospheric effects (~80% of the measured signal in the blue – Gordon 1978) to give water leaving radiances. From these purely optical signals, it is possible to derive a wide range of higher level products such as chlorophyll concentration, diffuse attenuation coefficients, photosynthetically available radiation (PAR) and a wide range of inherent optical properties (IOPs) to name but a few.

In terms of surface area and primary productivity, the global ocean is heavily dominated by deep, oceanic waters, where the optical properties are driven by phytoplankton, associated dissolved organics and water itself. It is little surprise then that early standard OCRS products were developed for optimal performance over these globally significant regions. Standard chlorophyll algorithms were developed using changes in blue-green reflectance ratios (e.g. O'Reilley et al., 1998) that can be related to the effect of changing concentrations of microscopic scale (1µm-200µm) phytoplankton (Kirk,1983) forming blooms that can stretch for thousands of km. More recently, attention has shifted to economically important coastal regions where, for example, harmful algal blooms have potential to cause significant societal and economic impact. OCRS algorithms have been developed to specifically aid in the monitoring of both toxic species e.g. *Karenia brevis* in the Gulf of Mexico (Stumpf et al., 2003), and also to monitor for extreme eutrophication events where excessive levels of phytoplankton cause the reduction of oxygen dissolved in the water column (hypoxia) leading to animal mortality (e.g. Mallin et al., 2006).

The optically complex nature of coastal waters, more generally, presents a particular problem for OCRS applications in these regions. Shallow shelf seas and other inshore waters are subject to the influence of sediment resuspension and freshwater discharge bringing additional loads of coloured dissolved organic materials (CDOM). This results in multiple, independently varying, optically significant components, each of which influences the water leaving radiance spectrum making interpretation of spectral changes significantly more difficult. Many studies have demonstrated the breakdown in performance of standard algorithms (e.g. Chl, McKee et al. 2007) in optically complex coastal waters.

In this paper we will focus on the effect of suspended sediment on optical properties of the water column. Suspended sediment has long been known to influence light penetration (Gordon and McCluney, 1975) which can limit primary production and also contribute to hypoxia (Greig et al., 2005). There is interest in monitoring sediment concentration for coastal erosion applications and various OCRS algorithms have been developed that exploit the relatively strong backscattering properties of sediment. For example, Doxaran et al. (2002) successfully presented a sediment algorithm for the highly turbid Gironde estuary. More recently a radiative transfer approach was used to refine this type of approach to incorporate the potential impact of other materials on the red reflectance values that support sediment algorithms (Neil et al., 2011). This algorithm provides estimates of maximum and minimum sediment load concentrations assuming reasonable potential ranges of Chl and CDOM for coastal waters. The aim of this paper is to determine the extent to which the Neil et al. algorithm, which was developed for Irish Sea waters, can be applied to data collected in the North Sea. The ultimate goal is to assess the potential for using OCRS data to monitor suspended sediment concentrations in coastal waters, with monitoring marine turbine arrays an obvious and potentially important application.

## 06/2 OCEAN COLOUR REMOTE SENSING: FUNDAMENTAL CONCEPTS

### 06/2.1 WHAT DOES AN OCEAN COLOUR SATELLITE MEASURE?

Ocean colour is given by the spectral reflectance R at the sea surface for a given wavelength $\lambda$. This radiance reflectance, $R$, can be related to two inherent optical properties of the water column, the absorption $a(\lambda)$ and the backscattering $b_b(\lambda)$ (Sathyendranath et al., 1989).

$$R = f(a, b_b) \quad (1)$$

where the back scattering coefficient can be expressed as:

$$b_b = \int_{\pi/2}^{\pi} \beta(\theta) \sin\theta \, d\theta \quad (2)$$

and $\beta(\theta)$ is the volume scattering function at the angle $\theta$. However, what OCRS satellites actually measure is the radiance at the top of the atmosphere, $L_t(\lambda)$, which includes photons scattered from within the sea, the sea surface and by aerosols and molecules in the atmosphere. The TOA radiance can be expressed as (Chen and Lu, 2009):

$$L_t(\lambda) = L_r(\lambda) + L_a(\lambda) + L_{ra}(\lambda) + T(\lambda)L_g(\lambda) + L_b(\lambda) + t(\lambda)L_{wc}(\lambda) + t(\lambda)(1-w)L_w(\lambda) \quad (3)$$

where the terms in the equation are:

- $L_r(\lambda)$ Rayleigh scattering radiance.
- $L_a(\lambda)$ Aerosol scattering radiance.
- $L_{ra}(\lambda)$ Multiple scattering between Rayleigh and aerosol radiances.
- $T(\lambda)$ Direct transmittance of the atmosphere or Beam Transmittance.
- $L_g(\lambda)$ Contribution from specular reflection of direct sunlight from the sea surface (sun glitter).
- $L_b(\lambda)$ Radiance from the bottom of the water.
- $t(\lambda)$ Diffuse transmittance between sea surface and sensor.
- $L_{wc}(\lambda)$ Contribution from sunlight and skylight reflecting by wave white capping.
- $w$ Covering rate of whitecaps
- $L_w(\lambda)$ Water-leaving radiance.

By carefully constraining sun-sensor angles, view angles and by making a number of reasonable assumptions (Gordon and Wang, 1992; 1994a; Robinson et al., 2000), it is possible to simplify Eq 3 to:

$$L_t(\lambda) = L_r(\lambda) + L_a(\lambda) + t(\lambda)L_w(\lambda) \quad (4)$$

The reflectance and the radiance are related by:

$$L_t(\lambda) = \frac{R(\lambda)F_0(\lambda)\cos\theta_0}{\pi} \quad (5)$$

where $L_t(\lambda)$ is the total radiance received by the sensor, $F_o$ is the extra-terrestrial solar irradiance at a wavelength $\lambda$ and $\theta_0$ is the solar zenith angle. Given this relationship, it is possible to express Eq 4 in terms of reflectance rather than radiance as follows:

$$R_t(\lambda) = R_r(\lambda) + R_a(\lambda) + t(\lambda)R_w(\lambda) \quad (6)$$

in which the $R_w$ term takes in account of corrections due to whitecapping, gas absorption, glitter and multiple scattering (Ruddick et al., 2000):

$$R_w(\lambda) = \frac{R_c(\lambda) - R_{am}(\lambda)}{t(\lambda)} \quad (7)$$

where $R_c$ is the Rayleigh corrected reflectance, that can be written (Goyens et al., 2013):

$$R_c(\lambda) = R_t(\lambda) - R_r(\lambda) - t_v(\lambda)R_{wc}(\lambda) \quad (8)$$

while $R_{am}$ is the multiple scattering term and is defined as:

$$R_{am}(\lambda) = R_a(\lambda) + R_{ra}(\lambda) \quad (9)$$

The TOA radiance signal is heavily dominated by the contributions from atmospheric scattering (~80%). For algorithms that require accurate estimates of water leaving radiance or surface remote sensing reflectance, it is therefore essential that an appropriate atmospheric correction is performed.

## 06/2.2 ATMOSPHERIC CORRECTION (AC)

Early atmospheric correction algorithms assumed that the water-leaving radiance term $(L_w)$ was zero for wavelengths in the near-infrared $(NIR)$. The so-called 'black pixel' approximation was based on the idea that absorption by water was sufficiently strong at NIR wavelengths that photons entering the water would not be reflected back. If true, equation (7) would reduce to:

$$R_{am}(NIR) = R_C(NIR) \quad (10)$$

With the implication that the multiple scattering term for NIR wavelengths is equal to the Rayleigh corrected reflectance, allowing selection of a suitable aerosol model that could be extrapolated to visible wavelengths in order to complete the correction.

However the black pixel approximation is not valid for turbid coastal waters where strong backscattering from suspended sediments is sufficient to ensure that some NIR photons that enter the water column are reflected, resulting in a non-zero water leaving radiance in the NIR (Ruddick et al, 2000; Dall'Olmo et al., 2005). Various AC approaches have been developed for operations over turbid waters. The improved NIR model for standard NASA ocean colour data processing uses an iterative approach that begins by assuming zero water leaving radiance in the NIR, generating a visible $L_w$ spectrum that is used to estimate an initial $Chl$ value. This data is fed into a bio-optical model that gives a new value of $L_w$ in the NIR and the algorithm iterates until the chlorophyll concentration is within 20% of the previous iteration, up to a maximum of four iterations, after which it terminates (Bailey et al., 2010; Stumpf et al., 2003). This algorithm was designed for operation in open ocean and coastal waters dominated by phytoplankton, but is known to perform poorly in coastal waters where sediment contributes strongly to the water leaving radiance signal.

An alternative, the MUMM atmospheric correction algorithm (Ruddick et al., 2000) was specifically designed for operation over highly turbid coastal waters and is built on two main assumptions: 1) the atmosphere composition does not vary significantly spatially within a reasonably sized scene, and 2) total absorption in the NIR region is largely determined by pure water absorption, which is invariant. The algorithm allows the user to choose two calibration parameters: the aerosol reflectance ratio, $\varepsilon$, and the water leaving reflectance ratio, $\alpha$, where these ratios are defined as:

$$\varepsilon^{(7,8)} \equiv \frac{R_{am}^{(7)}}{R_{am}^{(8)}} \quad (11)$$

$$\alpha \equiv \frac{a_w^{(8)}}{a_w^{(7)}} \quad (12)$$

and $R_{am}^{(i)}$ is the multiple-scattering aerosol reflectance at waveband $i$, and $a_w(i)$ is the pure water absorption coefficient at waveband $i$. Wavebands 7 and 8 for MODIS correspond to wavelengths of 748 and 869 nm respectively, in NIR region. These parameters are used to select an appropriate aerosol model for extrapolation into the visible.

## 06/2.3 AEROSOL MODELS

Having used the first part of the AC procedure to determine $R_{am}$ in the NIR region, and using this to establish $\varepsilon$, the two closest aerosol models are chosen from a look-up table. Various aerosol models have been proposed (Antoine and Morel, 2011; Gohin et al., 2002; Gordon and Wang, 1994b; Shettle and Fenn, 1979; Wang, 2000):

- Oceanic: This model has the lowest value of $\varepsilon$ of all the models available in SeaDAS.
- Tropospheric: This model has no oceanic contributions. It represents the particles that are present above the boundary layer, that are not as easily affected by local sources. And has a very high value of $\varepsilon$ compared to the other models.
- Maritime: 99% of the particles in this model have tropospheric characteristics, and 1% oceanic. Refraction and particle radius depend on the relative humidity. The value of $\varepsilon$ for this model is close to 1.

- Coastal: 99.5% of the particles in this model have tropospheric characteristics, and 0.5% oceanic. Refraction and particle radius depend on the relative humidity. The value of $\varepsilon$ for this model is typically quite high.

Each of these models depends on the wavelength and relative humidity. Having selected an appropriate aerosol model, the atmospheric correction process is completed by using the aerosol model to extrapolate NIR atmospheric signals into the visible where they can be subtracted from the TOA signal, leaving the desired water-leaving signal as the residual.

## 06/2.4 OCRS DATA SOURCE AND PROCESSING TOOLS

The Ocean Biology Processing Group (OBPG) at NASA's Goddard Space Flight Center maintains a database of OCRS data (Ocean Color Web) for a series of sensors going all the way back to CZCS (starts 1978, with gap from 1986 when CZCS stopped to 1996 when SeaWiFS started). NASA provides free access to the historic time series. The SeaWiFS Data Analysis System (SeaDAS) software was developed by NASA (Fu et al., 1998) for processing data from this source.

## 06/3 SUSPENDED SEDIMENT ALGORITHM

The remote sensing reflectance, $R_{rs}(\lambda)$, is defined as (Mobley, 1994):

$$R_{rs}(\lambda) = \frac{L_u(\lambda)}{E_d(\lambda)} \quad (13)$$

where $L_u$ is the upwelling radiance above the surface and $E_d$ is the downwelling irradiance above the surface, both at a given wavelength $\lambda$. $L_u$ can be related to the water-leaving radiance, $L_w$, as follows (Austin, 1980):

$$L_w = 0.544\, L_u \quad (14)$$

As discussed above, $R_{rs}$ can also be related to the ratio of backscattering to absorption (Kirk, 1994):

$$R_{rs} \approx \kappa \frac{b_b}{a} \quad (15)$$

where $\kappa$ is not exactly a constant of proportionality, but can be treated as such for conditions relevant for satellite ocean colour remote sensing.

Total backscattering and absorption coefficients can be modelled as consisting of components due to water, phytoplankton $(Chl)$ and mineral suspended solids $(MSS)$, with absorption including an additional term due to CDOM which is assumed to be non-scattering (Mobley, 1999; Kirk, 1994). $R_{rs}$ can therefore be related to optical constituents via:

$$R_{rs} \approx \frac{b^*_{b\,W} + b^*_{b\,MSS} MSS + b^*_{b\,CHL} CHL}{a_W + a^*_{MSS} MSS + a^*_{CHL} CHL + a^*_{CDOM} CDOM} \quad (16)$$

where the $a^*$ and $b_b{}^*$ parameters are concentration-specific IOPs. Absorption at red / NIR wavelengths is dominated by the component due to water for most natural waters, except for extremely turbid waters where the component due to $MSS$ can become significant or even dominate. High levels of $MSS$ in turbid coastal waters results in $MSS$ dominating the backscattering signal. Neil et al. (2011) performed a radiative transfer simulation study with realistic values of specific IOPs for UK coastal waters (McKee and Cunningham, 2006) and demonstrated the well known relationship between red remote sensing reflectance and $MSS$ for moderately turbid waters. Importantly, however, they also demonstrated the potential impact of $Chl$ and $CDOM$ on the relationship between $R_{rs}667$ and $MSS$, leading to development of an algorithm that estimates upper and lower bounds for $MSS$ for a given $R_{rs}667$ value. These bounds are based upon reasonable assumptions of the maximum impact of other constituents for typical UK coastal water concentration ranges. The resulting relationships were found:

$$MSS_{(u)} = 26014 \times (R_{rs}667)^2 + 916 \times (R_{rs}667) - 0.13 \quad (17)$$

$$MSS_{(l)} = 2508 \times (R_{rs}667)^2 + 768 \times (R_{rs}667) - 0.77 \quad (18)$$

A subsequent study highlighted the possibility of using this algorithm to investigate physical processes such as the onset and break down of stratification in shallow shelf seas using ocean colour remote sensing (Neil et al., 2012).

## 06/4 ALGORITHM VALIDATION AND APPLICATION FOR THE EAST COAST OF SCOTLAND

The Neil et al. (2011) sediment algorithm was developed using SIOPs obtained in the Irish Sea and other west coast areas. Before it can be routinely applied to other areas, it is necessary to perform a local validation to ensure that it provides reasonable estimates for the region of interest where there is potential for SIOPs to be significantly different. The algorithm was applied to MODIS data downloaded directly from NASA GSFC and processed in SeaDAS using the improved NIR and MUMM atmospheric correction algorithms (separately). All available clear sky images for the east coast of Scotland between 2008 and 2011 were identified, downloaded and processed, with a 5 x 5 pixel array centred on the main Marine Scotland sampling site off Stonehaven selected for subsequent analysis. OCRS sediment concentrations were compared with data from vertical profiles of turbidity (Formazine Turbidity Units (FTU), proportional to SPM ($g.m^{-3}$)) which were measured at 0.5m depth intervals and up to weekly intervals over the period 2008-2011 (Bresnan et al. 2008, Serpetti et al. 2012, Serpetti 2012; Heath et al., subm. a, Heath et al., subm b.). Figures 6.1 and 6.2 show preliminary results which indicate that there is good correspondence between OCRS estimates of sediment concentration using the Neil et al. algorithm and in situ measurements of turbidity (Clement 2014). The choice of atmospheric correction does have an impact on individual OCRS data points, but the overall picture is broadly similar. Further analysis is required to determine which AC approach provides the best match with in situ data (work currently in progress).

Figures 6.3-6.6 show seasonally averaged upper bound $MSS$ distributions for the east coast of Scotland. Sediment levels are generally low for offshore waters, with levels decreasing further in summer and autumn when thermal stratification occurs and tidally stirred sediment does not reach surface waters. High sediment concentrations are restricted to a narrow region close to shore in autumn – spring, but even this diminishes significantly in summer. The tidal basin at Montrose appears to be a candidate source for enhanced local sediment concentrations. Figures 6.7 and 6.8 show the difference in upper bound $MSS$ estimates for choice of atmospheric correction algorithm by season. In both cases the maximum difference is approximately 2 g $m^{-3}$ with the spring data showing greater variation than autumn. Although these differences are not massive, there is clearly an imperative to establish an optimal data processing scheme that may require an adaptive approach that varies by season or even on a pixel-by-pixel basis.

## 06/5 CONCLUSIONS

This study has presented a preliminary demonstration of ability to observe spatial and temporal patterns of variability in sediment distributions from OCRS data. Further work is required to refine the data processing steps and to establish robust error budgets for the OCRS sediment products. In associated TeraWatt position papers, Heath et al. (submitted a and b) propose an algorithm based on in situ data to predict suspended sediments from a set of physical variables. OCRS data could be useful for assimilation into and validating this model. The next step will be to prepare monthly mean and seasonal maps of sediment distributions for the Pentland Firth area to support establishment of baseline properties for areas where tidal stream renewables arrays will be located. It is anticipated that these may prove useful in demonstrating the impact (or otherwise) of such arrays on sediment loading and associated light field parameters.

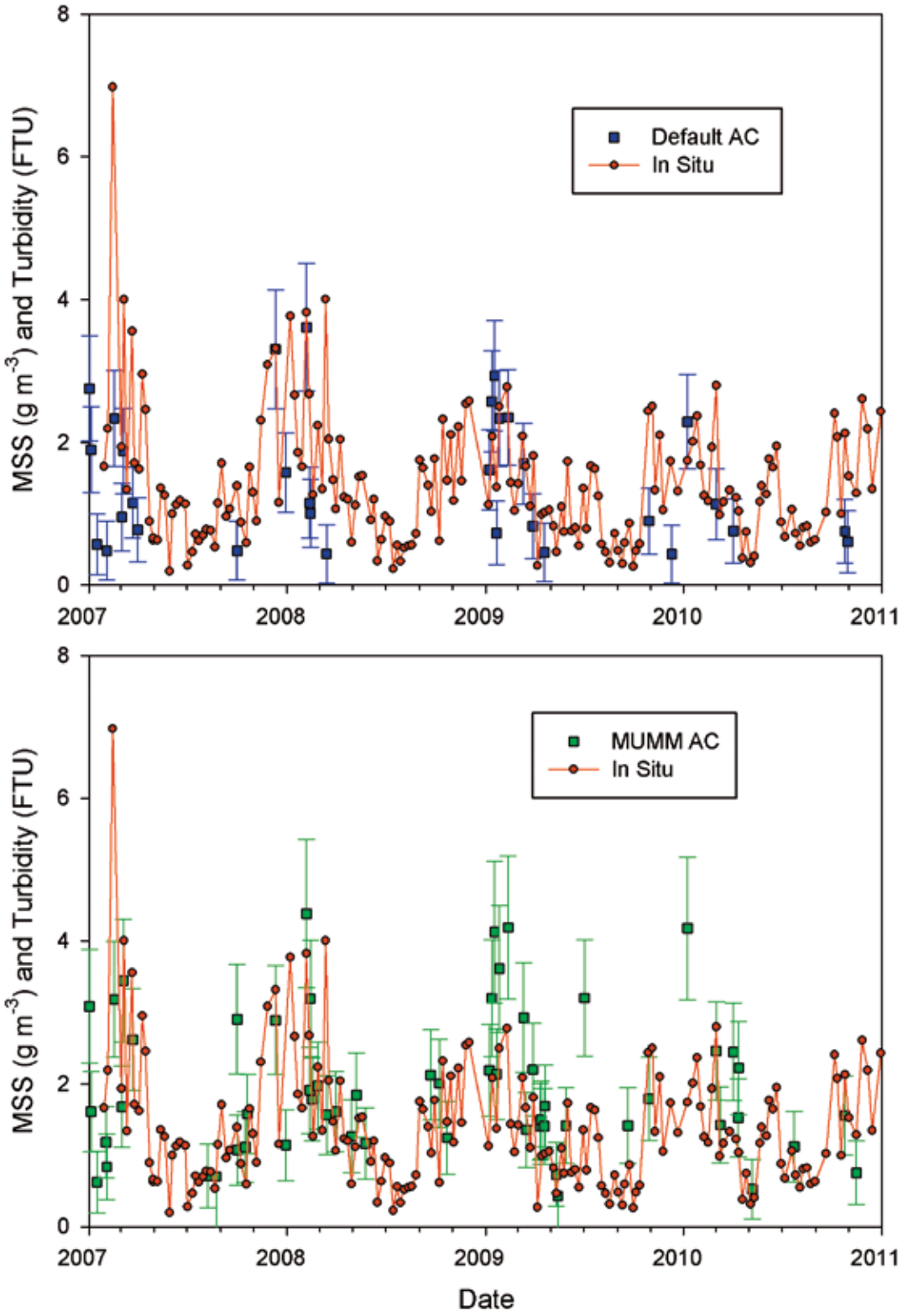


**Fig 6.1 & 6.2** Time series data for the different AC algorithms applied. The top time series (Figure 6.1) shows the satellite-derived MSS levels from using the default AC algorithm, represented by the error bars to show the upper and lower bounds of these levels. The bottom time series (Figure 6.2) has the MUMM AC algorithm applied to the MSS data, where it is represented by green error bars to show the upper and lower bounds. Figures adapted from Clement (2014).

back to contents

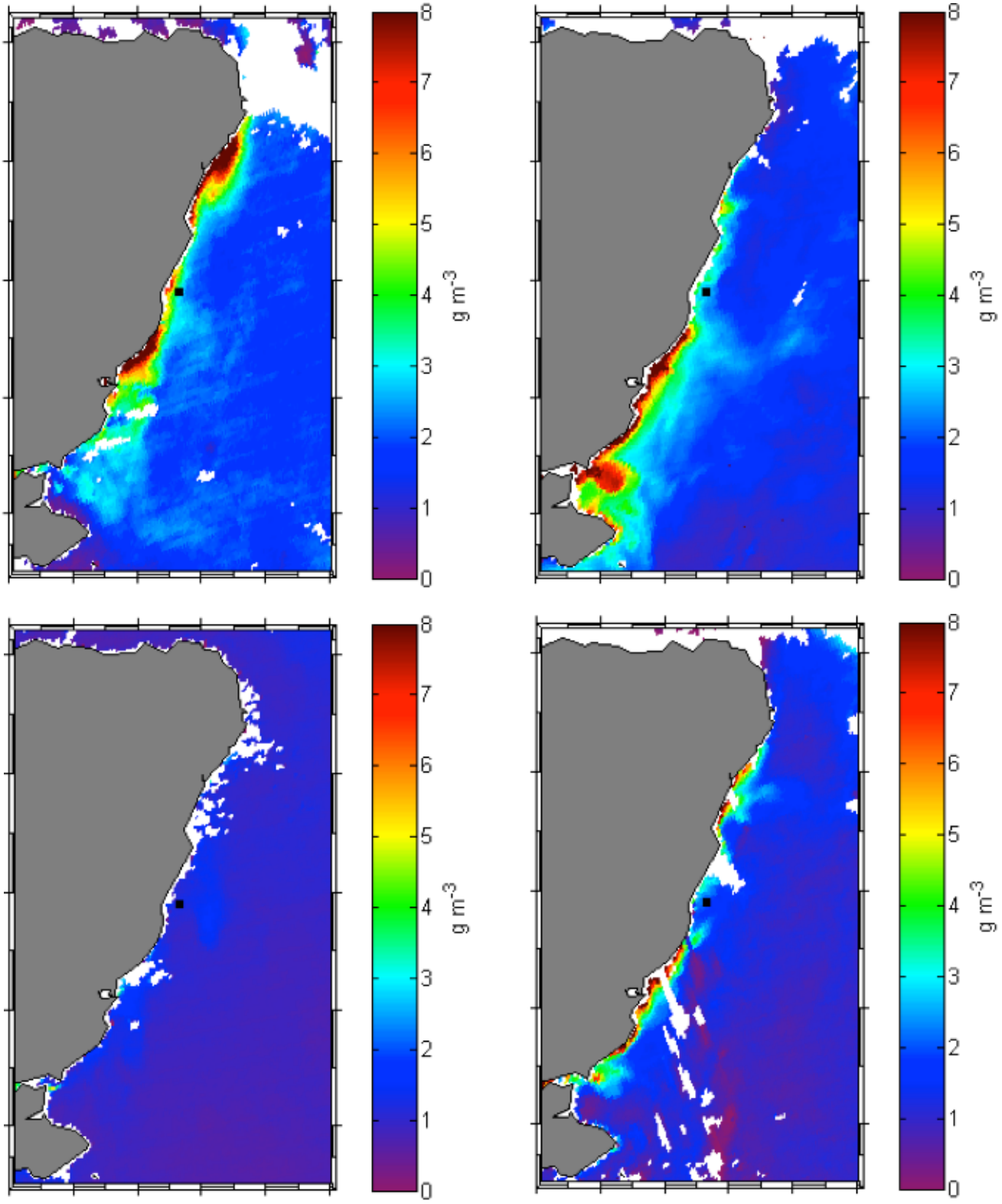


**Fig 6.3 - 6.6** Seasonal variation in the MSS upper level.
Figure 6.3 Top left – winter (02/01/2007),
Figure 6.4 Top right – spring (29/03/2009),
Figure 6.5 Bottom left – summer (08/08/07) and
Figure 6.6 Bottom right – autumn (25/10/10).
These were produced with the MUMM AC algorithm (average $\varepsilon$ used = 0.9825). Figures from Clement (2014).

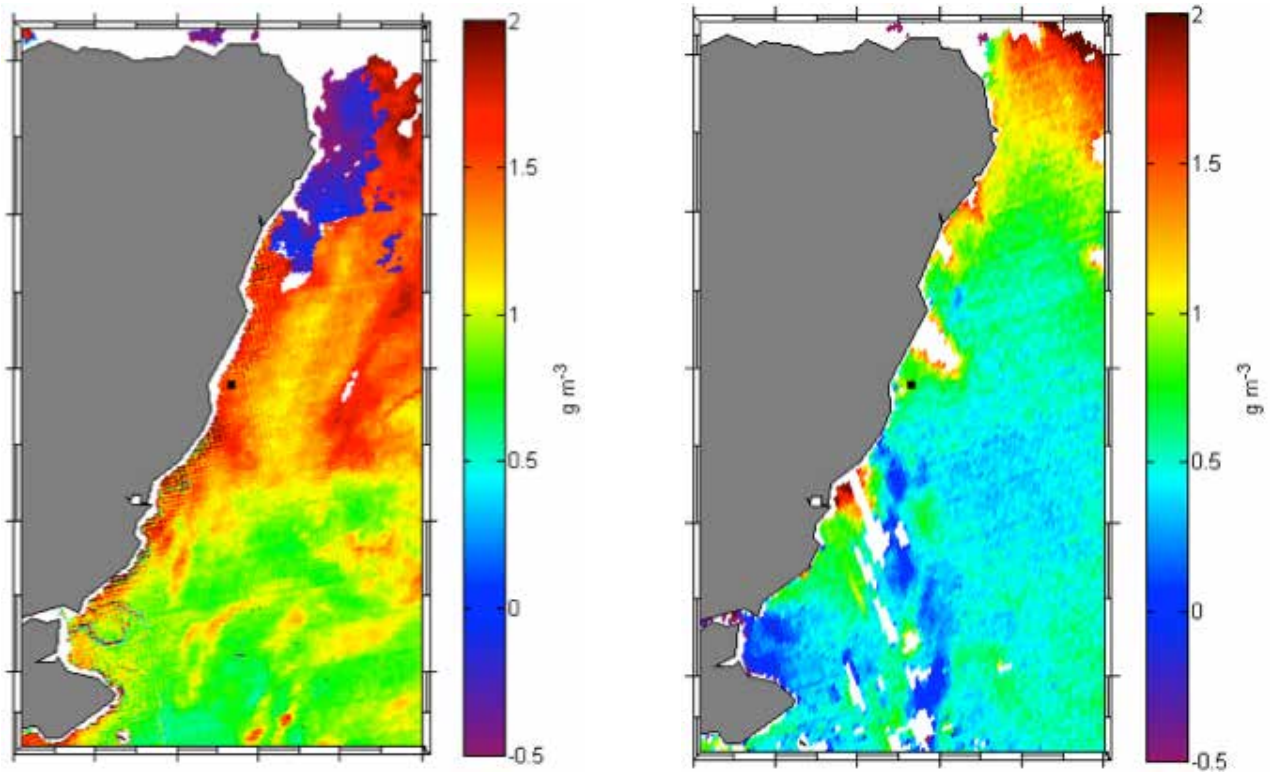


**Fig 6.7 & 6.8** Difference in MSS level for the upper bound, for the MUMM and default AC algorithms.
Figure 6.7: Left – spring difference (29/03/2009)
Figure 6.8: Right – autumn difference (25/10/10). Figure from Clement (2014).

## 06/6 REFERENCES

Antoine, D., Morel, A. (2011). *MERIS ATBD 2.7 - Atmospheric Correction of the MERIS observations Over Ocean Case 1 waters*. [report] Laboratoire D'Océanographie De Villefranche.

Austin, R. (1980). *Gulf of Mexico, ocean-color surface-truth measurements.*Boundary-Layer Meteorology, 18 (3), pp. 269-285.

Bailey, S. W., Franz, B. A., Werdell, P. J. (2010). *Estimation of near-infrared water-leaving reflectance for satellite ocean color data processing.* Optics Express, 18 (7), pp. 7521-7527.

Bresnan, E., Hay, S., Hughes, S.L., Fraser, S., Rasmussen, J., Webster, L., Slesser, G., Dunn, J., Heath, M.R. 2008. Seasonal and interannual variation in the phytoplankton community in the north east of Scotland. Journal of Sea Research 61, 17-25.

Chen, X., Lu, Z. (2009). *Remote sensing of water environment.* In: Li, D., Shan, J., Gong, J. eds. (2009). Geospatial technology for earth observation. New York: Springer, pp. 431-471.

Clement, R. (2014). *Mapping Marine Sediments from Space for Renewable Energy Applications.* PH450 Project Report.

Dall'Olmo, G., Gitelson, A. A., Rundquist, D. C., Leavitt, B., Barrow, T., Holz, J. C. (2005). *Assessing the potential of SeaWiFS and MODIS for estimating chlorophyll concentration in turbid productive waters using red and near-infrared bands.* Remote Sensing of Environment, 96(2), 176-187.

Doxaran, D., Froidefond, J. M., Lavender, S., Castaing, P. (2002). *Spectral signature of highly turbid waters: Application with SPOT data to quantify suspended particulate matter concentrations.* Remote sensing of Environment, 81(1), 149-161.

Fu, G., Baith, K. S., McClain, C. R. (1998). *SeaDAS: The SeaWiFS data analysis system.* In Proceedings of the 4th Pacific Ocean remote sensing conference, Qingdao, China (pp. 28-31).

Gohin, F., Druon, J., Lampert, L. (2002). *A five channel chlorophyll concentration algorithm applied to SeaWiFS data processed by SeaDAS in coastal waters.* International Journal Of Remote Sensing, 23 (8), pp. 1639-1661.

Gordon, H. R., McCluney, W. R. (1975). *Estimation of the sunlight penetration in the sea for remote sensing.* Applied Optics, 14, 413 – 416.

Gordon, H. R. (1978). *Removal of atmospheric effects from satellite imagery of the oceans.* Applied Optics, 17, 1631-1636.

Gordon, H. R., Wang, M. (1994a). *Influence of oceanic whitecaps on atmospheric correction of ocean-color sensors.* Applied Optics, 33 (33), pp. 7754-7763.

Gordon, H. R. , Wang, M. (1994b). *Retrieval of water-leaving radiance and aerosol optical thickness over the oceans with SeaWiFS: a preliminary algorithm.* Applied Optics, 33 (3), pp. 443-452.

Gordon, H. R., Wang, M. (1992). *Surface-roughness considerations for atmospheric correction of ocean color sensors. I: The Rayleigh-scattering component*. Applied Optics, 31 (21), pp. 4247-4260.

Goyens, C., Jamet, C., Schroeder, T. (2013). *Evaluation of four atmospheric correction algorithms for MODIS-Aqua images over contrasted coastal waters.* Remote Sensing Of Environment, 131, pp. 63-75.

Greig, S. M., Sear, D. A., Carling, P. A. (2005). *The impact of fine sediment accumulation on the survival of incubating salmon progeny: implications for sediment management.* Science of the Total Environment, 344(1), 241-258.

Heath, M.R., Sabatino, A.D., O'Hara Murray, R.B. (submitted a). *Scoping the impact of tidal and wave energy extraction on suspended sediment concentrations and underwater light climate.*

Heath, M.R., Sabatino, A.D., McCaig, C., O'Hara Murray, R.B. (submitted b). *Modelling spatial and temporal patterns of turbidity off the east coast of Scotland.*

Kirk, J. T. O. (1983). *Light and photosynthesis in aquatic ecosystems.* Cambridge [England]: Cambridge University Press.

Kirk, J. T. O. (1994). *Light and photosynthesis in aquatic ecosystems (2nd edition).* Cambridge [England]: Cambridge University Press.

Mallin, M. A., Johnson, V. L., Ensign, S. H., MacPherson, T. A. (2006). *Factors contributing to hypoxia in rivers, lakes, and streams.* Limnology and Oceanography, 51(1part2), 690-701.

McKee, D., Cunningham, A. (2006). *Identification and characterization of two optical water types from in situ inherent optical properties and seawater constituents.* Estuarine, Coastal and Shelf Science, 68, 305–316.

McKee, D., Cunningham, A., Wright, D., Hay, L. (2007). *Potential impacts of nonalgal materials on water-leaving Sun induced chlorophyll fluorescence signals in coastal waters.* Applied Optics, 46(31), 7720-7729.

Mobley, C. D. (1994). *Light and Water.* San Diego: Academic Press.

Mobley, C. D. (1999). *Estimation of the remote-sensing reflectance from above-surface measurements.* Applied Optics, 38, 7442–7455.

Neil, C., Cunningham, A., McKee, D. (2011). *Relationships between suspended mineral concentrations and red-waveband reflectances in moderately turbid shelf seas.* Remote Sensing of Environment, 115(12), 3719-3730.

Neil, C., Cunningham, A., McKee, D., Polton, J. A. (2012). *Remote sensing of seasonal stratification d ynamics in the southern Irish Sea.* Remote Sensing of Environment, 127, 288-297.

O'Reilley, J. E., Maritorena, S., Mitchell, B. G., Siegel, D. A., Carder, K. L., Garver, S. A., Kahru, M., McClain, C. (1998). *Ocean color chlorophyll algorithm for SeaWiFS.* Journal of Geophysical Research, 103 (C11), 24937 – 24953.

Robinson, W. D., Schmidt, G. M., McClain, C. R. & Werdell, P. J. (2000). *Changes Made in the Operational SeaWiFS Processing.* In: Hooker, S. B. & Firestone, E. R. eds. (2000). NASA Tech. Memo. 2000-206892. Vol 10. Greenbelt, Maryland: NASA Goddard Space Flight Center, pp12-28.

Ruddick, K. G., Ovidio, F., Rijkeboar, M. (2000). *Atmospheric correction of SeaWiFS imagery over turbid coastal waters.* Applied Optics, 39 (6), pp. 897-912.

Sathyendranath, S., Prieur, L., Morel, A. (1989). *A three-component model of ocean colour and its application to remote sensing of phytoplankton pigments in coastal waters.* International Journal of Remote Sensing, 10(8), 1373-1394.

Serpetti, N. 2012. *Modelling and mapping the physical and biogeochemical properties of sediments on the North Sea coastal waters.* PhD Thesis, University of Aberdeen. 249pp.

Serpetti, N., Heath, M., Rose, M. and Witte, U. (2012). *Mapping organic matter in seabed sediments off the north-east coast of Scotland (UK) from acoustic reflectance data*. Hydrobiologia 680, 265–284.

Shettle, E. P. , Fenn, R. W. (1979). *Models for the aerosols of the lower atmosphere and the effects of humidity variations on their optical properties.*

Stumpf, R. P., Culver, M. E., Tester, P. A., Tomlinson, M., Kirkpatrick, G. J., Pederson, B. A., Truby, E., Ransibrahmanakul, V., Soracco, M. (2003). *Monitoring Karenia brevis blooms in the Gulf of Mexico using satellite ocean color imagery and other data.* Harmful Algae, 2(2), 147-160.

Wang, M. (2000). *The SeaWiFS atmospheric correction algorithm updates.*
Seawifs Postlaunch Calibration And Validation Analyses, Part, 1, pp. 57-63.

# SCOPING THE IMPACT TIDAL AND WAVE ENERGY EXTRACTION ON SUSPENDED SEDIMENT CONCENTRATIONS AND UNDERWATER LIGHT CLIMATE

07

M.R. Heath[1], A.D. Sabatino[1], N. Serpetti[2], and R.B. O'Hara Murray[3]

1 DEPARTMENT OF MATHEMATICS AND STATISTICS,
UNIVERSITY OF STRATHCLYDE, 16 RICHMOND STREET, GLASGOW, G1 1XQ

2 SCOTTISH ASSOCIATION FOR MARINE SCIENCE, SCOTTISH MARINE INSTITUTE, OBAN, PA37 1QA

3 MARINE SCOTLAND SCIENCE,
SCOTTISH GOVERNMENT, MARINE LABORATORY, 375 VICTORIA ROAD, ABERDEEN, AB11 9DB

back to contents

## 07/1 INTRODUCTION

The depth to which sunlight penetrates below the sea surface is one of the key factors determining the species composition and productivity of marine ecosystems. The effects range from the rate and fate of primary production, through the performance of visual predators such as fish, the potential for refuge from predators by migrating to depth, to the scope for seabed stabilisation by algal mats. Light penetration depends partly on spectral absorption by seawater and dissolved substances, but mainly on the scattering caused by suspended particulate material (SPM). Some of this SPM may be of biological origin, but in coastal waters the majority is mineral material originating ultimately from seabed disturbance and land erosion, the latter being deposited in the sea by rivers and aerial processes. SPM is maintained in the water column or deposited on the seabed depending on combinations of hydrodynamic processes including baroclinic (density-driven) or barotropic (mainly tidal and wind driven) currents, and wave action (Ward et al. 1984; Huettel et al. 1996). Since tidal and wave energy extraction must alter these hydrodynamic properties at some scales depending on the nature of the extraction process, we can expect some kind of impact on the concentration of the SPM. If these are large enough, we may have to consider the extent to which these may impact the underwater light environment and the local or regional ecology.

Whilst several coupled hydrodynamic-sediment models exist to predict SPM distributions in aquatic systems, their skill level in open coastal and offshore marine waters is acknowledged to be relatively low. This is largely because the processes are not well understood and the formulations are largely based on empirical relationships rather than fundamental physical principles. The models are also highly demanding in terms of calibration data and computational resources. Hence their utility for predicting relatively subtle effects arising from changes in flow or wave environments due to energy extraction devices seems rather low. Here, we summarise the key mathematical functions describing the processes involved in sediment suspension, and propose a lightweight one-dimensional (vertical) model which can be used to scope the effects of changes in flow and wave energy on SPM.

## 07/2 BRIEF REVIEW OF PROCESSES AND EQUATIONS INVOLVED IN MODELLING SUSPENDED SEDIMENT PROCESSES

### 07/2.1 INITIATION OF PARTICLE MOVEMENT ON THE SEABED AND THE ERODIBILITY OF SEDIMENTS

With constant uniform water flow over a smooth bed, particle movement will occur when the instantaneous fluid force on a particle is larger than the instantaneous resisting force. The latter is related to the submerged particle size or weight and the friction coefficient. Cohesive forces are also important when the bed consists of appreciable amounts of clay and silt particles or biological material. The shear stress to which a particle is subjected is a function of its size, the flow speed, and the densities of the fluid and particles. The critical value of shear stress required to initiate motion is often estimated from the empirically-based 'Shield diagram' (Shields 1936), which relates a dimensionless measure of critical shear stress to the Reynolds number of a particle in a given flow.

The dimensionless Reynolds number $(R)$ is given by (Reynolds 1883):

$$R = \frac{u^* \cdot d}{v}$$

where $u^*$ = the bed shear velocity (m.s$^{-1}$), $\rho$ = fluid density (kg.m$^{-3}$), $d$ = particle diameter (m), and $v$ = kinematic viscosity (m2.s$^{-1}$) of the fluid. The Reynolds number accounts for the ratio between the momentum forces with the viscous forces.

The bed shear velocity is related to the bed shear stress $(\tau_b)$ by:

$$u^* = \sqrt{\frac{\tau_b}{\rho}}$$

The dimensionless Shield number or Shield stress $(\tau^*)$ is then given by

$$\tau^* = \frac{\tau_b}{(\rho_s - \rho) \cdot g \cdot d}$$

where $\rho_s$ is the density of sediment grains (kg.m$^{-3}$), and $g$ is the acceleration due to gravity (m.s$^{-2}$).

back to contents

The critical value of Shield stress for the initiation of particle motion $(\tau_c{}^*)$ is typically estimated from an empirical relationship between $\tau_c{}^*$ and $R$. An approximate parameterisation of this relationship is given by Wilcock et al (2009):

$$\tau_c{}^* = 0.105 \cdot R^{-0.3} + 0.045 \cdot e^{-35 \cdot R^{-0.59}}$$

Movement of particles is assumed to be initiated when the shear stress $\tau^*$ is higher than the above threshold $\tau_c{}^*$.

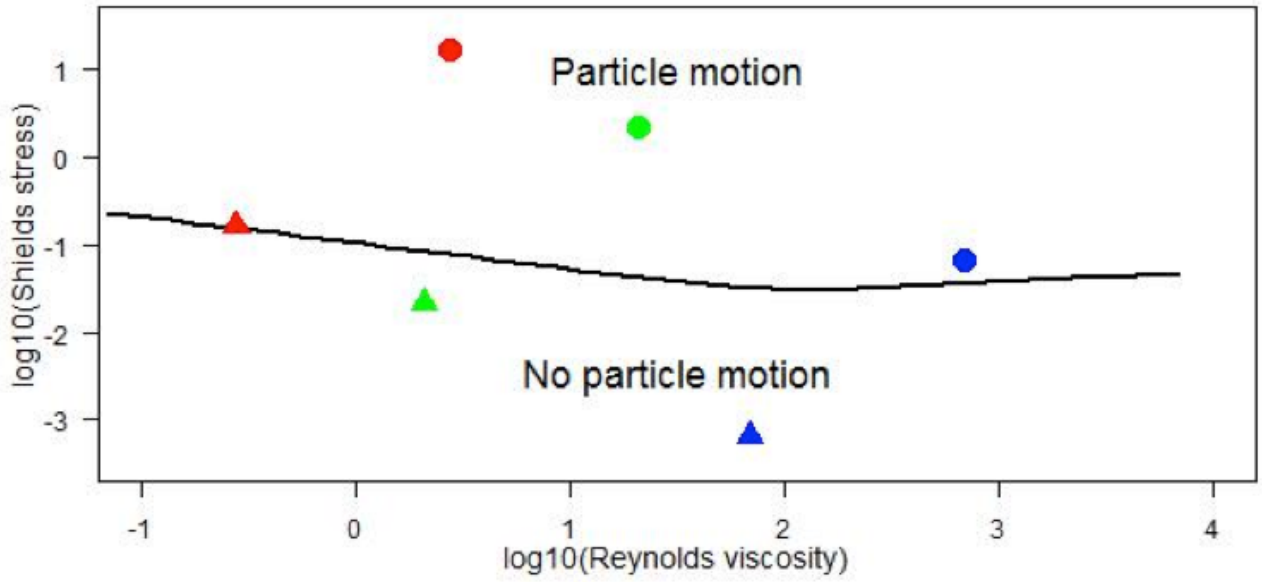


**Fig 7.1** Shields diagram. Solid line represents the critical Shields stress for particle motion $\tau_c{}^*$. Symbols represent three different particle grain diameters and two values of bed shear velocity: red = mud (40 μm), green = sand (300 μm), blue = pebble (1 cm); circles = bed shear velocity 10 cm.s$^{-1}$; triangles = bed shear velocity 1 cm.s$^{-1}$.

Shields identified four regions of the critical bed stress relationship $\tau_c^* = f(R)$ corresponding to the extent to which sediment particles are submerged with in the viscous micro-layer close to the sediment boundary which determines whether the flow regime is laminar, smooth or rough turbulent. The net results is that sand grain sized particles have the lowest critical velocity for initiation of movement. Muddy sediment have higher critical velocities due to smooth flow and cohesive properties, whilst coarser sediments have higher critical velocities to do greater mass of individual particles.

The distinction between non-cohesive sediment mixtures and cohesive mixtures is related to the proportion of fine-grained particles, and arises partly from electrochemical forces between the grains which bind the sediment matrix together. Mud particles are those smaller than approximately 0.06 mm diameter, and clay as those smaller than approximately 0.005 mm. Cohesive properties become dominant for erosion, leading to higher critical Shields stress, when the clay-fraction is larger than about 5% to 10%. Assuming a clay-mud ratio of 0.5 to 0.25 for natural mud beds, the critical mud content will be about 20-40%.

The Shields relationship has been extended, reviewed and scrutinised many times as additional data have become available. For example, Paphitis (2001) defined upper and lower bounds of Shields stress for the initiation of motion. However, a fundamental objection has been that the relationship involves the bed shear stress in both the abscissa and ordinate axes. Consequently, the critical bottom shear stress for a given grain size cannot be determined directly from the Shields curve and requires an iterative procedure. To overcome this issue, Paphitis (2001) recast the Shields relationship in terms of a critical bed shear velocity expressed in terms of a movability number (M, Collins and Rigler 1982) that was firstly introduced by Liu (1957), as function of either grain size, or a dimensionless grain size number ($D_*$, Van Rijn 1993):

$$M = \frac{u^*}{\omega_s}$$

where $\omega_s$ is the fall velocity of particles, and $u^*$ is the shear velocity at the seabed. The obvious advantage of this approach is that the diameter and the density of the particles are replaced by just one single parameter, the settling velocity (Armitage and Rooseboom 2010).

The dimensionless grain size number is given by (Van Rijn 1993):

$$D_* = d \cdot \left[ \frac{(\rho_s - \rho)}{\rho \left( \frac{g}{v^2} \right)} \right]^{\frac{1}{3}}$$

Paphitis (2001) presented piecewise equations to predict the upper and lower bounds and central tendency of relationships between movability, and the implied bed shear velocity or stress given grain settling velocity, and both particle grain size and grain size number. Similarly, Beheshti and Ataie-Ashtiani (2008) derived piecewise empirical functions to describe the critical movability number $(M_c)$ for the onset of particle motion in relation to grain size number, as

$$\frac{u_{*c}}{\omega_s} = \begin{cases} 9.6674 \cdot D_*^{-1.57}, & D_* \leq 10 \\ 0.4738 \cdot D_*^{-0.226}, & D_* > 10 \end{cases}$$

These forms seem conceptually more appealing than the original Shields relationship. However, they have two additional problems. First, the published parameterisations are based on an assumption of fluid density and viscosity of freshwater as 20 °C, which corresponds to the typical laboratory conditions under which the majority of the contributing empirical data were gathered. The relationships have not been transformed to realistic seawater temperature and salinity conditions which imply 2-3% higher fluid density. Secondly, and probably more importantly, they involve assumptions or further empirically based equations to estimate particle sinking velocities $(\omega_s)$ as a function of grain size.

## 07/2.2 PARTICLE SINKING VELOCITY

The downward sinking velocity of particles at equilibrium - where the sum of the gravity force, buoyancy force and fluid drag force are equal to zero – depends on the density and viscosity of the fluid, and the density, size, shape, and surface texture of the particle. The classical Stokes equation for the fall velocity of a particle assumes a spherical shape and laminar flow (Reynolds numbers less than 1). Despite extensive research

there is still no analytical solution to predict the fall velocity of natural shaped particle, or particles large enough to generate turbulent flow. Many investigators have proposed empirically based relationships to predict particle fall velocities with varying degrees of complication and success. Sadat-Helbar et al. (2009) reviewed 17 published relationships and identified that developed by Wu and Wang (2006) as being one of the most reliable formulations for the sinking velocity:

$$\omega_s = \frac{A \cdot v}{B \cdot d'}\left[\sqrt{\frac{1}{4}+\left(\frac{4 \cdot B}{3 \cdot A^2} D'^{3}_{*}\right)^{\frac{1}{a}}} - \frac{1}{2}\right]^{a}$$

where $A$, $B$ and $a$ are coefficients and $D'$ represents the nominal grain size diameter. Empirical calibration against a wide range of sediments provided coefficient values as:

$$A = 53.5 \cdot e^{-0.65 \cdot S_f}$$
$$B = 5.65 \cdot e^{-2.5 \cdot S_f}$$
$$a = 0.7 + 0.9 \cdot S_f$$

where $S_f$ is the Corey shape factor – typically taken to be 0.7 (Camenen 2007).

Sadat-Helbar et al. (2009) also provided their own somewhat simpler generalised piecewise relationship in where fall velocity increases as a power function of particle diameter, without incorporating any shape parameter terms:

$$\omega_s = \begin{cases} 0.033 \cdot \dfrac{v}{d}\left(\dfrac{d^3 g(s-1)}{v^2}\right)^{0.963} & D_{gr} \le 10 \\ 0.510 \cdot \dfrac{v}{d}\left(\dfrac{d^3 g(s-1)}{v^2}\right)^{0.553} & D_{gr} > 10 \end{cases}$$

where $D_{gr} = d \cdot \left(\dfrac{g \cdot (s-1)}{v^2}\right)^{\frac{1}{3}}$

and $s = \dfrac{\rho_s}{\rho}$

Although these relationships perform reasonably well at predicting the central tendency of the accumulated experiment data on settling velocities of naturally occurring mineral grains, there remains a considerable amount of unexplained variability. Since the settling velocity appears as the denominator in the grain mobility function and, for mud grains, is a small number relative to the bed shear velocity, even small variations can have a large effect on predictions of the critical shear stress required to initiate motion of given grain sizes. Hence, despite the objections and the many proposed alternatives, the original Shields relationship describing the critical stress for initiation of particle motion remains in widespread use.

## 07/2.3 ERODIBILITY OF MIXED GRAIN SIZE SEDIMENT

The Shields and other equivalent relationships refer to unimodal sediment grain sizes, whilst natural marine sediments are frequently composed of multiple modes spanning a wide range of sizes, and often layers of different composition. Laboratory and field observations have shown that erosion of sand beds is inhibited by the presence of the mud particles, and vice versa, so that the shear stress required to initiate particle motion is significantly increased (Van Rijn 1993, Bartzke et al. 2013, Mitchener and Torfs 1996). In addition, material in different layers may exhibit widely varying erosion shear thresholds, especially when recently deposited fine grained material is overlaid onto older coarse beds (Amos et al 1992, El Ganaoui et al. 2004).

## 07/2.4 EFFECTS OF BED-FORMS

The morphology of the sea bed (plane or rippled bed) has a significant role in the erodibility of sediments. The architecture of the sea bed controls the near-bed velocity profile, the shear stresses and the turbulence and, thereby, the mixing and transport of the sediment particles. Ripples in the sediment surface reduce the near-bed velocities, but it enhances the bed-shear stresses, turbulence and the entrainment of sediment particles, resulting in larger overall suspension rates. Several types of bed forms can be identified, depending on the type of wave-current motion and the bed material composition. For fine sand (grain size 0.1 to 0.3 mm), as bed shear increases beyond the critical Shields stress the surface initially develops rolling grain ripples, then vortex ripples, and finally plane bed with sheet flow of sediment

grains. Soulsby and Whitehouse (2005) developed algorithms for predicting bedforms in sandy sediments in relation to bed shear velocities, and their evolution during time-varying flows.

## 07/2.5 EFFECTS OF CONSOLIDATION ON SEDIMENT ERODIBILITY

The empirically-based Shields relationship takes account of cohesive forces between particle grains, but not the effects of consolidation. Various processes lead to natural sediments becoming more resistant to erosion post-deposition, producing marked deviations from the expected Shields particle motion thresholds. Compaction occurs when sediment volume is reduced and density increased due to expulsion of pore water by stress from overlying material. Other natural processes which lead to the consolidation of sediments and their increased resistance to erosion include chemical dissolution and/or precipitation of minerals, and biological activity. These processes are referred to as diagenesis in geological and ecological literature.

No general relationships to represent consolidation and its effect on sediment erodibility have emerged (McCave 1984). The early formulation of Partheniades (1965) remains widely used in models of sediment erosion (e.g. Whitehouse et al. 2000; Ribbe and Holloway 2001; Kuhrts et al., 2004; Pandoe and Edge 2004; Van den Eynde 2004), though it merely deals the problem by posing an unknown site and time specific parameter (E) to represent erodibility:

$$S_E = \begin{cases} E \cdot \left(\frac{\tau_b}{\tau_c} - 1\right)^n & \tau_b > \tau_c \\ 0 & \tau_b \leq \tau_c \end{cases}$$

where $S_E$ is the erosion rate (kg.m$^{-2}$.s$^{-1}$), $E$ is the erodibility (kg.m$^{-2}$.s$^{-1}$), and $\tau_c$ is the critical threshold for erosion, equivalent to the Shields critical stress.

For a soft or partly consolidate sediment:

$$S_E = E \cdot \left(e^{\alpha\sqrt{(\tau_b - \tau_c)}}\right) \quad \tau_b > \tau_c$$

(Parchure and Mehta 1985)

Biological processes leading to consolidation may take many forms and are therefore extremely difficult to generalise. Secretion of sticky organic molecules by microbes (Grant and Gust 1987, Lubarsky et al. 2010), benthic algae and microbes clogging the pore spaces and binding grains together (Austen et al 1999, Paterson and Black 1999, Nowell et al. 1981, Sutherland et al. 1998), and forming mats on the sediment surface all lead to inhibition of sediment erosion (Oppenheim and Paterson 1990, Fonseca 1989, Paterson 1989). Living algal mats are most prevalent in shallow waters since the micro-organisms concerned require light to photosynthesise. Other biological processes may have the opposite effect on sediment erodibility due to de-stabilisation of the sediment structure. These include bioturbation by burrowing and sediment ingesting macrofauna and meiofauna which reprocesses sediment into faecal granules (Lumborg et al. 2006, Montague 1986, Rowden et al. 1998).

The key issues is the extent of spatial and temporal variability in biologically induced consolidation and erodibility. The problem is well known and extensively studies in tidal mud-flats and shallow estuaries where the sediments are predominantly fine cohesive muds and the effects of biological activity are very obvious (Andersen 2001, Widdows et al. 2000, Le Hir & Karlinkow 1992, Austen et al. 1999, Paterson et al. 2000). In fact, it has become apparent that seasonal variation in erodibility mediated by biological activity may be the dominant factor controlling water turbidity in shallow tidal regions such as the Wadden Sea (De Vires and Borsje 2008, Borsje et al. 2008, Lumborg et al. 2006). Various measurements have been investigated as potential indicators of biologically-mediated erodibility, for example, algal pigment content of sediments (Riethmuller et al. 2000), but so far none have shown general applicability.

Early models of sediment suspension and transport in deeper open shelf systems generally assumed that spatial, and especially temporal, variability in biological consolidation and erodibility of sediments could be regarded as negligible (e.g. Pohlmann and Puls 1994, Ribbe and Holloway 2001, Kuhrts et al. 2004, Pandoe & Edge 2004, van den Eynde 2004). However, recent research shows that this cannot be assumed (Stevens et al. 2007, Briggs et al. 2015). Operational formulations for including variability of biologically-mediated consolidation in shelf sea sediment models is lacking. For example, Dobrynin (2009) found that

a model of suspended sediment concentrations in the southern North Sea was unable to explain the distribution of surface concentrations derived from satellite remote sensing without resorting to alternative summer and winter parameterisations of erodibility.

## 07/2.6 LIFTING OF BED-LOAD PARTICLES INTO THE WATER COLUMN

When the value of the bed-shear velocity becomes sufficiently high relative to the particle fall velocity, the bed-load particles can be lifted into suspension. Usually, the behaviour of the suspended sediment particles is described in terms of the sediment concentration, which is the solid volume ($m^3$) per unit fluid volume ($m^3$) or the solid mass (kg) per unit fluid volume ($m^3$). Observations show that the suspended sediment concentrations $(C)$ decrease with altitude up from the bed $(z)$. The rate of decrease depends on the fall velocity of particles $(\omega_s)$ and the vertical distribution of vertical diffusivity (Ks) through the water column.

The vertical flux of particulate mass can be described by the differential equation:

$$\omega_s \cdot C = -K_s \cdot \frac{dC}{dz}$$

or

$$C(z) = C_a . exp\left(-\int_{z_a}^{z} \frac{\omega_s}{K_s} dz\right)$$

Where $C(z)$ is the concentration at altitude $z$ above the seabed, and $C_a$ is the concentration at a reference altitude $z_a$.

Predictions of vertical distributions of concentration therefore depend on assumptions about the vertical profile of diffusivity. Commonly used alternatives are to assume a constant diffusivity with depth, a linear decrease or a parabolic variation with peak diffusivity in mid-water.

With a linear diffusivity assumption, the concentration profile is given by

$$C(z) = C_a \left(\frac{z}{z_a}\right)^{-\left(\frac{\omega_s}{\beta \cdot \kappa \cdot u^*}\right)}$$

Where $u^*$ is the shear velocity at the seabed, $\kappa$ is the von Kármán constant (0.4), and $\beta$ is a coefficient relating eddy viscosity to eddy diffusivity (taken to be 1) (Rouse 1937, Van Rijn 1984, 1993).

The exponent $\omega_s/(\beta \cdot \kappa \cdot u^*)$ is referred to as the Rouse number.

Alternative assumptions regarding the vertical distribution of diffusivity give different expectations for the vertical profile of concentration, but the Rouse approach is most commonly applied.

Sensitivity analysis of the Rouse profile combined with the dependency of fall velocity on particle size shows that suspended sediment concentration profiles are likely to be highly sensitive to the grain size composition of sediments. Particles larger than approximately 0.1 mm are likely to remain concentrated close to the seabed except at high bed shear velocities (>10 $cm.s^{-1}$). On the other hand, particles smaller than 0.06 mm, which make up the majority of muddy sediments in shelf seas, are likely to be lifted throughout the water column by shear velocities between 0.25 and 2.5 $cm.s^{-1}$. With respect to the underwater light climate, the fine particles (<0.1 mm) are of most interest. At equivalent weight or volumetric concentrations in the water column, fine particles create more light scattering than coarse particles.

## 07/2.7 PARTICLE AGGREGATION IN THE WATER COLUMN

Particle-particle collisions during suspension in the water column may lead to aggregation and formation of flocs with potentially enhanced sinking rates, depending on the physical cohesive properties of particle grains and their stickiness due to biological coatings (e.g. Krone 1978, Andersen and Pejrup 2002, Mehta 1989; Winterwerp 2002; You 2004). The probability of collisions will be a function of the suspended sediment concentration. Experimental studies have found that settling velocity of for mud and silt particles is independent of concentration below 0.4 g/l. Between 0.4 and 2.0 g/l, settling velocity increases with concentration due to flocculation. Above 2.0 g/l settling velocity rapidly decreases due to break-up of flocs, flocs mutual hindrance and interactions between the flows around adjacent ones that tend to increase upward friction (Cancino and Neves 1999).

An empirical relationship describing this process (Burt 1986) is of the form:

$$\omega_s = k \cdot \left(\frac{C}{\rho_s}\right)^{\gamma}$$

where $k$ and $\gamma$ are constants, and $C$ lies between a lower threshold for particle-particle interactions, and an upper threshold at which particles begin to interfere and the effective settling velocity is reduced. The upper concentration corresponds to values found in e.g. mud slides, where the water-sediment mixture forms a super-dense liquid (e.g. Richardson and Zaki 1954), and is not relevant in typical shelf-sea marine situations.

## 07/2.8 LATERAL TRANSPORT AND TIME-DEPENDENT VERTICAL PROFILES OF SUSPENDED SEDIMENT

The velocity of suspended particles in a longitudinal direction is almost equal to the fluid velocity. So lateral transport of suspended sediment is simply the product of the vertical profile of sediment concentration and the vertical profile of water velocity (Van Rijn 1993). Hence, horizontal bed-load transport is relatively easily modelled because vertical processes affecting the particles are limited to the onset and cessation of motion on the seabed. However, suspended loads require time to adjust to changing conditions as particles are redistributed vertically in response to fluctuating conditions. Effective modelling of suspended sediment transport therefore requires dynamic representation of vertical convection-diffusion processes in order to resolve short term fluctuations in vertical concentration gradients.

In accelerating flows there always is a net vertical upward transport of sediment particles due to turbulence-related diffusive processes, which continues as long as the sediment transport capacity exceeds the actual transport rate. Conversely, during decelerating flow, there is a net downward sediment transport because particle sinking dominates, yielding smaller concentrations and transport rates. As a result, empirical studies show that sediment concentrations over, for example, a fine sand bed show a continuous adjustment to oscillating flow velocities, such as tidal flows, with a lag period in the range of 0 to 60 minutes. The time lag period is equivalent to the interval between maximum flow and the point at which the transport capacity is equal to the actual transport rate. In the case of case of fine grained sediments or deep water columns, the settling process can continue during the slack water period giving a large time lag, which is then defined as the period between the time of zero transport capacity and the start of a new erosion cycle. Time lag effects can be neglected for sediments larger than about 0.3 mm for which the settling velocity is large, so that bed-load transport of coarse-grain sediments can be effectively modelled using a quasi-steady state approach (Van Rijn 1984, 1993).

# 07/3 SCOPING THE IMPACT OF WAVE AND TIDAL ENERGY EXTRACTION ON SUSPENDED SEDIMENT CONCENTRATIONS.

## 07/3.1 SIMPLE 1-DIMENSIONAL SUSPENDED SEDIMENT MODEL

Formally, simulation of the impact of wave and/or tidal energy extraction on suspended sediment concentrations requires the solution of equations representing erosion and deposition of sediment from the seabed, together with partial differential equations at each node in a 3-dimensional water column grid, describing the vertical and horizontal fluxes of particles. The latter depends on advection, convection, diffusion and settling velocities (e.g. Teisson 1991). All of this adds considerably to the already intensive computational and parameterisation demands of solving the hydrodynamic equations for wave propagation, and wind-driven and tidal current velocities at sufficiently high resolution to be of value for studying the impact of energy extraction devices. There are several models available for this task (e.g. Gerritsen et al. 2000, Mercier and Delhez 2007), including the MIKE by DHI Mud Transport Module (Danish Hydraulics Institute 2013). However, the task of calibrating the parameters of such models requires considerable investment in field data collection and model run-time, and none yet include adequate or any representation of the seasonality of sediment erodibility due to biological processes which is emerging from recent field investigations as a key issue for sediment dynamics. Hence, we propose here a lightweight, one-dimensional (vertical), modelling approach for basic scoping of the impact of energy extraction, incorporating simple caricatures of the basic

erosion and deposition processes outlined in the review above.

The approach is to predict an instantaneous vertical profile of suspended sediment, given seabed depth, shear and the mud content of seabed sediment, incorporating time-dependent erodibility and a time-series autocorrelation effect for the bed-stress to caricature the lag effects arising from the dynamics of erosion and deposition. Clearly, this approach cannot take account of lateral transport of suspended sediment, so its use must be limited to area where the majority of sediment material in the water column arises from seabed local resuspension rather than horizontal transport.

**Input variables**

$h$ Mean sea surface height above the seabed
$S$ Seabed sediment mud content (proportion by weight of grain size <0.06 mm)
$\tau_t$ Bed shear stress at time t, where t is in days from 1 January in some reference year)

**Parameters given as physical constants**

$\rho_s$ Density of sediment material (2650 kg.m$^{-3}$)
$\rho$ Density of seawater (1026 kg.m$^{-3}$ at salinity 35 and 10 °C)
$\kappa$ von Kármán constant (0.4),

**Parameters requiring to be fitted or assumed**

$T_a$ Autocorrelation time scale for bed stress hindcasting
$\mu$ Decay rate for bed stress hindcasting
$\alpha$ Scaling coefficient
$\omega_s$ Particle sinking rate
$\varepsilon$ Seabed mud content exponent term
$\delta$ Bed stress exponent term
$\gamma$ Sinking rate exponent term
$\beta$ Time-varying erodibility exponent
$t_\beta$ Phase shift for time-varying erodibility cycle

**Intermediate terms**

$\pi_t$ Exponentially declining time-weighting function
$\tau_a$ Time weighted average bed stress
$u_a^*$ Time weighted average bed shear velocity
$E$ Time-varying component of erodibility term
$C_b$ Near-seabed (1 m altitude) suspended sediment concentration

**Output**

$C_z$ Suspended sediment concentration at altitude $z$ above the seabed

**Equations**

To take account of the lag effect of fluctuating wave orbital velocities and tidal current speeds on the vertical profile of suspended sediment, we assume that the bed stress generating a vertical profile of suspended sediment is a time-weighted average of the stress over some period prior to the instant of prediction.

We define an exponentially declining time-weighting function

$$\pi_t = e^{\mu \cdot t}$$

where t is a series of shear observation times prior to the instant at which a prediction is required, $T_a \geq t \geq 0$, and $T_a$ is a negative number representing the autocorrelation time scale relevant to the formation of the suspended sediment profile.

The time-weighted shear is then given by

$$\tau_a = \sum_{T_a}^{0} \frac{\tau_t \cdot \pi_t}{\sum_{T_a}^{0} \pi_t}$$

The corresponding time weighted bed shear velocity is then given by:

$$u_a^* = \sqrt{\frac{\tau_a}{\rho}}$$

Biological activity in the seabed sediment leading to natural consolidation and changes in erodibility is expected to follow a seasonal cycle dictated by temperature and the input of fresh organic matter settling from the spring and summer plankton blooms. We do not know the exact form of this, though observational data on phyto-detritus pigments in the sediments, oxygen consumption and nutrient fluxes indicate a peak of activity in June/July and a minimum in December/January. In addition, we know that pigment concentrations and microbial fluxes increased with the mud content of sediments

(Serpetti et al. 2012, Serpetti 2012). So, we caricature the erodibility of sediments in two parts – a sediment dependent term (power function of mud content), and a time dependent term represented by a cosine function scaled to vary between 0.5 and 1.0, and phase shifted by a period $t_\beta$ relative to the solar cycle:

$$E = 0.75 + \left( \frac{\cos\left(\frac{2\pi}{365.25}(t - t_\beta)\right)}{4} \right)$$

Then, we represent the near-bed suspended sediment concentration by:

$$C_b = \alpha \cdot \left(S^\epsilon \cdot E^\beta\right) \cdot {\tau_a}^\delta$$

This expression contains three components: the scaling coefficient $\alpha$ which equates the modelled concentration to observed measurement units; an erodibility term $\left(S^\epsilon \cdot E^\beta\right)$, and bed shear stress term $\left({\tau_a}^\delta\right)$ which corresponds to the erosion rate expression of e.g. Partheniades (1965). We do not set an explicit threshold of shear stress for the initiation of particle motion, since we are not addressing sediment fluxes or steady state concentrations under constant flows. Rather, we aim to caricature transient concentrations in a time varying system, where the concentration near the seabed at any instant reflects the balance between deposition and erosion fluxes, and deposition fluxes include time-lagged signals of past erosion events.

The suspended sediment concentration at altitude $0 < z \leq h$, is then given by:

$$C_z = C_b \cdot z^{-\left(\frac{\omega_S \cdot {C_b}^\gamma}{\kappa \cdot u_a^*}\right)}$$

The exponent here corresponds to the Rouse number but including an expression to reflect increasing particle-particle aggregation in the water column with increasing sediment concentration (Burt 1986).

## 07/3.2 ESTIMATING BED SHEAR STRESS ($\tau_t$) FROM TIME SERIES OF MODELLED OR OBSERVED TIDAL CURRENT AND WAVE PROPERTIES

In a natural situation the shear stress at the seabed is the result of velocities due to tidal currents, orbital velocities arising from wind and swell waves, and residual flows due to density gradients and surface wind forcing. Combining these components to predict the shear velocity in the boundary layer at the seabed, and hence the bed shear stress, is a challenging task. The methodology needs to take account of transitions between laminar, smooth and rough turbulent flows depending on flow velocity and bed roughness, as these have very different consequences for bed-shear. Most existing theories for wave-current interactions only deal with the rough-turbulent case. Computational oceanographic models for shelf seas typically use simple caricatures of the wave current interaction to estimate bed shear stress. For example, MIKE by DHI uses the radiative stress due to wave action to attenuate or amplify the bed stress due to tidal flow depending on the relative directions of the two.

### 07/3.2.1 CALCULATING BED SHEAR STRESS ARISING FROM TIDAL AND RESIDUAL CURRENTS

Seabed shear-stress ($\tau_b$, N.m$^{-2}$) can be estimated from the vertically averaged current speed throughout the water column using the "law-of-the-wall" method (Soulsby and Clarke 2005) which assumes a logarithmic decrease in velocity with proximity to the sediment-water interface:

The calculation depends on whether the flow is taken to be laminar or turbulent. This is estimated from the Reynolds viscosity $(R_e)$:

$$R_e = \frac{\overline{U}h}{\nu}$$

If $\overline{U}$ is the vertically averaged current speed, h is the water column depth, $\nu$ is the kinematic viscosity (m$^2$.s$^{-1}$) of the fluid.
Then,

If $\overline{U} = 0$, $\tau_b = 0$

If $\bar{U} > 0$,

If $R_e \leq 2000$ then laminar flow and $\tau_b = \frac{3\rho\nu\bar{U}}{h}$

If $R_e > 2000$ then turbulent flow and

$\tau_{bs} = (0.0001615.\exp(6(R_e)^{-0.08})).\rho\bar{U}^2$ (smooth bed surface)

$\tau_{br} = \left(\frac{0.40}{\ln\left(\frac{h}{z_0}\right)-1}\right)^2.\rho\bar{U}^2$ (rough bed surface; $z_0$ = bed roughness length = $d_{50}/12$)

$\tau_b = \max(\tau_{bs}, \tau_{br})$

where, $\rho$ is the fluid density (kg.m$^{-3}$), and $d_{50}$ is the median particle size on the seabed.

## 07/3.2.2 CALCULATING ORBITAL VELOCITIES BENEATH SURFACE SWELL AND WIND WAVES

Orbital velocities generated by surface waves penetrate into the water column, decreasing in amplitude with depth. Calculation of orbital velocities at the seabed given information on wave height, period and direction can be performed according to Soulsby (2006; summarising the work of Soulsby (1987) and Soulsby and Smallman (1986)). Combining orbital velocities with tidal current speeds to estimate bed shear stress can then be performed according to Soulsby and Clarke (2005; summarising earlier work by Soulsby (1995, 1997)).

Calculation of seabed orbital velocity (Uw) according to Soulsby (2006):

| | |
|---|---|
| $T_p$ | Peak wave period (s) |
| $T_z$ | Zero crossing period (s) |
| $T_m$ | Mean wave crossing period (s) |
| $T_n$ | Natural scaling period (s) |
| $H_s$ | Significant wave height (m) |
| $g$ = 9.81 | Acceleration due to gravity (m.s$^{-2}$) |
| $U_w$ | Wave orbital velocity (m.s-1) |

For a JONSWAP spectrum it is a reasonable approximation to take

$$T_z = T_m = \frac{T_p}{1.28}$$

Different models and observational devices variously provide different indices of the wave spectrum. Hence, if only data on peak wave period $(T_p)$ are available, then

$$T_z = \frac{T_p}{1.28}$$

If only data on mean wave period $(T_m)$ are available, then

$$T_z = T_m$$

$$T_p = 1.28 \cdot T_m$$

$$T_n = \sqrt{\frac{h}{g}}$$

Then:

$$t_{pw} = \frac{T_n}{T_z}$$

$$A_{pw} = \left(6500 + \left(\left(0.56 + \left(15.54 \cdot t_{pw}\right)\right)^6\right)\right)^{\frac{1}{6}}$$

And finally,

$$U_w = \frac{\left(\frac{H_s}{4}\right)}{\left(T_n \cdot \left(\left(1 + \left(A_{pw} \cdot {t_{pw}}^2\right)\right)^3\right)\right)}$$

## 07/3.2.3 COMBINING BED STRESS ARISING FROM CURRENT FLOWS WITH STRESS DUE TO WAVE ORBITAL VELOCITIES

For combining wave orbital velocity $(U_w)$ with tidal current velocity, to derive bed shear stress under laminar and turbulent flow regimes, refer to Appendix A (Algorithm for calculating mean, maximum and r.m.s bed shear-stresses for laminar, smooth-turbulent and rough-turbulent wave-plus-current flows) in Soulsby and Clarke (2006).

## 07/4 EXAMPLE CASE STUDY OF PREDICTED SUSPENDED SEDIMENT CONCENTRATIONS COMPARED TO OBSERVED DATA

Vertical profiles of turbidity (Formazine Turbidity Units (FTU), proportional to SPM ($g.m^{-3}$)) measured at 0.5 m depth intervals and up to weekly intervals over the period 2008-2011, at 9 coastal sites off Stonehaven (NE Scotland) by Marine Scotland Science, were available for parameterising the suspended sediment model. Full information on the sites, seabed sediment properties, and data collection methods are provided elsewhere (Bresnan et al. 2008, Serpetti et al. 2012, Serpetti 2012). The seabed sediment mud content of the sites ranged from 0.6 to 38%, and the water depth from 28-50 m. Methods are summarised in Appendix 1 but very briefly, time series of bed shear stress due to combined tidal currents and waves at each sampling site were simulated by a MIKE by DHI hydrodynamic model (Sabatino et al. in preparation), and used as inputs to the sediment model. The model was then fitted to a calibration subset of the measured turbidity data by optimising the 9 parameters, and evaluated by comparing predicted turbidities with a validation subset of the measured data. The optimised parameter set provided a statistically highly significant fit of the model to both the calibration and the validation data subsets. The fitted parameters and standard errors are shown in Table 7.1 and full details are presented by Heath et al. (in preparation). Figure 7.2 shows the scatter plot of fitted and measured turbidities for the calibration period, and Figure 7.3 for the validation period. Figure 7.4 shows the fitted model for the calibration and validation periods as a time series at one of the sampling sites.

| PARAMETER | DESCRIPTION | FITTED VALUE | STANDARD ERROR |
|---|---|---|---|
| $T_a$ | Autocorrelation time scale for bed stress hindcasting (d) | 4.723 | 0.207 |
| $\mu$ | Decay rate for bed stress hindcasting | 0.652 | 2.281 |
| $\alpha$ | Scaling coefficient | 54.711 | 342.517 |
| $\omega_s$ | Particle sinking rate ($m.s^{-1}$) | 0.000210 | |
| $\varepsilon$ | Seabed mud content exponent term | 0.1422 | 1.169 |
| $\delta$ | Bed stress exponent term | 0.729 | 2.326 |
| $\gamma$ | Sinking rate exponent term | 0.823 | 0.295 |
| $\beta$ | Time-varying erodibility exponent | 1.708 | 3.186 |
| $t_\beta$ | Phase shift for time-varying erodibility cycle (d) | 0.0275 | 105.480 |

**Table 7.1** Parameter values and their standard deviations from Nelder Mead optimisation of the model to the calibration data set of measured turbidity profiles.

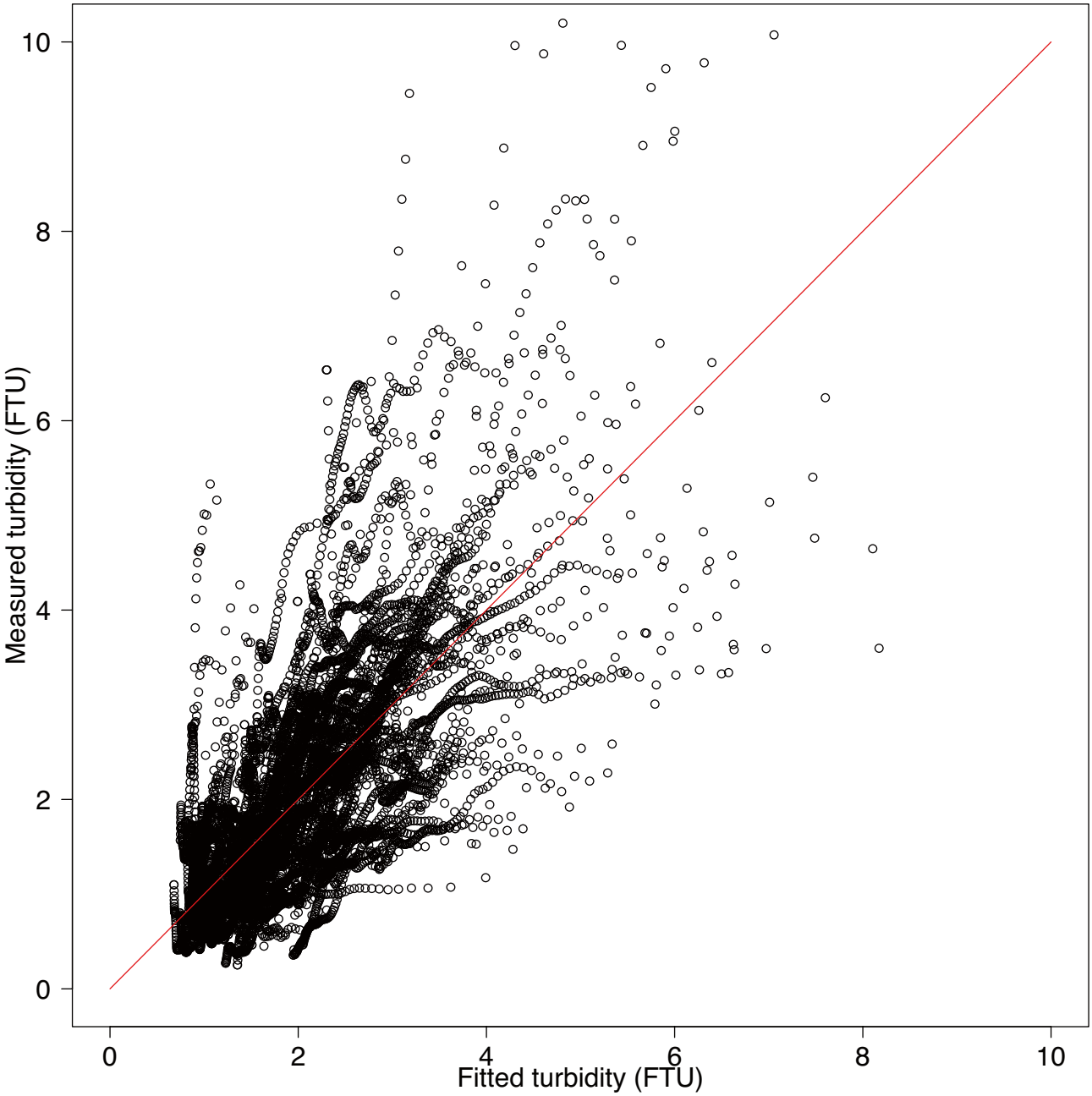


**Fig 7.2** Scatterplot of fitted and measured turbidities for the calibration dataset. Pearson correlation coefficient between measured and fitted turbidity in the calibration data set = 0.699, 95% confidence interval: 0.689 - 0.708. $t$ = 104.04, $df$ = 11343, $p\text{-}value < 2.2e^{-16}$.

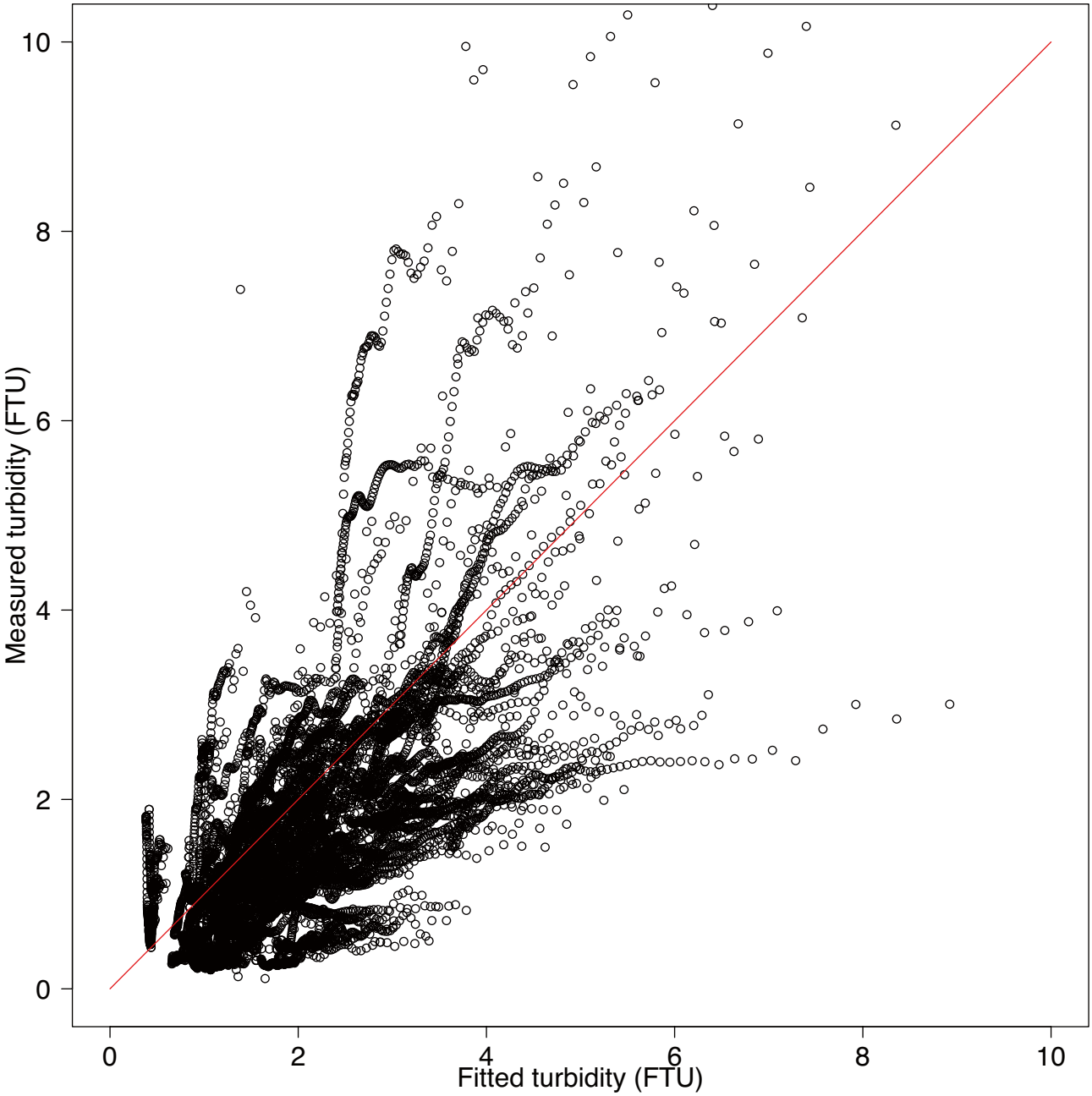


**Fig 7.3** Scatterplot of fitted and measured turbidities for the validation dataset period. Pearson correlation coefficient between measured and fitted turbidity in the validation data set = 0.620, 95% confidence interval: 0.608 - 0.630. $t$ = 86.619, $df$ = 12042, $p\text{-}value < 2.2e^{-16}$.

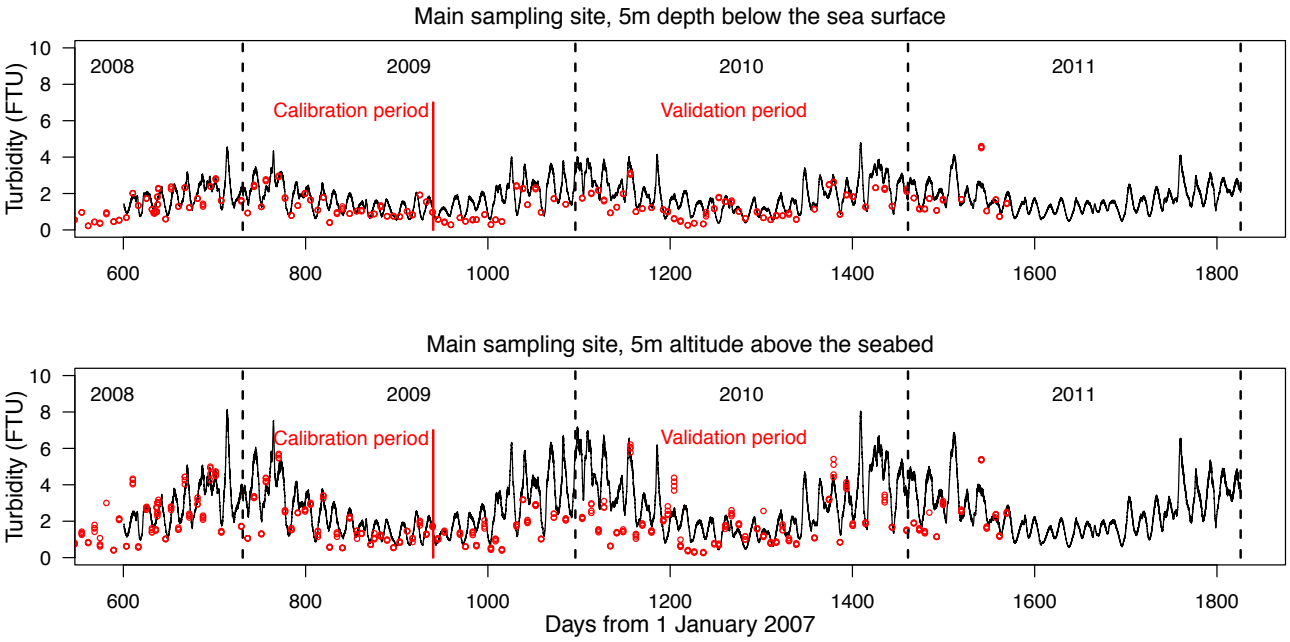


**Fig 7.4** Fitted model predictions and observed data on turbidity at two horizons in the water column (5 m depth below the sea surface (upper), 5 m altitude above the seabed (lower)). Red symbols represent the measured turbidity on each sampling occasion at ±1 m of the modelled horizon. Solid black lines are the model predictions using the optimised parameters set based on the calibration period (to the left of the red vertical line). Data to the right of the red vertical line represent a validation of the model since the measured values were not involved in the optimisation.

## 07/4.1 TRANSLATING TURBIDITY INTO LIGHT PENETRATION DEPTH

Prior to the study period reported here (February 2007-May 2008), vertical profiles of photosynthetically active radiation (PAR) had been collected simultaneously at the seas surface and in vertical depth profiles on each weekly visit to one of the sampling sites. From these data, and empirical relationship between the vertical attenuation coefficient (natural logarithmic) of downwelling sea surface irradiation, and turbidity was established. The relationship also involved the in-situ concentration of phytoplankton chlorophyll which absorbs a portion of the downwelling light. The fitted relationship was:

PAR attenuation ($m^{-1}$) = 0.1473 + 0.0620 · turbidity + 0.0082·chlorophyll; $p < 0.001$

where turbidity is given in FTU as elsewhere in this study, and chlorophyll in $mg.m^{-3}$.

Using this relationship, we can estimate the depth of the 1% sea surface isolume in the absence of any chlorophyll from the turbidity at 5 m depth predicted by our sediment model (Figure 7.5). The 1% sea surface irradiance approximately corresponds to zero net photosynthesis i.e. gross photosynthetic uptake of carbon equals respiration. So the depth of this isolume is a measure of the euphotic zone thickness.

## 07/4.2 IMPACT OF TIDAL OR WAVE ENERGY EXTRACTION SCENARIOS

In order to scope the impact on euphotic zone thickness of the extraction of tidal or wave energy, we re-ran the bed shear stress calculation using the MIKE by DHI simulation outputs for the sampling sites, but assuming some removal of either tidal power by diminishing the depth mean current speed, or wave power by diminishing the significant wave height (but not the wave period).

Provide that the water depth is larger than half the wavelength, the power associated with a wave train is

$$P_w = \frac{\rho g^2}{64\pi} H^2 T$$

Where $P_w$ is the power per metre of wave front ($W.m^{-1}$), $H$ is the wave height and $T$ is the wave period.

The equivalent measure for a current flow (power per metre at the sea surface perpendicular to the flow) is given by:

$$P_c = \frac{1}{2}\rho h V^3$$

where h is the seabed depth and V is the depth mean current speed.

Averaged over the three calendar years 2009, 2010 and 2011, the mean wave power at the sampling site illustrated in Figure 7.4 was 7.37 $KW.m^{-1}$, s.d. 15.18 $KW.m^{-1}$. The corresponding figure for the tidal flow was 20.49 $KW.m^{-1}$, s.d. 11.65 $KW.m^{-1}$.

Removing an arbitrary value of half of the total available wave power at this site (averaged over the three years = 3.685 $KW.m^{-1}$) would be equivalent to reducing the significant wave height to $\sqrt{0.5} = 0.71$ of the unexploited state. Removing the same quantity of power by attenuating the tidal flow would represent only an 18% draw-down of the long terms average current power, or a diminishing of the tidal speed to $\sqrt[3]{0.82} = 0.936$ of the unexploited state.

We independently attenuated the significant wave height and the depth mean tidal current speed in the MIKE by DHI outputs, and recomputed the bed shear stress, the turbidity and the 1% irradiance depth for each case. The results showed that removing power equivalent to half of the wave power at this site had an imperceptible effect on the light environment (mean and s.d. of 1% irradiance depths: unexploited system 18.46 m s.d. 3.20 m; removing 50%l of wave power 18.98 m s.d. 3.20 m; removing equivalent power as tidal attenuation 18.87 m s.d. 3.08 m).

The wave power resource at the study site is small, so we also assessed the impact of removing a larger quantity of power (10 $kW.m^{-1}$, approximately half of the long-term average tidal resource) purely by attenuating the tidal current speed

(current speed reduced to 70% of unexploited system). The impact on 1% irradiance depth was small but perceptible (3-year mean 20.14 m s.d. 3.18 m). Much larger decreases in the depth averaged current speed were required to produce significant effects on the 1% irradiance depth. For example, a 50% reduction in speed, corresponding to and 87.5% removal of power, produced a 4.5 m deepening of the 1% irradiance depth (3-year mean 23.05 m s.d. 3.09 m; Figure 7.5)

Overall, it is clear that the level of power extraction at this site which would have any noticeable effect on light penetration depths would be so large as to require massive engineering structures which would have other more serious implications for the environment and ecology. This is exactly the sort of first-order advice that is required, without the need to embark on large and expensive simulations relying on computationally intensive approaches.

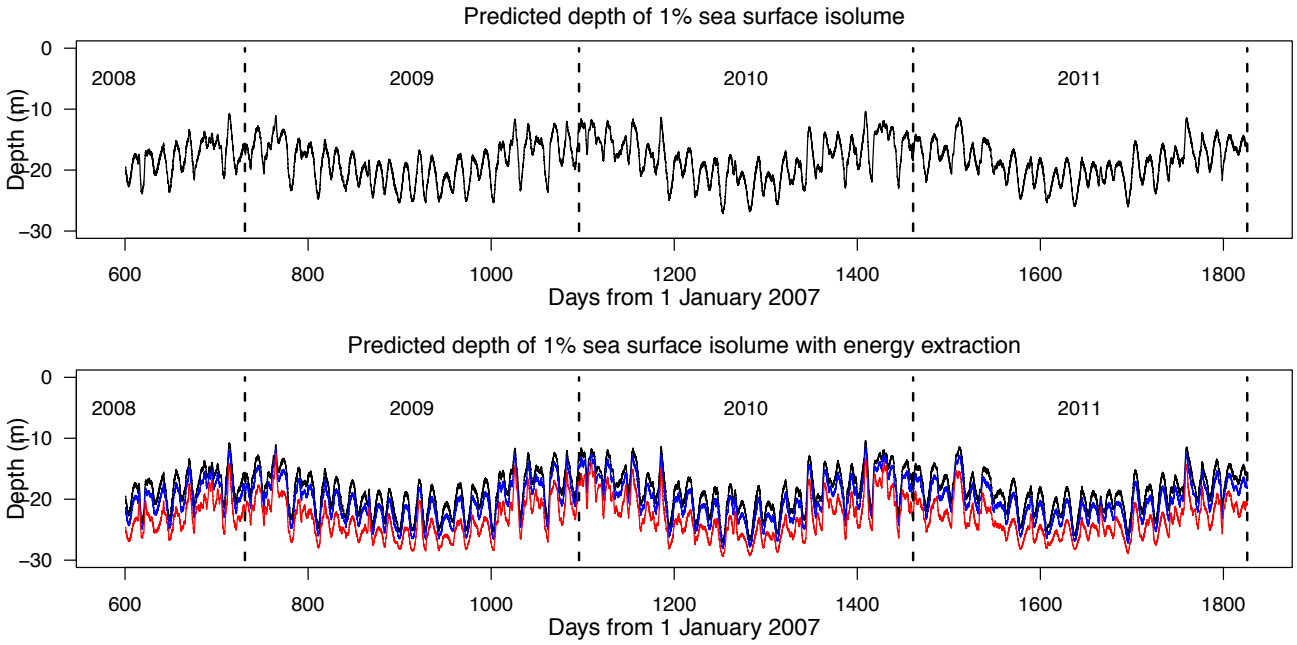


**Fig 7.5** Predicted depths of the 1% sea surface isolume based on downwelling light attenuation coefficients estimated from 5 m depth turbidity derived by the suspended sediment model. The predictions assume zero chlorophyll in the water column so that light attenuation is due only to suspended sediment. Upper panel, 1% light depth predicted using the simulations of actual tidal currents and wave climate from the MIKE by DHI simulations. Lower panel, 1% light depth predicted using energy extraction scenarios. Blue line, reduction in depth mean tidal current speed corresponding to 10 $kW.m^{-1}$ power removal (current speed reduced to 81.5%). Red line, 50% reduction in current speed, corresponding to 87.5% power extraction. The attenuation depth in the unexploited system is indicated by the black line

## 07/5 CONCLUSIONS

- The hydrodynamic principles of how particle grains are mobilised and lifted into suspension by current shear stresses, and settle back to the sea floor are well understood. Functional relationships can be effectively calibrated from controlled laboratory experiments.

- Real-world sediments composed of multiple grain-size classes in sorted layers, and containing active microbial ecosystems and macrofauna, cannot easily be replicated in laboratory experiments. There is a lack of understanding of how ecology affects sediment erodibility, but a growing realisation that it is important, even dominant in some situations, even in open shelf seas.

- Fully three-dimensional models of shelf sea suspended sediment are computationally intensive and require extensive data resources for calibration. Even so, none effectively include the seasonality of sediment erodibility due to biological consolidation processes.

- We propose a lightweight, one-dimensional (vertical) model of suspended sediment concentrations which caricatures the essential hydrodynamic processes, as a tool for quick assessments of the impact of energy extraction. In a case study, the model was parameterised by fitting to observational data, and showed that realistic levels of energy extraction are likely to produce only imperceptible effects on suspended sediment concentrations, light attenuation and predicted euphotic zone depths.

## 07/6 APPENDIX 1

Summary of methods for fitting and validating the sediment model at Stonehaven

Time series of depth averaged current speed and direction at 15 min intervals over 2008-2011 were reconstructed for each sampling site, using tidal harmonics extracted from a calibrated high resolution tidal model of the region constructed in MIKE 3D by DHI (Sabatino et al. submitted).

Significant wave height, mean wave period and mean wave direction at 15 min intervals from the UK Wavenet Firth of Forth monitoring buoy approximately 50km from the study area, were available for estimating wave orbital velocities at the sampling sites from July 2008 onwards. Time series of wave properties at each turbidity sampling site were predicted from the Wavenet buoy data using statistical relationships extracted from a spatially resolved, coupled wave-current model for the region constructed in MIKE by DHI (Sabatino et al., submitted).

Time series of orbital velocities at the seabed were derived from the estimated 15 minute significant wave height and peak wave period at each site using the algorithm of Soulsby (2006).

Time series of seabed shear stress at 15 min intervals were derived from the combination of depth averaged tidal current speed and direction and the wave orbital velocities and directions, following the algorithm detailed in Soulsby and Clarke 2005.

back to contents

The 371 vertical profiles of turbidity (30,433 individual measurements of turbidity at depth) were divided into two parts: data collected prior to 1 August 2009 (145 profiles, 12,044 measurements, referred to as the calibration period), and data collected after 1 August 2009 (226 profiles, 18,389 measurements, referred to as the validation period).

All 9 parameters of the model were fitted by minimising the r.m.s error between the entire calibration set of observed turbidity at depth at all sampling sites, and predicted values assuming the inputs of bed shear stress time series, seabed mud content, and sea surface altitude above the seabed at each site. Minimisation was performed by standard Nelder Mead optimisation using the 'optim' function in R,, with hessian matrix output so as to derive the standard errors of the parameters. The quality of the fit was measured with the Pearson correlation coefficient.

The fitted parameters of the model were then used to predict the time series of turbidity at two horizons in the water column at each site (5 m altitude above the seabed, and 5 m depth below the sea surface) for the full duration of the available bed shear stress time series at each site (July 2008 – December 2011). The predictions for the calibration and validation period at each site where then compared with the measured turbidity using the Pearson correlation coefficient.

## 07/7 REFERENCES

Amos, C.L., Daborn, G.R., Christian, H.A., Atkinson, A. & Robertson, A. 1992. *In situ erosion measurements on fine-grained sediments from the Bay of Fundy.* Marine Geology 108, 175-196.

Andersen, T.J. 2001. *Seasonal variation in erodibility of two temperate, microtidal mudflats.* Estuarine, Coastal and Shelf Science 53, 1-12.

Andersen, T.J. & Pejrup, M., 2002. *Biological mediation of the settling velocity of bed material eroded from an intertidal mudflat, the Danish Wadden Sea.* Estuarine, Coastal and Shelf Science 54, 737-745.

Armitage, N. & Rooseboom, A., 2010. *The link between Movability Number and Incipient Motion in river sediments.* Water SA, 36(1), 89-96.

Austen, I., Andersen, T.J. & Edelvang, K. 1999. *The influence of benthis diatoms and invertebrates on the erodibility of intertidal mudflats, the Danish Wadden Sea.* Estuarine, Coastal and Shelf Science 49, 99-111.

Bartzke, G., Bryan, K.R., Pilditch, C.A. & Huhn, K. 2013. *On the stabilizing influence of silt on sand beds.* Journal of Sedimentary Research 83, 691-703.

Beheshti, A.A. & Ataie-Ashtiani, B. 2008. *Analysis of threshold and incipient conditions for sediment movement.* Coastal Engineering 55 (2008) 423–430.

Borsje, B.W., Hulscher, S.J.M.H., de Vries, M.B. & de Boer, G.J. 2008. *Modelling large scale cohesive sediment transport by including biological acgtivity.* River, Coastal and Estuarine Morphodynamics: RCEM 2007 – Dohmen-Janssen & Hulscher (eds). Taylor & Francos Group, London.p 255-262.

Bresnan, E., Hay, S., Hughes, S.L., Fraser, S., Rasmussen, J., Webster, L., Slesser, G., Dunn, J. & Heath, M.R. 2008. *Seasonal and interannual variation in the phytoplankton community in the north east of Scotland.* Journal of Sea Research 61, 17-25.

Briggs, K.B., Cartwright, G., Friedrichs, C.T. & Shivarudruppa, S. 2015. *Biogenic effects on cohesive sediment erodibility resulting from recurring seasonal hypoxia on the Louisiana shelf.* Continental Shelf Research 93, 17-26.

Burt, N. 1986. *Field settling velocities of estuary muds.* In: Estuarine cohesive sediment dynamnics, Ed. Mehta, A.J. Springer-Verlag, Berlin, Heidelberg, New York, Tokyo, p 126-150.

Camenen, B., 2007. *Simple and general formula for the settling velocity of particles.* J. Hydraul. Eng. 133 (2), 229–233.

Cancino, L. & Neves, R., 1999. *Hydrodynamic and sediment suspension modelling in estuarine systems. Part I: description of the numerical models.* Journal of Marine Systems 22, 105-116.

Collins, M.B. & Rigler, J.K., 1982. *The use of settling velocity in defining the initiation of motion of heavy mineral grains, under unidirectional flow.* Sedimentology 29, 419–426.

Danish Hydraulics Institute 2013. *MIKE21 and MIKE3 Flow Model FM. Mud Transport Module Short Description.* DHI Denmark, 12pp.

De Vires, M.B. & Borsje. B.W. 2008. *Organisms influence fine sediment dynamics on basin scale.* PECS 2008 – LIVERPOOL – UK.

Dobrynin, M. 2009. *Investigating the Dynamics of Suspended Particulate Matter in the North Sea Using a Hydrodynamic Transport Model and Satellite Data Assimilation.* Dissertation zur Erlangung des Doktorgrades der Naturwissenschaften im Department Geowissenschaften der Universität Hamburg Petersburg. Hamburg 2009. 109pp.

El Ganaoui, O., Schaaff, E., Boyer, P., Amielh, M., Anselmet, F. & Grenz, C. 2004. *The deposition and erosion of cohesive sediments determined by a multi-class model.* Estuarine, Coastal and Shelf Science 60, 457-475.

Fonseca, M.S., 1989. *Sediment stabilization by Halophila decipiens in comparison to other seagrasses.* Estuarine Coastal Shelf Sci., 29: 501-507.

Gerritsen, H., Vos, R.J., van der Kaaij, T., Lane, A. & Boon, J.G. 2000. *Suspended sediment modelling in a shelf sea North Sea.* Coastal Engineering 41, 317–352.

Grant J. & Gust, G. 1987. *Prediction of coastal sediment stability from photopigment purple sulphur bacteria.* Nature 330, 244-246.

Heath, M.R., Sabatino, A.D., McCaig, C. & O'Hara Murray, R.B. (in preparation). *Modelling spatial and temporal patterns of turbidity off the east coast of Scotland.*

Huettel, M., Ziebis, W. & Forster, S., 1996. *Flow-induced uptake of particulate matter in permeable sediments.* Limnology and Oceanography, 41(2), 309-322.

Krone, R.B., 1978. *Aggregation of suspended particles in estuaries.* In: Kjerfve, B. (Ed.), Estuarine Transport Processes. University of South Carolina Press, Colombia, pp. 177-190.

Kuhrts, C., Fennel, W. & Seifert, T., 2004. *Model studies of transport of sedimentary material in the western Baltic.* Journal of Marine Systems 52, 167-190.

Le Hir, P. & Karlikow, N., 1992. *Sediment transport modelling in a macrotidal estuary: do we need to account for consolidation processes?* Proceedings of the Coastal Engineering Conference 3, 3121-3133.

Liu, H. K., 1957. *Mechanics of sediment-ripple formation.* Journal of the Hydraulics Division, 83(2), 1-23.

Lubarsky HV, Hubas C, Chocholek M, Larson F, Manz W, et al. (2010). *The Stabilisation Potential of Individual and Mixed Assemblages of Natural Bacteria and Microalgae.* PLoS ONE 5(11): e13794. doi:10.1371/journal.pone.0013794.

Lumborg, U., Andersen, T.J. & Pjirup, M. 2006. *The effect of Hydrobia ulvae and microphytobenthos on cohesive sediment dynamics on an intertidal mudflat described by means of numerical modelling.* Estuarine, Coastal and Shelf Science 68, 208-220.

McCave, N. 1984. *Erosion, transport and deposition of fine-grained marine sediments.* Geological Society, London, Special Publications 1984, v. 15, p. 35-69.

Mehta, A.J., 1989. *On estuarine cohesive sediment suspension behaviour.* Journal of Geographical Research 94 (C10), 14303e14314.

Mercier, C. & Delhez, E.J.M. 2007. *Diagnosis of the sediment transport in the Belgian Coastal Zone.* Estuarine, Coastal and Shelf Science 74, 670-683.

Mitchener, H. & Torfs, H. 1996. *Erosion of mud/sand mixtures.* Coastal Eng., 29, 1–25.

Montague, C.L., 1986. *Influence of biota on erodibility of sediments.* In: Mehta, A.J. (Ed.), Estuarine Cohesive Sediment Dynamics. Springer-Verlag, Berlin, Heidelberg, NewYork, Tokyo, pp. 251-269.

Nowell, A.R.M., Jumars, P.A. & Eckman, J.E., 1981. *Effects of biological activity on the entrainment of marine sediments.* Marine Geology 42, 133-153.

Oppenheim, D.R. & Paterson, D.M., 1990. *The fine structure of an algal mat from a freshwater maritime antarctic lake.* Can. J. Bot., 68: 174-183.

Pandoe, W.W. & Edge, B.L., 2004. *Cohesive sediment transport in the 3D hydrodynamic-baroclinic circulation model: study case for idealized tidal inlet*. Ocean Engineering 31, 2227-2252.

Paphitis, D., 2001. *Sediment movement under unidirectional flows: an assessment of empirical threshold curves Coas.* Eng. 43, 227–245.

Parchure, T.M.. & Mehta, A.J. 1985. *Erosion of soft cohesive sediment deposits.* Journal of Hydraulic Engineering – ASCE 111 910), 1308-1326.

Partheniades, E. 1965. *Erosion and Deposition of Cohesive Soils.*
Journal of the Hydraulics Division 91, 105-139.

Paterson, D. M. & Black, K.S. 1999. *Water flow, sediment dynamics and benthic biology.* Advances in Ecological Research 29. Academic Press. ISBN 0120139294.

Paterson, D. M., Tolhurst, T. J., Kelly, J.A., Honeywill, C., De Deckere, E.M.G.T., Huet, V., Shayler, S.A., Black, K.S., De Brouwer , J. & Davidson, I. 2000. *Variations in sediment properties, Skeffling mudflat, Humber Estuary, UK.* Continental Shelf Research 20, 1373-1396.

Paterson, D.M., 1989. *Short-term changes in the erodibility of intertidal cohesive sediments related to the migratory behaviour of epipelic diatoms.* Limnology and Oceanography 34, 223-234.

Pohlmann, T. & Puls, W., 1994. *Currents and transport in water.* In: Sundermann, J. (Ed.), Circulation and contaminant fluxes in the North Sea. Springer Verlag, Berlin, pp. 345-402.

Reynolds, O., 1883. *An experimental investigation of the circumstances which determine whether the motion of water shall be direct or sinuous, and of the law of resistance in parallel channels*. Philosophical Transactions of the Royal Society 174 (0): 935–982.

Ribbe, J. & Holloway, P., 2001. *A model of suspended sediment transport by internal tides.* Continental Shelf Research 21, 395-422.

Richardson, J.F. & Zaki, W.N. 1954. *Sedimentation and fluidization, Part I.* Transcations of the Institution of Chemical Engineers 32, 35-53.

Riethmuller, R., Heineke, M., Kuhl, H. & Keuker-Rudiger, R., 2000. *Chlorophyll a concentration as an index of sediment surface stabilisation by microphytobenthos?* Continental Shelf Research 20, 1351-1372.

Rouse, H. 1937. *Nomogram for the settling velocity of spheres.* In: Division of Geology and Geography, Exhibit D of the Report of the Commission on Sedimentation, 1936-37, National Research Council, Washington, D.C., pp. 57-64.

Rowden, A.A., Jago, C.F. & Jones, S.R. 1998. *Influence of benthic macrofauna on the geotechnical and geophysical properties.* Continental Shelf Research 18, 1347-1363.

Sabatino, A.D., McCaig, C., O'Hara Murray, R.B. & Heath, M.R. (in preparation). *Modelling surges and waves on the east coast of Scotland.*

Sadat-Helbar, S.M., Amiri-Tokaldany, E. Darby, S. & Shafaie, A. 2009. *Fall Velocity of Sediment Particles.* Proceedings of the 4th IASME / WSEAS Int. Conference on Water Resources, Hydraulics and Hydrology (WHH'09) pp. 39-45.

Serpetti, N. 2012. *Modelling and mapping the physical and biogeochemical properties of sediments on the North Sea coastal waters.* PhD Thesis, University of Aberdeen. 249pp.

Serpetti, N., Heath, M., Rose, M. & Witte, U. (2012). *Mapping organic matter in seabed sediments off the north-east coast of Scotland (UK) from acoustic reflectance data.* Hydrobiologia 680, 265–284.

Shields, A., 1936. *Application of Similarity Principles and Turbulence Research to Bedload Movement.* English Translation of the original German Manuscript., Hydrodynamics Laboratory, California Institute of Technology, Publication No. 167.

Soulsby, R.L 1995. *Bed shear-stresses due to combined waves and currents.* In: Advances in Coastal Morphodynmaics, Eds: Stive, M.J.F., De Vriend, H.J., Fredsoe, J., Hamm, L., Soulsby, R.L., Teisson, C. and Winterwerp, J.C. pp 4-20 - 4-23. Delft Hydraulics, Delft, NL. ISBN 90-9009026-6.

Soulsby, R.L. 1987. *Calculating bottom orbital velocity beneath waves.* Coastal Engineering 11, 371-380.

Soulsby, R.L. 1997. *Dynamics of marine sands: a manual for practical applications.* Thomas Telford, London. ISBN 0-7227-2584-X.

Soulsby, R.L. 2006. *Simplified calculation of wave orbital velocities.* HR Wallingford Report TR 155. February 2006. 28pp.

Soulsby, R.L. and Clarke. S. 2005. *Bed shear-stresses under combined waves and tides on smooth and rough beds.* Estuary Processes Research Project. HR Wallingford Report TR 137. August 2005. 52pp.

Soulsby, R.L. & Smallman, J.V. 1986. *A direct method of calculating bottom orbital velocity under waves.* Hydraulics Research Limited, Report SR 76, 14pp.

Soulsby, R.L. & Whitehouse, R.J.S. 2005. *Prediction of ripple properties in shelf seas. Mark 2 predictor for time evolution.* HR Wallingford Report TR 154. 97pp.

Stevens, A.W., Wheatcroft, R.A. & Wiberg, P.L. 2007. *Seabed properties and sediment erodibility along the western Adriatic margin, Italy.* Continental Shelf Research 27, 400–416

Sutherland, T.F., Grant, J. & Amos, C.L., 1998. *The effect of carbohydrate production by the diatom Nitzschia curvilineata on the erodibility of sediment.* Limnology and Oceanography 43, 65-72.

Teisson, G. 1991. *Cohesive suspended sediment transport: Feasibility and limitations of numerical modelling.* Journal of Hydraulic Research 29, 755-769.

back to contents

Van den Eynde, D., 2004. *Interpretation of tracer experiments with fine grained dredging material at the Belgian continental shelf by the use of numerical models.* Journal of Marine Systems 48, 171-189.

Van Rijn, L.C. 1984. *Sediment Transport, Part II: Suspended Load Transport.* Journal of Hydraulic Engineering 10, 1613–1641.

Van Rijn, L.C., 1993. *Principles of Sediment Transport in Rivers, Estuaries and Coastal Seas.* Amsterdam, Aqua Publications

Ward, L. G., Kemp, W. M. & Boynton, W. R., 1984. *The influence of waves and seagrass communities on suspended particulates in an estuarine embayment*. Marine Geology, 59(1), 85-103.

Whitehouse, R.J.S., Soulsby, R.L., Roberts, W. & Mitchener, H.J., 2000. *Dynamics of Estuarine Muds.* HR Wallingford Limited and Thomas Telford Limited, pp. 210.

Widdows, J., Brown, S., Brinsley, M.D., Salkeld, P.N. & Elliot, M., 2000. *Temporal changes in intertidal sediment erodability; influence of biological and climatic factors.* Continental Shelf Research 20, 1275-1289.

Wilcock, p., Pitlick, J. & Yantao, C.. 2009. *Sediment transport primer: estimating bed-material transport in gravel-bed rivers.* Gen. Tech. Rep. RMRS-GTR-226. Fort Collins, CO: U.S. Department of Agriculture, Forest Service, Rocky Mountain Research Station. 78 p.

Winterwerp, J.C., 2002. *On the flocculation and settling velocity of estuarine mud.* Continental Shelf Research 22, 1339e1360.

Wu, W. & Wang, S.S.Y., 2006. *Formulas for sediment porosity and settling velocity.* J. Hydraul. Eng. 132 (8), 858–862.

You, Z.-J., 2004. *The effect of suspended sediment concentration on the settling velocity of cohesive sediment in quiescent water.* Ocean Engineering 31, 1955-1965.

ISBN 978-0-9934256-1-5

www.masts.ac.uk

MASTS: Company Number – SC485726; Charity Number – SC045259.

**Dr Mark James**
+44 (0)1334 467 312
maj8@st-andrews.ac.uk

**MASTS**
C/O Scottish Oceans Institute
East Sands
St Andrews, Fife
KY16 8LB
Scotland/UK

**Prof Jonathan Side**
+44 (0)1856 850 605
j.c.side@hw.ac.uk

**Heriot Watt University**
The Old Academy
Back Road
Stromness, Orkney
KW16 3AW
Scotland/UK